LEIBNIZ-INSTITUT
FÜR
ATMOSPHÄREN
PHYSIK
IAP

INAUGURAL-DISSERTATION

am Leibniz-Institut für Atmosphärenphysik in Kühlungsborn
zur Erlangung der Doktorwürde
der Mathematisch-Naturwissenschaftlichen Fakultät
der Universität Rostock

Thermal structure and gravity waves in the Arctic middle atmosphere above ALOMAR (69.3° N, 16.0° E)

von
Armin Schöch

Abstract:

The ALOMAR Rayleigh/Mie/Raman lidar observes the polar middle atmosphere above Northern Norway (69.3° N, 16.0° E). It probes temperatures in the entire middle atmosphere, noctilucent clouds and polar stratospheric clouds since summer 1994. This thesis gives a comprehensive overview of the middle atmosphere temperatures measured with the lidar between 1997 and 2005. During night-time, the lidar temperature measurements cover the altitude range 30 km to 85 km while in the Arctic summer daylight conditions, temperatures can be derived from 30 km to 65 km altitude.

The seasonal temperature variation measured with the lidar matches the ECMWF analyses at the lower end of the altitude range and the Luebken1999 rocket climatology in summer at the upper end. Comparisons to other reference atmospheres show larger differences, especially in winter. Part of these can be explained by sudden stratospheric warmings and the generally larger temperature variability in winter. Stratospheric warmings in winter are found to be accompanied by a simultaneous cooling in the middle mesosphere in most cases. Mesospheric inversion layers are observed in 4.6% of all measurements only.

Gravity waves are observed as short-periodic temperature fluctuations in the middle atmosphere. Their energy in the stratosphere is largest in winter and summer and smallest around the equinoxes. The differences in amplitude growth with height indicate stronger wave damping in winter than in summer. The influence of the background wind field on gravity wave propagation is demonstrated in a case-study applying wavelet analyses to a winter measurement. A case-study from the MaCWAVE/MIDAS rocket campaign in summer 2002 shows the large advantage of using joint lidar, radar, falling sphere and radiosonde measurements in studying gravity waves.

Postal address:
Schloss-Str. 6
18225 Ostseebad Kühlungsborn
Germany

IAP Kühlungsborn
July 2007
IAP Nr. 21/2007
ISSN 1615–8083

LEIBNIZ-INSTITUT
FÜR
ATMOSPHÄREN
PHYSIK

Thermal structure and gravity waves in the Arctic middle atmosphere above ALOMAR (69.3° N, 16.0° E)

von
Armin Schöch

Dieser Forschungsbericht wurde als Dissertation von der Mathematisch-Naturwissenschaftlichen Fakultät der Universität Rostock angenommen.

Gutachter:	**Prof. Dr. F.-J. Lübken (Universität Rostock)**
	Prof. Dr. U.-P. Hoppe (Forsvarets forskningsinstitutt, Kjeller, Norwegen)

verteidigt am: 13. Juli 2007

Abstract

The ALOMAR Rayleigh/Mie/Raman lidar observes the polar middle atmosphere above Northern Norway (69.3° N, 16.0° E). It probes temperatures in the entire middle atmosphere, noctilucent clouds and polar stratospheric clouds since summer 1994. This thesis gives a comprehensive overview of the middle atmosphere temperatures measured with the lidar between 1997 and 2005. During night-time, the lidar temperature measurements cover the altitude range 30 km to 85 km while in the Arctic summer daylight conditions, temperatures can be derived from 30 km to 65 km altitude.

The seasonal temperature variation measured with the lidar matches the ECMWF analyses at the lower end of the altitude range and the Luebken1999 rocket climatology in summer at the upper end. Comparisons to other reference atmospheres show larger differences, especially in winter. Part of these can be explained by sudden stratospheric warmings and the generally larger temperature variability in winter. Stratospheric warmings in winter are found to be accompanied by a simultaneous cooling in the middle mesosphere in most cases. Mesospheric inversion layers are observed in 4.6% of all measurements only.

Gravity waves are observed as short-periodic temperature fluctuations in the middle atmosphere. Their energy in the stratosphere is largest in winter and summer and smallest around the equinoxes. The differences in amplitude growth with height indicate stronger wave damping in winter than in summer. The influence of the background wind field on gravity wave propagation is demonstrated in a case-study applying wavelet analyses to a winter measurement. A case-study from the MaCWAVE/MIDAS rocket campaign in summer 2002 shows the large advantage of using joint lidar, radar, falling sphere and radiosonde measurements in studying gravity waves.

Zusammenfassung

Das ALOMAR Rayleigh/Mie/Raman-Lidar wird zur Beobachtung der polaren mittleren Atmosphäre über Nord-Norwegen (69,3° N, 16,0° O) eingesetzt. Es untersucht seit 1994 die Temperatur in der gesamten mittleren Atmosphäre, leuchtende Nachtwolken und polare Stratosphärenwolken. Diese Doktorarbeit gibt einen Überblick der mit dem Lidar zwischen 1997 und 2005 gemessenen Temperaturen in der mittleren Atmosphäre. Dabei können bei Dunkelheit Temperaturen im Höhenbereich 30 km – 85 km bestimmt werden, während im polaren Sommer bei Tageslicht der Höhenbereich 30 km – 65 km untersucht werden kann.

Der Jahresgang der mit dem Lidar gemessenen Temperaturen passt am unteren Rand dieses Höhenbereichs sehr gut zu ECMWF Analysen und an seinem oberen Rand im Sommer zur Lübken1999 Raketen-Klimatologie. Beim Vergleich zu anderen Referenz-Atmosphären ergeben sich insbesondere im Winter teilweise große Differenzen. Diese Temperaturunterschiede sind zu großen Teilen durch stratosphärische Erwärmungen und die insgesamt höhere Variabilität im Winter zu erklären. Während stratosphärischer Erwärmungen wird oft eine Abkühlung in der mittleren Mesosphäre beobachtet. Mesosphärische Inversionsschichten treten nur in 4,6% aller Messungen auf.

Schwerewellen werden in der mittleren Atmosphäre als kurz-periodische Temperaturschwankungen beobachtet. Die Wellenenergie in der Stratosphäre hat Maxima im Winter und Sommer und Minima in den Übergangs-Jahreszeiten. Das unterschiedliche Amplituden-Wachstum mit steigender Höhe weist auf stärkere Wellen-Dämpfung im Winter als im Sommer hin. Der Einfluss des Hintergrundwinds auf die Wellen-Ausbreitung wird anhand von Wavelet-Transformationen in einer Winter-Fallstudie gezeigt. Eine Fallstudie aus der MaCWAVE/MIDAS Raketen-Kampagne im Sommer 2002 zeigt die Vorteile der Kombination von Lidar-, Radar-, Raketen- und Radiosonden-Messungen für die Schwerewellen-Analyse.

Contents

Chapter 1

Introduction

The Earth's atmosphere is a delicate and complex layer surrounding the Earth which is indispensable for all oxygen-breathing life-forms including us humans [e.g. *Kerr*, 2005a, b]. If the whole atmosphere would be compressed to the pressure at the Earth's surface, the resulting layer would have a height of only ~8 km. But as will be shown later, the pressure in the atmosphere decreases exponentially with height and it is therefore difficult to define the border between atmosphere and space. Atmospheric dynamics is an interplay of external forcings mainly by radiation from the sun and internal circulation patterns on all spatial and temporal scales. Important dynamical processes include the global pole-to-pole circulation, planetary waves, atmospheric tides, weather systems and mesoscale phenomena like single thunderstorms, bands of thunderstorms (squall lines) or fronts. On smaller scales, gravity waves, acoustic waves and turbulence are also important [*Holton*, 1992; *Andrews et al.*, 1987]. All these forcings together create the wind and thermal structure of the atmosphere.

For observations this implies that once the thermal structure of an atmosphere together with the radiation absorbed and emitted in it are known, it is possible to infer a lot of information about the dynamics and the circulation patterns needed to sustain such a thermal structure.

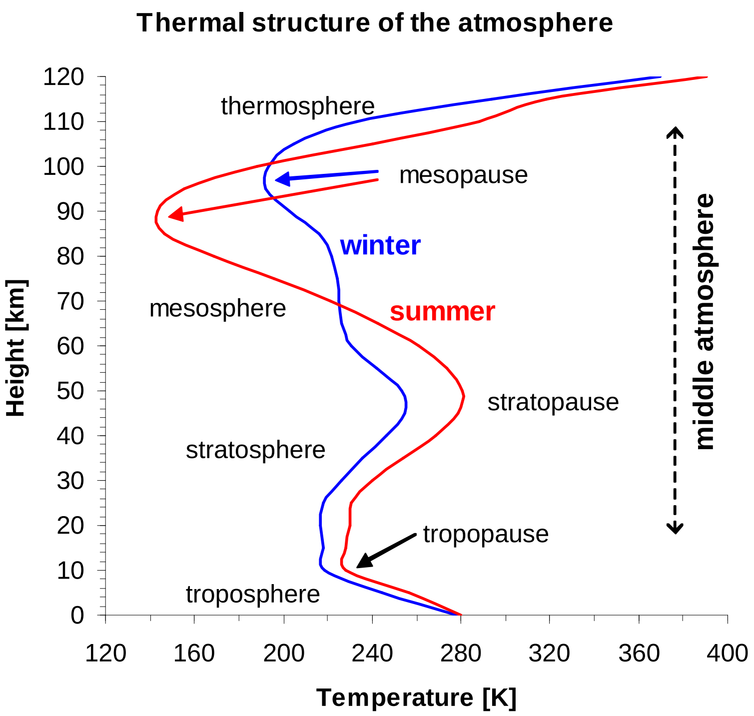

Figure 1.1: Mean temperature structure of the Earth's atmosphere from a climatological model (CIRA86, *Fleming et al.* [1990]) for summer and winter solstice conditions at 70° N.

The vertical thermal structure may be used to divide the Earth's atmosphere into several levels where temperature extrema are used to separate the different layers (see Fig. 1.1). The stratosphere, mesosphere and lower thermosphere together are called the middle atmosphere (≈ 10 km – 100 km). The results shown in this thesis will concentrate on the height range of the stratosphere and mesosphere. In the polar upper mesosphere and mesopause region, the temperature follows a counter-intuitive seasonal cycle. Temperatures are very low in summer when the atmosphere is lit all around the clock by the midnight sun and comparably high in winter when there is no solar radiation at all during the polar night. The reason for this large deviations of up to 90 K from radiative equilibrium is a mean vertical upwelling of $\sim 5\,\mathrm{cm\,s^{-1}}$ over the summer pole which induces an adiabatic cooling of $\sim 50\,\mathrm{K\,d^{-1}}$ [e.g. *Garcia and Solomon*, 1985; *Berger and von Zahn*, 2002]. A corresponding downwelling over the winter pole leads to adiabatic warming of the winter mesopause region. The main driver of this ageostrophic flow is momentum deposition by breaking of internal atmospheric waves. The most important group of these waves are called gravity waves.

Gravity waves are periodic oscillations in density, temperature, wind and chemical composition that propagate like sound waves through the atmosphere. But unlike sound waves where the restoring force is the air's compressibility, the restoring force for these waves is Earth's gravity. Acoustic or sound waves and gravity waves cover different parts of the spectrum. While acoustic waves have wavelengths of up to a few meters and periods in the sub-second range, gravity waves have horizontal wavelengths of a few up to some thousands of kilometres and periods between a few minutes up to many hours.

Gravity waves are excited in the lower troposphere by flow over orographic obstacles [e.g. *Hines*, 1989; *Nastrom and Fritts*, 1992; *Wu*, 2006], during strong convective activity [e.g. *Fritts and Nastrom*, 1992; *Preusse et al.*, 2006], at vertical wind shears, during thunderstorms [e.g. *Alexander and Holton*, 2004], in geostrophic adjustment events around the jet streams [e.g. *Fritts and Nastrom*, 1992; *Pavelin and Whiteway*, 2002], during Rossby wave breaking [e.g. *Polvani and Saravanan*, 2000; *Zülicke and Peters*, 2006] or through wave-wave interaction. Most gravity waves propagate upward until they dissipate or break in the stratosphere or mesosphere when reaching dynamical or convective instability layers or are reflected downwards [e.g. *Booker and Bretherton*, 1967; *Stockwell and Lowe*, 2001b]. The energy and momentum deposited during this process both drive the ageostrophic flow that leads to the observed cold summer mesopause and influence the circulation patterns in the stratosphere which are acting back on tropospheric weather [e.g. *Baldwin et al.*, 2003; *Christiansen*, 2005].

A number of different techniques have been used to observe and analyse gravity waves in the lower and middle atmosphere. Ground-based remote sensing of gravity waves uses lidars in the entire height range [e.g. *Chanin and Hauchecorne*, 1981; *Schöch*, 2001; *Rauthe et al.*, 2006]. In the troposphere and mesosphere, radars observe gravity waves in the wind field [e.g. *Rüster et al.*, 1996; *Serafimovich et al.*, 2005]. Airglow imager measure temperature and brightness variations in constant layers around the mesopause which are also influenced by gravity waves [e.g. *Stockwell and Lowe*, 2001a; *Suzuki et al.*, 2004]. In the troposphere and lower stratosphere radiosondes and balloons are used to obtain gravity wave parameters [*Nastrom et al.*, 1997; *Hertzog et al.*, 2002]. Rocket measurements have been used as well to analyse the seasonal and latitudinal variation of gravity wave variances [e.g. *Hirota*, 1984]. Recently, also an imaging riometer has been used to detect gravity waves in the mesopause region [*Jarvis et al.*, 2003]. A global perspective of gravity waves is obtained from satellite measurements of radiative variances, temperature, and ozone fluctuations in the middle atmosphere [e.g. *Wu and Waters*, 1996; *Eckermann and Preusse*, 1999; *Wu*, 2006]. In-situ measurements have been done with sensors on commercial aircrafts to investigate differences in the gravity waves over mountainous terrain and over the ocean [e.g. *Jasperson et al.*, 1990]. All these observational techniques resolve different parts of the gravity wave spectrum. While rockets and radiosondes measure single vertical profiles with high spatial resolution, only continuous observations with lidars, radars or airglow imagers provide information about gravity wave periods. Satellites deliver global measurements but do not have the temporal or spatial resolution to resolve the details of small-scale, short-periodic gravity waves. Numerous modelling studies have helped to better understand gravity wave spectra, their propagation and breaking as well as to quantify their impact on the atmospheric circulation and thermal structure [e.g. *VanZandt*, 1985; *Eckermann*, 1992; *Becker*, 2004].

The results presented in this thesis were obtained with a lidar located at the ALOMAR[1] observatory in Northern Norway (see map in Fig. 1.2). A lidar instrument uses laser light and a telescope coupled to photon detectors to study the vertical profiles of density, temperature and wind in the atmosphere as well as aerosols and cloud particles. It is a remote-sensing instrument capable to cover the entire lower and middle atmosphere applying different lidar techniques in the troposphere, middle atmosphere and lower thermosphere [e.g. *Hauchecorne and Chanin*, 1980; *Alpers et al.*, 2004].

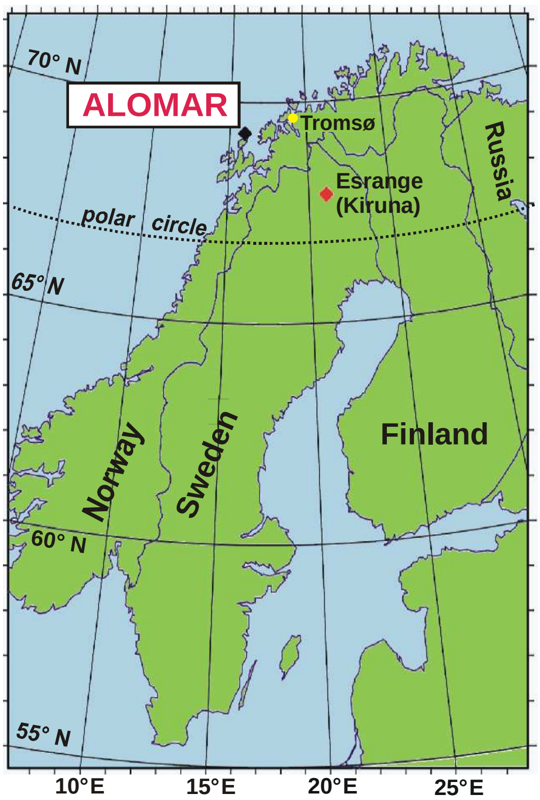

Figure 1.2: Geographical location of the ALOMAR observatory on the island of Andøya in Northern Norway.

When the laser was invented at the end of the 1950's, it was soon used to construct a lidar for atmospheric studies [*Fiocco and Smullin*, 1963]. An early review of lidar techniques has been published by *Kent and Wright* in 1970. Since then the lidar principle has been continually improved and extended to different scattering mechanisms like Rayleigh scattering [e.g. *Hauchecorne and Chanin*, 1980], resonant scattering [e.g. *Fricke and von Zahn*, 1985], Raman scattering [e.g. *Nedeljkovic et al.*, 1993] and Mie scattering on aerosols. Today lidar instruments are used in many different fields including atmospheric remote sensing of aerosols [e.g. *Ansmann et al.*, 1990; *Stein et al.*, 1994], pollution monitoring in urban areas, wake and clear-air-turbulence detection onboard aircrafts, fishery management and many more.

The ALOMAR observatory (see Fig. 1.3) is located on top of the Ramnan mountain at 378 m a.s.l. on the island of Andøya in Northern Norway 250 km north of the polar circle (Fig. 1.2) at (69.28° N, 16.01° E) and a few kilometres south of the Andøya Rocket Range (ARR). Together, these two constitute a unique place for studies in the Arctic atmosphere because it assembles not only a rocket launch site but also many other geophysical instruments like lidars, radars, ionosondes, riometers, radiometers, spectrometers and many more. All instruments are installed close together and are able to investigate a common volume above the site [*von Zahn et al.*, 1995; *Skatteboe*, 1996]. This thesis will concentrate on results from observations with the Rayleigh/Mie/Raman (RMR) lidar installed in the ALOMAR observatory but will use data from other instruments where this is useful to complete the picture of the atmosphere and better understand the processes determining the temperature structure and the amplitude and spectrum of gravity waves at this Arctic site.

The ALOMAR Rayleigh/Mie/Raman (RMR) lidar used in this study was developed through a collaboration of the Leibniz-Institute of Atmospheric Physics Kühlungsborn (Germany) with the University of Bonn (Germany), the Service d'aéronomie du CNRS at Verrières

[1]All acronyms are listed on page 146

Figure 1.3: ALOMAR observatory above the sea fog on the Ramnan mountain during operation of the RMR lidar in June 2005.

(France) and the University College London (UK). The lidar uses two lasers and two 1.8 m diameter tiltable telescopes to be able to perform simultaneous measurements in different viewing directions. It was installed in summer 1994 and has since been continually improved [*von Cossart et al.*, 1995; *Fiedler et al.*, 1997; *von Zahn et al.*, 2000].

This thesis will present some of the physics and theory of middle atmosphere temperatures and gravity waves in Chap. 2, focused on the main topics explored later with RMR lidar observations. The lidar principle and the ALOMAR RMR lidar are described in detail in Chap. 3. Chap. 4 will start with an introduction to the observations used in this thesis and will show the seasonal temperature structure above ALOMAR. The latter is investigated using the mean temperature profiles of each measurement. It is also compared to other climatological data sets and to model simulations. Proceeding to shorter time-scales, Chap. 5 will present more detailed analysis of the single mean temperature profiles focusing on mesospheric inversion layers and sudden stratospheric warmings. Both phenomena are special features of the background temperature structure and have been observed extensively with the RMR lidar. Their occurrence rate and typical characteristics are presented in Chap. 5. Chap. 6 is devoted to gravity waves which have typical time-scales of a few hours. This work investigates their seasonal variability, spectral distribution and also includes a section covering the international MaCWAVE/MIDAS rocket campaign that was conducted at ARR and ALOMAR in July 2002 and at ALOMAR and Esrange (see map in Fig. 1.2) in January 2003. Finally Chap. 7 summarises the results and presents the conclusions of this work and an outlook.

Additional tables, data processing algorithms and technical improvements of the instruments are comprised in the appendix starting on page 102. More detailed information about the technical improvements are assembled in a separate technical report [*Schöch*, 2007]. For the reader's convenience, all abbreviations used in the text are listed on page 146. All symbols used are listed on page 148.

Chapter 2

Basics of Atmospheric and Gravity Wave Theory

Before presenting the measurements in the next chapters, the following sections will give a short overview of the density, pressure and temperature structure of the lower and middle atmosphere. The static stability of the different layers in the atmosphere will be described since it influences the propagation of waves in the atmosphere. The second part of this chapter is devoted to gravity waves and will present some basics of the mathematical framework for these waves as far as it is needed in this work. A much more comprehensive review has recently been published by *Fritts and Alexander* [2003]. A short explanation of stratospheric warmings and mesospheric inversion layers will conclude this chapter.

In the whole thesis the usual meteorologic coordinate system is used where the x-axis points eastward, the y-axis northward and the z-axis upwards with the origin at the Earth's surface. Motion or averaging along the x-axis and y-axis is called "zonal" and "meridional", respectively. Positive and negative zonal winds or zonal wave phase speeds are called "eastward" (to the east) and "westward" (to the west), respectively. In the literature, the terms "easterly" (from the east) and "westerly" (from the west) are used as well but they will not be used here to avoid confusion. All heights used are geometric heights. Northern latitudes and eastern longitudes are positive, southern latitudes and western longitudes negative.

2.1 Pressure and density

The Earth's atmosphere can be treated as being in hydrostatic equilibrium for most processes. Only when the typical vertical scale H of a dynamical process in the atmosphere is in the same order or larger than its horizontal scale L, i.e. $H/L \gtrsim 1$, non-hydrostatic fluid dynamics have to be applied to describe it [*Pielke*, 1984, p. 37]. Or stated differently, a hydrostatic description can be used as long as the vertical accelerations are much smaller than the difference between pressure gradient force in the vertical and gravitation (see Eq. 2.11 in Sec. 2.5.1). For typical applications in atmospheric physics, a non-hydrostatic description is only necessary when the horizontal scale is $\lesssim 10\,\mathrm{km}$ (e.g. sound waves, squall lines, thunderstorms). As this is not the case in this work, the hydrostatic approximation will be used in the following description of the atmosphere.

The pressure p at any altitude z is then determined by the air mass above that altitude, independently of the details of the overlying density profile, and the Earth's gravitational acceleration g. The air mass can be expressed either as mass density ρ or as number density n

times the mean molecular weight of air M of 28.97 g mol^{-1} [*Wallace and Hobbs*, 1977] which is constant in the so-defined homosphere from the ground to ∼100 km due to strong vertical mixing and a short mean free path of the molecules. The differential expression is

$$dp = -g(z) \cdot \rho(z) \cdot dz = -g(z) \cdot M \cdot n(z) \cdot dz \; . \tag{2.1}$$

Combining Eq. 2.1 with the ideal gas law for pressure, number density, Boltzmann constant k_B and temperature T and integrating gives an exponential relationship with decreasing pressure with height which depends on the pressure in the start altitude z_0 and on the temperature profile of the atmosphere

$$p(z) = p(z_0) \cdot \exp\left(-\frac{M}{k_B} \cdot \int_{z_0}^{z} \frac{g(z')}{T(z')} \cdot dz' \right) \; . \tag{2.2}$$

Assuming an isothermal atmosphere and a constant gravitational acceleration, this expression simplifies to a direct exponential relation for the pressure

$$p(z) = p(z_0) \cdot \exp\left(-\frac{z - z_0}{H} \right) \; , \tag{2.3}$$

with the so defined scale height $H = \frac{k_B T}{g M}$ which is the e-folding scale of the pressure. The exact pressure profile still depends on the altitude-dependence of the scale height which varies between 5 km and 8 km in the middle atmosphere [*Dubin et al.*, 1976]. By analogy it can be shown that the density ρ follows a similar exponential decrease with height. The scale height in the middle atmosphere is ≈ 7 km. This implies that pressure and density decrease by one order of magnitude every ≈ 16 km.

2.2 Temperature

Temperature is one of the main physical quantities that determine the state of the Earth's atmosphere. Two examples for the temperature structure are shown in Fig. 1.1 in the introduction. The mean temperature structure of the atmosphere is determined by a combination of adiabatic heating and cooling in vertical motions, heating through absorption of solar UV radiation, radiative cooling at IR wavelengths and heat conduction. The major radiatively active gases are listed in Tab. 2.1 for the different altitude regions in the troposphere and middle atmosphere. Their concentrations vary with height and the net radiative contribution is warming in the troposphere and stratosphere and cooling in the mesosphere. The temperature decrease with increasing height in the troposphere is roughly $-6.5\,\mathrm{K\,km^{-1}}$ including latent heat released during water vapour condensation. The temperature maximum at the stratopause is due to strong absorption of solar UV radiation by ozone in the ozone layer between 20 km and 40 km [*Brasseur and Solomon*, 1986]. In the mesosphere, adiabatic processes and radiative cooling dominate the heat budget. The strong increase above the mesopause is again caused by absorption of solar radiation by molecular oxygen. Since this radiation is only available during the day, the temperature in the thermosphere varies strongly (up to a few 100 K) between day and night. In the lower and

Altitude	**UV heating**	**IR cooling**
thermosphere	O_2	CO_2, O, NO
mesosphere	O_2, O_3	CO_2, O_3
stratosphere	O_3	CO_2, O_3
troposphere	H_2O	CO_2, H_2O

Table 2.1: The major radiatively active gases in the lower and middle atmosphere [*Brasseur and Solomon*, 1986].

middle atmosphere, these tidal variations are observed as well. There they are due to absorption of solar radiation by ozone (in the stratosphere) and water vapour (in the troposphere) but they have much smaller amplitudes [e.g. *Forbes and Groves*, 1990].

2.3 Stability and Brunt-Väisälä frequency

When air parcels are moved up or down in the atmosphere, they follow in close agreement adiabatic changes of their intrinsic parameters like pressure, temperature and volume. This approximation is valid for most dynamical processes in the atmosphere that do not involve precipitation [*Holton*, 1992]. The potential temperature Θ is defined as the temperature an air parcel would have if it would be moved adiabatically to standard pressure $p(z_0)$. It is related to the entropy S through $S = c_p \log\Theta + const.$ and is calculated using the adiabatic index γ [e.g. *Wallace and Hobbs*, 1977] from

$$\Theta(z) = T(z) \cdot \left[\frac{p(z_0)}{p(z)}\right]^{1-\frac{1}{\gamma}} . \tag{2.4}$$

Here γ is defined as the ratio of the specific heats at constant pressure c_p and constant volume c_v to be $\gamma = \frac{c_p}{c_v} = \frac{c_v+R}{c_v}$, where R is the universal gas constant. Air parcels that move adiabatically do not change their potential temperature and thus keep their entropy, i.e. they move isentropically ($dS = 0$).

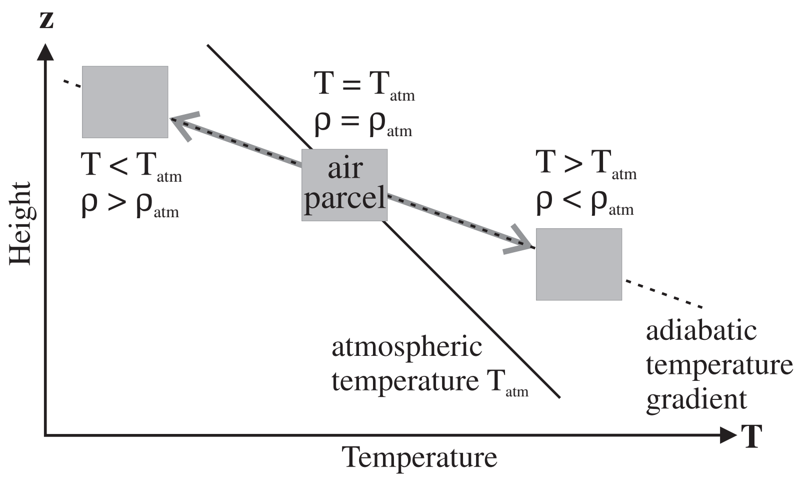

Figure 2.1: Schematic principle of buoyancy oscillations in the atmosphere.

Buoyancy oscillations can occur if the temperature gradient in the atmosphere is less than the adiabatic gradient which is roughly $-6.5\,\mathrm{K\,km^{-1}}$ in the presence of water vapour in the troposphere and $-9.8\,\mathrm{K\,km^{-1}}$ in the dry middle atmosphere. An air parcel moved up (or down) has a larger (or smaller) density than its surroundings and will fall (or rise) back to its original height. Thus an initial displacement will lead to oscillations around the original height (see schematic drawing in Fig. 2.1). The frequency of these oscillations is given by the Brunt-Väisälä frequency N which is also known as the buoyancy frequency [e.g. *Andrews et al.*, 1987]. It is defined as

$$N^2 = \frac{g}{\Theta}\frac{d\Theta}{dz} = \frac{g}{T}\left(\frac{dT}{dz} + \frac{g}{c_p}\right) = -\frac{g}{\rho}\frac{\partial\rho}{\partial z} - \frac{g^2}{c_s^2} = \frac{\gamma-1}{\gamma}\frac{g^2 M}{k_B T} , \tag{2.5}$$

where $c_s = \sqrt{\gamma R T}$ is the speed of sound. The period of such an oscillation is then given by $T_{BV} = \frac{2\pi}{N}$ and varies between 180 s and 360 s in the middle atmosphere, depending on the background temperature profile.

The Brunt-Väisälä frequency is often used to characterise the static stability of the atmosphere. If the Brunt-Väisälä frequency is larger than zero, the atmosphere is stable and oscillations are possible. A negative Brunt-Väisälä frequency results from a temperature gradient that is larger than the adiabatic gradient. In this case, a displaced air parcel will not oscillate but simply continue to rise (or fall). Thus an instable atmosphere will return to an at least marginally stable atmosphere by itself because of these movements. Super-adiabatic gradients are seldom observed in the atmosphere and in those cases where they are observed, they can only persist if there is a strong forcing that works against the balancing tendency of the atmosphere [*Sica and Thorsley*, 1996]. As soon as the forcing disappears, the atmosphere will return to a stable state.

In the troposphere and mesosphere, the temperature decreases with height. An additional local decrease in temperature due to the cold phase of a passing wave may lead to local static instability if the wave amplitude is large enough. The positive temperature gradient in the stratosphere would require a very large amplitude wave to induce instability. As the name stratosphere (from Greek "stratos" meaning "layer") implies, instability which would lead to vertical mixing occurs very seldom in the stratosphere.

2.4 Atmosphere dynamics

The movement of particles in a liquid or gas is governed by the sum of forces acting on the particle. For air moving in the atmosphere of a rotating Earth, the Navier-Stokes equation for changes in time t or position $\vec{x}$ takes the following form [*Holton*, 1992, Chap. 2]:

$$\frac{D\vec{u}(\vec{x},t)}{dt} = -\frac{1}{\rho} \cdot \vec{\nabla} p(\vec{x},t) + \vec{g} - 2\,\vec{\Omega} \times \vec{u}(\vec{x},t) + \vec{X}(\vec{x},t) \;, \tag{2.6}$$

where the change in the wind $\vec{u}$ is given in the Eulerian view (looking at a fixed position like a lidar instrument does) as the sum of the intrinsic change and the advection $\frac{D\vec{u}(\vec{x},t)}{dt} = \frac{\partial \vec{u}(\vec{x},t)}{\partial t} + \vec{u}(\vec{x},t) \cdot \vec{\nabla}\vec{u}(\vec{x},t)$.

The term on the left hand side of Eq. 2.6 describes the acceleration acting on each particle. The terms on the right list the different forces that have to be taken into account in the Earth's atmosphere:

- $-\frac{1}{\rho} \cdot \vec{\nabla} p(\vec{x},t)$ Pressure gradient force resulting from the spacial variation of the pressure field. Air parcels will move from places of relative high pressure towards those of low pressure.
- $\vec{g}$ The Earth's gravitational acceleration. For the following treatment, a spherically homogeneous distribution of the Earths mass is assumed so that this force only acts in the vertical direction.
- $-2\,\vec{\Omega} \times \vec{u}(\vec{x},t)$ Coriolis force. This pseudo force is an effect of the Earth's angular rotation rate Ω combined with its spherical shape which lead to different rotation speeds at different latitudes. Air parcels that moves southwards on the northern (southern) hemisphere will experience a force towards the west (east). Northward flow is deflected towards the east (west) on the northern (southern) hemisphere.
- $\vec{X}(\vec{x},t)$ This is a drag or friction force. At the Earth's surface, the interaction of atmosphere and orography creates surface friction decelerating the air. In the entire atmosphere, wave dissipation or breaking contributes to this term. When waves are dissipated or break, they loose some or all of their energy and momentum to the background

atmosphere. Although many waves and eddies on a large range of scales can contribute to this term, it is restricted to the effect of gravity waves in this thesis. The gravity wave drag can lead to both acceleration or deceleration of the background flow depending on whether the projection of the propagation direction of the wave to the background flow is parallel or anti-parallel to it. Sec. 2.6 shows how this term leads to an additional ageostrophic circulation in the middle atmosphere which explains the cold summer mesosphere – warm winter mesosphere paradox.

Two more equations are needed to describe motions in the real atmosphere. The continuity equation states that any change in density has to come from either convergence or divergence of the wind field or from a compression or expansion of the air

$$\frac{D\rho(\vec{x},t)}{dt} + \rho(\vec{x},t)\vec{\nabla}\cdot\vec{u}(\vec{x},t) = 0 \ . \tag{2.7}$$

Finally an energy equation is needed that relates the different variables through changes of state. For the motions considered in this thesis, all processes are treated as adiabatic changes implying $\frac{D\Theta}{dt} = 0$. Therefore differentiating Eq. 2.4 and combining with the ideal gas law for adiabatic processes gives

$$\frac{Dp(\vec{x},t)}{dt} - \frac{\gamma p(\vec{x},t)}{\rho(\vec{x},t)} \cdot \frac{D\rho(\vec{x},t)}{dt} = 0 \ . \tag{2.8}$$

The three Eqs. 2.6, 2.7 and 2.8 together form a consistent description of adiabatic processes in the atmosphere. As coupled differential equations, they are very difficult to solve in a general way. Instead, they have to be adapted and simplified according to the problem under investigation.

2.5 Gravity waves

The Earth's atmosphere contains waves on a large range of scales from the short-scale acoustic waves with wavelengths of ≤ 10 m to planetary waves with periods of days and horizontal wavelengths of some 10,000 km. In the middle of the spectrum of possible oscillations, a family of waves is called "gravity waves" or "buoyancy waves" according to the restoring force for these kind of waves.

Depending on where they propagate, gravity waves are classified as surface waves (e.g. waves on lakes and oceans) or internal waves (inside a fluid, either in the atmosphere or inside lakes [e.g. *Wiegand and Carmack*, 1986], oceans [e.g. *Nash and Moum*, 2005] or even the sun [e.g. *Charbonnel and Talon*, 2005]). At the long scale end of the internal wave spectrum, the Coriolis force has to be included in the mathematical description of the waves. These waves are then called inertio-gravity waves [*Andrews et al.*, 1987, Chap. 4.6].

Since gravity waves play an important role in driving the large-scale circulation system of the atmosphere, they have to be included in some way in all current climate models [e.g. *Becker and Fritts*, 2006; *Fritts and Alexander*, 2003, and references therein]. Usually a parameterisation is used for this purpose [e.g. *Lindzen*, 1984; *Kim et al.*, 2003] for computational reasons but recently the direct numerical simulation of gravity waves has become feasible [*Becker and Fritts*, 2006; *Berger*, 2007]. Gravity waves in the lee of mountain ranges have been studied already in the 1940s [e.g. *Scorer*, 1949]. *Hines* [1960] proposed that these kind of waves also occur higher up in the atmosphere. Recently *Fritts and Alexander* [2003] have reviewed the current state of gravity wave research. As mentioned in the introduction, gravity waves are observed with many different instruments including lidars, radars and spectrometers both from the ground and from space by satellite instruments.

2.5.1 Inertio-gravity waves

Inertio-gravity waves are waves which propagate inside a fluid and which have horizontal scales of up to a few thousand kilometres so that the Coriolis force has to be included. They are best described by a simplified Navier-Stokes equation (Eq. 2.6) where the surface friction and wave drag terms are omitted. Combined with the continuity equation (Eq. 2.7) for compressible air and the adiabatic energy equation (Eq. 2.8), we get the following equations for a Eulerian view where the wind is expressed through its components $\vec{u} = (u, v, w)$

$$\frac{Du}{dt} - fv + \frac{1}{\rho}\frac{\partial p}{\partial x} = 0 \qquad \text{(zonal component)} \qquad (2.9)$$

$$\frac{Dv}{dt} + fu + \frac{1}{\rho}\frac{\partial p}{\partial y} = 0 \qquad \text{(meridional component)} \qquad (2.10)$$

$$\frac{Dw}{dt} + \frac{1}{\rho}\frac{\partial p}{\partial z} + g = 0 \qquad \text{(vertical component)} \qquad (2.11)$$

$$\frac{1}{\rho}\frac{D\rho}{dt} + \frac{\partial u}{\partial x} + \frac{\partial v}{\partial y} + \frac{\partial w}{\partial z} = 0 \qquad \text{(compressible continuity eq.)} \qquad (2.12)$$

$$\gamma p\frac{D\rho}{dt} - \rho\frac{Dp}{dt} = 0 \qquad \text{(adiabatic energy eq.)}\ , \qquad (2.13)$$

and $f = 2\Omega\sin(\phi)$ is the Coriolis parameter treated as constant at a given latitude ϕ. The above equations are still non-linear (due to the advection terms) and coupled differential equations which cannot be solved analytically. Instead, a perturbation analysis is performed assuming a small perturbation of a constant background state. The linearisation process leading to the dispersion relation presented in the next section is described in appendix D.1.

2.5.2 Dispersion relation

The linearised versions of the above Eqs. 2.9 – 2.13 are shown in appendix D.1 in Eqs. D.9 – D.13. The linear set of equations Eq. D.14 only has a solution, if the determinant of its coefficients is zero. Using this condition, the dispersion relation for inertio-gravity waves as expressed for the vertical wave number m is derived as

$$m^2 = \frac{N^2 - \hat{\omega}^2}{\hat{\omega}^2 - f^2}(k^2 + l^2) - \frac{1}{4H_\rho^2} + \frac{\hat{\omega}^2}{c_s^2}\ , \qquad (2.14)$$

where k and l are the zonal and meridional wavenumbers, H_ρ is the density scale height and c_s is the speed of sound. $\hat{\omega}$ is the intrinsic frequency of the wave in a reference system moving with the mean background wind. It is defined as

$$\hat{\omega} = \omega - \vec{k}\vec{u}\ , \qquad (2.15)$$

where $\vec{k} = (k, l, m)$ is the wavenumber vector and ω the observed frequency of the wave. To first order, the observed frequency and the horizontal wavenumbers of a wave do not change while the wave propagates. Hence the intrinsic frequency depends on the background wind profile and can be Doppler-shifted by large amounts [e.g. *Scheffler and Liu*, 1986]. As the intrinsic frequency determines the vertical wavelength through the dispersion relation (Eq. 2.14) and influences the propagation of the waves (see Secs. 2.5.3 and 2.5.4), the background wind has a large influence on the wave propagation (see also Fig. 2.2).

Also Eq. 2.14 still comprises acoustic waves through the last term. For the typical intrinsic frequencies $\hat{\omega}$ of gravity waves, this term is very small and it will therefore be neglected in the further calculations. Then

$$m^2 = \frac{N^2 - \hat{\omega}^2}{\hat{\omega}^2 - f^2}(k^2 + l^2) - \frac{1}{4H_\rho^2} \tag{2.16}$$

$$\text{or equivalently} \qquad \hat{\omega}^2 = \frac{m^2 f^2 + (k^2 + l^2)N^2 + \frac{f^2}{4H_\rho^2}}{k^2 + l^2 + m^2 + \frac{1}{4H_\rho^2}} \ . \tag{2.17}$$

Eq. 2.16 shows directly that the range of possible intrinsic frequencies for inertio-gravity waves lies roughly between the Brunt-Väisälä frequency N (m^2 has to be positive) and the Coriolis parameter f (m has to stay finite)

$$f < \hat{\omega} < N \ . \tag{2.18}$$

Typical values for N in the middle atmosphere and f at 69° N are 5 min (at 45 km) and ∼13 hr, respectively. For so-called mid-frequency gravity waves ($f \ll \hat{\omega} \ll N$), the dispersion relation Eq. 2.16 simplifies to

$$m^2 = \frac{N^2(k^2 + l^2)}{\hat{\omega}^2} \ . \tag{2.19}$$

When m^2 becomes negative, m has an imaginary part which will lead to a term $\sim e^{-Im\{m\}z}$ in Eq. D.7 and thus to vertical damping of the waves. Waves in this regime $m^2 < 0$ are called evanescent or external waves [*Salby*, 1996, Chap. 14].

2.5.3 Vertical phase and group speeds

The propagation direction and speed of the phase lines of waves is given by the wave number vector $\vec{k} = (k, l, m)$ as $\vec{c_{ph}} = \frac{\omega}{\vec{k}} = \left(\frac{\omega}{k}, \frac{\omega}{l}, \frac{\omega}{m}\right)$. The vertical phase speed $c_{ph,z} = \frac{\omega}{m}$ is thus directed in the same direction as the vertical wave number m. Energy and momentum are transported with the group velocity $\vec{c_g} = \frac{\partial\omega}{\partial\vec{k}} = \left(\frac{\partial\omega}{\partial k}, \frac{\partial\omega}{\partial l}, \frac{\partial\omega}{\partial m}\right)$. Since the mean vertical wind is one to two orders of magnitude smaller than typical vertical phase and group speeds of gravity waves, it will be neglected in the following discussion ($c_{ph,z} \approx \hat{c_{ph,z}}$, $c_{g,z} \approx \hat{c_{g,z}}$). From Eq. 2.17 the vertical group speed is given by

$$c_{g,z} = -\frac{m(\hat{\omega}^2 - f^2)}{\hat{\omega}(k^2 + l^2 + m^2 + \frac{1}{4H_\rho^2})}, \tag{2.20}$$

and has the opposite sign as the vertical wave number. A gravity wave transporting energy and momentum upwards ($c_{g,z} > 0$) thus has a negative vertical wave number and hence its phase lines propagate downward ($c_{ph,z} < 0$). This is a very specific trait of gravity waves since for most other waves, phase and group velocity point in the same direction. The very simplified one dimensional gravity wave simulation shown in Fig. 2.2 illustrates this schematically for three upward propagating gravity waves. It also shows that for typical wave parameters, the vertical group velocity is in the order of 1 ms^{-1} (dashed line in Fig. 2.2A). As shown in Fig. 2.2 it may take several hours up to a few days for a gravity wave to propagate from the troposphere to the mesopause region depending on the wave parameters.

2.5.4 Critical levels and turning levels

When the intrinsic frequency $\hat{\omega}$ of a gravity wave approaches the Coriolis parameter f the dispersion relation in Eq. 2.16 shows that the vertical wavelength λ_z approaches zero ($m \to \infty$). This defines a so-called critical level where gravity waves are absorbed [e.g. *Booker and Bretherton*, 1967]. An estimate for the vertical group velocity shows that it approaches zero

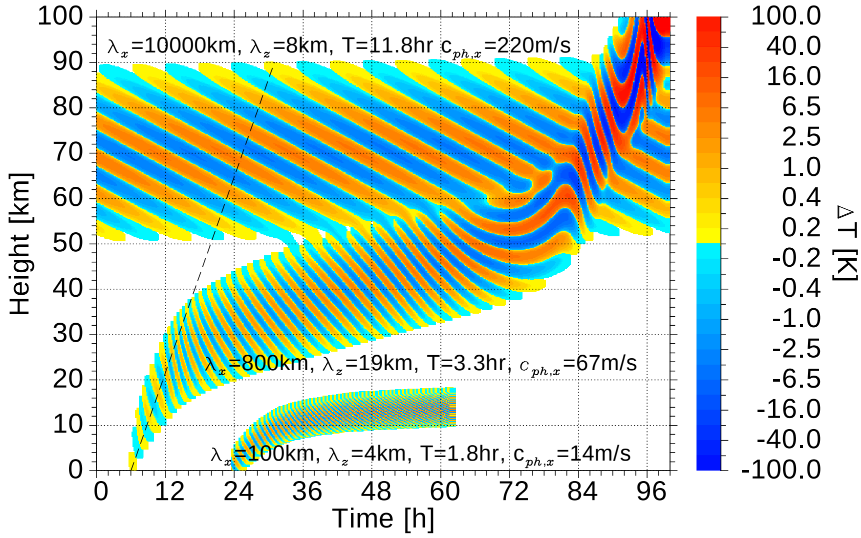

A) Temperature amplitudes vs. time

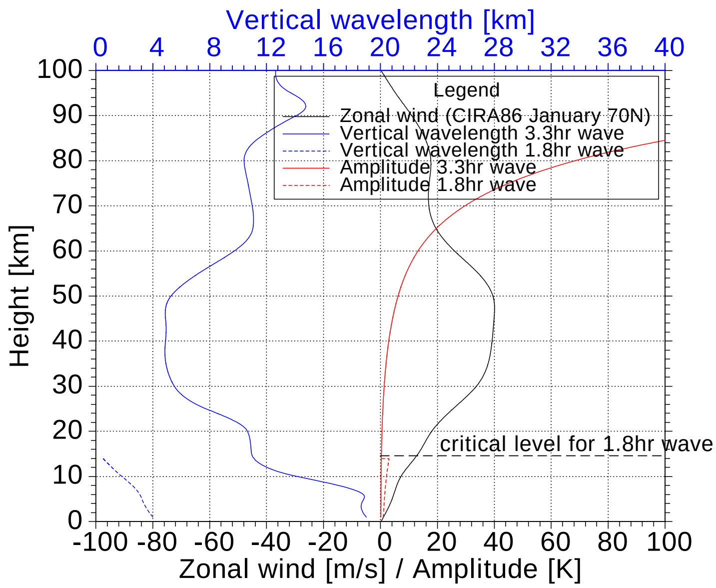

B) Zonal wind, vertical wavelength and amplitude vs. height

Figure 2.2: Simple simulation of three gravity waves propagating upwards through a background atmosphere taken from CIRA86 for January at 70° N. *Upper panel:* Temperature disturbances of the waves. Note the logarithmic colour bar. The change of vertical wavelength and group velocity is mainly due to the background wind. The dashed black line indicates an upward vertical group speed of 1 ms^{-1}. *Lower panel:* Background wind, amplitudes and vertical wavelengths. The 1.8 hr wave reaches a critical level at z=14.6 km which prevents further upward propagation. The 11.8 hr wave is omitted because its parameters do not change much.

as well when the wave comes close to the critical level. Thus in the linear approximation, the wave will never reach the critical level. The 1.8 hr wave in the simple gravity wave simulation in Fig. 2.2 shows this effect. The upper panel displays the temperature disturbance caused by the waves while the lower panel shows the background wind profile as well as the waves' amplitudes and vertical wavelengths. The upward propagation of the 1.8 hr wave in Fig. 2.2A becomes smaller and smaller as the wave approaches the critical level. This occurs at the altitude where the background wind is close to the horizontal phase speed of the wave (Fig. 2.2B). Non-linear modelling shows that the wave is able to penetrate the critical level but that it is heavily damped and will not propagate much further [*Salby*, 1996, Chap. 14]. Since the intrinsic frequency $\hat{\omega}$ depends on the background wind speed relative to the propagation direction of the waves via Eq. 2.15, critical levels are often formed by the background wind profile.

The second limit derived from Eq. 2.16 is given by $m \to 0$ (implying $\lambda_z \to \infty$). This case is reached when the intrinsic frequency $\hat{\omega}$ approaches a critical frequency ω_c

$$\hat{\omega_c}^2 = N^2 - \frac{N^2 - f^2}{4H_\rho^2\left(k^2 + l^2 + \frac{1}{4H_\rho^2}\right)} \quad . \tag{2.21}$$

In this case, the change in propagation conditions met by the wave is occurring on a scale much smaller than the vertical wavelength. The condition $m = 0$ therefore defines a turning level where the wave is reflected. If two such turning levels exist at different altitudes, they form a wave duct which restricts gravity wave propagation to a limited height range [e.g. *Isler et al.*, 1997]. Ducted gravity waves can travel over large distances nearly undamped. Eq. 2.21 depends on the Brunt-Väisälä frequency N which is dependent on the temperature gradient of the background atmosphere. Through Doppler-shifting of the wave, also winds can form wave ducts when the wind varies with height in a suitable way [*Chimonas and Hines*, 1986].

2.5.5 Gravity wave energy

When the amplitudes of the waves are known, their kinetic energy per mass $E_{kin,M}$ and available potential energy per mass $E_{pot,M}$ (also known as gravity wave potential energy density or GWPED) and total energy per mass $E_{tot,M}$ are given by

$$E_{kin,M} = \frac{1}{2}\left(\tilde{u}^2 + \tilde{v}^2 + \tilde{w}^2\right) \tag{2.22}$$

$$E_{pot,M} = \frac{1}{2}\frac{g^2}{N^2}\left(\frac{\tilde{\rho}}{\bar{\rho}}\right)^2 \approx \frac{1}{2}\frac{g^2}{N^2}\left(\frac{\tilde{T}}{\bar{T}}\right)^2 \tag{2.23}$$

$$E_{tot,M} = E_{kin,M} + E_{pot,M} \quad , \tag{2.24}$$

where the potential energy depends also on the Brunt-Väisälä frequency and hence on the background temperature profile (see Eq. 2.5). Since the amplitudes of the single waves are usually not known in observational studies which measure the net amplitude of many superimposed waves, temporal means of the amplitudes are used (e.g. $\tilde{T}(z) \approx \overline{T'(z,t)}$) when calculating Eqs. 2.22 and 2.23.

In the linear wave approximation and for small amplitudes, the wave action density A is conserved for a freely propagating gravity wave [*Andrews and McIntyre*, 1978, and references therein]:

$$A = \frac{E_{tot,M}}{\hat{\omega}} \tag{2.25}$$

$$\frac{\partial A}{\partial t} + \vec{\nabla} \cdot (\vec{c_g} A) = 0 \ . \tag{2.26}$$

Since the density is decreasing exponentially with height, the amplitude $\tilde{A}$ of an undamped upward propagating gravity wave of constant energy has to grow approximately like

$$\tilde{A} \propto A_0 \, \frac{\bar{T}}{g} \frac{N^2}{\hat{\omega}\, m^{\frac{1}{2}}} \ \exp\left(\frac{z}{2H}\right) \ \approx \ A_0 \, \frac{\bar{T}}{g} \frac{N^{\frac{3}{2}}}{c_{ph}^{\frac{1}{2}} (k^2 + l^2)^{\frac{1}{2}}} \ \exp\left(\frac{z}{2H}\right) \ , \tag{2.27}$$

where A_0 is the wave amplitude at the source. The factor in front of the exponential is derived from the approximate WKB solution for a slowly varying background state [see *Fritts*, 1984, and references therein]. The right approximation is only valid for mid-frequency waves with the simplified dispersion relation Eq. 2.19.

Since the standard RMR lidar technique cannot measure wind profiles in the middle atmosphere and radar techniques do not cover the entire height range under investigation in this thesis, the total gravity wave energy $E_{tot,M}$ has to be approximated by $E_{pot,M}$. As the energy of a wave moves back and forth between kinetic and potential energy, this is not a serious restriction. The exact partition between kinetic and potential energy has been studied by *Nastrom et al.* [1997] and *de la Torre et al.* [1999] who showed that it depends amongst others on the vertical wavelength of the gravity waves. The exponential amplitude growth from Eq. 2.27 can be strongly modified for a gravity wave in the real atmosphere since both the Brunt-Väisälä frequency in Eq. 2.23 and the intrinsic frequency in Eq. 2.25 vary with height.

Multiplying $E_{pot,M}$ with the density gives the potential energy per volume $E_{pot,V}$ which is approximately constant with altitude for an undamped propagating gravity wave

$$E_{pot,V} = E_{pot,M} \ \cdot \ \rho \approx \frac{1}{2} \frac{g^2}{N^2} \left(\frac{\tilde{T}}{\bar{\bar{T}}}\right)^2 \rho = \frac{1}{2} \frac{g^2}{N^2} \left(\frac{\tilde{T}}{\bar{\bar{T}}}\right)^2 Mn \ . \tag{2.28}$$

For lidar measurements, the density has to be taken either from reference atmospheres like CIRA86 [*Fleming et al.*, 1990] or NRLMSISE00 [*Picone et al.*, 2002]. When comparing gravity wave energy densities in the literature, care has to be taken as to whether the energy is given per mass or per volume.

Another prerequisite for the calculation of the gravity wave energy is the correct identification of the gravity wave induced fluctuations of the temperature T'. How this is done in detail is described in Sec. 3.4. The main aim is to filter out temperature changes due to turbulence, acoustic waves, tides, Rossby waves and other long-period planetary waves which obey other dispersion relations and would disturb the interpretation of the gravity waves analyses. With the limitations mentioned, $E_{pot,M}$ is a valid estimate of the gravity wave energy in the atmosphere and is accessible for lidar measurements.

2.5.6 Gravity wave breaking

In the previous section it was shown that upward propagating gravity waves increase in amplitude like $e^{\frac{z}{2H}}$. As the amplitude grows, the temperature disturbance of the background state gets larger as well. When the temperature gradient of the modulated background state approaches the adiabatic temperature gradient, the Brunt-Väisälä frequence N (Eq. 2.5) approaches zero which implies that the atmosphere gets unstable and buoyance oscillations are no longer possible. The upward propagating gravity waves is said to break at this level due to static or convective instability. A simple model proposed by *Lindzen* [1981] assumes that the gravity wave amplitude will be saturated above the breaking level [see *Andrews et al.*, 1987, Chap. 4.6]. Depending on the background atmosphere, the amplitude will no longer increase exponentially or even start to decrease with height.

Even when the atmosphere is statically stable ($N > 0$), gravity waves may break when the vertical wind shear becomes too large. This is called dynamical or shear instability and occurs when the Richardson number Ri is less than the threshold for the onset of turbulence

$$Ri = \frac{N^2}{\left(\frac{\partial u}{\partial z}\right)^2 + \left(\frac{\partial v}{\partial z}\right)^2} < \frac{1}{4} \quad . \tag{2.29}$$

The role of this so-called Kelvin-Helmholtz instability in gravity wave breaking has been described in detail by *Fritts and Rastogi* [1985]. They also discussed the limit of $\frac{1}{4}$ which is a mean value that may be both larger or smaller for a particular wave depending on its horizontal wavelength and the background wind profile. Especially for short-scale gravity waves, *Achatz* [2005, 2007] found that turbulence also occurs at larger Richardson numbers.

The excess energy and momentum of the breaking gravity wave is transferred to smaller scales creating atmospheric turbulence [e.g. *Hodges*, 1967; *Zink and Vincent*, 2004]. Finally it ends up as drag on the background flow and heating of the atmosphere. These forcings can reach magnitudes of up to $100\,\mathrm{m\,s^{-1}\,d^{-1}}$ and $6\,\mathrm{K\,d^{-1}}$ [*Alexander and Dunkerton*, 1999; *Becker and Fritts*, 2006]. *Fritts et al.* [2006] have summarised the different ways gravity waves influence the middle atmosphere in much more detail and provide many references to further work on this field.

2.6 Diabatic meridional circulation

The general circulation in the atmosphere is a very complex interplay of many different external and internal forcings that act as drivers for the wind and circulation systems. In the following, some of its features will be described with a focus on the summer mesopause region to explain why it is 90 K colder than expected from radiative equilibrium. The mean zonal winds for solstice conditions are shown in Fig. 2.3A together with the mean diabatic circulation (Fig. 2.3B). They are mainly driven by the difference in solar absorption between the equator and the poles. The summer (winter) stratosphere and mesosphere are sunlit for more (less) hours each day at the poles than at the equator. Therefore they should be warmer (colder) at the poles compared to the equator. Through the thermal wind relation this induces an equatorward (poleward) flow in the summer (winter) hemisphere [*Holton*, 1992]. Deflected by the Coriolis force, this forms the westward (eastward) jet in the summer (winter) stratosphere and mesosphere. Mass continuity (Eq. 2.12) then requires upward (downward) motion above the summer (winter) extra-tropics which leads to diabatic cooling (heating) in the summer (winter) stratosphere and mesosphere. The vertical and meridional flow forms the so-called diabatic circulation depicted in Fig. 2.3B [*Andrews et al.*, 1987, Chap. 7.2].

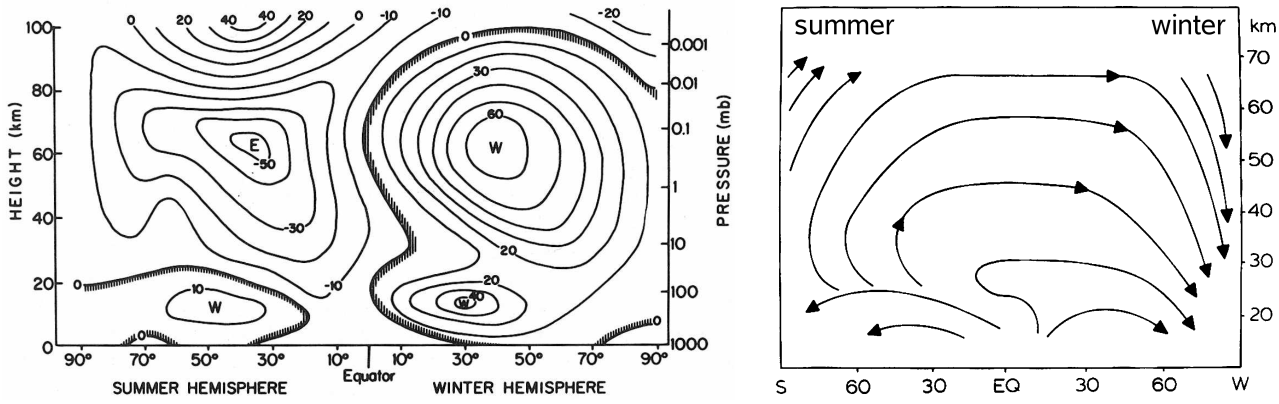

A) Observed mean zonal wind structure B) Streamlines of the diabatic circulation

Figure 2.3: *Left panel:* Mean zonal wind at solstice. Note the closure of the mesospheric jets in the mesopause region. The middle atmosphere westward summer jet ($u < 0$) is weaker than the eastward winter jet ($u > 0$) and is closed at a lower altitude. *Right panel:* Streamlines of the diabatic meridional circulation. Note the different scales on the height axis [*Andrews et al.*, 1987, Figs. 1.4 and 7.2].

Without any additional forces, the mesospheric jets would increase with height up into the thermosphere. As Fig. 2.3A shows, this is not the case in the real atmosphere. So there must be another forcing which decelerates the zonal wind in the upper mesosphere and even reverses the zonal wind in the lower thermosphere above 90 km in summer and 100 km in winter. This additional forcing is provided by breaking gravity waves. In the summer mesosphere, the westward jet blocks westward propagating waves through critical level filtering. Eastwards propagating waves however are not blocked and reach the mesopause region before breaking due to static instability. When they break, they exert an eastward drag on the background atmosphere which decelerates the westward jet in the mesopause region and even reverses the wind direction in the lower thermosphere. In winter, eastward waves are blocked and only westward waves reach the mesopause region. When breaking, they decelerate the eastward jet. Therefore both mesospheric jets decrease above ∼70 km and are said to be “closed”.

The gravity wave drag also induces an additional meridional circulation which is called “residual meridional circulation” because it adds to the diabatic meridional circulation described above [*Andrews et al.*, 1987, Chap. 7.3]. In the summer (winter) mesopause region, the breaking gravity waves transfer their momentum to the background atmosphere decelerating the westward (eastward) jet. This eastward (westward) wind component is deflected equatorwards (polewards) by the Coriolis force thus leading to an additional equatorward (poleward) meridional flow in the mesopause region. From the continuity equation (Eq. 2.12) this requires upward (downward) motion which leads to an additional diabatic cooling (heating) over the the summer (winter) pole (see App. D.2 for a mathematical derivation). This gravity wave driven meridional circulation amplifies the diabatic meridional circulation roughly by a factor of five. It also is the reason of the observed large deviations of the mesopause temperatures from radiative equilibrium above the polar regions.

Such an additional meridional circulation was already presumed by *Murgatroyd and Goody* [1958] from the comparison of radiative equilibrium calculations and observations of the mesopause temperature in summer. An instructive introduction of this meridional circulation and the need of gravity wave drag to explain it was presented by *Geller* [1983].

It is strongly based on the observation of rather large meridional winds in the summer mesopause region which cannot be explained otherwise [see e.g. *Nastrom et al.*, 1982, and references therein].

2.7 Sudden stratospheric warmings

During a sudden stratospheric warming (SSW) the temperature at the winter stratopause increases by up to 50 K during a few days. SSWs were discovered in 1952 by *Scherhag* [1952] in radiosonde ascents from Berlin. They occur only during winter and show both a large warming at the stratopause of up to 70 K in a few days and a cooling in the mesosphere [e.g. *Labitzke*, 1972b; *Siskind et al.*, 2005]. SSWs are very variable with different maximum temperatures and different heights of the temperature maximum. The typical duration of a SSW event is two weeks. Fig. 2.4 shows two SSW events above ALOMAR observed with the RMR lidar in early 1997.

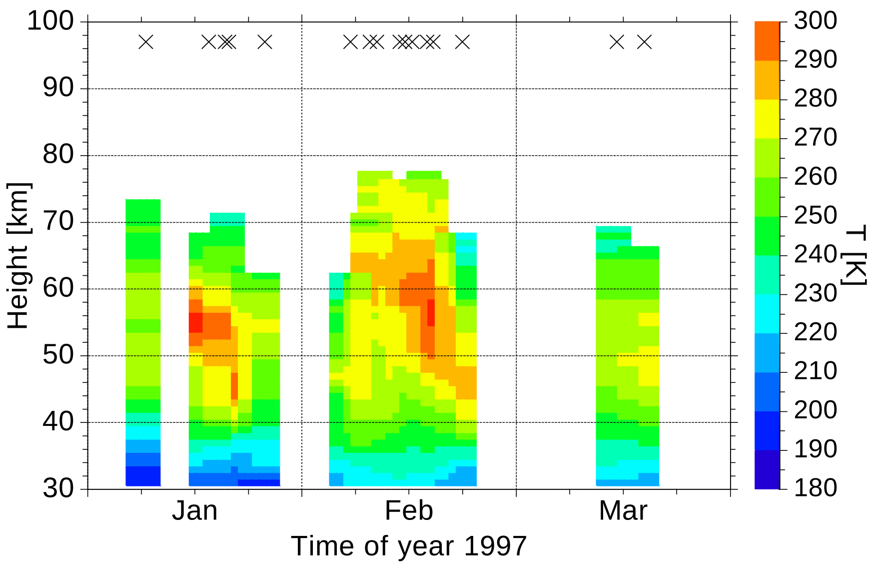

Figure 2.4: Two SSW events observed with the RMR lidar above ALOMAR in January and February 1997. The stratopause reaches temperatures of up to 307 K and 304 K, respectively.

SSWs are classified following the definition of the WMO into “minor”and “major” warmings. The latter are characterised by a reversal of the horizontal temperature gradient at 10 hPa between 60° and the pole and a reversal of the 10 hPa zonal wind in the polar stratosphere at 60° which is a sign of the break-down or equatorward displacement of the polar vortex [*Labitzke and Naujokat*, 2000]. Before 2002 when the first major warming was observed in the southern hemisphere [e.g. *Coy et al.*, 2005; *Krüger et al.*, 2005], major warmings were only observed on the northern hemisphere. A minor warming is characterised by a reversal of the horizontal temperature gradient due to strong warming at the polar stratopause without a corresponding wind reversal. Since the classification of SSWs is based on a hemispheric view, the distinction between major and minor warming cannot be made from temperature observations of the RMR lidar alone. When this distinction is needed, it has to be inferred from other data sets like the European Centre for Medium-Range Weather Forecasts (ECMWF) or other stratospheric analyses [e.g. *Pawson and Naujokat*, 1999; *Manney et al.*, 2005].

The development of SSWs during a typical winter has been described by *Labitzke* [1972a]. The current understanding of the development of SSWs is founded on the work of *Matsuno* [1971]. The description given here follows *Holton* [1992, Chap. 12.4]. In the undisturbed winter state, a strong eastward wind dominates the stratosphere (see Fig. 2.3A) and forms the so-called polar vortex. In the troposphere, planetary Rossby waves are excited at orography, longitudinal varying diabatic heating patterns or baroclinic instabilities. Rossby waves are created through an interplay of the latitudinally varying Coriolis force and the potential vorticity. The latter is the rotating atmosphere's equivalent to the angular momentum of a solid body and is conserved in adiabatic frictionless flow. Planetary waves oscillate meridionally and propagate always westwards relative to the zonal flow. In winter when there are on average stronger winds and more severe weather systems in the troposphere than in summer, planetary wave amplitudes are larger than in summer. If their amplitudes are large enough and the tropospheric wind field does not block them, the planetary waves can propagate upward and equatorward into the stratosphere.

In the mesosphere, the planetary waves encounter critical level filtering where the wind relative to the propagation direction of the wave is zero. This leads to a westward drag at the height of the critical level which decreases the eastward zonal flow. Analogously to the case of gravity wave breaking in the summer mesopause region, the breaking planetary waves induce a meridional circulation cell with rising air at latitudes of $40° - 60°$, poleward flow at the wave breaking altitude, sinking air over the poles and equatorward flow below the breaking altitude. The result is an adiabatic warming of the air below and polewards of the wave breaking and a corresponding adiabatic cooling where the air is rising [*Matsuno*, 1971; *Berger*, 1994]. Such cooling at low latitudes has indeed been observed during SSW events [*Fritz and Soules*, 1970].

As the wave drag decelerates the zonal wind, the critical level of zero wind speed tends to propagate downward with time as will the warming at the stratopause (see Fig. 2.4). When the deceleration is strong enough, it will break the polar vortex leading to the wind reversal which defines a major warming. As there is more orography on the northern hemisphere compared to the southern hemisphere, the planetary waves are stronger and are excited more often than in the southern hemisphere. Therefore stratospheric warmings are more common in the northern hemisphere than in the southern hemisphere.

At the same time when there is warming observed at the stratopause, the middle mesosphere is cooling [*Quiroz*, 1969; *Labitzke*, 1972b; *Cho et al.*, 2004]. This anti-correlation reverses at the mesopause and in the lower thermosphere where temperatures again have a positive correlation to the stratopause temperatures during a SSW [*Siskind et al.*, 2005]. Modelling studies of the connection between SSW events and temperature changes in the mesopause region show this link as well [e.g. *Holton*, 1983; *Miyoshi*, 2003]. The decrease or even reversal of the zonal wind in the Arctic stratosphere during a SSW changes the propagation conditions for westward propagating gravity waves which can no longer propagate upward into the mesosphere [*Dunkerton and Butchart*, 1984]. Since these waves drive the residual meridional circulation through wave-breaking in the mesopause region, a decrease in upward wave-flux weakens the residual meridional circulation in the mesopause region. The resulting decrease in subsidence leads to less adiabatic heating in the upper mesosphere which then radiatively cools to a lower temperature restoring the heat balance [*Holton*, 1983]. Some studies found the mesospheric cooling to precede the warming at the stratopause [e.g. *Walterscheid et al.*, 2000] while others did not detect such a correlation in airglow imager temperature measurements [*Sigernes et al.*, 2003; *Cho et al.*, 2004]. A study of SABER satellite data by *Siskind et al.* [2005] also shows that the correlation of the temperature at the stratopause and in the mesopause region has a negative maximum which lies below the height of the OH layer and turns positive again in the lower thermosphere. This may explain the difficulty of finding agreement in the timing of the mesospheric cooling in the different airglow imager temperature measurements [*Siskind et al.*, 2005].

Another example of the connection of the polar stratosphere to other parts of the atmosphere is the correlation between the quasi-biennial oscillation (QBO), a wind oscillation in the equatorial lower stratosphere [see *Baldwin et al.*, 2001, and references therein], and stratospheric warmings. During the west phase ($u > 0$) QBO, major warmings only occur when the solar cycle is in its maximum (sunspot number larger 100). During the east phase of the QBO, major warmings occur independently of the solar cycle [*Labitzke*, 1987; *van Loon and Labitzke*, 1990].

2.8 Mesospheric inversion layers

Mesospheric inversion layers (MILs) are regions of positive temperature gradient in the mesosphere, i.e. regions of increasing temperature with height, which stand out in the mesosphere where the temperature decreases with height under normal conditions. They were first reported in rocket temperature profiles from mid-latitudes [*Schmidlin*, 1976]. An example of two MILs observed with the RMR lidar is shown in Fig. 2.5. The difficulty of distinguishing MILs and large amplitude gravity waves is discussed in Sec. 5.2.1. While MILs are routinely observed at mid-latitudes with occurrence rates of 25 – 70% depending on the season [e.g. *Hauchecorne et al.*, 1987; *Leblanc et al.*, 1995], they are rather rare at high latitudes [e.g. *Cutler et al.*, 2001; *Leblanc and Hauchecorne*, 1997]. From lidar observations above Eureka/Canada (80° N), *Duck and Greene* [2004] inferred an occurrence rate of 5.4% only for this high-latitude site. Satellite observations show that these layers are a mesoscale phenomenon that can cover extended regions and persist for hours [*Clancy et al.*, 1994; *Leblanc et al.*, 1995].

The mechanism causing these MIL has been debated at length in the last twenty years. Many different sources for the formation of MILs have been suggested including breaking gravity waves [*Hauchecorne and Maillard*, 1990; *Liu and Meriwether*, 2004], gravity wave tidal wave interactions [e.g. *Sica et al.*, 2002], the breaking of planetary Rossby waves [*Salby et al.*, 2002; *Sassi et al.*, 2002] or chemical heating [*Meriwether and Mlynczak*, 1995]. It was also proposed that MILs could be an artifact due to incomplete sampling of strong tidal waves [*States and Gardner*, 1998]. Combining radar observations with lidar temperature observations, a possible link between MILs and polar mesospheric winter echoes was found by *Thomas*

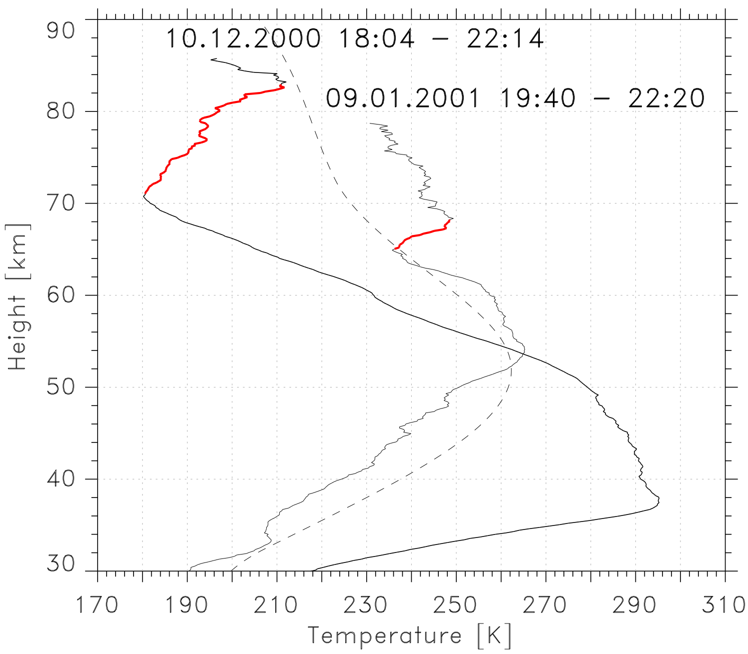

Figure 2.5: Two temperature profiles from the RMR lidar which both show a MIL marked in red. The profile from 10 December 2000 is additionally disturbed by a SSW. The dashed line shows the December temperature from the NRLMSISE00 reference atmosphere.

et al. [1996]. Only recently a consistent scheme for the descriptions of these two phenomena is emerging [see *Meriwether and Gerrard*, 2004, and references therein]. The description below follows this review.

There are two groups of MILs which are created through different mechanisms. The first group is observed in the upper mesosphere and lower thermosphere region above ∼85 km. These "upper" MILs are formed when a strong tidal wave non-linearly interacts with gravity waves propagating from below. Upper MILs propagate downward over time as tidal waves do. *Liu et al.* [2000] showed in a model study that breaking gravity waves can warm the air sufficiently for the formation of a MIL if the static stability of the mesosphere had been decreased by a tidal wave. Models and observations show that this group of MILs has an amplitude maximum during winter at mid-latitudes.

The second group of MILs occurs throughout the entire mesosphere. The amplitudes of these "lower" MILs are larger in winter than in summer while their mean heights are lower in winter than in summer at mid-latitudes [*Hauchecorne et al.*, 1987]. Lower MILs are believed to be caused by the breaking of upward propagating planetary Rossby waves when they encounter an altitude where the wind in the direction of wave propagation is zero. Due to the breaking waves at this height, this region is also called "mesospheric surf zone" [*Sassi et al.*, 2002]. Such breaking events can be an in situ source for gravity wave generation in the mesosphere. Lower MILs do not show the pronounced downward propagation found in upper MILs. This is one of the few features enabling the otherwise difficult distinction of upper and lower MILs.

Chapter 3

Lidar Instrument Basics

The term "lidar" is an acronym for "light detection and ranging" which describes the physical principle of the instrument. It is now used as the instrument name. Shortly after the invention of the laser at the end of the 1950's, the lidar principle was applied to atmospheric research by *Fiocco and Smullin* [1963]. An early review of the different lidar techniques was assembled by *Kent and Wright* [1970]. A lidar is very similar to a radar but it uses laser light instead of radio waves for the remote sensing of the atmosphere. This implies different scattering mechanisms (see Sec. 3.2) which makes it possible to investigate different aspects of atmospheric physics and chemistry with a lidar. The following description will focus on the operation mode of the RMR lidar used in this thesis.

The basic principle of a lidar instrument is sketched in Fig. 3.1. A laser is used to emit short pulses (∼10 ns) of light into the atmosphere. The light is scattered by the air molecules, aerosols, dust and cloud particles present in

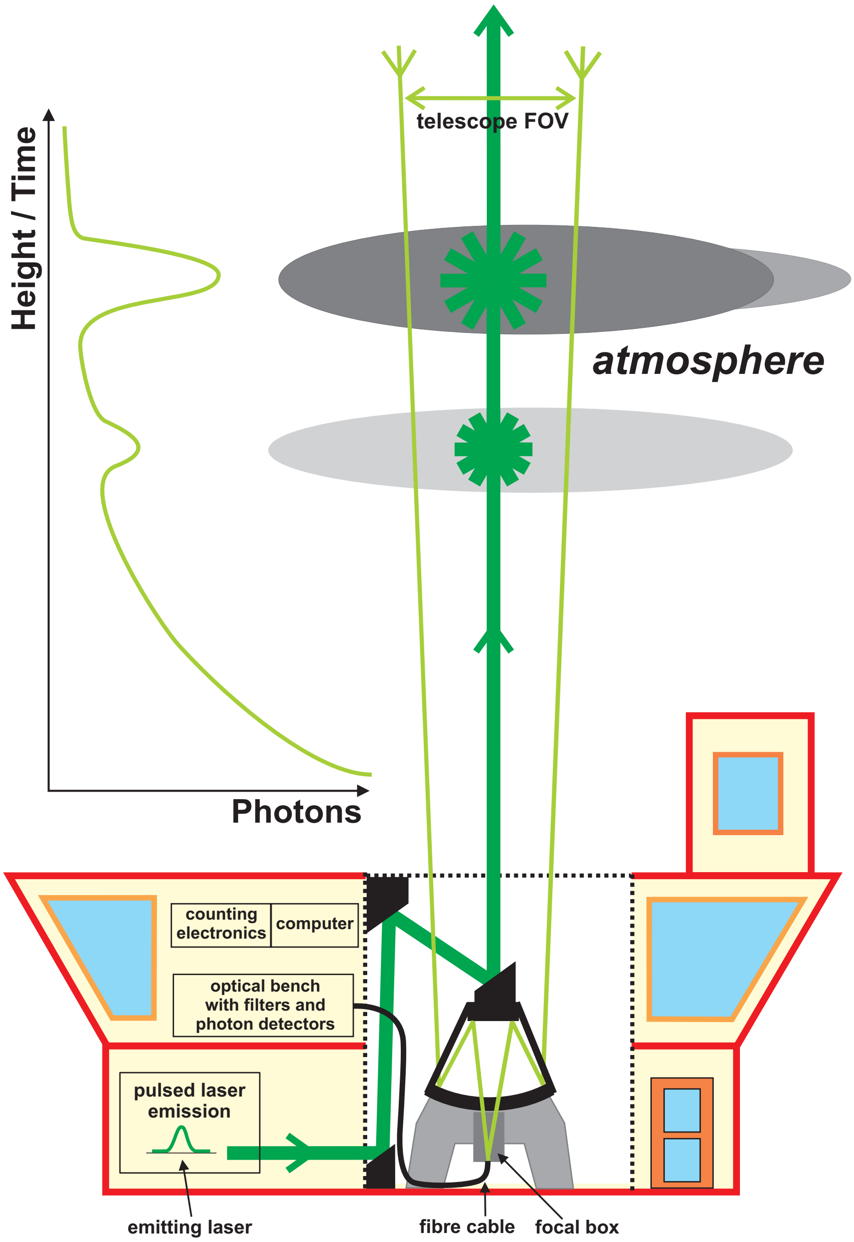

Figure 3.1: Simplified overview of the RMR lidar system at ALOMAR with the emitting laser, receiving telescopes and counting detectors. A qualitative lidar profile is shown as well (details in the text).

the atmosphere. Light scattered backwards is collected with a telescope and detected by photomultipliers or avalanche photodiodes and counted into time bins. Due to the finite speed of light, these time bins correspond to range bins. Therefore a lidar can measure amongst others height profiles of atmospheric density and aerosol concentrations. The density profile can then be converted to a temperature profile (see Sec. 3.3). The following section describes the different effects that have to be taken into account during the signal analysis to extract the true atmospheric signal from the lidar raw signal.

3.1 Lidar equation

The lidar signal received from the atmosphere contains information about the density height profile which is used in this work for further analysis and atmospheric aerosols. Additionally, the signal is influenced by the instrument geometry, the atmospheric transmission, noise from scattered light from airglow or moon during night-time and from the sun during daytime. In order to extract the atmospheric signal, the following equation describing the lidar return signal is useful.

$$I(\lambda^{\uparrow}, \lambda^{\downarrow}, z) = C(\lambda^{\uparrow}, \lambda^{\downarrow}, z) \cdot \frac{\beta(\lambda^{\uparrow}, \lambda\downarrow, z)}{z^2} \cdot \mathcal{T}^{\uparrow}(\lambda^{\uparrow}, z) \cdot \mathcal{T}^{\downarrow}(\lambda^{\downarrow}, z) + I_{background}, \tag{3.1}$$

where the different terms are described below:

$I(\lambda^{\uparrow}, \lambda^{\downarrow}, z)$	Lidar signal as recorded by the data acquisitioning system as a function of emitted wavelength $\lambda^{\uparrow}$, received wavelength $\lambda^{\downarrow}$ and altitude z ($\widehat{=}$ time).
$C(\lambda^{\uparrow}, \lambda^{\downarrow}, z)$	System constant describing the power of the emitting laser, the transmission of the receiver system and the efficiency of the detectors. A height dependency of this constant can be introduced through misalignment of the outgoing laser beam and the telescope field of view (FOV) or through non-linear detectors. For the Rayleigh lidar principle used in this work it is essential to avoid this height dependency (see Sec. 3.5 and App. B.2).
$\beta(\lambda^{\uparrow}, \lambda\downarrow, z)$	The volume backscatter coefficient is the basic geophysical parameter that is measured by a lidar instrument. It contains a contribution which is directly proportional to the number of scatterers and hence to the atmospheric density. When present, aerosols also contribute to the volume backscatter coefficient. Depending on the instrument design, there are different methods to separate the contributions of air density and aerosols.
$1/z^2$	Geometric factor accounting for the varying solid angle due to the changing distance between scatterer and telescope.
$\mathcal{T}^{\uparrow}(\lambda^{\uparrow}, z)$	Atmospheric transmission at the wavelength emitted from the laser between the ground and the scattering altitude.
$\mathcal{T}^{\downarrow}(\lambda^{\downarrow}, z)$	Atmospheric transmission at the wavelength received by the detectors between the scattering altitude and the ground. In case of Rayleigh, Mie and resonant scattering, this is equal to $\mathcal{T}^{\uparrow}$. But for Raman scattering, the emitted and received wavelength differ and the transmission has to be treated separately for the two wavelengths involved.

$I_{background}$ This noise contribution is independent of altitude and accounts for thermal noise from the detectors and counting electronics. Another noise source is solar light during daytime, or moonlight or airglow during night-time that is scattered into the FOV of the telescope.

Some of these quantities are not well known like the atmospheric transmission during a given measurement run. Therefore an iterative algorithm is used to correct for transmission effects. Together with the other steps necessary during the signal processing, this algorithm is described in App. B.2.

3.2 Scattering mechanisms

The lidar principle exploits the existence of scatters in the atmosphere that are used to infer different geophysical quantities like density, temperature, aerosol sizes, or aerosol compositions. The following list gives an overview of the different scattering mechanisms that are used in lidar instruments. A schematic description of the energy levels involved in these scattering processes is shown in Fig. 3.2.

Rayleigh:

Following *Young* [1981], the term "Rayleigh scattering" describes the sum of Cabannes and Rotational Raman scattering (see below). Rayleigh scattering occurs if the size of the scatterer is much smaller than the wavelength of the incident light. In this case, the scattering cross-section σ is inversely proportional to the wavelength like $\sigma \sim \frac{1}{\lambda^4}$, i.e. it is larger for smaller wavelengths. Together with the particle cross-section, this leads to a dependence on the particle radius r like $\sigma \sim r^6$. Due to the thermal speed of the scatterers, Rayleigh and Raman scattering shows Doppler-broadening of the returned signal.

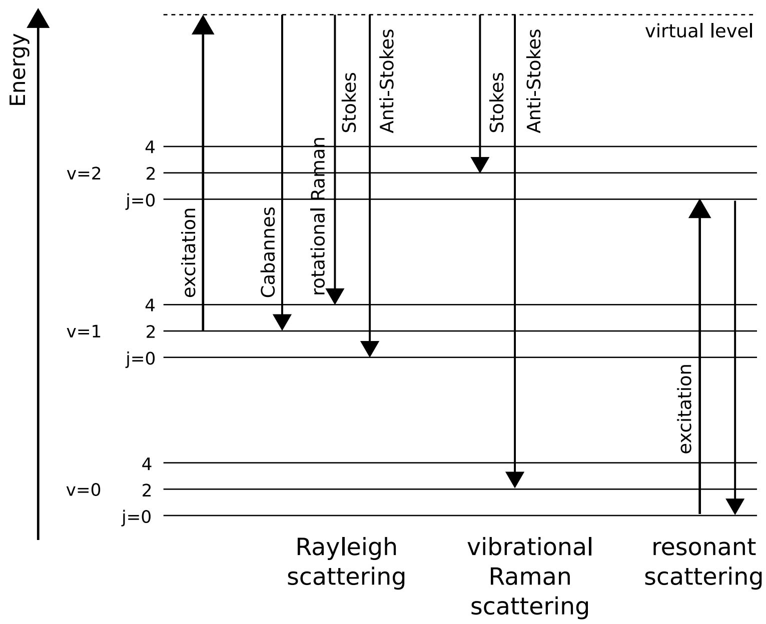

Figure 3.2: Schematic drawing of the energy levels involved in the different scattering processes. The energy levels of the scattering air molecules are labelled with their vibrational quantum number v and rotational quantum number j.

Cabannes:

The Cabannes line results from elastic scattering at an atom or molecule when an electron is lifted to a virtual level by the incoming photon. When the electron reverts to its original state, a photon is emitted with the same wavelength as the incoming one. The Cabannes line has a comparably large cross-section and accounts for most of the signal from air molecules in an RMR lidar.

Rotational Raman:

In this process the electron does not return to its original state but into another state with a different rotational quantum number. If the new state is energetically higher than the original state, the emitted photon has a lower energy than the incoming photon and a so-called Stokes line is excited. If the new state has a lower energy, the emitted photon has a higher energy resulting in an anti-Stokes line. The typical wavelength shift is in the order of 1 nm. The cross-section of Rotational Raman scattering is 10^4 times lower than that of the Cabannes line.

Vibrational Raman

analogous to Rotational Raman scattering, during vibrational Raman scattering the original and the end state differ in their vibrational quantum number. The wavelength shift in wave numbers only depends on the scattering molecule. In the atmosphere, the wavelength shift for oxygen and nitrogen is between 30 nm and 100 nm, depending on the wavelength of the incoming radiation. The cross-section for this process is three orders of magnitude lower than that of the Cabannes line.

Resonant:

If both the ground state and the excited state are real levels and the relaxation is back to the ground state, the process is called resonant scattering. Its cross-sections is $\sim$15 orders of magnitude larger than that of the Cabannes line which involves a virtual level.

Aerosol (Mie):

This term is used to describe scattering at atmospheric aerosols which may be either liquid or solid particles (but no atoms or small molecules) with sizes between 1 nm and 100 μm. The wavelength does not change during this process and the angular distribution of the cross-section as well as its magnitude depend heavily on the size and shape of the scattering particles [*Mishchenko et al.*, 1999]. The special case of scattering on spherical particles is called Mie scattering [*Mie*, 1908].

Each of these scattering mechanisms can be used in lidar instruments. Since the data used in this work all results from Rayleigh scattering profiles, only the Rayleigh lidar technique [*Hauchecorne and Chanin*, 1980] will be described in more detail here. Due to the technical setup of the ALOMAR RMR lidar (see Sec. 3.5), the Rayleigh scattering profiles in this work consist of the Cabannes line only. Following its use elsewhere in the literature, this thesis nevertheless sticks to the term Rayleigh scattering.

3.3 Rayleigh lidar temperature method

The raw signal from a lidar can be used to deduce a height profile of the atmospheric density through Eq. 3.1. Assuming hydrostatic equilibrium, this density profile can then be converted to a height profile of the atmospheric temperature through integration [e.g. *Kent* *and Wright*, 1970; *Hauchecorne and Chanin*, 1980]. Combining the ideal gas law with the integral form of Eq. 2.1, the temperature can be expressed as

$$T(z) = -\frac{M}{k_B} \int_z^\infty g(z') \cdot \frac{n(z')}{n(z)} \cdot dz' \ . \tag{3.2}$$

This equation still includes an integral to ∞ whereas the lidar signal has an upper limit of z_0 defined by the decreasing signal-to-noise (S/N) ratio. Splitting the integral at this height gives two integrals the second of which only includes the density profile in the altitude range accessible to the lidar:

$$T(z) = -\frac{M}{k_B} \left(\int_{z_0}^\infty g(z') \cdot \frac{n(z')}{n(z)} \cdot dz' + \int_z^{z_0} g(z') \cdot \frac{n(z')}{n(z)} \cdot dz' \right) \ . \tag{3.3}$$

The first integral can now be expressed by the density n_0 at the upper limit of the lidar signal and the atmospheric temperature T_0 at this altitude:

$$T(z) = \frac{n_0}{n(z)} \cdot T_0 + \frac{M}{k_B} \int_{z_0}^{z} g(z') \cdot \frac{n(z')}{n(z)} \cdot dz' \ , \tag{3.4}$$

Since this start temperature is not known a-priori, it has to be taken from a reference atmosphere like CIRA86 [*Fleming et al.*, 1990] or NRLMSISE00 [*Picone et al.*, 2002] or from another independent lidar system like a metal resonance lidar [*Alpers et al.*, 2004]. Since such a lidar only recently became available at ALOMAR [*She*, 2001; *She et al.*, 2002], all temperature profiles used in this work are calculated from start temperatures taken from NRLMSISE00. The advantage of the above algorithm is that the integral converges towards the true atmospheric temperatures within one to two scale heights below the start height z_0. Applying error propagation, the statistical uncertainty at each altitude of the resulting temperature profile can be estimated.

The lidar signal is sampled in discrete altitude bins. Therefore the integral in Eq. 3.4 is calculated as a sum over the altitude bins z_i which have a spacing of Δz defined by the temporal resolution of the detection system:

$$T_i = T\left(z_i - \frac{\Delta z}{2}\right) = \frac{n_0}{\sqrt{n(z_{i+1})n(z_i)}} \cdot T_0 + \frac{M}{k_B} \sum_{j=1}^{i} g\left(z_j - \frac{\Delta z}{2}\right) \cdot \frac{n(z_j)}{\sqrt{n(z_{i+1})n(z_i)}} \cdot \Delta z \ , \tag{3.5}$$

where the density inside a layer is given by the geometric mean of the density at the upper and lower edge of the layer. All the Eqs. 3.2 – 3.5 only involve density ratios. Therefore the instrument constant C in Eq. 3.1 does not have to be known for calculating temperatures from the lidar raw signal. But it does have to be independent of height and the analysis has to be restricted to heights where there are no aerosols in the atmosphere. When aerosols are present, they contribute to the lidar signal which then is no longer proportional to the air density. This defines the lower limit of 30 km for the analysis in this thesis to stay clear of the Junge aerosol layer in the lower stratosphere [*Junge et al.*, 1961]. After non-linearities of the detectors have been accounted for (see Sec. B.2), the relative density profiles from the lidar are used to calculate temperature profiles. The algorithm is neither sensitive to changes in the laser power nor to changes of the transmission of the receiving system or of the detector efficiency as long as these changes occur on timescales much larger than the 2 ms it takes to record one lidar profile. This is usually fulfilled for the ALOMAR RMR lidar.

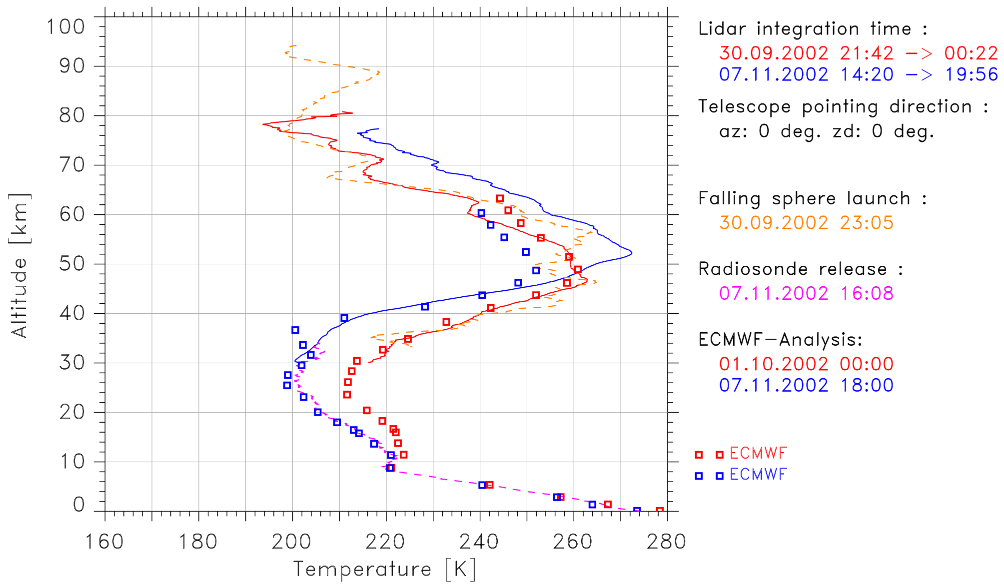

Figure 3.3: RMR lidar temperatures calculated from Eq. 3.5 for 30.09.2002 (red) and 07.11.2002 (blue). Temperature profiles from simultaneous falling sphere (orange) and radiosonde (violet) measurements as well as from ECMWF operational analyses at (70° N, 15° E) are included to show that the lidar temperature measurements agree with other independent methods.

As an example of this method and to show that it indeed yields true temperature profiles, Fig. 3.3 shows two RMR lidar temperature profiles from 30.09.2002 and 07.11.2002 together with simultaneous falling sphere, radiosonde and ECMWF operational analyses temperature profiles. On 30.09.2002, the temperature profiles of RMR lidar (solid red line) and falling sphere (dashed orange line) agree well considering the very different integration times of the two methods. The falling sphere measurement takes only a few minutes and therefore includes large gravity waves while the RMR lidar profile is integrated over almost three hours which filters out the short-periodic waves. The comparison of the RMR lidar temperature on 07.11.2002 (solid blue line) with a radiosonde measurement (dashed violet line) shows agreement to within a few Kelvin in the overlapping altitude region which is the combined statistical uncertainty of the two instruments at this altitude. The ECMWF temperatures for the time of the two measurements (red and blue squares) show the largest deviations at the upper end of the ECMWF profiles. Below 55 km (30.09.2002) or 45 km (07.11.2002) the differences between RMR lidar and ECMWF are smaller than a few Kelvin. A more detailed comparison of RMR lidar and ECMWF temperature profiles is presented in Sec. 4.5.

3.4 Gravity wave extraction

Lidar instruments measure height profiles of atmospheric density or temperature. These profiles describe the state of the atmosphere above the lidar instrument during the integration time used for calculating the profile. Gravity waves contribute to this state as short-periodic variations of a background state (see Sec. 2.5.1). To extract information about gravity waves from lidar profiles, the measured profile has to be split into the background state which is only slowly varying in time and the fluctuations about this background state which are then identified as gravity waves.

There are different ways of determining the background state from the measurement of single height profiles or a number of consecutive height profiles. A comparison of different algorithms using time-averaging or approximation of the background state by an exponential fit to the relative density profile has been published by *Mitchell et al.* [1990]. Another approach is to use piece-wise polynomials of low order to model the undisturbed background state [e.g. *Hirota*, 1984] or adaptive spline fits [e.g. *Blum*, 2003]. High-pass filtering is also used to separate the fluctuations from the background state [e.g. *Rowlett et al.*, 1978].

When using splines, polynomials or other fits, it is difficult to control the spectral characteristics of the filtering and the background state depends on the variable parameters of the fits. Therefore in this thesis, time-averaging of the single profiles during one measurement is used to define the undisturbed background state $\overline{T}$. The single temperature profiles T_i are calculated with an integration time of one hour and a time shift of successive profiles of 10 min. Subtracting the mean profile $\overline{T}$ from the single profiles T_i then gives the fluctuations T'

$$T'(z,t) = T_i(z,t) - \overline{T(z,t)} \quad . \tag{3.6}$$

Using this simple approach, the spectral characteristics of the separation of background state and gravity wave fluctuations depends only on the known duration of the measurement.

As all temperature profiles used in this work are based on at least one hour of integration time, acoustic waves and turbulence which have much shorter periods than the integration time are not included in the fluctuations determined from Eq. 3.6. On the long-periodic part of the spectrum, most measurements are shorter than 18 hr (see Sec. 4.1). So temperature changes due to planetary Rossby waves like the 2-day wave [e.g. *Salby*, 1981; *Plumb*, 1983] or the 5-day wave [e.g. *Rodgers*, 1976; *Prata*, 1989] have longer time scales than most of the measurements. Hence they do not influence the determination of the gravity wave fluctuations.

The approach described above does not eliminate atmospheric tides with periods of 24 hr, 12 hr, 8 hr, and 6 hr. Such periods are in the same range as the periods expected for gravity waves. One way to remove at least the sun-synchronous tides is to average the single temperature profiles T_i by local time. Any contributions from gravity waves which have random phases are removed by this averaging. Combining all single profiles from one month, mean amplitudes and phases of the migrating sun-synchronous tides can be determined for the height range of the lidar measurements. Once the amplitudes and phases are known, they may be subtracted from the gravity wave fluctuations determined from Eq. 3.6. The remaining fluctuations are then mainly due to gravity waves. Non-migrating tides may contribute as well and cannot be removed easily.

3.5 Technical data

The ALOMAR RMR lidar was specifically developed for its location in the Norwegian Arctic at 69.3° N. At this high latitude, a major challenge for lidar observations is the four month period around summer solstice when it never gets dark. A lidar placed in this region therefore needs to be able to measure during daylight conditions if measurements should continue during the summer months. Therefore the ALOMAR RMR lidar was designed and tuned in all its technical realisation amongst other goals to achieve this capability. This requires narrow band-pass optical filtering technology using single and double Fabry-Perot interferometers (etalons) [*Rees et al.*, 2000; *Eckart*, 2004].

	Emitter system		
	Laser:		
2x	power lasers	Wavelength stabilised to an external seeder and equipped with an active emitted beam direction control loop. Pulse rate: 30.3 Hz each, interlaced	
1x	seeder laser 1064 nm, 532 nm	thermally controlled and stabilised to a iodine absorption line at $\sim$532.24 nm (in vacuum)	Spectral stability: $\Delta\lambda < 1$ fm $\widehat{=}\ \Delta\lambda/\lambda = 10^{-9}$
	Emitted wavelengths:		
	fundamental wavelength		1064 nm (IR) $\widehat{=}$ average 14 W
	first harmonic of 1064 nm		532 nm (VIS) power 14 W
	second harmonic of 1064 nm		355 nm (UV) 5 W
	All wavelengths are emitted coaxially in one beam.	Beam parameters (after beam widening): beam diameter beam divergency beam pointing stability	 20 cm (near Gaussian profile) $< 70\,\mu$rad $< 1\,\mu$rad
	Receiver system		
2x	Telescope	Cassegrain design	f = 8.345 m, FOV = 180 μrad
	Primary mirror (coated)	diameter weight	1.80 m (spherical, concave) 1450 kg (Al substrate)
	Secondary mirror (coated)	diameter weight	0.60 m (aspherical, convex) 60 kg (Al substrate)
	The telescopes can be tilted up to 30° off-zenith for azimuth ranges of 90° – 180° and 270° – 360°.		
	Detectors		
	Mechanical chopper and electronic gating for detector overload protection. Mechanical fibre selector for alternating detector use with both telescopes. Spectral filtering through interference filters and etalons.		
	Receiving channels:		
	APD	1064 nm (IR)*	Rayleigh‡ and aerosol scattering
	DH,DM,DL	532 nm (VIS)†	Rayleigh‡ and aerosol scattering
	AH,AL	355 nm (UV)†	Rayleigh‡ and aerosol scattering
	TR1	529.4 nm (from 532 nm)†	N_2 Rotational Raman scattering
	TR2	530.1 nm (from 532 nm)†	N_2 Rotational Raman scattering
	AU	387 nm (from 355 nm)†	N_2 Vibrational Raman scattering
	DS	608 nm (from 532 nm)†	N_2 Vibrational Raman scattering
	More technical specifications		
	Computers	9 PCs control the system	
	Operation:	One trained operator can run the entire system since most tasks are automated during routine measurements.	

Table 3.1: Overview of the technical specifications of the ALOMAR RMR lidar. More detailed informations can be found in *Baumgarten* [2001] and *von Zahn et al.* [2000]. Two additional channel have recently been installed by *Eckart* [2004].

* Detected with an avalanche photodiode
† Detected with photomultipliers
‡ Due to the separated Rotational Raman channels, this is from the Cabannes line only.

The RMR lidar consists of two Cassegrain type telescopes with 1.8 m diameter primary mirrors and 60 cm diameter secondary mirrors each. The telescope is mounted on motorised sockets which allow them to be tilted up to 30° off-zenith. Each telescope covers a 90° azimuth range so that one can be tilted to all azimuths between west and north (270° − 360°) and the other between east and south (90° − 180°). This configuration allows common-volume observations with both telescopes pointing vertically as well as simultaneous measurements at two different places in the atmosphere [*Baumgarten et al.*, 2002b]. The telescope adjustment procedures have been described in detail by *Siebert* [1996] and *Baumgarten* [2001]; the influence of the proper focusing of the telescope on the temperature calculations have been investigated by *Baumgarten* [2001]. The latter is crucial for the accuracy of the calculations since de-focusing of the telescope leads to systematic errors in the temperature calculations. The mechanical and optical setup (focal box) used until March 2000 at the focus of the telescopes below the primary mirror has been described by *Schlüter* [1996] and has since been improved to accommodate the ALOMAR Weber sodium lidar [*She*, 2001] as detailed in *Nelke and Hayk* [2000].

Since a constant overlap of laser beam (beam divergence $< 70\,\mu$rad) and telescope FOV ($180\,\mu$rad $\widehat{=}$ 18 m at 100 km altitude) at all times is needed for accurate determination of atmospheric temperatures with the RMR lidar, an automatic beam stabilisation system has been included as described by *Hübner* [1994] and later improved [*Wagner*, 2000] which uses a camera to observe the position of the laser beam in the FOV at 1 km height and moves the last laser beam guiding mirror (see Fig. C.1 in App. C.1) to keep the laser beam centred inside the FOV. During this thesis, the system hardware has been upgraded and the software has been rewritten to allow for faster corrections to the laser beam position. The new beam stabilisation system allows for very stable measurements even in marginal weather conditions when clouds drift through the FOV (see App. C.1 and *Schöch and Baumgarten* [2003]).

The emitter system of the ALOMAR RMR lidar uses two seeded Nd:YAG power lasers which produce the short laser pulses with pulse lengths of around 10 ns used to probe the atmosphere. The fundamental wavelength of the Nd:YAG lasers is 1064 nm. Two other wavelengths of 532 nm and 355 nm are produced through doubling and tripling of the frequency of the laser light by nonlinear processes in optical crystals. The seeder is a continuous-wave Nd:YAG diode laser with frequency doubling that is stabilised through iodine absorption spectroscopy [*Fiedler and von Cossart*, 1999]. The seeding is applied to attain a small bandwidth for the pulses of the power lasers (near Gaussian pulse shape) and to keep the centre wavelength of the power lasers stable. Both characteristics are needed for the spectral filters applied to be able to measure during daylight conditions [*Rees et al.*, 2000]. On the laser table, a beam direction stabilisation is installed to keep the direction of the beam that leaves the laser table constant [*Enke*, 1994]. Before leaving the laser table, the beam is widened from 1 cm diameter to 20 cm diameter to reduce the divergence of the laser beam to less than $70\,\mu$rad. Additionally, this avoids nonlinear effects during the propagation through the atmosphere as discussed e.g. by *Martin and Winfield* [1988].

The lidar data analysed in this thesis has been recorded with a temporal resolution of 1 min − 3 min and an altitudinal resolution of 130 m − 150 m (depending on the elevation of the telescopes). Summation in time and smoothing in height has been applied during the analyses to increase the S/N ratio. The data processing is described in detail in Sec. B.2.

A condensed summary of the technical specifications of the ALOMAR RMR lidar used in this thesis is given in Tab. 3.1. More details can be found in tables assembled by *Baumgarten* [2001] and in the description of the whole ALOMAR RMR lidar by *von Zahn et al.* [2000].

Chapter 4

Data Set and Mean Temperatures

This chapter will present the accumulated data set of the ALOMAR RMR lidar from the last nine years, i.e. from January 1997 to August 2005. Since the development and improvement of the RMR lidar is an ongoing project, the quality of the retrieved data also improved through the years. The next section will discuss the data set and its limitations for temperature and gravity wave analysis.

Lidar temperature measurements at Andøya started about ten years before the installation of the RMR lidar with a Na resonance lidar [*Fricke and von Zahn*, 1985]. Summer and winter temperatures from the altitude region 80 km – 105 km were published by *Neuber et al.* [1988] and *Kurzawa and von Zahn* [1990]. Climatological mean temperatures for the 50 km – 120 km altitude range have been derived from metal resonance lidar, falling sphere and in situ rocket measurements by *Lübken and von Zahn* [1991] for winter (October to March) and summer (June, July) at 69° N. Some years later, *Lübken* [1999] published an updated summer (late April to September) climatology for the 35 km – 93 km altitude range based on only falling sphere measurements from the years 1987 – 1997.

Only a few years of RMR lidar temperature data have been published so far. *Hübner* [1998] has analysed temperature measurements performed between January 1995 and April 1996. In 1999, *Fiedler et al.* published a total of 86 temperature profiles covering the year 1998. A stratospheric warming event in the winter 1997/98 was investigated by *von Zahn et al.* [1998a]. However, a comprehensive analysis of the temperature data is not yet available. This chapter will present the first coherent multi-year analysis of the middle atmospheric RMR lidar temperatures covering the altitude range 30 km to 85 km during winter and 30 km to 65 km in summer. The temperature climatology derived from the RMR lidar measurements will be compared to other reference atmospheres like CIRA86 [*Fleming et al.*, 1990], NRLMSISE00 [*Picone et al.*, 2002] and Luebken1999 [*Lübken*, 1999] in the entire altitude range and to ECMWF analyses in the upper stratosphere. The lidar data is also combined with the falling sphere summer climatology and the ECMWF analyses below 30 km to yield a consistent temperature climatology for the 0 km – 85 km altitude range at 69° N.

4.1 Data basis

Operating a lidar at an Arctic site like the ALOMAR observatory at 69° N poses not only technical challenges due to the midnight sun in summer but also considerable operational challenges due to the very variable weather conditions. Since a lidar uses light to probe the atmosphere, a clear sky is needed to acquire atmospheric data. At the ALOMAR observatory,

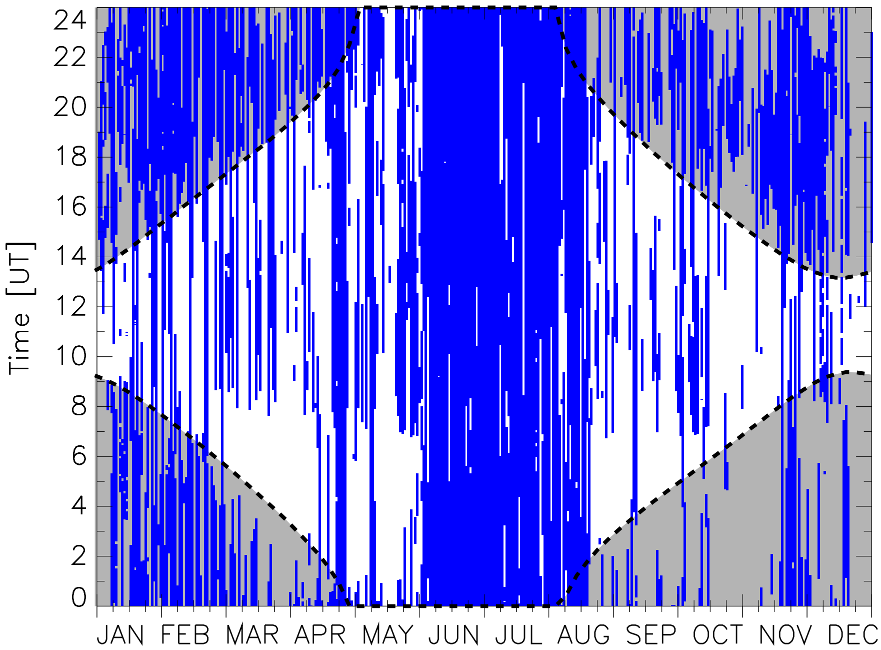

Figure 4.1: Distribution of the combined 1997 – 2005 data set as a function of time of day and season. The dashed line marks civil twilight (solar elevation angle -5°). Night-time conditions are shaded. The data coverage is good for all times of day and all seasons.

high winds and drifting snow can hinder operations in winter even though the sky is clear. Taking all these prerequisites into account, it is a large achievement for the RMR lidar to be able to measure on average 100 days per year for a total of 600 – 1200 hours per year.

The first measurements with the RMR lidar were performed on 19 June 1994, starting with only one laser and a 60 cm telescope [*von Cossart et al.*, 1995]. The large telescopes were installed in summer 1996 and the regular operation of one of the large telescopes started in 1997. Since May 1999 both systems can be operated simultaneously. While working through the data set, it became clear that a consistent quality of the derived temperature profiles was only found from 1997 onwards. This is due to frequent changes to the system prior to 1997 which do not allow a coherent software based derivation of the temperatures. In September 2005 the telescopes were refurbished with new primary mirrors which might affect the focusing and hence the overlap of the laser and the telescope FOV (see App. C.1). This effect has not been investigated yet. Therefore the analysis in the following sections comprises the nine years from 1997 to August 2005.

In this work, a measurement is defined as a period of RMR lidar operation with constant tilting angle of the telescope and gaps not larger than three hours. When both lasers and telescopes were operated, it was counted as two measurements since it produced twice the amount of data and in many cases from different regions of the sky when one or both telescopes were tilted. The total number of measurements since 1997 exceeds 1580 with a total length of more than 8160 hours. The detailed numbers for each year are listed in Tab. A.1 in App. A.1. The daily and seasonal coverage of all the RMR lidar measurements from 1997 to 2005 is shown in Fig. 4.1 where night-time conditions are shaded. The measurements covers nearly all 24 hr during the summer months and most of the day during winter. There are some gaps during the early morning hours in spring and autumn and at the end of December. Daytime measurements in spring and autumn have only been possible after a change in the detector setup in autumn 2001 which enabled a fast switch-over between daytime and night-time configuration of the detection channels. Since the major commitment of

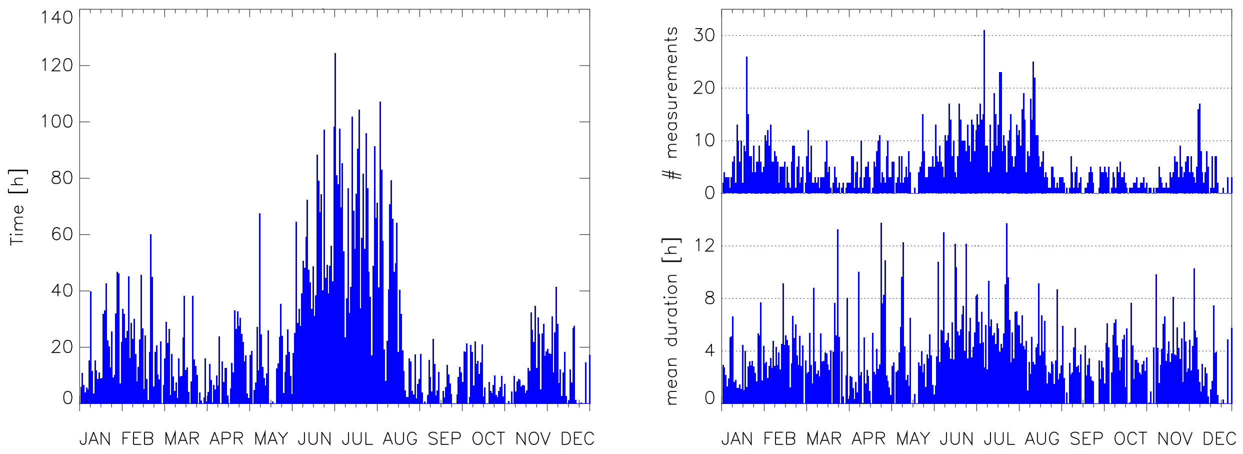

A) Total time vs. day of year

B) Duration and number vs. day of year

Figure 4.2: Cumulative measurement distribution for the years 1997 – 2005 showing total time per day (left panel) and number of measurements and mean duration per day as a function of season (right panel).

the RMR lidar team also has been to noctilucent cloud measurements in summer and polar stratospheric cloud measurements in winter, the measurement efforts were concentrated on these seasons which is then also visible in the measurement distribution. Another reason for the gaps in spring and autumn is the weather which is dominated by low pressure systems and overcast weather at ALOMAR during these times of the year. Nevertheless, since the detector upgrade in 2001, a number of measurements have been performed so that there are only few remaining gaps with no measurements.

Fig. 4.2 displays the cumulative measurement hours per day (Fig. 4.2A), number of measurements per day and their mean duration (Fig. 4.2B) for the years 1997 – 2005. Again, the intensive summer measurement campaigns in June, July and August and the winter campaigns in early December, January and February show clearly in the measurement hours and number per day. However, the mean duration is only slightly larger in summer than during the rest of the year and is larger than three hours for most of the year.

The distribution of the measurement lengths is depicted in Fig. 4.3. The majority of measurements has a length of a few up to eight hours. There are a number of measurements which lasted for up to 18 hours and only very few that are even longer (note the non-linear scale on the x-axis in Fig. 4.3A). Cumulated percentages for the same binning in measurement length are plotted in in Fig. 4.3B for the number of measurements (blue) and the total time of measurements (black). It shows e.g. that 40% of all measurements were shorter than two hours but these measurement contributed only 7% to the total measurement time while the 10 measurements longer than 48 hr account for 10% of the total measurement time. Two hours integration time has also shown to be enough to get a vertical temperature profile which reaches up to 85 km in winter and 65 km in summer with a statistical error at the upper end of less than 5 K. Longer integration times give only slightly larger upper limits of the temperature profile. Therefore the analysis of mean temperatures in the remaining chapter is restricted to measurements longer than two hours. This is a good trade-off between the number of measurements available and the quality of the derived temperature profiles. It also excludes all waves with periods shorter than two hours from the temperature profiles in order to get a more representative mean profile for the measurement.

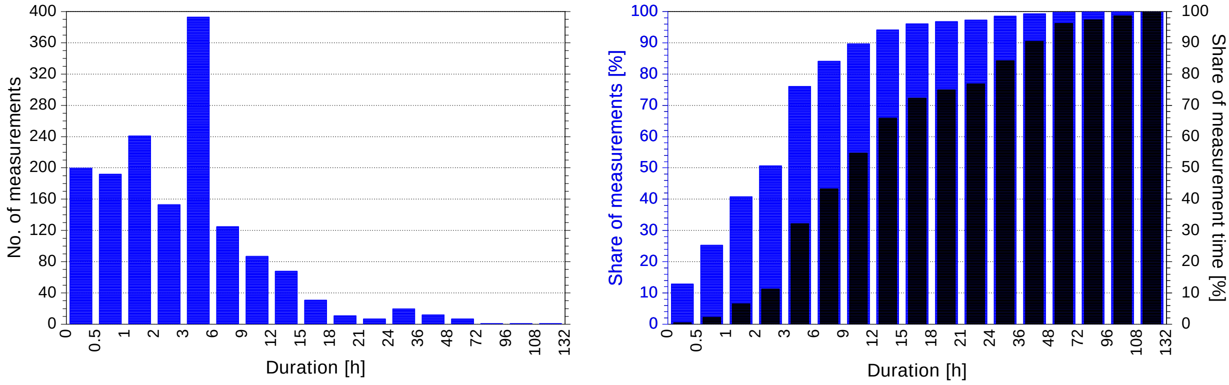

A) Histogram of measurement lengths   B) Cumulated measurements

Figure 4.3: *Left panel:* Histogram of the measurement lengths for the years 1997 – 2005. Note the non-linear scale on the x-axis. *Right panel:* Cumulated percentages of number of measurements (blue) and measurement time (black) shorter than a threshold given on the x-axis. Note the non-linear scale on the x-axis (see text for details).

4.2 Yearly resolved seasonal temperature variation

All temperature profiles shown in this thesis are calculated from the RMR lidar signal at 532 nm and are restricted to statistical uncertainties of 5 K or less. The details of the data selection and processing are described in App. B.1 and B.2. Examples of RMR lidar temperature profiles have been shown in Fig. 3.3 in Sec. 3.3. Only measurements with at least two hours of data are used in the analyses presented in this chapter. The data set adhering to these restrictions is shown in Fig. 4.4 for all nine years from 1997 to 2005. When there were more than one measurement on a certain day either because both systems were used or because clouds interrupted a measurement, a daily mean was calculated as the arithmetic average of the single measurements. A 15-day running-average filter is used to smooth the data and fill short gaps without measurements. Days with measurements are marked by 'X' in the upper part of the plot. White regions mark altitudes or times where no measurements are available. The upper altitude limit of the temperature profiles is lower in summer due to the higher solar background compared to the winter time measurements.

Apart from the winter 2001/2002, the RMR lidar has observed at least one sudden stratospheric warming (SSW) every year (see red diamonds in Fig. 4.4). This high occurrence rate of SSW is a particular trait of the late 1990s (see e.g. the hemispheric analyses by *Manney et al.* [2005]). No SSW was observed at the end of 1999, but there was a SSW in the first days of 2000 which probably started already at the end of 1999 where the RMR lidar could not make observations. SSWs will be discussed in more detail in Chap. 5 which also explains how they are identified.

4.3 Monthly means

The plots in Fig. 4.4 consist of 834 temperature profiles from the years 1997 to 2005. These can be sorted by month to find monthly mean profiles and the variability of the temperatures around this monthly means. Fig. 4.5 presents this analysis for all mean temperature profiles. For comparison, the corresponding profiles from the CIRA86 [*Fleming et al.*, 1990] and NRLMSISE00 [*Picone et al.*, 2002] reference atmospheres as well as from the rocket climatologies at 69° N from *Lübken and von Zahn* [1991] and *Lübken* [1999] are shown.

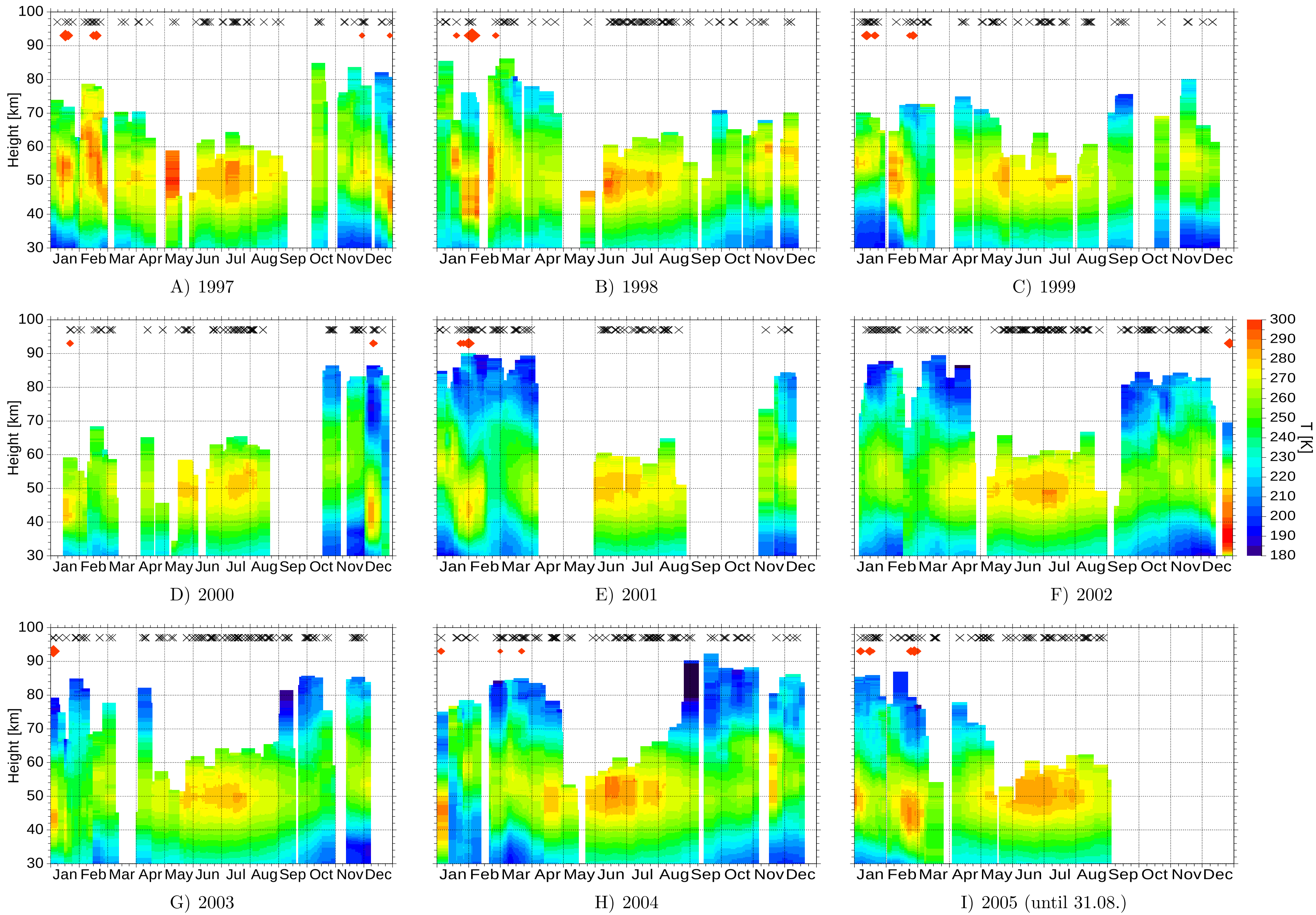

Figure 4.4: Seasonal temperature variations for the years 1997 – 2005 smoothed with a 7-day running-average filter. Crosses mark the times of measurements. SSW events are marked with red diamonds. The symbol size is proportional to the amplitude of the warming. The colour bar is the same for all plots.

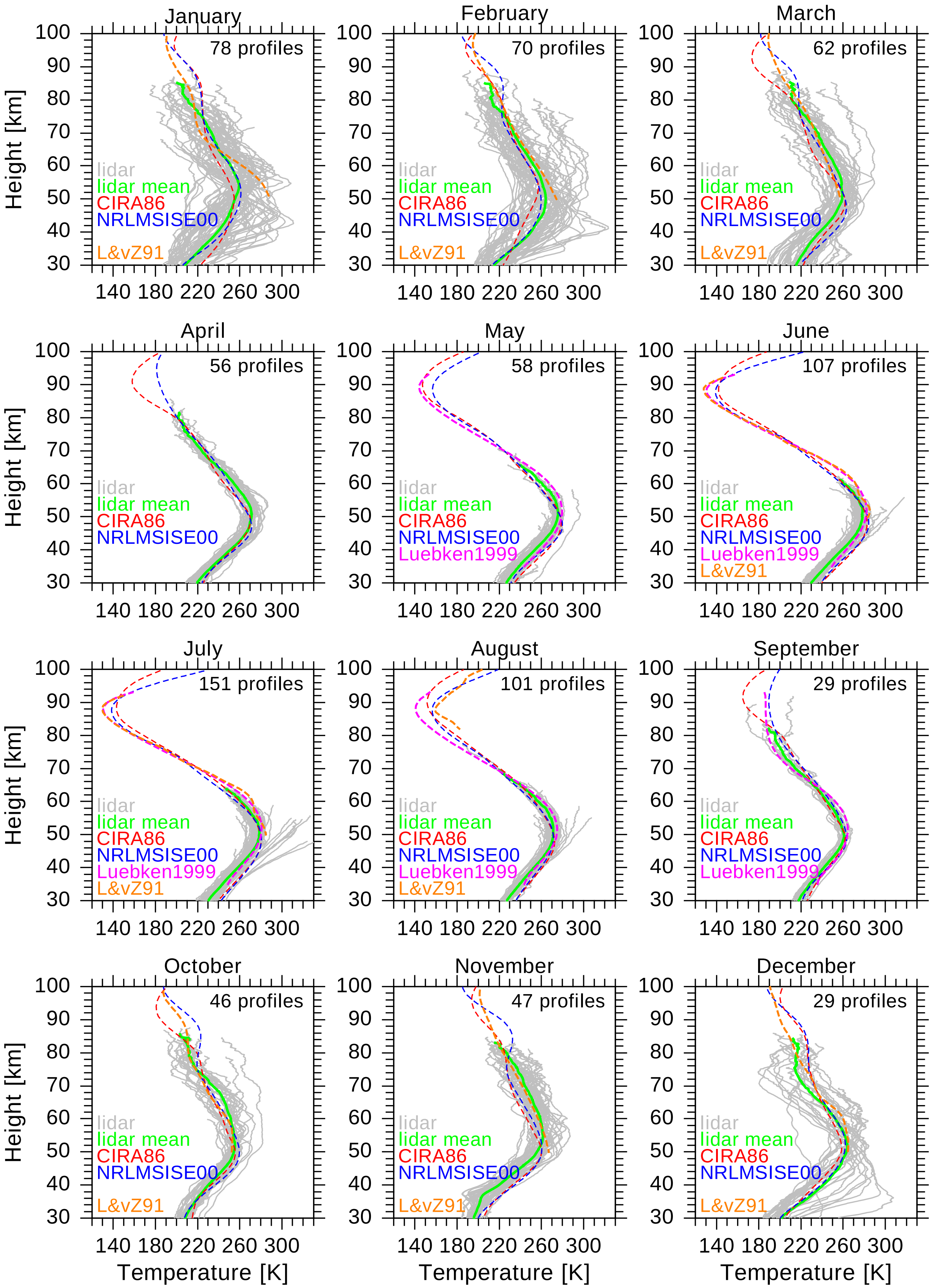

Figure 4.5: Monthly means (green line) and single profiles (gray lines). For comparison, different reference atmospheres are plotted as well (see text for details). The monthly mean temperatures are tabulated in Tab. A.3 in App. A.2.

The variability of the middle atmospheric temperatures in the summer months is much smaller than during the winter months. This is consistent with the observations from falling spheres at Andøya published by *Lübken* [1999] and is is an expression of the stronger wave activity in winter (both planetary and gravity waves) compared to summer [e.g. *Theon et al.*, 1967; *Lübken and von Zahn*, 1991]. A major reason for this difference is the westward jet in the upper polar stratosphere/lower mesosphere in summer which prevents the upward propagation of planetary waves. In winter this jet is eastward and thus does not prevent planetary waves from propagating upwards (see the zonal mean wind structure in Fig. 2.3A). Gravity waves in the middle atmosphere have both eastward and westward horizontal phase speeds. Therefore they can always propagate upward. However, due to the location of ALOMAR on the coast in Northern Norway, it is expected that a major part of the gravity waves above ALOMAR are mountain waves excited at the Scandinavian mountain ridge. Since tropospheric winds are usually stronger in winter than in summer, larger gravity wave amplitudes and occurrence rates would be expected in winter. This point will be elucidated in more detail in Chap. 6.

Even though there is great variability of the single profiles during winter (October – March), the monthly mean lidar profile follows very well the different reference atmospheres and climatologies. The only exception occurs in January for the *Lübken and von Zahn* [1991] profile at the stratopause which deviates significantly from both the lidar mean and the other reference atmospheres. In the lower mesosphere the *Lübken and von Zahn* [1991] temperatures for January are calculated from measurements in the years 1984 and 1990. Fig. 4.5 shows that these two years were not representative for the January mean temperature of the lower mesosphere. The *Lübken and von Zahn* [1991] January temperatures at the stratopause are nearly 30 K higher than the mean RMR lidar which indicates that they are biased by temperature profiles obtained during the stratospheric warming in late January 1984 [*Labitzke and collaborators*, 2002]. The detailed differences between the new RMR lidar data presented here and the reference atmospheres and climatologies will be shown in Sec. 4.5 below. The monthly mean RMR lidar temperatures are tabulated in App. A.2 in Tab. A.3.

4.4 Mean seasonal temperature variation

The next step to map the temperature structure above ALOMAR is to abandon monthly means and investigate the seasonal variation of the middle atmospheric temperatures above ALOMAR. Towards this end, the 834 temperature profiles were used to calculate daily means from all measurements in the years 1997 to 2005. As the altitude coverage of the single profiles on one day varied depending on the strength of the RMR lidar signal during the measurements, the number of measurements entering the daily means varies slightly at the upper end of the profiles. This explains the higher variability of the temperatures at the higher altitudes in Fig. 4.6 which shows the mean seasonal variation of the temperatures above ALOMAR. The number of measurements on each day is given by the black bars in the upper part of the diagram (1 km corresponding to 1 measurement). There are a few gaps e.g. in November and at the end of December which are caused by missing data due to adverse weather conditions.

To get a better estimate of the mean seasonal temperature variation, the daily profiles in Fig. 4.6 were smoothed in time by a 15-day running-average filter. No additional smoothing in height was applied. Fig. 4.7 shows that this procedure smoothes over the gaps and gives a continuous temperature climatology from roughly 30 km to 85 km in winter and 65 km during

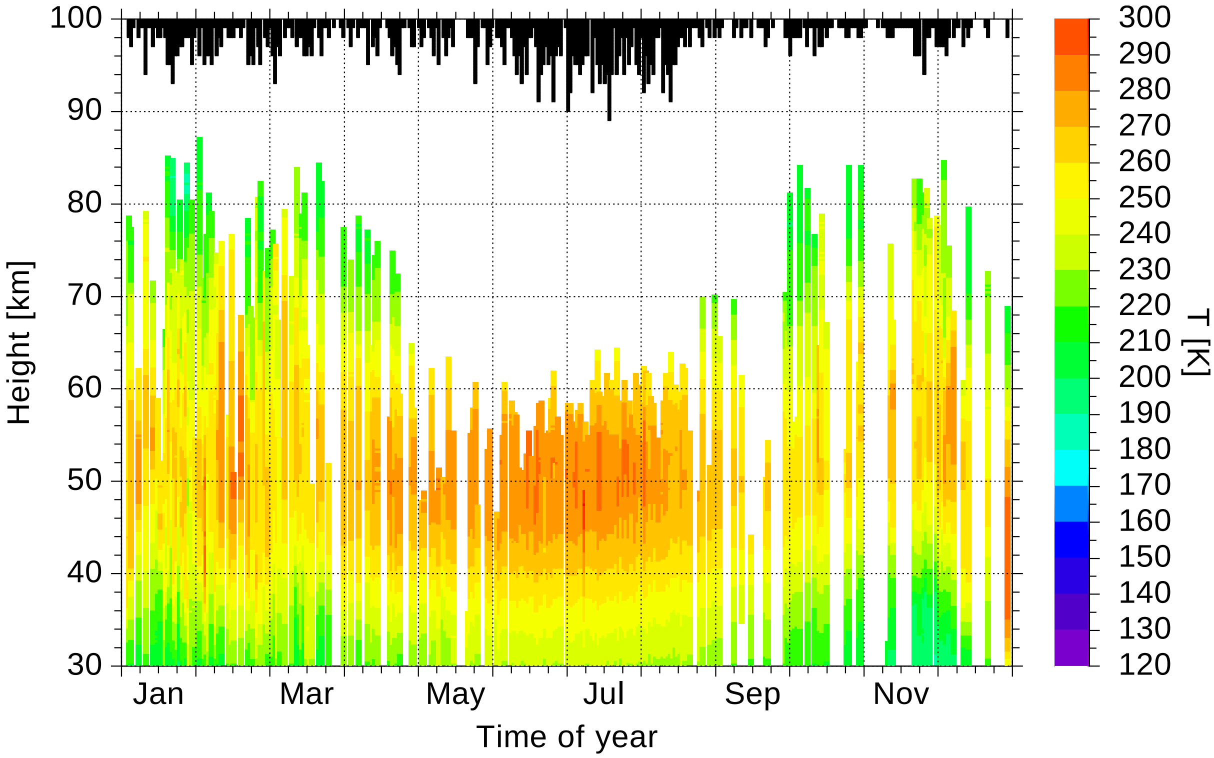

Figure 4.6: Seasonal temperature variation during the years 1997 − 2005. Multiple measurements on the same day are averaged. The black bars give the number of measurements on each day. The gaps in mid-May and at the end of December are caused by missing data due to unfavourable weather conditions.

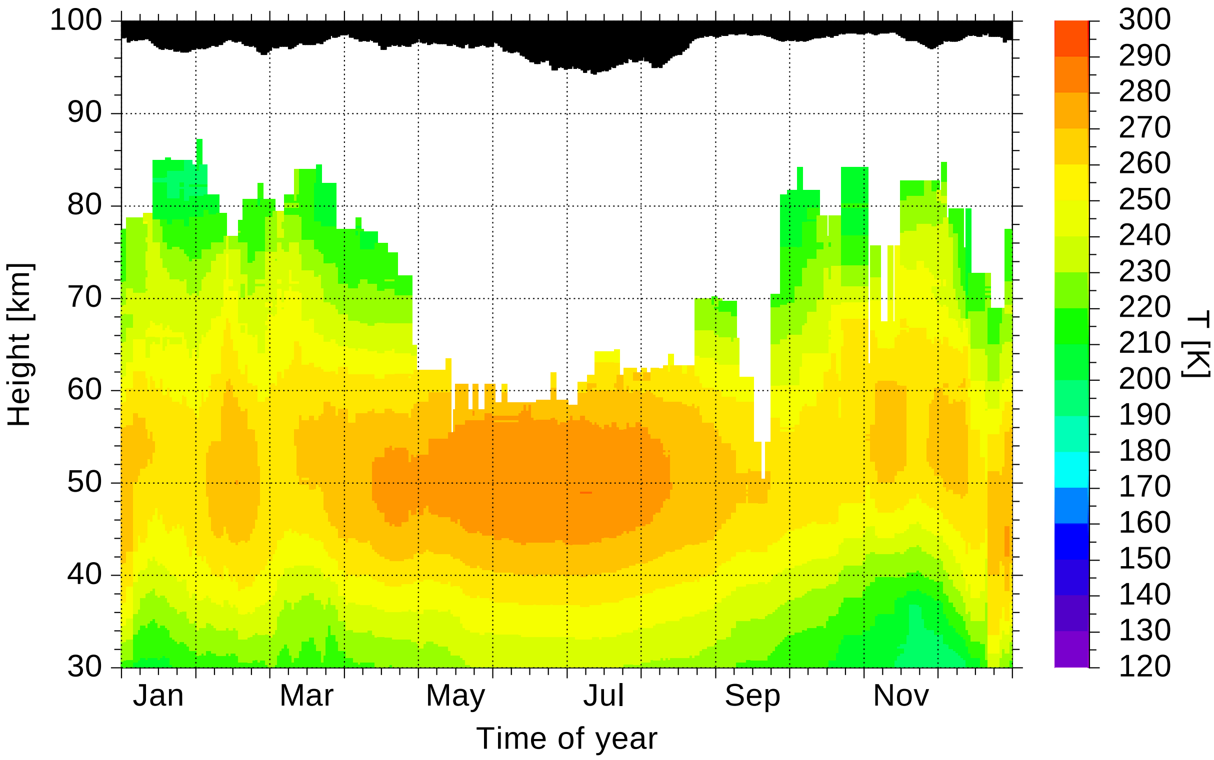

Figure 4.7: Same as in Fig. 4.6 but the profiles were smoothed in time by a 15-day running-average filter which removes the data gaps. No additional smoothing in height was applied. The seasonal temperature variations are tabulated in Tabs. A.4 and A.5 in App. A.3.

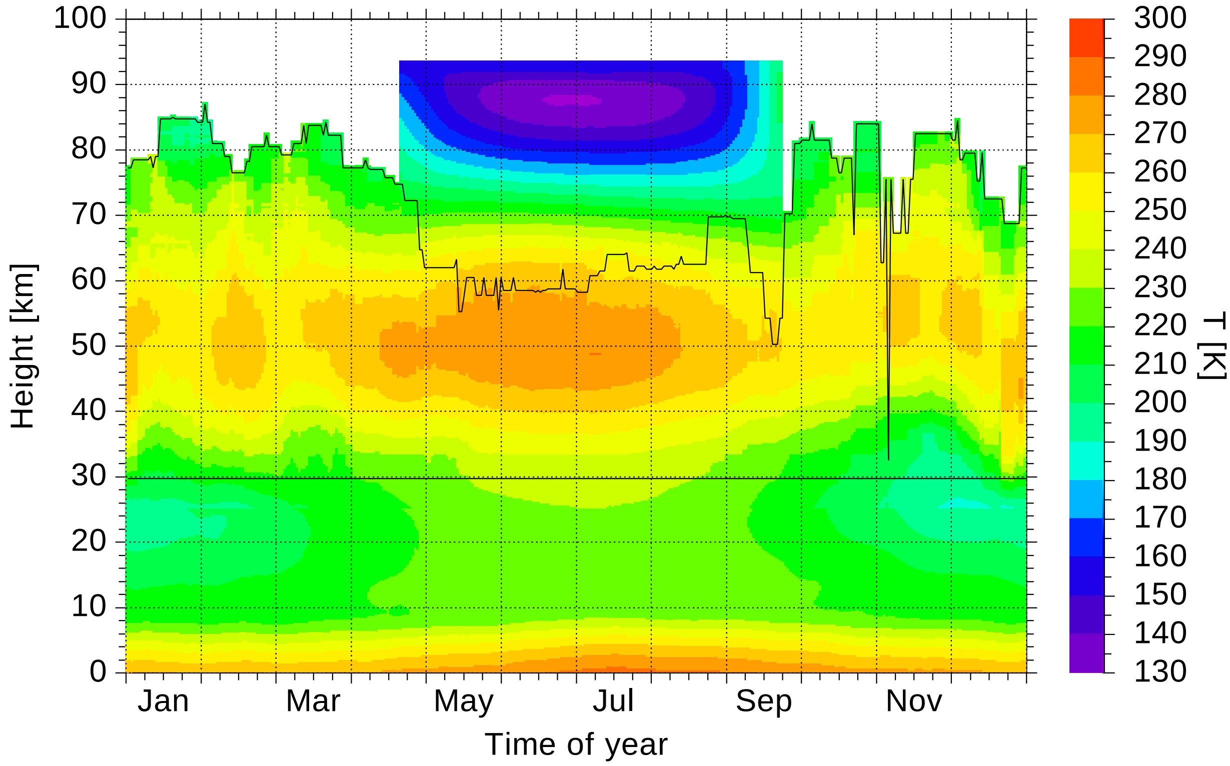

Figure 4.8: Combination of the RMR lidar temperatures from Fig. 4.7 with the *Lübken* [1999] climatology in the summer upper mesosphere and the mean ECMWF temperatures interpolated to (70° N, 15° E) for 1997 to 2005 below 30 km. The latter were smoothed with a 15-day running-average filter. The upper and lower limits of the RMR lidar data are marked by black lines. See text for details of the interpolation at the borders.

summer months. The lower stratosphere is approximately 20 K warmer in summer than in winter. At the stratopause, the difference is around 15 K. As shown earlier in Fig. 4.4, there was a SSW in nearly every winter in the years 1997 – 2005 discussed here. This is also apparent in the mean winter stratopause temperatures in Fig. 4.7. While the overall mean temperature of the stratosphere in winter (October – March) is around 260 K over ALOMAR (see green monthly means in Fig. 4.5), even the mean seasonal temperature is larger than 260 K for a number of periods (e.g. late December, early January, mid-February). The stratopause height and temperature variations are analysed in more detail in Sec. 4.6.

Fig. 4.8 shows a combination of three data sets: RMR lidar, *Lübken* [1999] in the summer upper mesosphere and a mean ECMWF field at 0 UT for 1997 to 2005 below 30 km. The ECMWF data was interpolated to the geographical location (70° N, 15° E) and smoothed with a 15-day running-average filter to have a similar temporal resolution as the lidar data. The black line marks the upper and lower limits of the RMR lidar data where it overlaps with the Luebken1999 and ECMWF temperatures. The transition from one data set to another was smoothed by a linear interpolation over 8 km around the black line. The remaining discontinuities are very small. This combined temperature climatology covering the entire lower and middle atmosphere during the whole year is listed in App. A.3, Tabs. A.4 and A.5. The differences between these three data sets will be discussed in the next section.

4.5 Comparison with other data sets

The difficulties of operating a lidar station in the Arctic have already been mentioned. Besides the ALOMAR RMR lidar, there are only three other large lidar stations at comparable northern latitudes: The Bonn University lidar at the Esrange in northern Sweden (69° N) [*Blum and Fricke*, 2005], the ARCLITE lidar in Søndrestrøm on Greenland (67° N) [*Thayer et al.*, 1997] and the Eureka lidar in the Canadian Arctic (80° N) [*Whiteway and Carswell*, 1994]. Although some wintertime temperatures have been published from these lidar stations [e.g. *Duck et al.*, 2000; *Blum*, 2003; *Blum et al.*, 2006], none of these lidar systems has so far produced a temperature data set that spans the whole year including the summer. Reasons for this are the technical difficulties of measuring temperatures in the polar summer middle atmosphere by lidar, the large effort and manpower needed to operate an Arctic lidar system and the weather conditions. This implies that it was not possible to compare the ALOMAR RMR lidar seasonal temperature variation to other lidar derived data sets. The large variability in winter even at one site and the geographical spread of the lidar stations prevent a useful comparison of the winter data sets. Instead, comparisons with the reference atmospheres CIRA86, NRLMSISE00 and Luebken1999 and with ECMWF analyses of the operational model version (“operational ECMWF”) will be shown.

A statistical comparison of the RMR lidar and the operational ECMWF analyses taken from the running model at the ECMWF is shown in Fig. 4.9. The operational ECMWF analyses were available every six hours at 0 UT, 6 UT, 12 UT and 18 UT for the location

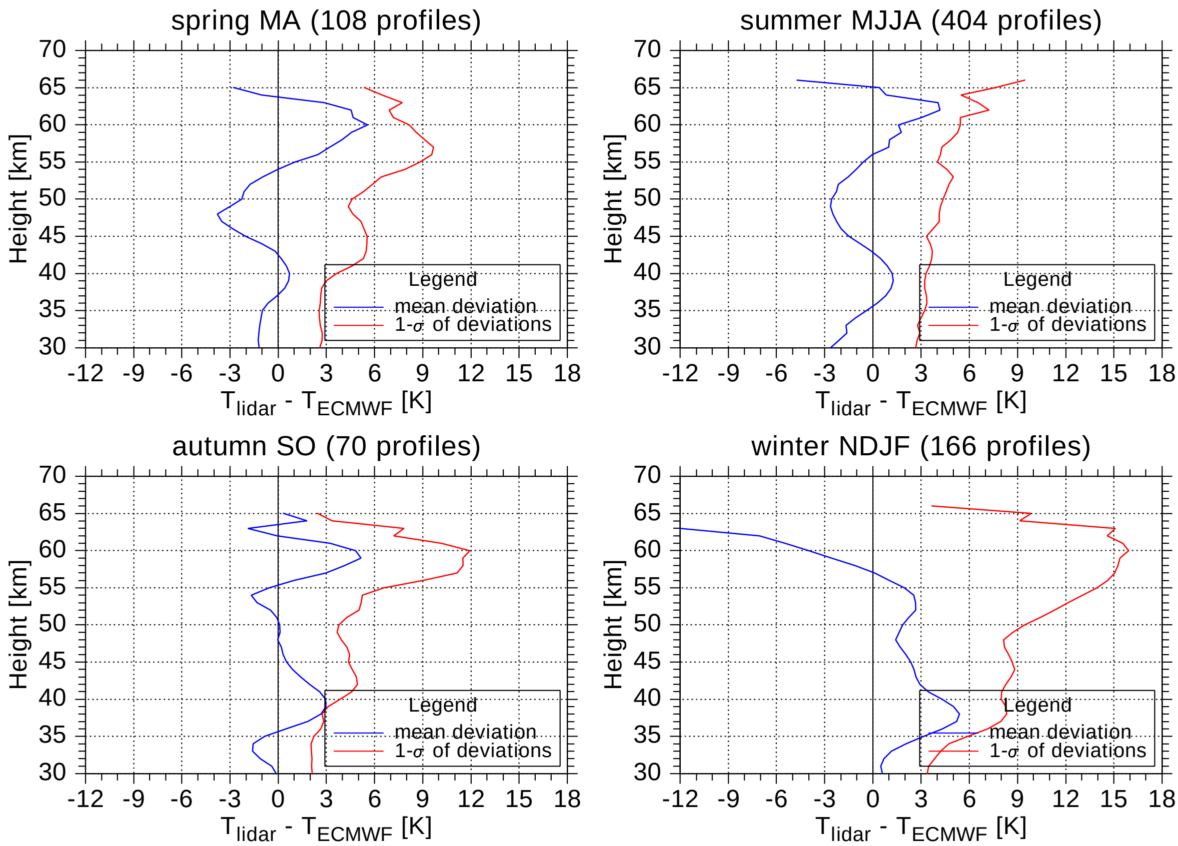

Figure 4.9: Statistical analysis of the deviations between RMR lidar and ECMWF operational analyses temperatures divided by seasons. Positive mean deviations (blue line) signify heights were the ECMWF calculates temperatures which are lower than those measured by the RMR lidar. The red line gives the 1-σ range of the deviations.

(70° N, 15° E). For each lidar measurement, the ECMWF profile closest in time to the centre-time of the lidar measurement was selected. Then the measurements were grouped into seasons for spring (March, April), summer (May, June, July, August), autumn (September, October) and winter (November, December, January, February). The differences were calculated by subtracting the ECMWF profile from the RMR lidar temperature profile. Fig. 4.9 shows the mean deviation for each season and the standard deviation (1-σ spread) of the set of differences around the mean for each season. The error of the mean is typically <0.5 K.

For all seasons except winter, the mean deviations grow with height as does the spread of the profiles. At the same time, the mean deviations are more or less centred around zero. The latter implies that the ECMWF gives a good approximation of the real temperature structure with no systematic deviations. Since ECMWF is mostly assimilating data from radiosondes and satellites in the lower atmosphere and only fewer data from higher altitudes, it is expected that the spread of the differences grows with height. Also the vertical distance between the pressure level of the ECMWF model grows with height. This makes it more difficult for the model to resolve the correct stratopause height and temperature, especially when the stratopause temperature maximum is confined to a small altitude region.

In winter however, there seems to be a systematic shift of the ECMWF temperatures towards too low values below 55 km. Above 60 km and hence at the upper border of the ECMWF model, the ECMWF temperatures are on average too high. This implies that the stratopause is on average too high in the ECMWF temperature profiles during winter. Also the spread of the differences around the mean at each altitude is up to three times larger than in the other seasons. Part of these differences are probably due to movements of the polar vortex and stronger planetary wave activity in winter which are not completely resolved by the ECMWF analyses.

Fig. 4.10 describes the detailed seasonal variation of the differences between RMR lidar and ECMWF for all years between 1997 and 2005. Prior to March 1999, the uppermost ECMWF model level was not higher than 33 km so there is only very little overlap with the RMR lidar temperature profiles during this period (Figs. 4.10A and 4.10B). During the summer months, the differences in the upper stratosphere are less than 5 K while they can reach 10 K in the lower mesosphere. Comparing the year 1999 (Fig. 4.10C) to later years, it becomes visible that the operational ECMWF model is improving over the years. In summer 1999, there was a cold bias in the upper stratosphere and a warm bias in the lower mesosphere. In later years, the sign of the deviation during summer is more evenly distributed in height. However in winter, the deviations of the ECMWF analyses from the RMR lidar measurements reach up to 30 K in both directions. Comparing the wintertime differences in Fig. 4.10 to the absolute temperatures shown previously in Fig. 4.4, it becomes clear that the strongest differences are observed during SSW events (see e.g. December 2000, February 2001 or January 2004). Remarkably, the SSW events in January and February 2005 (Figs. 4.4I and 4.10I) have been captured much better in the ECMWF analyses. A particular observation is that the stratopause of the ECMWF model in summer 2005 (April – August) is lower than observed by the RMR lidar while there is no such systematic difference in the previous years.

This tendency of good agreement between RMR lidar and ECMWF operational analyses in summer and larger deviations in winter is also reproduced when comparing the seasonal difference averaged for the years 1997 to 2005. Fig. 4.11 displays the deviations of the mean ECMWF temperatures above 30 km from the mean RMR lidar seasonal temperature variations shown in Fig. 4.8. Again, the agreement is good in summer with differences generally below 5 K as was shown already for the single years in Fig. 4.10. In the lower

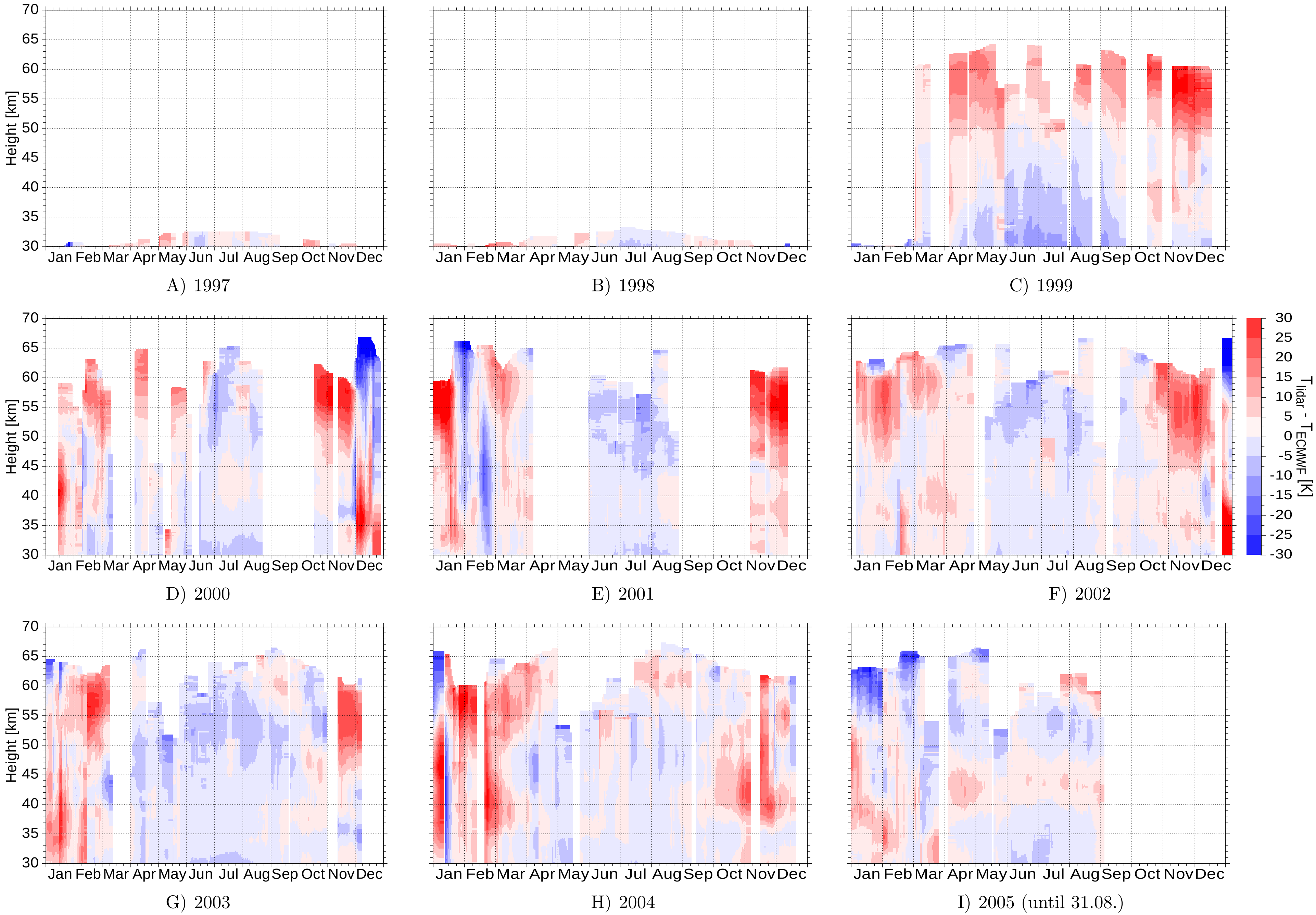

Figure 4.10: Seasonal temperature difference between measurements with the RMR lidar and the corresponding operational ECMWF temperature profiles interpolated to (70° N, 15° E). Red denotes areas where the lidar temperatures are higher than the ECMWF analyses.

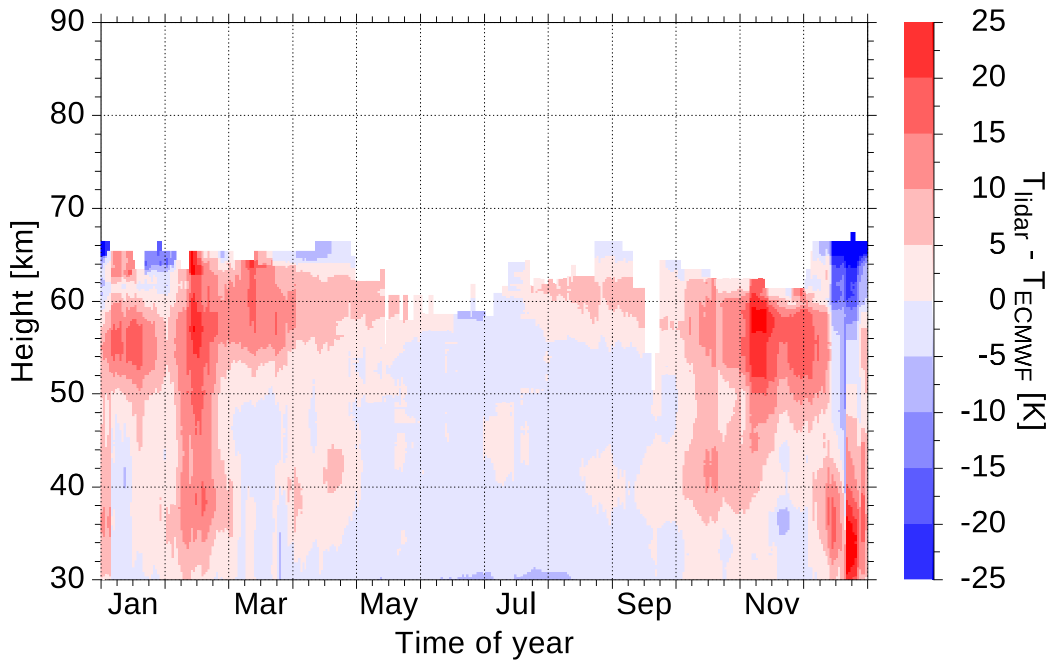

Figure 4.11: Comparison of the RMR lidar seasonal temperature variation to the mean ECMWF temperature at (70°, 15° E) during the years 1997 − 2005 which were smoothed with a 15-day running-average filter for this comparison.

mesosphere during winter, the deviations of the ECMWF temperatures from the RMR lidar temperatures are much larger than in summer. For most height regions the temperatures from ECMWF are lower than those of the RMR lidar. In the upper winter stratosphere, the deviations are largest during times of SSW events reaching up to 25 K. Only in December in the lower mesosphere, the mean ECMWF temperatures are much higher than the RMR lidar temperatures. This is due to the strong SSW events at the end of December 2000 and 2002 which dominate the mean RMR lidar temperature during this time of the year and where ECMWF does not resolve the mesospheric cooling associated with SSW events correctly (see Sec. 5.1.1 for more details on this cooling during SSW).

Turning to the comparison of the RMR lidar temperatures to reference atmospheres, Fig. 4.12 presents the difference between the RMR lidar seasonal mean temperature field and the NRLMSISE00, CIRA86 and Luebken1999 reference atmospheres. The NRLMSISE00 data set was calculated for the latitude 69° N. The solar parameters that can be specified for NRLMSISE00 were held constant at mean values ($F_{10.7}$=150, AP=4). This is advised in the NRLMSISE00 code for altitudes below 80 km. In summer, the NRLMSISE00 reference atmosphere is colder than the RMR lidar in the upper stratosphere and warmer in the lower mesosphere (Fig. 4.12A). The differences reach up to 15 K which is three times the maximum differences seen in summer between RMR lidar and ECMWF analyses. In winter, the differences are even larger but follow the same pattern. In the upper mesosphere above 75 km the NRLMSISE00 reference atmosphere is colder than the mean RMR lidar temperatures. Similarly large differences between temperature measurements and NRLMSISE00 at high latitudes have been found by *Pan and Gardner* [2003] for measurements above South Pole. In February and at the end of December the RMR lidar temperatures in the stratosphere are higher than NRLMSISE00 because of the SSW events that dominate the RMR lidar mean during these times of the year (see Fig. 4.4). At the end of December, the mesospheric cooling during the SSW event leads to lower RMR lidar temperatures compared to NRLMSISE00 in the lower mesosphere.

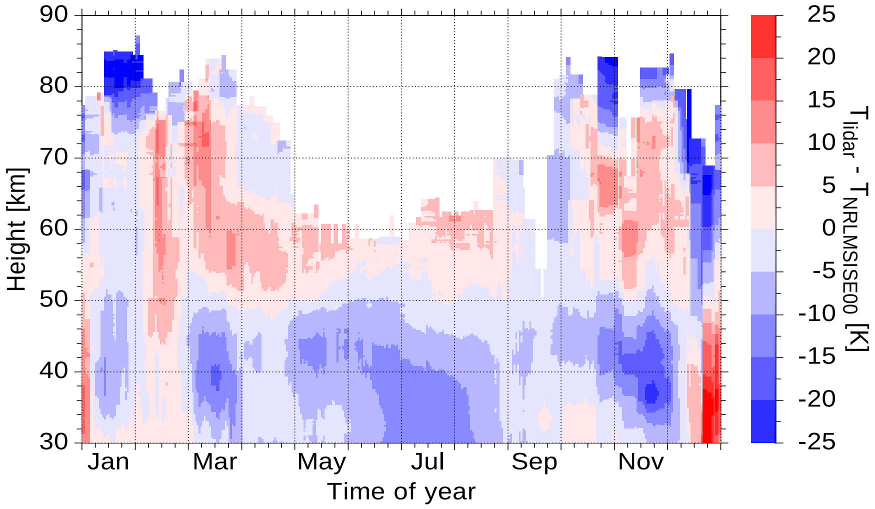

A) Difference between RMR lidar mean temperatures and NRLMSISE00

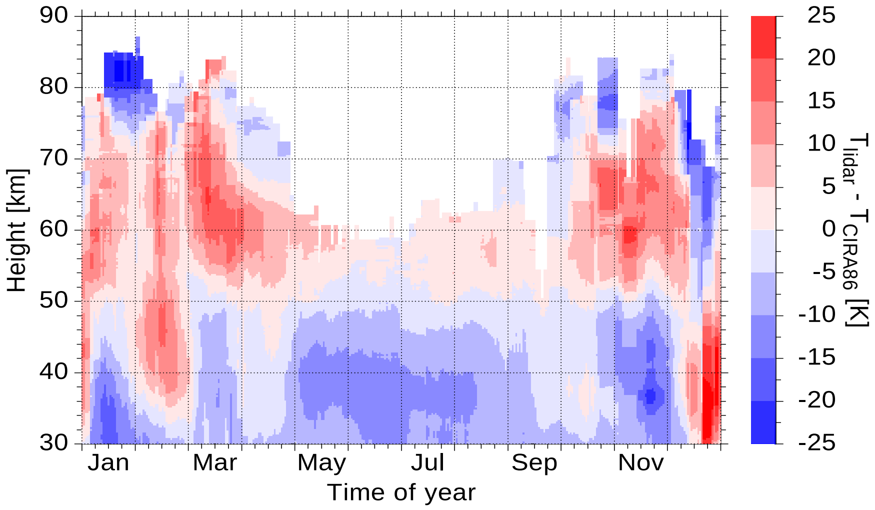

B) Difference between RMR lidar mean temperatures and CIRA86

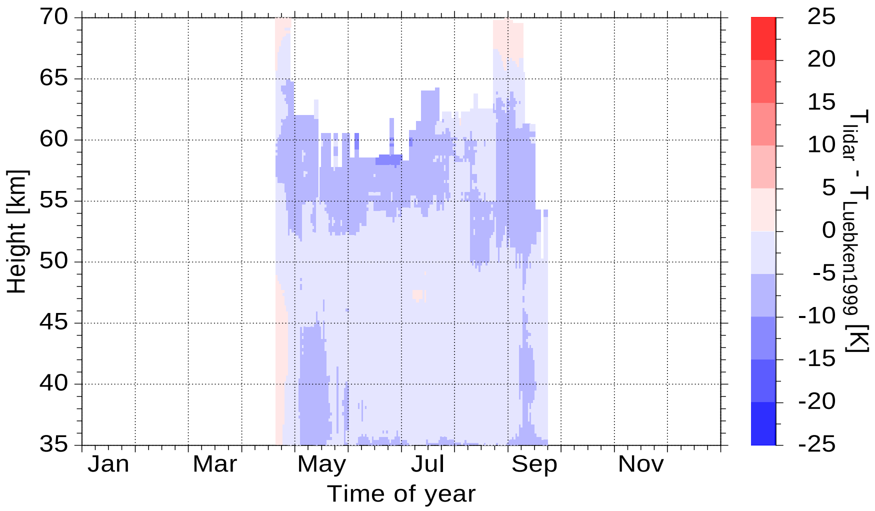

C) Difference between RMR lidar mean temperatures and Luebken1999

Figure 4.12: *Upper panel:* Comparison of RMR lidar temperatures to the NRLMSISE00 reference atmosphere at 69° N. *Middle panel:* Comparison of RMR lidar temperatures to the CIRA86 reference atmosphere at 70° N interpolated by cubic splines from the monthly values. *Lower panel:* Comparison to the Luebken1999 reference atmosphere.

Fig. 4.12B shows the differences between mean RMR lidar temperatures and the CIRA86 reference atmosphere [*Fleming et al.*, 1990]. This is an older standard atmosphere which is known to be inaccurate in the polar regions. CIRA86 provides temperature profiles for the middle of each month which have been interpolated by cubic splines to get temperature profiles for every day of the year. The deviations of the CIRA86 temperatures from the RMR lidar temperatures follow the same patterns as for the NRLMSISE00 reference atmosphere but are somewhat larger, especially in the winter mesosphere. The comparison to CIRA86 is shown here because it is still widely used in the scientific community.

The Luebken1999 reference atmosphere (see Fig. 4.12C) only covers the period from end of April to late September. It was calculated from 89 falling sphere flights during the years 1987 – 1997. The RMR lidar temperatures are higher than Luebken1999 in the upper mesosphere at the end of April and in September while they are lower than Luebken1999 during the entire time in the stratosphere and lower mesosphere. The difference reaches up to -10 K around 60 km. In June and July, part of this difference may be due to the proximity to the upper border of the RMR lidar altitude range where there may still be a small influence of the start temperature taken from NRLMSISE00 which is ∼10 K colder than Luebken1999 in the lower mesosphere. Remember that the RMR lidar profiles have a statistical uncertainty of 5 K at the upper border (including the uncertainty of the start temperature) which could explain half of the observed differences. Another reason may be the different years that were used to calculate the Luebken1999 (1987 – 1997) and the RMR lidar (1997 – 2005) temperatures.

4.6 Stratopause heights and temperatures

The stratopause separates the stratosphere from the mesosphere. The comparison of RMR lidar temperatures to ECMWF and three reference atmospheres in the last section has shown that its altitude is an indicator to assess the agreement of different data sets. This section will examine the stratopause height and temperature in the RMR lidar, ECMWF and NRLMSISE00 data sets in more detail. For these analyses, the stratopause is defined as the first maximum in the temperature profile above 35 km which is followed by a decrease of temperature with height of at least 10 K until the upper end of the profile. For the RMR lidar the night-mean profiles were used to derive the stratopause height and temperature. Temperature profiles that do not show a clear stratopause are excluded. Such cases are found in summer when the profiles do not reach much higher than the stratopause or in the aftermath of a SSW event when the middle atmosphere shows a near isothermal temperature structure. For the same reason, the search is restricted to altitudes below 70 km. The ECMWF stratopause was determined from the mean temperature field for the years 1997 – 2005. After inspection of the mean temperature field, the search was restricted to altitudes below 55 km and the required decrease in temperature with height above the stratopause was set to 3 K only. Since the highest pressure level in the ECMWF profiles used in this thesis is at 0.1 hPa, this adaption to the algorithm was necessary to reliably find the stratopause in the mean temperature field.

The height and temperature of the stratopause are shown in Fig. 4.13. The stratopause parameters derived from the RMR lidar temperature profiles for the nine years from 1997 to 2005 are shown in different colours. The height of the stratopause shown in Fig. 4.13A experience a large variability of up to 25 km in winter and around 8 km in summer. A similar behaviour is seen in the stratopause temperatures presented in Fig. 4.13B. The

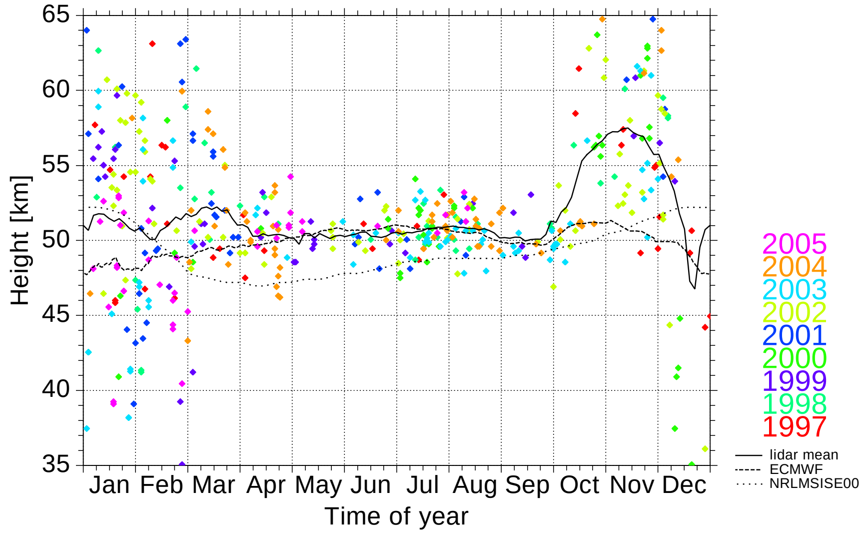

A) Stratopause heights

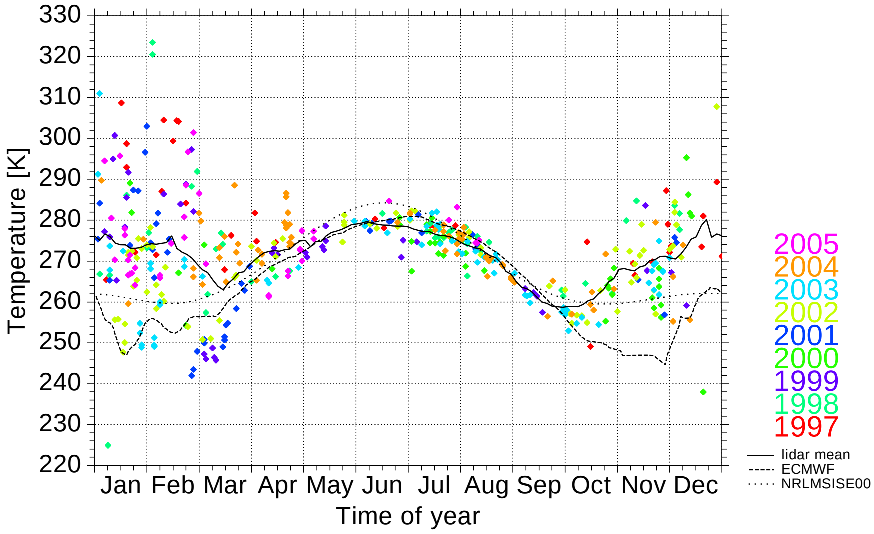

B) Stratopause temperatures

Figure 4.13: Stratopause heights (upper panel) and temperatures (lower panel) above ALOMAR as a function of season. Different years are plotted in different colours. The solid black line is the 31-day running average of the RMR lidar measurements. ECMWF stratopause height and temperature are shown as dashed line (smoothed by a 15-day running average filter). The dotted line is calculated from NRLMSISE00.

variability is less than 15 K in summer and up to 80 K in winter. The large variability of wintertime stratopause heights and temperatures is a result of the frequent SSW events in the Arctic middle atmosphere. The solid black line is a 31-day running average which shows the mean seasonal behaviour of the stratopause above ALOMAR. The stratopause heights and temperatures calculated from ECMWF and NRLMSISE00 are shown as dashed and dotted lines, respectively. In summer there is general agreement within a few Kelvin of the stratopause temperatures from the different data sets. The stratopause heights in the NRLMSISE00 reference atmosphere are 2 − 3 km to low compared to the RMR lidar and ECMWF data. The differences in stratopause height and temperature between the three data sets in winter are much larger and reach up to 7 km and 25 K, respectively.

Several studies have shown that the 11-year solar cycle can influence the temperature in the stratosphere [e.g. *McCormack and Hood*, 1996; *Labitzke*, 2001] and in the mesosphere [*Kodera and Kuroda*, 2002; *Keckhut et al.*, 2005]. While the effect is easily observed in many data sets, the physical mechanism behind it is still not well understood [*Shibata and Kodera*, 2005]. The increased UV radiation during solar maximum compared to solar minimum leads to warming in the stratosphere by increased absorption in the ozone layer as well as increased ozone production. But there is also a dynamical feedback which is difficult to quantify [*Shibata and Kodera*, 2005]. Since the stratopause is separating the stratosphere and the mesosphere, it seems natural to look for a signature of the 11-year solar cycle in its temperature and height. As the RMR lidar data presented here covers nine years which is not even one full solar cycle, it is difficult to identify the solar cycle influence unambiguously. However, it is possible to look for correlations between the solar cycle and the stratopause height and temperature.

For these correlations, the composite Lyman-α irradiation from the LASP Interactive Solar Irradiance Datacenter (http://lasp.colorado.edu/lisird/) is used to represent the state of the solar cycle. From Fig. 4.13 one would expect it to be easier to find a solar cycle signal in summer when the day-to-day variability is lower than in winter. But when calculating the correlations, it is found that there is no correlation between the stratopause temperature and the solar cycle in summer (not shown). Only in winter, a significant correlation between solar irradiance and stratopause temperature is found as shown in Fig. 4.14. It gives the mean stratopause temperatures for the winter months (October-March) over ALOMAR as a function of Lyman-α irradiation for all nine years analysed in this work. The error bars give the 1-σ spread of the winter stratopause temperatures for each year. The black solid line is a linear least-squares fit to the yearly values. The 1-σ uncertainty of the linear fit is given by the dotted lines. The stratopause heights show no significant correlation with the solar cycle, neither in summer nor in winter.

Keckhut et al. [2005] investigated the solar cycle influence in the stratosphere and mesosphere in the tropics and at mid-latitudes. They found a stronger solar cycle influence in winter than in summer with a maximum around 50° N (their Fig. 5). The temperature difference between solar maximum and solar minimum was found to be less than 6 K in the upper stratosphere at 44° N. The observations at 69° N in this study which does not even cover a whole solar cycle show temperature differences at the stratopause of more than -15 K between high solar activity and low solar activity, namely the stratopause is colder when the solar activity is high and warmer when it is low. This temperature difference is much larger than the solar cycle influence observed by *Keckhut et al.* [2005] at mid-latitudes. What is more

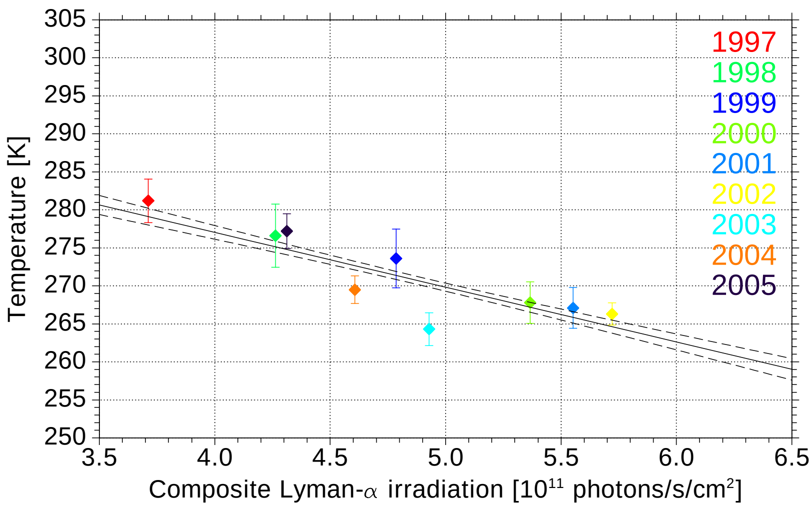

Figure 4.14: Correlation of stratopause temperature above ALOMAR and solar composite Lyman-α index for the winter months October to March. Each year is plotted in a different colour. The black lines gives a linear regression with its 1-σ error bounds. The correlation is significant with R^2=0.72.

surprising is the opposite sign of the solar cycle influence compared to mid-latitudes. A solution to this may be dynamical feedbacks included in the calculations of *Shibata and Kodera* [2005]. Their Fig. 16 shows a negative correlation of temperatures at high northern latitudes during January above 1 hPa which is explained through dynamical responses of the atmosphere to the changed solar UV radiation. Since the mean stratopause height (Fig. 4.13A) in the RMR lidar measurements is larger than 50 km ($\sim$0.8 hPa) for most of the winter, this may explain the negative sign of the correlation.

4.7 Summary

In this chapter, the first comprehensive overview of nine years of RMR lidar temperature measurements above ALOMAR was presented. It has been shown that a large effort over many years is needed to obtain a complete yearly coverage of the middle atmosphere. This is only achieved by combining temperature profiles measured between 1997 and 2005. Monthly mean profiles as well as a seasonal climatology covering the altitude range 30 km – 85 km in winter and 30 km – 65 km in summer have been shown to generally agree with the mean ECMWF temperature field and with the CIRA86, NRLMSISE00 and Luebken1999 reference atmospheres within $\pm$5 K in summer and $\pm$15 K in winter.

There are however significant deviations between the RMR lidar temperatures and the other data sets in certain altitude regions and times of the year. Since the geophysical variability is smaller in summer than in winter, the differences between the data sets also is smaller in summer than in winter. The largest deviations were found at times of SSW events which are not included in the reference atmospheres. The ECMWF analyses include the SSW events but timing and the magnitude of the SSW above ALOMAR are not well resolved by the ECMWF analyses. The RMR lidar temperature climatology therefore is a good candidate to validate middle atmosphere models like the new Leibniz-Institute Middle Atmosphere model [*Berger*, 2007].

Stratopause heights and temperatures above ALOMAR have also been investigated and compared to ECMWF and NRLMSISE00. Also here, the differences between RMR lidar measurements and ECMWF analyses and NRLMSISE00 reference atmosphere are smaller in summer than in winter. While the general seasonal variation agrees in the summer, there are large differences in the winter months. At the stratopause the temperature gradient of the atmosphere changes sign from increasing temperature with height below the stratopause to decreasing temperature with height above. The temperature gradient influences gravity wave propagation through the Brunt-Väisälä frequency (Sec. 2.3) which may lead to gravity wave breaking (Sec. 2.5.6). Temperature profiles with a correct stratopause height therefore are important when modelling gravity waves (see Chap. 6 for more details on gravity waves).

Even though the stratopause height does not change during the solar cycle, the stratopause temperatures during winter are higher during solar minimum than during solar maximum. The size of this effect and its sign is larger than anticipated from previous observations and model calculations. However, most of the previous analyses concentrated on low- and mid-latitudes and did not cover the polar regions. A recent model study by *Shibata and Kodera* [2005] is qualitatively and quantitatively consistent with the observed correlation.

Chapter 5

Sudden Stratospheric Warmings and Mesospheric Inversion Layers

After studying the mean state of the thermal structure above ALOMAR in the last chapter, two distinct phenomena found in the temperature profiles at certain times will be presented in this chapter. First sudden stratospheric warmings (SSWs) will be analysed. The first RMR lidar observation of a very high temperature of 322 K at the Arctic stratopause in February 1998 has been reported by *von Zahn et al.* [1998a]. They mentioned that the highest stratopause temperature ever seen above ALOMAR is 326 K, measured in February 1984 by falling spheres during the MAP/WINE campaign [*Petzoldt et al.*, 1987]. One focus of this chapter will be the connection between warming at the stratopause and associated cooling in the mesopause region.

Mesospheric inversion layers (MILs) are investigated in the second part of this chapter. They are routinely observed at mid-latitudes [e.g. *Hauchecorne et al.*, 1987; *Leblanc et al.*, 1995] but are rather rare at high latitudes [e.g. *Cutler et al.*, 2001; *Duck and Greene*, 2004]. This chapter will show a few examples of MILs and then present the first MIL statistic for the ALOMAR site including their occurrence rate and height distribution. MILs are analysed in both RMR lidar and falling sphere temperature profiles. The comparison of these two techniques allows conclusions about the temporal behaviour of MILs.

5.1 Sudden stratospheric warmings

Above ALOMAR, SSWs are observed nearly every winter in the years 1997 – 2005 (see Fig. 4.4 and *Manney et al.* [2005]). Their effect is even visible in the nine year temperature average for ALOMAR (Fig. 4.7) which shows temperature maxima at the stratopause in e.g. early and late December and mid-February which are caused by SSW events in the single years. It is therefore difficult to establish a “normal” winter temperature which is not influenced by SSW events. How this is done here will be described below.

Apart from the winter 2001/2002, the RMR lidar observed at least one sudden stratospheric warming (SSW) every year (see red diamonds in Fig. 4.4). This high occurrence rate of SSW is a particular trait of the late 1990s [*Manney et al.*, 2005]. As an example, Fig. 5.1 shows the winters 2000/2001 and 2004/2005 where the RMR lidar captured the evolution of SSWs above ALOMAR. The red diamonds mark profiles during SSW events which were identified with the following algorithm.

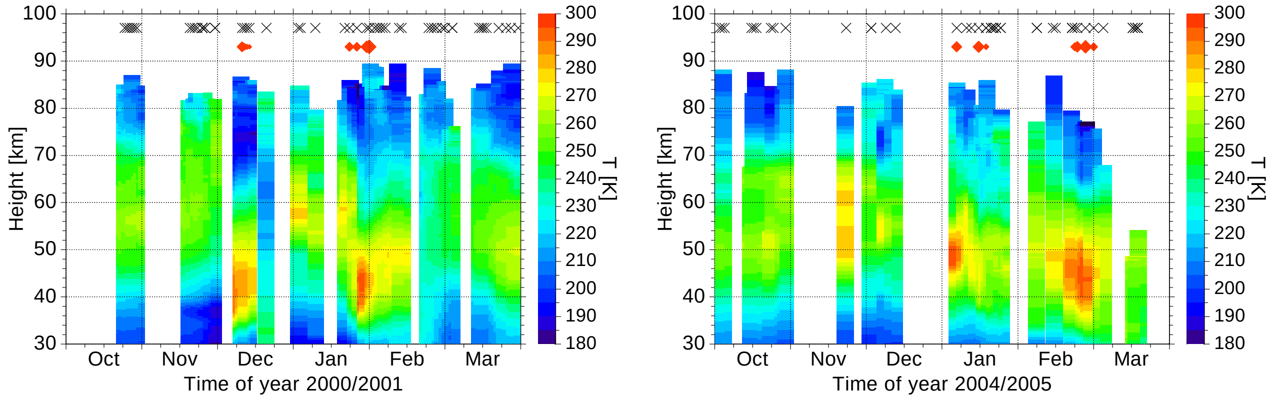

A) Winter 2000/2001 B) Winter 2004/2005

Figure 5.1: SSW above ALOMAR in the winters 2000/2001 and 2004/2005. Measurements are marked by 'X' in the upper part of the plot. The red diamonds mark profiles during SSW events. Their size is proportional to the amplitude of the warming.

First the undisturbed winter state is approximated by a 31-day median filter applied to the daily mean temperature profiles in Fig. 4.6. The median value is used to be independent of outliers with high temperatures during SSW events. Then the stratopause height and temperature are calculated for the undisturbed winter state and the night-mean profiles for each day (see Sec. 4.6). SSW events are positively identified if the stratopause of the night-mean profile is at least 25 K warmer than the stratopause of the undisturbed winter case and if it is not more than 7 km higher than the stratopause of the undisturbed profile. When the actual stratopause is more than 7 km lower than the undisturbed stratopause at this day, a temperature difference of at least 10 K is required for the profile to be classified as SSW. These criteria were determined from the temperature profiles to avoid false positives. From the 332 winter temperature profiles presented in the last chapter, only 44 fulfil the criteria for a SSW. The identified SSW profiles are marked with red diamonds in Figs. 4.4 and 5.1. They are also listed in App. A.4. Only one SSW is observed in November and seven SSWs in December. Hence the majority of SSWs observed with the RMR lidar took place in January and February.

The SSW event at the end of January 2001 in Fig. 5.1A follows the classical development as described in Sec. 2.7. The warming starts around 60 km and then propagates downward and intensifies. At the same time, the mesosphere is cooling between 65 km and 85 km. Whether there is a small temporal offset between stratospheric warming and mesospheric cooling cannot be determined from the RMR lidar measurements because due to the weather conditions in winter, continuous lidar observations during the entire SSW event were not possible. The apparent step in altitude and temperature of the SSW from 23 January to 26 January is due to missing measurements in between. A similar but much smaller downward movement is seen for the SSW in the second half of February 2005 in Fig. 5.1B. The SSW in early January 2005 however does show neither downward motion nor cooling in the mesosphere. This illustrates that the SSW events observed above ALOMAR are very variable in both the amount of the warming and the vertical structure. One reason for this variability are changes of the Artic polar vortex. Depending on the location of ALOMAR relative to the vortex, the SSW events show different signatures in the RMR lidar temperature profiles. For single events, this may be investigated further by analysing the stratospheric wind field from ECMWF.

5.1.1 Connection to mesospheric cooling

At the same time when there is intense warming in the stratosphere, temperatures in the mesosphere are lower than the undisturbed winter state (see also Sec. 2.7). This connection between stratospheric warming and mesospheric cooling is investigated in Fig. 5.2. The upper panel shows the temperature differences between profiles identified as SSW and the undisturbed winter state for the corresponding day of the year (blue and violet lines). Profiles which do not reach at least 70 km are not shown. The maximum warming is 80 K relative to the undisturbed winter state. Of the 30 profiles shown, mesospheric cooling is absent from 5 profiles (17%) which are plotted in violet. The red line is the average of the remaining 25 profiles (restricted to altitudes where there are at least 3 profiles). It shows a mean warming in the upper stratosphere of 36 K and a mean cooling in the mesosphere of up to 22 K. On average, warming is observed between 30 km and 54 km while there is cooling above up to an altitude of ∼82 km. As the number of profiles decreases at the upper end, the upper end of the cooling and its reversal to warming again in the mesopause region cannot be determined with great accuracy. In the lower panel of Fig. 5.2, the temperature differences have been normalised to the temperature difference at the stratopause of each profile. Also the height is now given relative to the stratopause:

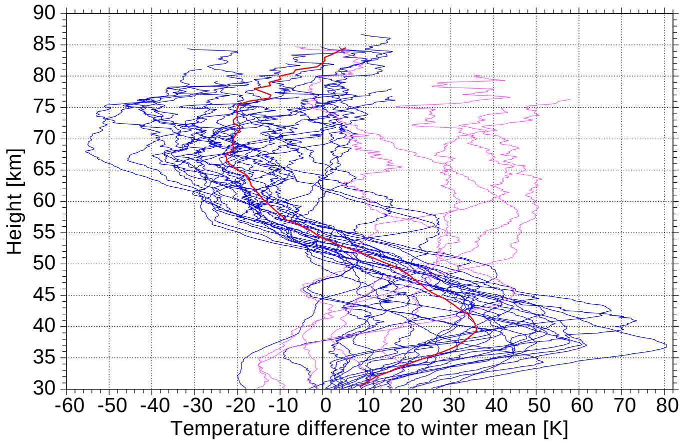

A) Temperature differences

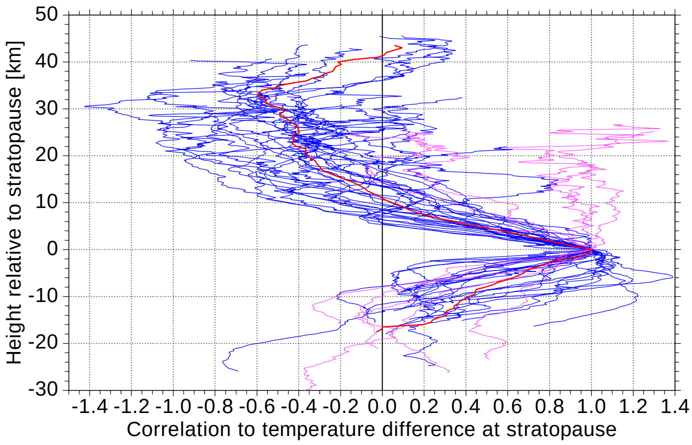

B) Correlation of temperature differences relative to stratopause

Figure 5.2: *Upper panel:* Temperature differences between SSW profiles and the undisturbed winter mean state. The violet lines don't show signs of mesospheric cooling. The red line is the mean of the blue profiles. Only profiles reaching at least 70 km are shown. *Lower panel:* Correlation of temperature differences to the difference at the stratopause with the altitude also given relative to the stratopause.

$$corr(z' = z - z_{stratopause}) = \frac{T_{SSW}(z) - T_{undist.}(z)}{T_{SSW}(z_{stratopause}) - T_{undist.}(z_{stratopause})} \tag{5.1}$$

This normalisation highlights the similarity in the altitudinal structure of the SSW events. By definition, the relative deviation is unity at the stratopause ($z' = 0$ km). On average, the warming is restricted to a region from 16 km below to 10 km above the stratopause. The mesospheric cooling is observed in a layer of 30 km thickness starting 10 km above the stratopause. The average cooling in the mesosphere in Kelvin, relative to the undisturbed winter state, is 60% of the corresponding warming at the stratopause. In some cases, the cooling is even larger than the warming at the stratopause ($corr < -1.0$).

The correlations presented in Fig. 5.2 can be qualitatively compared to Fig. 3 in *Siskind et al.* [2005]. In this study, SABER satellite temperature fluctuation time-series in the stratosphere, mesosphere and lower thermosphere during three periods in February 2002 and January/February 2003 at 80° N and in August 2002 at 70° S are correlated to the temperature fluctuations at 10 hPa (∼30 km). A negative correlation is found for the altitude region 1 hPa – 0.01 hPa (∼47 km – 78 km). Although in this thesis the temperature differences are compared with the temperature fluctuations at the stratopause which is on average at 40 km (Fig. 5.2A), the general shape and the altitude region of the negative correlation is similar. The magnitude of the mesospheric cooling is 70% – 90% of the value at 10 hPa in the study by *Siskind et al.* [2005]. Thus the mesospheric cooling observed by *Siskind et al.* [2005] is within the range of mesospheric cooling observed with the RMR lidar. However, it is slightly larger than the mean mesospheric cooling of 60% observed with the RMR lidar (red line in Fig. 5.2B). This is probably due to the selection of three specific events in the study by *Siskind et al.* [2005] while the analysis presented here is based on 25 SSW events. Another advantage of this study is the improved vertical resolution of the RMR lidar compared to the SABER measurements. This is reflected in the higher variability of the RMR lidar observed temperature differences and correlations compared to the SABER measurements.

Fig. 5.2A also shows that the mesospheric cooling is restricted to the middle mesosphere below 82 km which implies that the temperatures in the altitude region of the OH layer around 87 km are not correlated to the stratopause temperature. As noted by *Siskind et al.* [2005] this explains why previous OH imager studies did not find conclusive evidence of cooling during SSWs [*Walterscheid et al.*, 2000; *Sigernes et al.*, 2003; *Cho et al.*, 2004].

Comparing the middle mesosphere temperatures during SSWs to calculated mesospheric radiative equilibrium temperatures shows that for all but the cases with the largest observed cooling, the temperatures do not drop below the radiative equilibrium temperature [*Shine*, 1987]. From the theoretical understanding of the meridional circulation (see Sec. 2.6) this indicates that the westward travelling gravity waves responsible for the relatively warm undisturbed winter mesosphere are blocked by the weakening or even reversal of the mesospheric jet. However, no eastward propagating gravity waves reach the mesosphere because they would force temperatures to drop below radiative equilibrium contrary to the observations.

The 30 temperature profiles during SSW events shown in Fig. 5.2A show the large variability of the altitudinal structure of the stratospheric warmings above ALOMAR. The maximum warming reaches up to 80 K and occurs anywhere between 35 km and 60 km altitude. However, the SSW events with the largest warmings show the maximum warming below 45 km. Interestingly, when the altitudes are scaled relative to the altitude of the stratopause, the altitudinal structure of the stratospheric warming is much more uniform as shown in Fig. 5.2B. This seems to indicate an important role of the stratopause during the development of SSWs.

5.2 Mesospheric inversion layers

As their name implies, mesospheric inversion layers (MILs) are regions in the mesosphere where the temperature gradient is positive, i.e. the temperature increases with height in contrast to the normal mesosphere temperature profile which shows decreasing temperatures with height. MILs are a very rare phenomenon at high latitudes and it is sometimes difficult to distinguish MILs and (gravity) waves. The latter can also cause temperature inversions in a single temperature profile but these are averaged out in the night-mean temperature profiles due to the vertical phase speed of the waves.

5.2.1 Detection criteria

By definition, MILs are only found above the stratopause. When a MIL propagates downwards in the mesosphere, its maximum will blend into the background temperature profile at the stratopause. For a MIL that is located only a few kilometres above the stratopause, the temperature at its maximum may be higher than the stratopause temperature of the undisturbed temperature profile and will thus define a new stratopause according to the stratopause definition used in Sec. 4.6. To demonstrate the difficulties of identifying MILs, Fig. 5.3 shows five night-mean RMR lidar temperature profiles from winter 2002/2003. The MILs are marked by thick lines while an adiabatic temperature gradient is shown as black dashed line. A typical feature of MILs is the near-adiabatic temperature gradient above the MIL which is especially clearly seen in the profiles of 7 December 2002 and 27 January 2003. The orange profile from 30 October 2002 shows an ambiguous case. Following Sec. 4.6, the stratopause for this profile is at 61 km and no MIL is identified (hence the missing thick part of the orange line in Fig. 5.3). An alternative view would be to interprete the temperature maximum at 50 km as the stratopause and to identify a MIL in the height range 53 km – 61 km. However, for the analyses in this thesis the former interpretation is used, i.e. the stratopause is defined as the absolute temperature maximum.

The distinction of MILs and large amplitude gravity waves is sometimes also difficult. The temperature profiles in Fig. 5.3 demonstrate that the lower boundary of a MIL is marked by a sudden change in the temperature gradient whereas a gravity wave would give a smoother transition between negative and positive temperature gradients. However, the purple profile from 27 January 2003 shows that this distinction sometimes is not well-defined. The temperature maxima at 55 km, 60 km, 64 km and 70 km could also be interpreted as a gravity wave with a vertical wavelength of 5 km. Another property of MILs is their persistency. As the MIL analysis in this thesis is performed on the night-mean temperature profiles, vertically

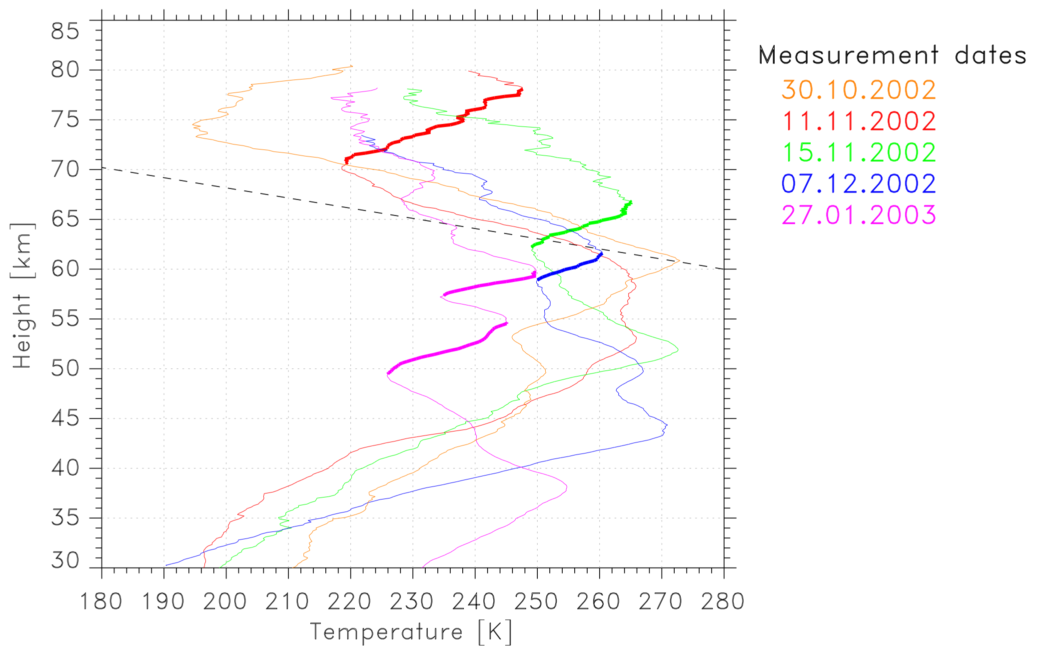

Figure 5.3: Example for MILs in the mesosphere above ALOMAR during winter 2002/2003. Plotted are nightly mean profiles for the given dates. Identified MILs are marked by thick lines except for 30.10.2002 where no MIL was found according to the criteria used in this thesis (see text for details). The dashed line shows an adiabatic temperature gradient.

propagating gravity waves are smoothed while a stable MIL is still present even after the temporal integration. However, “upper” MILs also propagate downward (see Sec. 2.8) and hence persistency only partially resolves the ambiguity of MILs and large amplitude gravity waves.

For the MIL statistics presented here, the following definition of a MIL was applied, following *Duck and Greene* [2004] who analysed temperature profiles from a lidar in Eureka (80° N) in the Canadian Arctic. First the stratopause was determined from the RMR lidar nightly mean profiles according to Sec. 4.6. Profiles without a stratopause were discarded. Then the temperature gradient is calculated with a three-point formula [*Burden and Faires*, 1993, Chap. 4] and smoothed with a 17-point (∼2.5 km) running-average filter to discard small-scale variations due to gravity waves with short vertical wavelengths and simplify the search for MILs. Now regions of at least 16-points (∼2.4 km) with a positive gradient are identified. The upper end of the MIL is defined by the return to a negative temperature gradient over at least 1 km. The latter condition excludes profiles where the positive temperature gradient is found at the upper end of the profile and thus could be due to a low mesopause followed by a positive temperature gradient above in the lower thermosphere. The amplitude of the inversion is defined as the temperature difference between the upper and the lower end of the inversion. Inversion layers that have amplitudes of less than 10 K are discarded as an additional constraint to assure that the layer of positive temperature gradient is indeed due to a MIL and not part of a gravity wave. The limit of 10 K has been determined from the measured temperature profiles. A list of the 45 MILs identified in the RMR lidar temperature profiles can be found in Tab. A.7 in App. A.5. The occurrence rates of the MILs are discussed below in Sec. 5.2.3.

In addition to the 834 nightly mean RMR lidar profiles, 194 temperature profiles from falling spheres were analysed for MILs. They were launched from the Andøya Rocket Range close to ALOMAR and the Esrange near Kiruna in northern Sweden between 1987 and 2005. The details of the falling sphere measurement technique have been described by *Schmidlin* [1976, 1991]. The data set used here has been assembled and analysed previously by *Müllemann* [2004]. To avoid erroneous MIL detections in the FS temperature profiles due to uncertainties at the upper altitude limit of this measurement technique, MILs where the lower limit of the inversion is above 80 km were discarded during the analysis of the FS data. A list of the 56 MILs identified in the FS temperature profiles can be found in Tab. A.8 in App. A.5.

5.2.2 Seasonal variation and mean parameters

Studies of MILs at mid-latitudes have shown a variation of the MIL occurrence rate with season with maximum in winter of ∼70% and half of this in summer [e.g. *Hauchecorne et al.*, 1987]. The seasonal variation of MIL occurrence above ALOMAR is shown for the RMR lidar in Fig. 5.4A and for the falling sphere profiles in Fig. 5.4B. The blue bars give the height range of the inversions and the red dots mark their amplitudes. The dates of measurements are marked by ’X’ in the upper part of the plots. It shows the near continuous seasonal coverage of the RMR lidar and a good coverage of the falling sphere profiles above Andøya at the beginning of the year, in summer and in early autumn. The dashed line in Fig. 5.4A gives the maximum altitude of the RMR lidar temperature profiles which is lower in summer than in winter due to the higher solar background when operating the lidar under daylight conditions in summer.

Both RMR lidar and falling spheres detect most MILs during winter where they are found throughout the entire mesosphere. In 56 falling sphere profiles from October to March, 36 profiles contained at least one MIL. Amplitudes of more than 30 K are only found for four

MILs in the falling sphere profiles in January (Fig. 5.4B). From April to September, no MILs have been observed with the RMR lidar. The 138 falling sphere profiles from this time period only show two MILs in summer in the lower mesosphere and three in late September. So there are very few MILs in the FS summer profiles and their amplitude is below 15 K. These summer MILs are obviously rare events which have been caught by change by the FSs on 26.05.1992 and 17.06.1987. The shape of the two FS temperature profiles at the height of the MIL (not shown) as well as the small amplitude suggest that the observed inversions were either due to a short-lived weak MIL or may have been caused by a gravity wave. Since the RMR lidar started observations in 1994 only, RMR lidar measurements cannot be used to decide this case. The fact that the RMR lidar did not observe MILs in summer supports the short lifetime of such inversions so that the FSs occasionally catch such an event while the RMR lidar with its longer integration time does not detect these summer MILs in the lower mesosphere. No MILs were observed in the FS summer profiles above 60 km and to the upper detection limit at 80 km. So besides two somewhat ambiguous MIL detections by FS, there are no MILs in the lower and middle mesosphere in summer.

To investigate MIL height and thickness more closely, Figs. 5.5 and 5.6 show height vs. amplitude and height vs. thickness distributions for the MILs observed with RMR lidar and falling spheres. The height on the y-axis is the middle height of the MIL. There seems to be a tendency towards higher amplitudes and larger thicknesses at higher altitudes but this is based on only a few MILs with large amplitudes or large thicknesses. Hence no significant correlation between MIL height and amplitude or MIL height and thickness is found. Although these high amplitude/large thickness MILs seem to be outliers, the corresponding temperature profiles do not show other peculiarities which would support to discard them. From the available temperature profiles, these high amplitude/large thickness MILs are real although rare events.

Current MIL theory (see Sec. 2.8 and *Meriwether and Gerrard* [2004, and references therein]) distinguishes

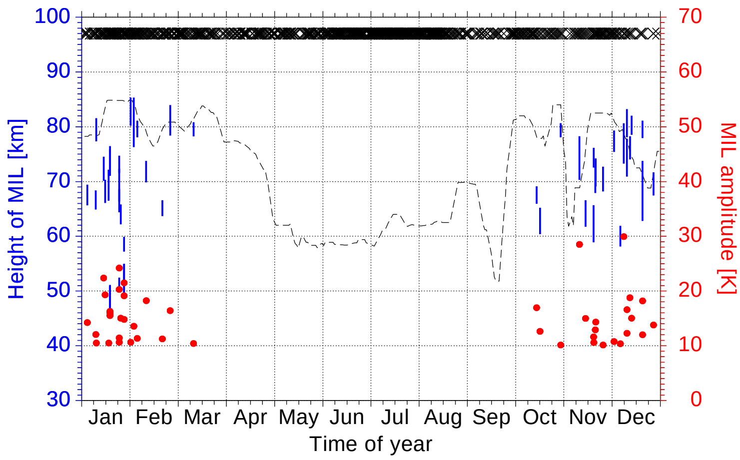

A) RMR lidar (1997 – 2005)

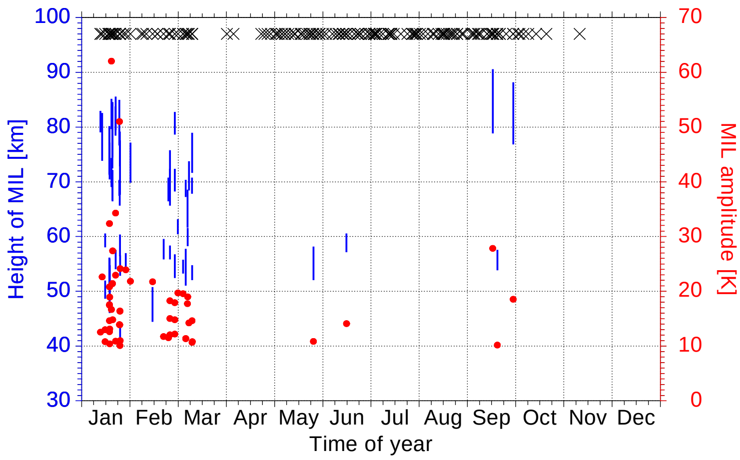

B) Falling spheres (1987 – 2005)

Figure 5.4: Height (blue bars, left scale) and amplitude (red dots, right scale) of the 46 MILs observed above ALOMAR vs. season. The upper panel shows the MILs found from RMR lidar night-mean profiles where the dashed black line indicates the upper limit of the lidar data taken from Fig. 4.7. MILs found in 194 falling sphere temperature profiles above Andøya are shown in the lower panel. The times of the lidar and falling sphere profiles are marked by 'X' in the upper part of the plots.

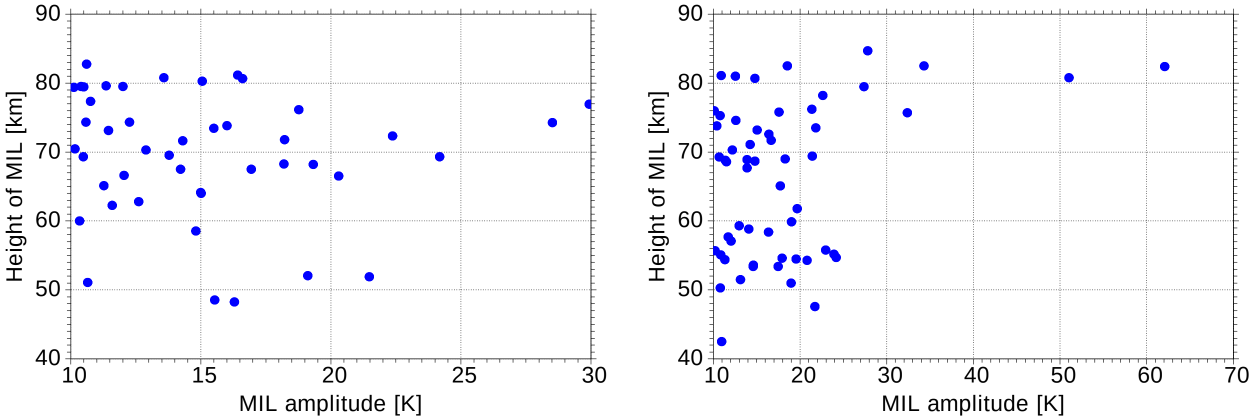

A) RMR lidar (1997 – 2005) B) Falling spheres (1987 – 2005)

Figure 5.5: Height of MILs vs. their amplitude for the MILs observed with the RMR lidar (left panel) and with falling spheres (right panel). Note the different amplitude scales.

between “upper” and “lower” MILs as found in previous studies at mid-latitudes. Typical heights for these two groups of MILs are 85 km – 100 km and 65 km – 80 km, respectively. Since neither RMR lidar nor FS cover the upper MIL height region, it is not possible to check whether there are two distinct groups of MILs at high latitudes as well. The height distribution of the MILs observed by falling spheres in Fig. 5.5B covers a slightly larger altitude range than the MILs in the RMR lidar data in Fig. 5.5A. The absence of MILs above 85 km is due to the upper altitude limit of the RMR lidar and FS measurement technique. The smaller number of MILs below 60 km in the RMR lidar measurements compared to the FSs may give a hint that the MILs observed in this height range propagate downwards in height during the measurement or that they occur for short times only. In both cases they would be averaged out in the RMR lidar data analysis.

The MIL height, thickness, amplitude and mean temperature gradient observed above ALOMAR are summarised in Tab. 5.1. It gives mean, minimum, maximum and the standard deviation for these four parameters. The minimum thickness of 2.2 km and minimum amplitude of 10.1 K for both instruments is given by the algorithm used to identify the MILs (see

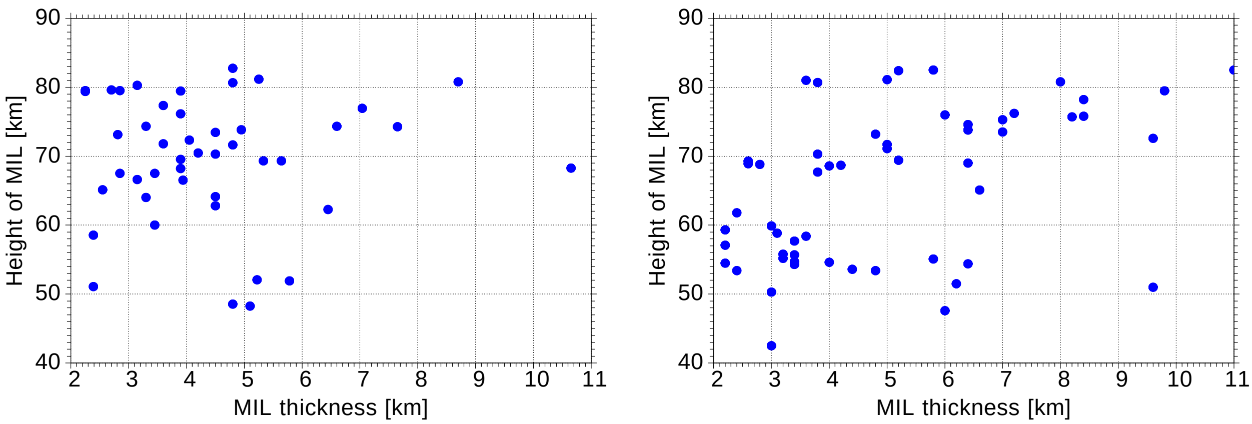

A) RMR lidar (1997 – 2005) B) Falling spheres (1987 – 2005)

Figure 5.6: Height of MILs vs. their thickness for the MILs observed with the RMR lidar (left panel) and with falling spheres (right panel).

Parameter	Instrument	Mean	Min	Max	Std.dev.
Height [km]	RMR lidar	69.7	48.2	82.8	9.2
	FS	66.1	42.5	84.7	11.1
Thickness [km]	RMR lidar	4.4	2.2	10.6	1.7
	FS	5.2	2.2	11.4	2.4
Amplitude [K]	RMR lidar	15.1	10.1	29.9	4.8
	FS	18.2	10.1	62.1	9.4
Mean temperature	RMR lidar	3.7	1.6	6.2	1.1
gradient [$\mathrm{K\,km^{-1}}$]	FS	4.0	1.5	11.9	2.1

Table 5.1: Range of heights (middle of layer), thickness, amplitude and mean temperature gradient of the observed MILs above ALOMAR for RMR lidar and falling sphere profiles (see text for details). The errors of the mean values are less than 0.2 km, 0.05 km, 0.2 K and 0.2 $\mathrm{K\,km^{-1}}$ for height, thickness, amplitude and mean temperature gradient, respectively.

previous section). The mean temperature gradient is calculated as the ratio of amplitude to thickness. Although the spread of these parameters is large, their standard deviation is less than 10 km in height, less than 2 km in thickness, less than 5 K in amplitude and around 1 $\mathrm{K\,km^{-1}}$ in mean temperature gradient for the RMR lidar profiles. These values describe a rather uniform set of MILs observed above ALOMAR. One of the reasons for this may be that all MILs reported here were observed during the winter from mid-September to the beginning of April. While the RMR lidar cannot observe MILs in the summer upper mesosphere due to the high solar background during summer, the FS technique does not have this restriction and nevertheless does not observe MILs during the summer months. This could be a hint to the role of planetary waves in generating MILs which cannot propagate in the summer mesosphere due to the westward mesospheric jet in summer. In contrast, gravity waves can propagate during the whole year and it will be shown in Chap. 6 that their amplitudes are not very different in summer and winter above ALOMAR.

The MIL parameters from the falling sphere observations are listed in Tab. 5.1 as well. Their mean height is a bit lower than the MILs observed with the RMR lidar but they cover a similar altitude range. On average, the FS MILs are less than 1 km thicker and their amplitude is $\sim$3 K larger than for the RMR lidar MILs. The maximum MIL amplitude observed with falling spheres is twice as large as the largest RMR lidar observation but these very large values are restricted to a few cases as shown by the standard deviation of less than 10 K. The average mean temperature gradient is similar to the RMR lidar observations but the maximum gradient is nearly twice as large. However, the standard deviation of 2.1 $\mathrm{K\,km^{-1}}$ shows that the largest gradients are rare events. Considering the skewed distributions of MIL amplitude and thickness shown in Figs. 5.5 and 5.6 the close agreement of the mean values is a sign of the similarity of the MIL characteristics observed with RMR lidar and FSs.

5.2.3 Occurrence rate

The MILs found in the 834 nightly mean RMR lidar and the 194 FS temperature profiles can be used to calculate the occurrence rate for MILs above ALOMAR. Tab. 5.2 summarises the results and shows that only 38 RMR lidar profiles contained a MIL. This gives an occurrence rate of 4.6%. Only 6 profiles showed more than one MIL and none contained

	RMR lidar	**FS**
Profiles with MIL(s)	38	41
Profiles with 1 MIL	32	17
Profiles with 2 MILs	5	13
Profiles with 3 MILs	1	1
Total observed MILs	45	56

Table 5.2: Number of profiles with MILs from 834 nightly mean RMR lidar profiles above ALOMAR between 1997 – 2005 and 194 falling sphere profiles launched from Andøya and Esrange between 1987 – 2005.

more than three MILs. If the profiles with an inversion at their upper end are included, the total number of MILs is 59 and the occurrence rate increases to 6.2%. The table also includes the corresponding numbers from the analysis of the FS profiles. Of the 194 falling sphere temperature profiles, 41 contained up to three MILs. The MIL occurrence rate for the falling sphere profiles thus is 21% which is roughly five times more than for the RMR lidar night-mean profiles.

The only other statistical study of MILs at high latitudes was published by *Duck and Greene* [2004] and found an occurrence rate of 5.4% at 80° N from lidar profiles. All these numbers are much less than the occurrence rates found from lidar observations at mid-latitudes which are in the range of 20% – 70% depending on the season (with the larger values in winter) [e.g. *Hauchecorne et al.*, 1987]. The lidar observed occurrence rate of 4.6% – 6.2% at 69° N thus fits to the decrease of MIL occurrence with increasing latitude and to the value found by *Duck and Greene* [2004] at 80° N. A similar latitudinal structure is also seen in northern hemisphere MIL observations from satellites which show a maximum in MIL occurrence about mid-latitudes and a decrease in MIL observations towards the pole and the equator [e.g. *Leblanc et al.*, 1995].

An important point to keep in mind when comparing the numbers in Tab. 5.2 from RMR lidar and falling sphere profiles is the very different integration time for both techniques. While for the RMR lidar profiles all data from one measurement is summed giving a temporal mean over many hours, the falling sphere takes a snapshot of the atmosphere. The long temporal mean of the lidar smoothes the temperature profiles much stronger than the few minutes it takes the falling sphere to fall through the atmosphere. MIL layers that do not propagate downwards during the observation time are thus fully represented in the lidar temperature profiles while the group of MILs that propagate downward with time are smoothed in the lidar temperature profile and might be missed by the detection algorithm if their smoothed amplitude is below the detection threshold of 10 K. However, according to current understanding (Sec. 2.8), the MILs observed in this study belong to the "lower" group which does not show pronounced downward phase propagation. Temporal smoothing is another possible reason for the observed difference of the MIL occurrence rates.

While both smoothing in altitude and in time may have some influence on the MILs observed with the RMR lidar, the MILs parameters listed in Tab. 5.1 show that smoothing does not have a large influence on the character of the observed MILs. The small difference of the mean thickness between RMR lidar and FS measurements indicates that the MILs are not propagating downward because such a downward motion should produce a thicker MIL in the RMR lidar profile. The similar amplitudes oppose the suggestion given above of short-lived MILs. If the MILs exist only during parts of the RMR lidar measurement time, their mean amplitude should be significantly lower in the RMR lidar measurements compared to the FSs. Since the difference in the mean thickness is only 0.8 km and the difference in the mean amplitude is only 3 K ($\approx$ 20%), neither downward phase propagation nor intermittency of the MILs can explain the observed difference in occurrence rate of a factor of five. The reason for this difference therefore is presumably not an instrumental effect but a result of the different years sampled in the RMR lidar and FS measurements. While the RMR lidar measured on 60 – 150 days each year from 1997 to 2005 (see Tab. A.1

in App. A.1), the FS measurements were conducted during focused campaigns in the years 1987 – 2005 and 32 of the 56 MILs observed with FSs were detected in 1990 and 2005 (see Tab. A.8 in App. A.5).

5.3 Summary

The RMR lidar has observed SSW events in nearly every winter since 1997. Only in winter 2001/2002 no SSW was observed above ALOMAR. The high occurrence rate of SSW in the last nine years is a specific feature of this time period [*Manney et al.*, 2005]. At the same time when the stratosphere is warmer than in the undisturbed winter case, the mesosphere is observed to be colder than during undisturbed winter conditions. The mesospheric cooling during SSWs is restricted to the altitude region 55 km – 82 km. This implies that OH imagers are not suitable to detect this cooling because the mean OH layer height is ∼87 km. Unfortunately, the RMR lidar did not observe the temporal development of the SSWs, so the exact timing of the mesospheric cooling relative to the stratospheric warming could not be investigated. The vertical structure of the warming and cooling is remarkably similar for all SSW events when it is scaled to the stratopause altitude. This hints at the importance of the change of temperature gradient at the stratopause for the wave propagation and breaking that leads to the observed warming and cooling during SSWs. From the observed cooling it can be inferred that the mesospheric jet reversal during SSWs blocks westward propagating waves but that no eastward propagating waves reach the mesosphere because they should lead to an even larger cooling than observed.

MILs are observed in ∼5% of the RMR lidar nightly-mean temperature profiles. This occurrence rate is comparable to lidar measurements in the Canadian Arctic at Eureka (80° N) but much lower that at mid-latitudes. The occurrence rate of MILs in FS profiles at 69° N is 21%. The large difference of the MIL occurrence rate derived from RMR lidar and FS observations is presumable due to the different years sampled with the two instruments and not due to instrumental effects. To test this hypotheses, a large number of simultaneous measurements with RMR lidar and FS would be desirable. Such a data set is not available, though. So a conclusive explanation of the different MIL occurrence rates in RMR lidar and FS observations is still missing.

Although RMR lidar and FSs observe quite different MIL occurrence rates, other MIL characteristics like amplitude and layer thickness are remarkably similar in both data sets. And neither data set shows a correlation of MIL height to MIL amplitude or MIL thickness. The near absence of MILs at high latitudes in summer is also found with both RMR lidar and FSs. result. Since the "lower" MILs investigated are believed to be created by Rossby wave breaking, the absence of MILs in the summer mesosphere proves the efficiency of the Rossby wave filtering at lower altitudes in summer due to the eastward stratospheric/mesospheric jet. The low overall occurrence rate should help to quantify the amount of planetary wave breaking in the polar mesosphere.

Chapter 6

Gravity Waves

The preceding two chapters have dealt with mean temperature profiles integrated over the entire measurement. This chapter now presents gravity wave analyses using a shorter integration time of one hour only. This highlights the temperature variations which occur *during* a measurement. From the theoretical understanding of possible motions in the atmosphere, these short-periodic temperature variations can be attributed to atmospheric gravity waves. In the middle atmosphere, gravity waves mostly propagate upwards from sources in the troposphere or lower stratosphere until they break in the stratosphere or mesosphere. These waves are observed in nearly all RMR lidar measurements.

The first gravity wave analyses of RMR lidar temperature have been performed by *Schöch* [2001]. Using eleven ALOMAR RMR lidar measurements from the years 2000 and 2001, he determined vertical phase speed and vertical wavelength of the largest waves and estimated their intrinsic periods and horizontal wavelengths. Also gravity wave potential energy values were calculated. *Loßow* [2003] investigated 20 measurements from June and July 2002, the summer of the international MaCWAVE/MIDAS summer rocket campaign. He used wavelet analyses to identify the dominant waves and their periods during these two months. This work also contains some estimates of the expected shift of vertical wavelength due to the change of the background wind with height. The two rocket salvo nights of the MaCWAVE/MIDAS summer campaign were analysed in more detail by *Birkeli* [2003] using height-dependent integration times and Fourier analyses. He compared temperature profiles from RMR lidar, falling sphere and radiosonde measurements and calculated the gravity wave potential energy densities for these two nights. A case-study of the gravity waves in the troposphere and stratosphere during salvo 2 of the MaCWAVE/MIDAS summer campaign has been presented by *Schöch et al.* [2004] and is discussed below in Sec. 6.9.

This thesis will show some analyses of the gravity waves observed above ALOMAR based on the much larger data set of RMR lidar measurements from 1999 to August 2005. First the selection of the data sets used for the analysis is explained. As an introduction to gravity wave analysis, a case-study during a long night-time measurement in February 2001 investigates gravity wave filtering. Then the seasonal variability of the gravity wave energy density in the middle atmosphere above ALOMAR is presented and compared to other high-latitude gravity wave studies with a lidar and falling spheres. The variation of wave energy with height is shown to investigate seasonal differences in wave dissipation. To aid the understanding of the gravity wave sources, the wave energy is correlated to the winds in the lower atmosphere. Correlations of wave energy in the stratosphere to a wave transmission index are also presented looking for an explanation of the observed variability of gravity wave amplitudes. Gravity waves are also known to influence noctilucent clouds (NLCs)

[*Rapp et al.*, 2002]. Using the large NLC data set from the RMR lidar, this connection is investigated. At the end of this chapter, another case-study presents results from the second salvo of the MaCWAVE/MIDAS summer rocket campaign in July 2002 combining measurements from the RMR lidar, the ALWIN VHF radar and falling spheres.

6.1 Data selection for the gravity wave analysis

The temperature fluctuations caused by gravity waves are determined as the difference between the single one hour integration time profiles and the average of all temperature profiles during one measurement (see Sec. 3.4). The part of the gravity wave spectrum that is resolved by the RMR lidar therefore depends on the length of the measurement. For short measurements, the average profile still contains the longer period waves and hence the difference between the single profiles and the average profile comprises only the short-periodic gravity waves. For very long measurements, the average profile represents the geophysical mean state of the atmosphere and waves of all scales contribute to the calculated temperature fluctuations. The short-periodic limit of the spectral range of this method is given by the integration time which is chosen as one hour to cover the altitude region 30 km – 80 km in winter and 30 km – 60 km in summer with a maximum statistical uncertainty of the calculated temperatures of 5 K. The spectral range resolved by the gravity wave analyses presented here thus covers wave periods between the integration time of one hour and the length of the measurement. Since the latter varies between a few hours and many days (Fig. 4.3A), the spectral range of the observed gravity waves varies widely between the different lidar measurements.

When comparing the RMR lidar gravity wave observations with other gravity wave measurements, it is important to account for the differences in the gravity wave spectrum observed by each instrument. Fig. 6.1 shows the range of horizontal wavelengths, periods and vertical wavelengths observed by six different instruments, including the RMR lidar (black shaded regions). The given ranges are estimates and may vary depending on the length of the measurement and the altitude range. The values shown in this plot are listed in Tab. B.1 in App. B.4. For most instruments, some of the parameters have to be estimated from the gravity wave dispersion relation Eq. 2.19 (for details see caption of Tab. B.1). While the RMR lidar has a high vertical resolution, it is restricted by the integration time to wave periods not shorter than one hour. Airglow imager (orange regions in Fig. 6.1) or SABER (violet regions) temperatures have a higher temporal resolution because they use a shorter integration time so they observe waves with periods down to the Brunt-Väisälä frequency of ≈ 5 min.

The gravity wave energy calculated from these measurements then varies not only due to geophysical variability but also due to the changing length of the measurements. This has been investigated in the case of the longest measurement available from 02.07.2005 lasting for 110 hrs. This measurement was divided into periods of 3 hrs, 6 hrs, 9 hrs, 12 hrs, 24 hrs and 48 hrs. Then the gravity wave potential energy density per mass (Eq. 2.23) was calculated for each period. Increasing the measurement length from 3 hrs to 6 hrs nearly doubled the calculated gravity wave energy density. A further increase of the measurement length gave only a moderate increase of the calculated gravity wave energy density. Hence a minimum length of six hours is needed to ensure that the calculated gravity wave energy does not vary considerably as a function of the length of the measurement. Therefore the gravity wave analysis presented in this chapter is restricted to measurements with durations

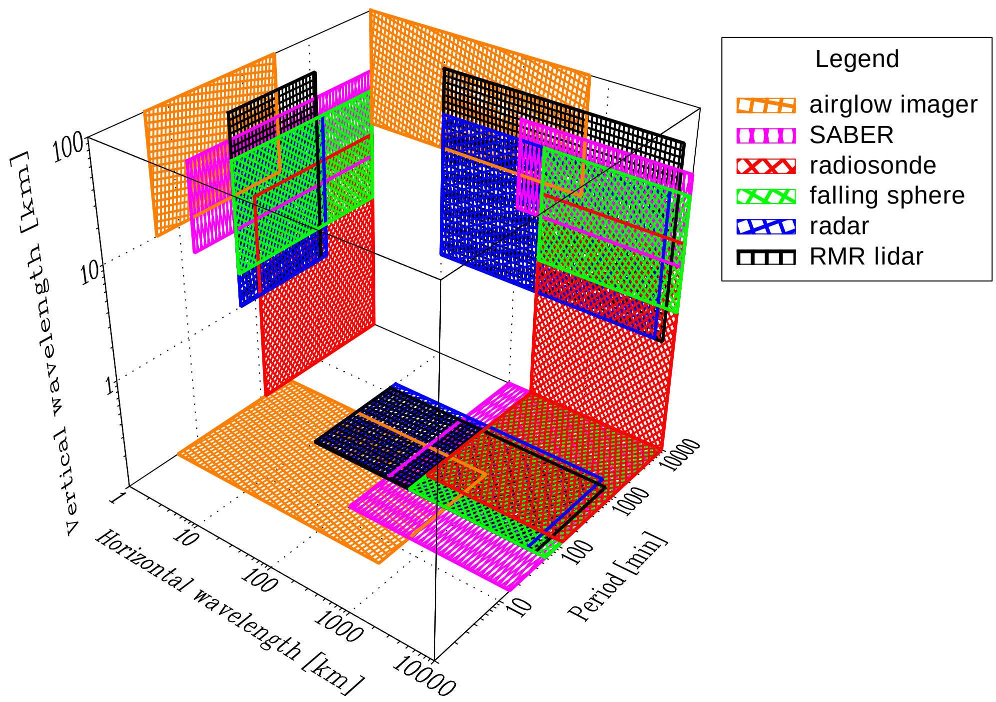

Figure 6.1: Schematic drawing of the different parts of the gravity wave spectrum observed by several instruments. As they all use different measurement techniques, they observe only waves within a specific range of horizontal wavelengths, periods and vertical wavelengths. The values used for this plot are listed in App. B.4 in Tab. B.1 which includes references for each instrument.

of six hours or longer. This gives a data set of 250 measurements from the years 1999 to 2005. Its seasonal and annual distribution is listed in Tab. A.2 in App. A.1. The requirement for long duration measurements leads to an uneven distribution of the measurements with more measurements during the summer months than during the winter because of the generally more unstable weather conditions in winter. In summer there are 144 long measurements during June to August while there are only 56 long winter measurements from November to February.

The integration time of one hour for the gravity wave analysis is a trade-off between spectral range and the upper limit of the calculated temperature profile. A longer integration time increases the S/N ratio which results in a larger altitude coverage but at the same time decreases the resolved spectral range. At lower heights where the atmospheric density is larger, the lidar count rate is higher and a shorter integration time is sufficient to achieve the S/N ratio needed for the temperature calculations. This leads to the idea of a height dependent integration time which increases with increasing height in order to keep the S/N ratio constant. Such an approach has been tested by *Birkeli* [2003]. He found that it works when atmospheric transmission and emitted laser power and hence the lidar signal strength are constant in time. But this method turned out to be very sensitive to small changes in the atmospheric transmission or the emitted laser power. Changes in atmospheric transmission are very common due to low drifting clouds or cirrus in the troposphere. A second drawback of this method is that it leads to a change with height of the spectral range of the observed waves. This complicates amongst other things the comparison of the energy of the gravity waves at different altitudes in the middle atmosphere. Therefore this approach has not been pursued further for the gravity wave analysis in this thesis.

The S/N ratio can also be increased by vertical smoothing of the relative density profiles prior to the integration which yields the temperature profiles (Eq. 3.2) or of the temperature profiles itself. However, this again leads to a decrease of the spectral range of the observed waves which complicates further analysis of the wave field. A similar argument as above applies for a vertical smoothing with a filter length that increases with height (used e.g. by *Rauthe et al.* [2006]). Therefore a constant vertical smoothing is used in this thesis as described in Sec. B.2 in the appendix.

6.2 Gravity wave case-study on 2 February 2001

As an example for the effect of gravity waves on the temperature field above ALOMAR, Fig. 6.2 shows a 12-hour measurement during winter 2001 from 2 February 2001 17:19 UT to 3 February 2001 04:59 UT. The upper panel shows the absolute temperatures variations during that night. It is obvious that the temperature is varying quite strongly at most altitudes but it is difficult to assess the amplitude of the temperature variations. Therefore in the middle panel, the average of the single profiles is subtracted and only the temperature fluctuations are shown. The amplitude reaches 15 K in some heights and there are signs of upward propagating waves, i.e. downward phase speeds (see Sec. 2.5.3). It is also clear that a superposition of many waves is observed which makes it difficult to identify vertical wavelengths, vertical phase speeds or amplitudes for the different waves present during that night. This is a typical situation during winter at the high-latitude site of ALOMAR. The lowermost panel in Fig. 6.2 gives the potential temperature Θ calculated from the observed temperatures following *Franke and Collins* [2003] as

$$\Theta(z,t) = T(z,t)\exp\left(\frac{1}{c_p}\int_{z_{min}}^{z}\frac{g\,dz'}{T(z',t)}\right) \quad . \tag{6.1}$$

Here z_{min} is the lowermost altitude of the measurements. To get absolute potential temperatures, the temperature profiles were extended below 30 km and to ground level with ECMWF analyses for the time of the measurement and the geographical location (70° N, 15°E). The potential temperature (Eq. 2.4) is a measure for the stability of the atmosphere. In a stable atmosphere, it is constant or increases with height. When the potential temperature decreases with height, the atmosphere becomes unstable. This is an indication for gravity wave breaking (see Sec. 2.5.6). Potential temperature profiles at three selected times during the same night as in Fig. 6.2 are shown in Fig. 6.3. They show convectively unstable regions at 74 km around 3 hrs (panel A) and at 71 km around 5 hrs (panel B). In these breaking events, the gravity waves transfer their momentum and energy to the background atmosphere. They thereby change the temperature of the background atmosphere both through direct heating when the energy is dissipated and through circulation changes leading to adiabatic heating or cooling. Therefore gravity waves are very important for the energy and momentum budget of the middle atmosphere.

The following discussion presents a case-study of the gravity wave filtering by the background wind during this RMR lidar measurement. It contains waves in the entire altitude range from the mid-stratosphere to the upper mesosphere. The temperature fluctuations plot (Fig. 6.2B) also shows that wave amplitudes, wavelengths and periods change with altitude. As expected, this behaviour is also found in the gravity wave potential energy density (GWPED) altitude profile in Fig. 6.4. For all analysis shown here, GWPED is calculated as $E_{pot,M}$ (Eq. 2.23 in Sec. 2.5.5) and not as $E_{pot,V}$ (Eq. 2.28) because the former is derived

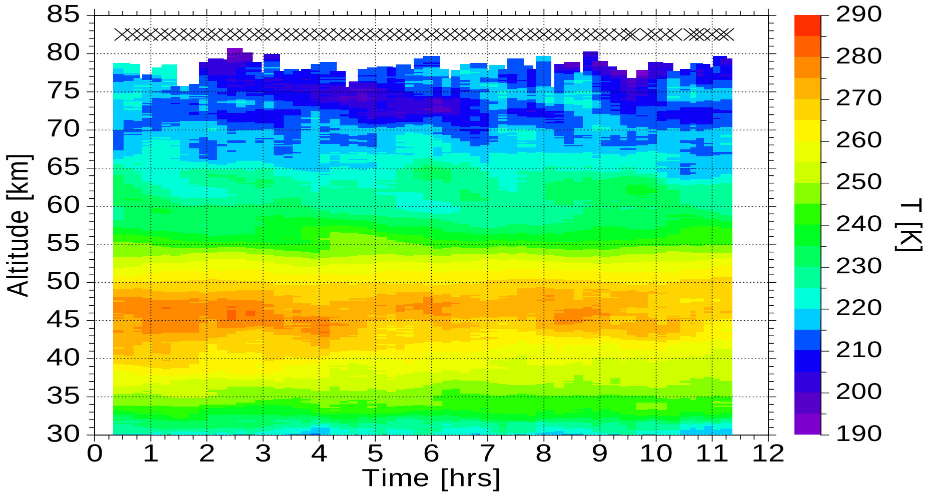

A) Absolute temperatures

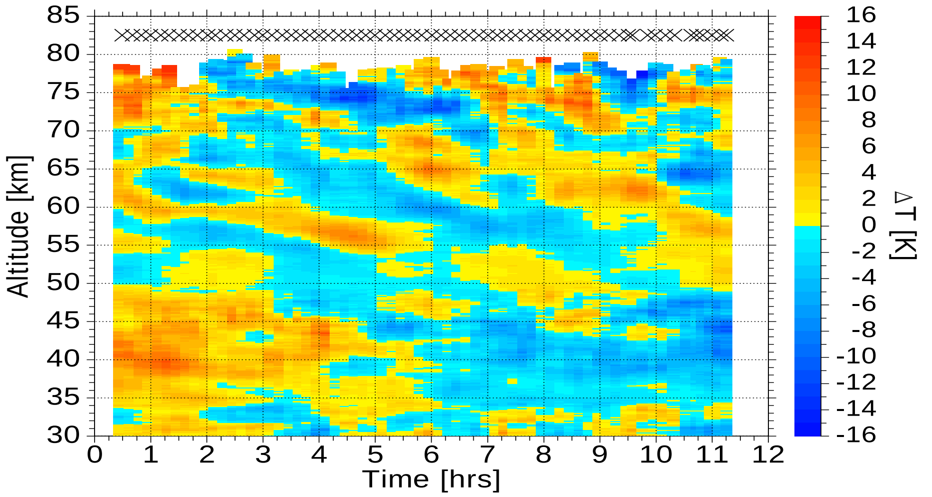

B) Temperature deviations from mean

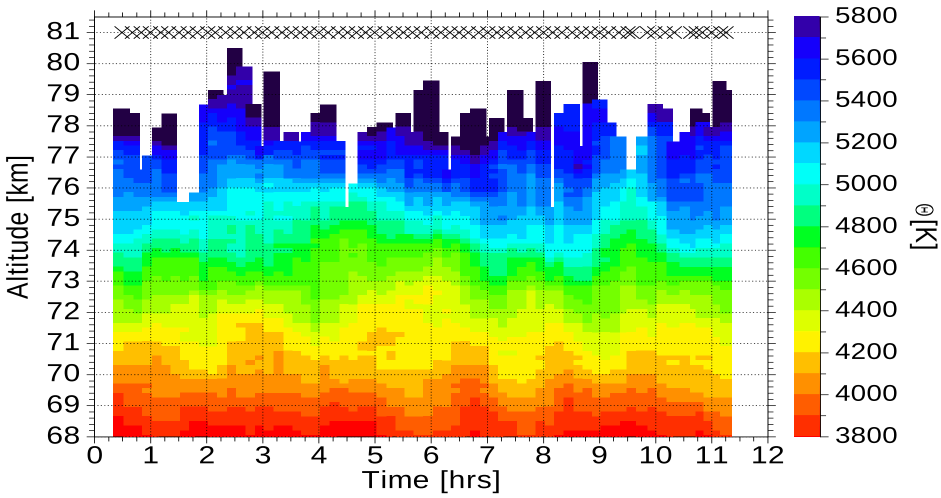

C) Potential temperatures

Figure 6.2: Example of a night-time measurement on 2 February 2001. Time is given in hours relative to the start of the measurement at 17:19 UT. *Upper panel:* Full temperature field. *Middle panel:* Temperature fluctuations after subtraction of the night-mean temperature. The temperature deviations show clear wave signatures of upward propagating waves (downward vertical phase speeds). *Lower panel:* Potential temperatures for the same measurement (see text for details and Fig. 6.3 for potential temperature profiles). The 'X' at the upper border give the times of the single profiles.

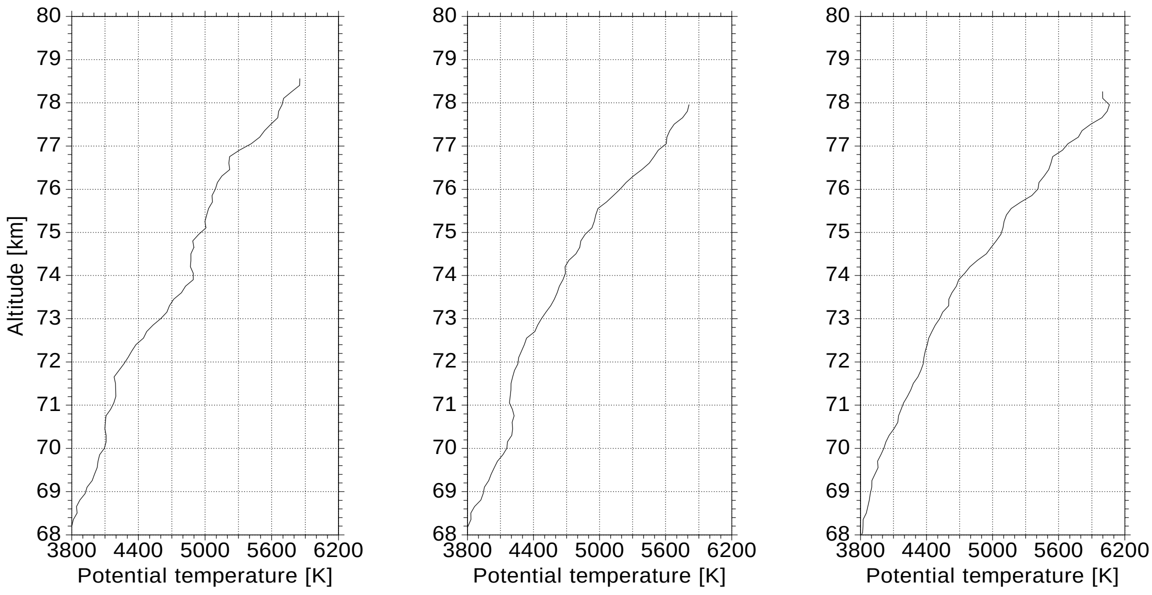

A) 2:51 hrs B) 5:11 hrs C) 6:40 hrs

Figure 6.3: Selected potential temperature profiles from the RMR measurement on 2 February 2001 extracted from Fig. 6.2C. The time of the profiles is again given relative to the start of the measurement at 17:19 UT. Note the convectively unstable regions (decrease of potential temperature with altitude) in panel A at 74 km and panel B at 71 km. Later during the same measurement the atmosphere was convectively stable again (panel C).

directly from the RMR lidar measurements and does not require additional information about the absolute density profile. The Brunt-Väisälä frequency needed for the GWPED calculations is computed from the nightly-mean temperature profile according to Eq. 2.5. As it depends on the temperature gradient, it is very sensitive to small numerical fluctuations of the temperature profile. Therefore the Brunt-Väisälä frequency profile is smoothed with a 3.5 km running-average filter before calculating the GWPED. All GWPED profiles are then limited to the height range where the GWPED value is larger than its statistical uncertainty. The GWPED profile in Fig. 6.2B clearly demonstrates regions of reduced gravity wave energies around 35 km, 52 km, 60 km and 68 km. Also the GWPED increase with height is much less than the exponential increase of an undamped gravity wave (see Eq. 2.27 and Sec. 6.5) shown with the dash-dotted line in Fig. 6.4. The goal of this section is to explain these strong variations of GWPED with altitude. This will be done using winds from ECMWF analyses for the stratosphere and lower mesosphere above ALOMAR.

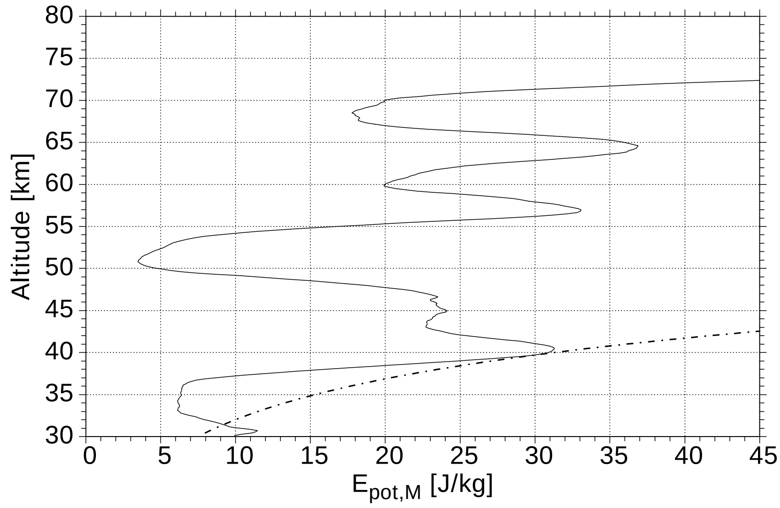

Figure 6.4: GWPED profile for the RMR lidar measurement on 02.02.2001 smoothed over 3 km in altitude. The dash-dotted line shows the exponential increase of an undamped wave. Note the relatively small values around 35 km and 52 km.

The three ECMWF profiles available for 2 February 2001

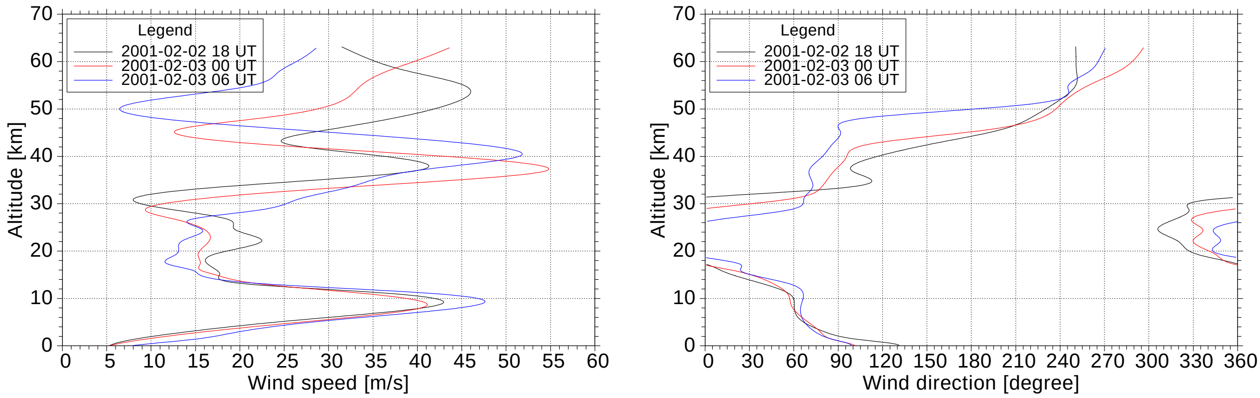

A) Wind speed B) Wind direction

Figure 6.5: ECMWF wind speed (left panel) and wind direction (right panel) above ALOMAR for 2 February 2001 18 UT and 3 February 2001 0 UT and 6 UT. Note the large wind shear of nearly 180° between 40 km and 50 km.

18 UT and 3 February 2001 0 UT and 6 UT are shown in Fig. 6.5 in black, red and blue. The maximum in the wind speed around 40 km increases from 42 ms^{-1} to 55 ms^{-1} before midnight and then decreases slowly again. In the lower mesosphere from 47 ms^{-1} at 18 UT to 7 ms^{-1} at 6 UT. The wind direction shown in Fig. 6.5B shows a large wind shear of up to 160° between 25 km and 35 km and another large wind shear of around 140° between 40 km and 50 km. The dispersion relation Eq. 2.16 give the following condition for propagating gravity waves, neglecting the Coriolis parameter f (Eq. 2.15)

$$\hat{\omega} = \omega - \vec{k}\vec{u} > 0 \quad . \tag{6.2}$$

using the same symbols as in Sec. 2.5.2. Large wind shears effectively block gravity waves since the vector product $\vec{k}\vec{u}$ in Eq. 6.2 gets large for waves with many different wave vectors $\vec{k}$ violating the condition for free propagation which leads to gravity wave breaking. Comparing the altitudes of the wind shears in Fig. 6.5 with the regions of reduced GWPED in Fig. 6.4 shows that the wind shears are found below the regions of reduced GWPED. This can be understood from gravity wave theory because a wave does not disappear completely right at the altitude where its intrinsic frequency becomes zero. Violation of the propagation condition in Eq. 6.2 leads to a negative m^2 and hence to a imaginary part of the vertical wavenumber m. The wave will then be damped as it propagates further upwards. Hence the layer with the large wind shear marks the beginning of the damping and the strongest effect on the GWPED is expected to be found somewhat above. This is nicely demonstrated in this case-study.

A more detailed look on the gravity wave field is achieved through the wavelet transformation technique [*Sato and Yamada*, 1994]. This analysis technique uses wave-packets rather than infinite sinusoids as an Fourier transformation to extract the wave content of an altitude profile or a time-series. One of the advantages of the wavelet transformation compared to the Fourier transformation is that it is better suited for geophysical signals where the waves change their properties with altitude or time. This is due to the finite length of the wave-packets used as the bases for the transformation (see *Torrence and Compo* [1998] for technical details of this technique). All wavelet transformation results presented in this thesis use a sixth order Morlet wavelet as the basis functions.

The wavelet transformations of the temperature fluctuations time-series at various altitudes are plotted in Fig. 6.6. It shows the temporal evolution of the wavelet coefficient amplitudes at different wave periods of up to six hours. The amplitudes are colour-coded

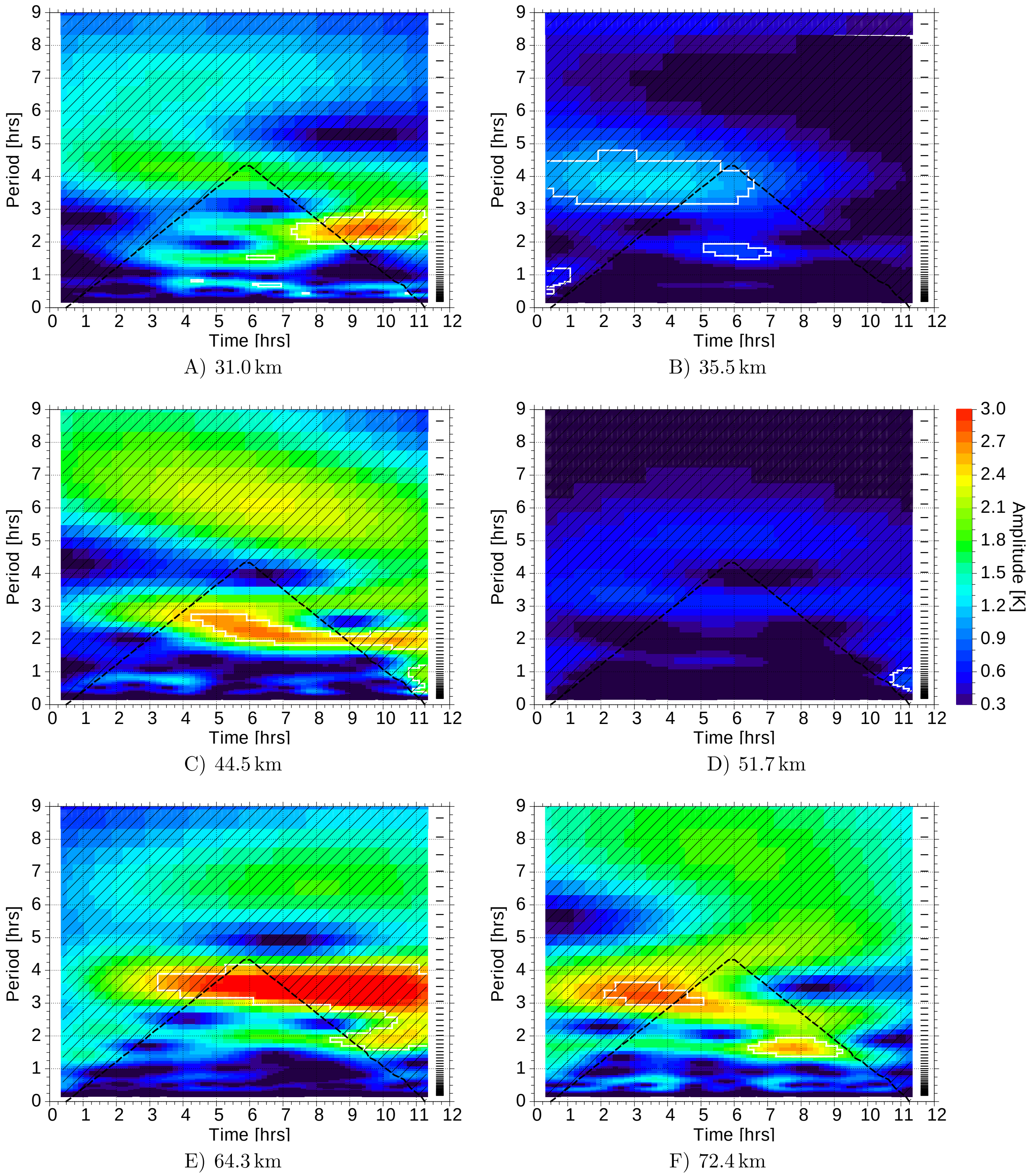

Figure 6.6: Wavelet transformations of the temperature fluctuations time-series during the RMR lidar measurement on 2 February 2001. Shown are the colour-coded amplitudes of the detected periods at different altitudes. The time scale is relative to the beginning of the measurement on 2 February 2001 17:19 UT. The white lines mark the 95% significance limit. The black dashed line gives the cone-of-influence. The hatched area in the plots is affected by boundary effects (see text for details). The black dashes on the right side of the diagram mark the periods resolved by the wavelet transformation.

using the same scaling for all six altitudes. The black dashed line gives the so-called cone-of-influence which marks the region which is unaffected by border effects due to the finite length of the measurement. The hatched area is affected by border effects. The black dashes on the right side of the diagrams mark the periods resolved by the wavelet transformation. Finally, the white lines mark the 95% confidence level calculated as described by *Torrence and Compo* [1998]. In this method, the noise in the data set is modelled as red noise using an univariate lag-1 autoregressive (or Markov) process. The lag coefficient is estimated from the temperature fluctuation time-series as described by *Torrence and Compo* [1998].

The first thing to note from the wavelet transformations shown in Fig. 6.6 is the large variation of the wave periods and amplitudes. This reflects the changing patterns seen for example in the temperature fluctuation time-series in Fig. 6.2B. The very small amplitudes at periods below one hour are a result of the one hour integration time of the temperature profiles which averages out waves with periods below one hour. The different plots also document that the wave structure is changing during the measurement. For example, at 44.5 km (Fig. 6.6C), a wave with a period of three hours is observed at the beginning of the measurement which later changes into a wave with an observed period of two hours. There is also a wave with a longer period of around six hours. But since this period is outside the cone-of-influence, the amplitude and its temporal evolution may not be properly reproduced by the analysis. These plots also show that typical observed periods during this measurement are between two and seven hours. The upper limit for the detected period is given by the length of the measurement of nearly twelve hours. The plots in Fig. 6.6 have been restricted to nine hours since the amplitudes of the longer periods are generally very small in this measurement. Coming back to the minima of GWPED in Fig. 6.4, they are also found in the wavelet transformation at 35.5 km (Fig. 6.6B) and 51.7 km (Fig. 6.6D). At 35.5 km, the largest amplitude detected does not exceed 1.4 K and is found at 3.8 hrs. At 51.7 km, the amplitudes are below 0.7 K and no waves are detected at the 95% confidence level.

The fact that there are significant wave amplitudes at altitudes above the regions with little or no waves shows that gravity waves must have propagated into the lidar beam from below at oblique angles. These waves have met a different wind field at the lower heights and are therefore not filtered out. Hence the waves observed above a depleted region do not contradict the explanation of wave filtering. Another possible source for these waves is the excitation of new waves at these altitudes, e.g. by geostrophic adjustment during the change of the stratospheric or mesospheric jets seen in the ECMWF winds in Fig. 6.5A.

As for the temperature fluctuations time-series, the altitude profiles can be analysed with a wavelet transformation as well. This is shown in Fig. 6.7 for the same measurement as before. Here the vertical wavelengths over the observed altitude range are shown for various times since the beginning of the measurement. The colour-code is the same as in Fig. 6.6. The resolved vertical wavelengths are indicated by the black dashes in the upper part of the diagrams. Again, the lower limit of around 2.5 km is given by the vertical smoothing applied during the calculation of the temperature profiles. Observed vertical wavelengths during this measurement fall in the range 3 km – 25 km. However, vertical wavelengths larger than 17 km fall outside the cone-of-influence at all heights and are thus disturbed by border effects from the finite altitude range of the temperature fluctuation profiles. The diagrams in Fig. 6.7 confirm again that the gravity waves change significantly during the night. In the first few hours, there are only waves with vertical wavelengths below 11 km (panels A and B). Later during the measurement, the vertical wavelength increases up to 20 km (panels D – F). At the end of the measurement (panel F), both the 5 km and the 20 km wave are found outside

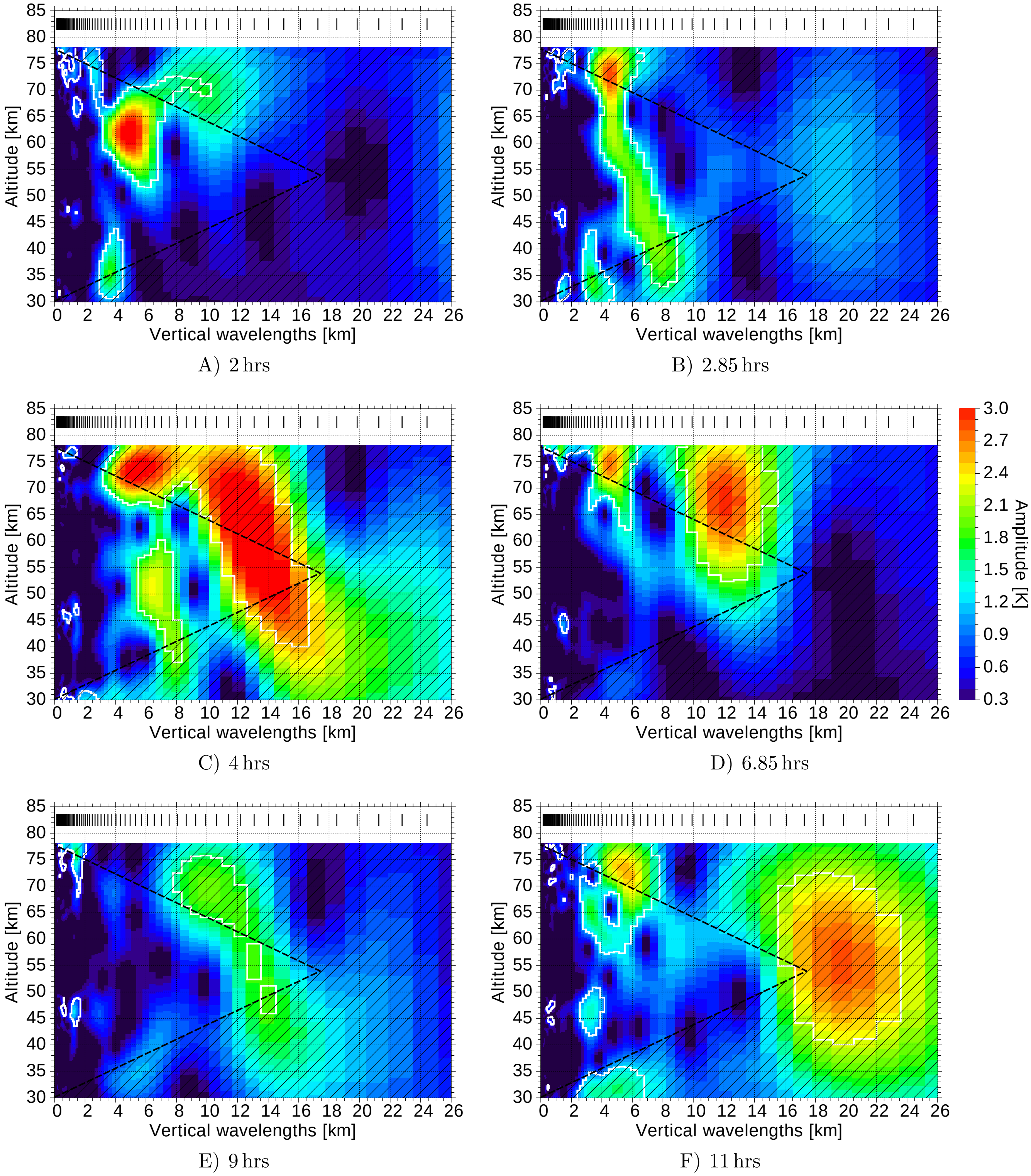

Figure 6.7: Wavelet transformations of the temperature fluctuations altitude profiles during the RMR lidar measurement on 2 February 2001. Shown are the colour-coded amplitudes of the detected vertical wavelengths at different times relative to the beginning of the measurement at 2 February 2001 17:19 UT. The white lines mark the 95% significance limit. The black dashed line gives the cone-of-influence. The hatched area in the plots is affected by boundary effects (see text for details). The black dashes in the upper part of the diagram mark the wavelengths resolved by the wavelet transformation.

the cone-of-influence so that their amplitude is influenced by border effect of the wavelet technique. Also this analysis confirms that there are both waves which propagate upward through the entire altitude region observed with the RMR lidar (panels B, C and E) and waves that are only observed in a small altitude region (panels A and D). The latter are either generated at these altitudes or propagate upward under an oblique angle reaching the FOV of the RMR lidar only at the larger altitudes.

During this measurement, there was a general increase of the wind speed above 45 km except for the end of the measurement Fig. 6.5A. This increase leads to a decreasing intrinsic frequency (Eq. 2.15) and hence to a smaller vertical wavelengths (see dispersion relation in Eq. 2.16). This effect of the background wind on the vertical wavelengths is indeed observed around 2.85 hrs (panel B), 4 hrs (panel C) and 9 hrs (panel E). In Fig. 6.7E the observed wave has a vertical wavelength of 15 km at 40 km altitude which is shifted by the increase of the background wind with height to 10 km at 70 km altitude. This is a good example of the advantages of the wavelet transform over the Fourier transform. The latter assumes a constant vertical wavelength with height and hence does not permit to investigate the influence of the background wind on the wave parameters.

The case-study of the RMR lidar measurement on 2/3 February 2001 presented in this section gives an overview of the variability of the gravity wave parameters even during a single measurement. Defining mean gravity wave properties (wavelengths, periods) for this measurement does not seem meaningful since these numbers could not describe the geophysical variability observed during the twelve hours of the measurement. Therefore determining mean gravity wave periods and vertical wavelengths for entire seasons is outside the scope of this work and will be the subject of further work with the ALOMAR RMR lidar temperature data set. Instead, the next sections will present the mean seasonal variation of the gravity wave potential energy density and the mean growth with altitude of this quantity.

6.3 Seasonal variation

Calculating the one hour integrated temperature profiles for the gravity wave analysis as described in Sec. 3.4 for each measurement gives a huge number of temperature profiles. One way to obtain a physical understanding of the variations in the gravity wave field is to calculate the gravity wave potential energy density (GWPED, Eq. 2.23) for each measurement as described in the previous section. This procedure reduces the data to one GWPED altitude profile per measurement. Since the GWPED is calculated from the temperature variance, its value at a specific altitude is still influenced by the phases of the waves at that altitude. Therefore averages over 10 km in altitude are used to compare the measurements and investigate the seasonal variation of the GWPED observed with the RMR lidar above ALOMAR.

Fig. 6.8 shows the seasonal GWPED variation for different altitude regions between 30 km and 75 km (shown in different colours). The dots and solid lines show the monthly mean values calculated from all years while the dashed lines give the median for each month. The error bars show the statistical uncertainty of the monthly mean values. The data gap during summer at altitudes above 55 km is caused by missing temperature data at these altitudes in summer due to the increased solar background during the summer daylight measurements. An extended version of this figure is presented in App. A.6 in Fig. A.1 which includes all single data points and the number of measurements per month and year. Fig. A.1 shows again that the majority of the long measurements which are used in the gravity wave analysis has been obtained during the summer months. The GWPED values of the single measurements

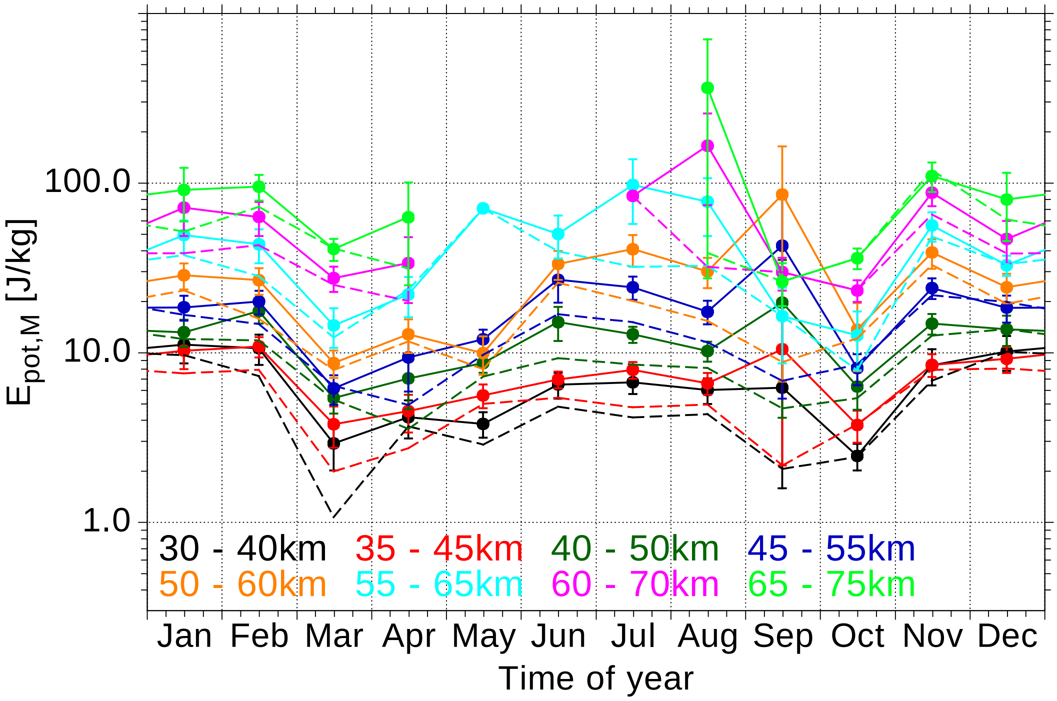

Figure 6.8: Seasonal variation of GWPED for different altitude regions. The dots and solid lines give the monthly mean of all years, the dashed lines the corresponding median. The error bars show the statistical uncertainty of the monthly mean GWPED values. Above 55 km there is only limited temperature data available during summer due to the high solar background. This causes the data gaps in summer at altitudes above 55 km. More detailed diagrams including the single data points and the number of measurements per month and year are included in App. A.6 in Fig. A.1.

range from a few $\mathrm{J\,kg^{-1}}$ up to a few hundred $\mathrm{J\,kg^{-1}}$ with a tendency of increasing GWPED with height which is also clearly seen in Fig. 6.8 and which is investigated in more detail in the next section.

Minima of the GWPED are found around the equinoxes in March/April and September/October at all altitudes. At these times of the year, the observed GWPED is five to ten times lower than in summer or winter. The sometimes big differences between larger mean and smaller median values in the summer months and during the equinoxes shows that there are a few measurements with very large GWPED values which increase the monthly mean values in comparison to the median values which are not affected by a few large outlier values. Therefore the median value represents the average GWPED better than the mean and the further discussions will be restricted to the median value. The comparison of summer and winter monthly median GWPED shows somewhat smaller GWPED values during summer than during winter in the lower altitudes and similar values at the stratopause and in the lower mesosphere. The differences depend on the altitude range and reach up to a factor of two in the stratosphere. In the upper part of the mesosphere there are too few GWPED measurements during summer to draw conclusion about the difference between summer and winter. The GWPED values shown in Fig. 6.8 are probably still influenced by the limited length of the measurements. As there are more measurements during summer than during winter and the really long measurements are mostly taken during summer, there may be a bias towards larger GWPED in summer simply due to the difference in the gravity wave spectrum which is included in the gravity wave analysis because of the difference in the length of the measurements.

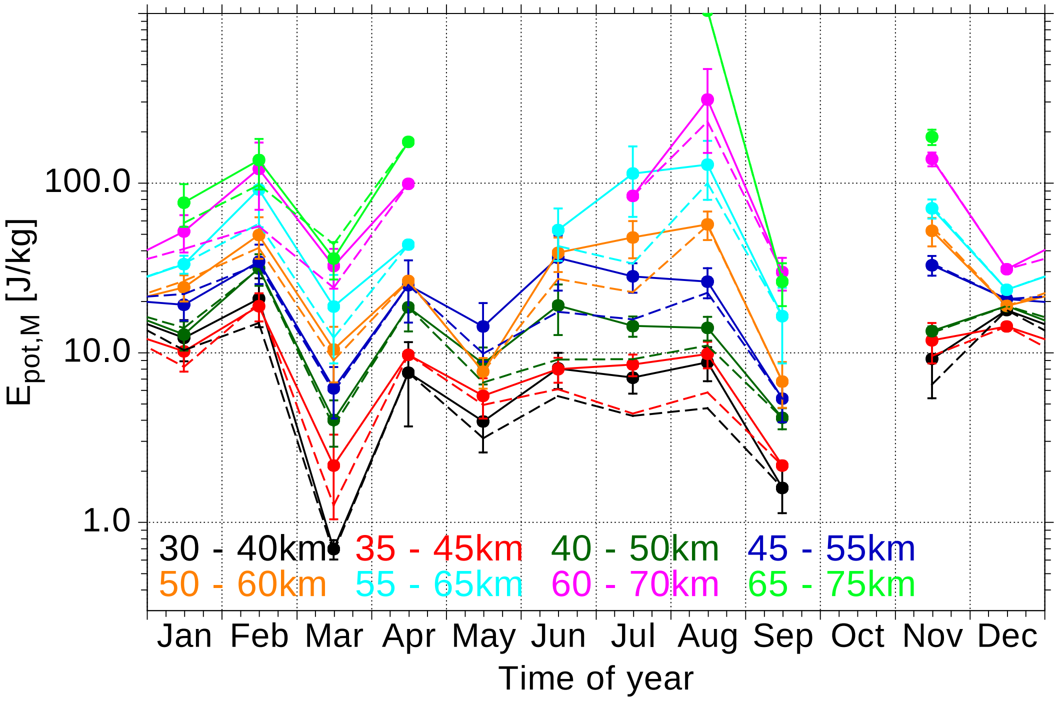

Figure 6.9: Same as Fig. 6.8 but using only measurements longer than 12 hours. This leads to much fewer measurements, especially outside the summer months. Nevertheless, the general behaviour of the seasonal variation of GWPED does not change much. More details for these long measurements are shown in Fig. A.2 in App. A.6.

Therefore Fig. 6.9 shows the same analysis as in Fig. 6.8 but now restricted to measurements longer than 12 hours. The most striking difference is the number of data points available for the GWPED analysis in this case. The number of available measurements is reduced from 250 measurements longer than 6 hours to 104 measurements which are longer than 12 hours. Especially during winter, the number of measurements is much lower (see coloured bars in the upper part of the diagrams in Fig. 6.9). The details of the seasonal GWPED variation differ between the full and the reduced data set but the general traits are the same with minima around the equinoxes and maxima in winter and summer. The median GWPED values are again somewhat smaller during summer than during winter. But the limited number of data points does not allow a definitive conclusion about the size of this difference. Fig. A.2 in App. A.6 is an extended version of this figure including the single data points and the number of measurements per month and year.

A different way of presenting these data is to look at the temperature fluctuations directly. The mean absolute temperature deviation

$$T_{deviation}(z) = \frac{1}{n}\sum_{i=1}^{n} |T'(z,t_i)| \quad , \tag{6.3}$$

where n is the number of one hour profiles during the measurement, is calculated directly from the RMR lidar measurements since it does not involve the Brunt-Väisälä frequency. However, the Brunt-Väisälä frequency still influences the gravity wave temperature deviations as shown in Eq. 2.27. The seasonal variation of the mean absolute temperature deviation is shown in Fig. 6.10 for different altitude regions. Monthly mean and median values are again shown by solid and dashed lines, respectively. The general form of the seasonal variation resembles the seasonal variation of the GWPED. The smallest temperature fluctuations are found around the equinoxes. In the upper stratosphere, the mean temperature fluctuations in winter are

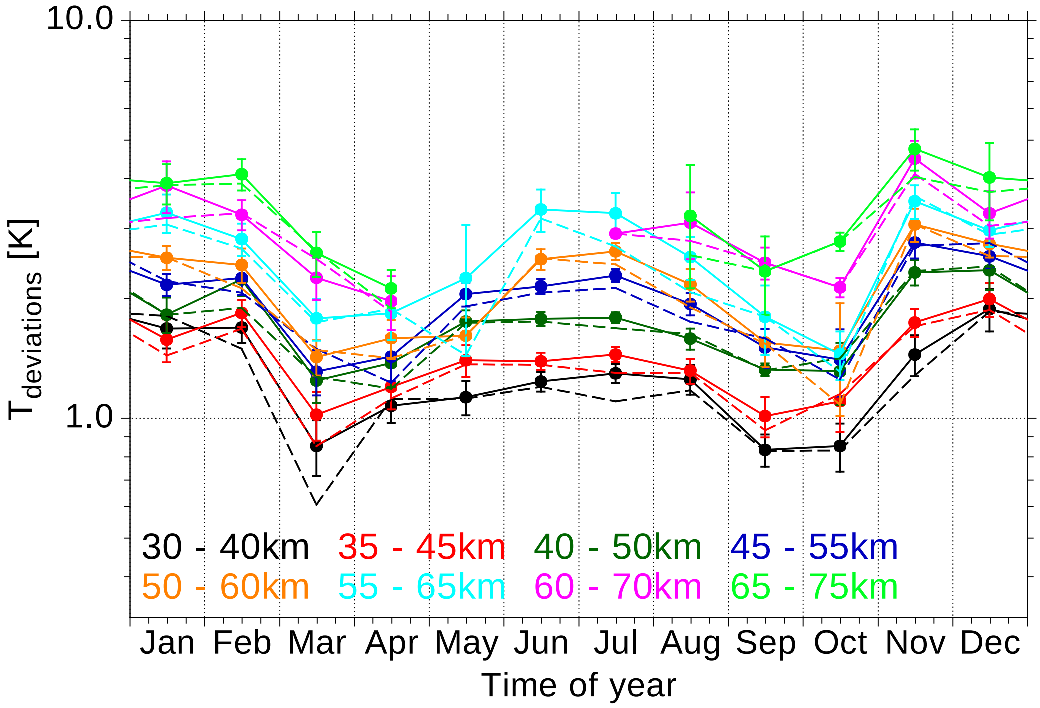

Figure 6.10: Same as Fig. 6.8 for all measurements but now showing the observed temperature fluctuations (Eq. 6.3). Diagrams showing all single data points are included in Fig. A.3 in App. A.6.

up to two times larger than in summer (see black, red and olive lines in Fig. 6.10). Above the stratopause, the mean temperature variations in winter and summer are similar. This is a surprising finding as other instruments have shown higher temperature variability in winter than in summer (see next section). As expected, also the mean temperature fluctuations grow with height similar to the GWPED shown in Fig. 6.8. The single data points and number of measurements per month and year are shown in Fig. A.3 in App. A.6.

So although the Brunt-Väisälä frequency changes with season as it depends on the background temperature profile, it does not change the general shape of the seasonal variation of gravity waves above ALOMAR. Whether looking at the GWPED or the temperature deviations, the maxima and minima are found at the same time of the year and the winter/summer ratio does not change much. But according to Eq. 2.27, even the mean absolute temperature deviations (Eq. 6.3) are not independent of the background atmosphere because the wave amplitude growth still depends on the Brunt-Väisälä frequency, the mean background temperature and the horizontal wavelength of the wave. As the amplitudes and horizontal wavelengths of the single waves during each measurement cannot be derived from a single lidar temperature measurement, the influence of this effect on the observed winter/summer differences of the mean temperature fluctuations cannot be evaluated. Therefore in this thesis GWPED, i.e. the energy of the waves, is used as parameter to quantify the gravity waves in the further analyses.

6.4 Comparison of seasonal variability to other data sets

Comparing this GWPED data set to other measurements is difficult since there are only few data sets available which include gravity wave energy or temperature variances at such high latitudes. Three data sets will be discussed here, namely *Blum* [2003], *Eckermann et al.*

[1995] and *Lübken and von Zahn* [1991]. *Blum* [2003] used Rayleigh lidar temperatures from the Bonn University lidar at the Esrange located on the eastern side of the Scandinavian mountain ridge close to Kiruna in northern Sweden. The ALOMAR RMR lidar and the University Bonn lidar at the Esrange are separated by about 250 km and studies have shown that while the large scale temperature structure is very similar on both sides of the Scandinavian mountain ridge, there are significant differences in the details of the temperature variability [*Blum et al.*, 2003, 2004]. Using data from a number of measurement campaigns from 1997 – 2003, *Blum* [2003] analysed the gravity wave field above this station and found lower GWPED values in summer than in winter in the height range 30 km – 40 km. But in the lower mesosphere (50 km – 60 km), this is only true for the first two years. Starting from 1999, the GWPED values are larger in summer than during winter for most years [*Blum*, 2003, Fig. 7.9]. This latter behaviour is similar to the observations above ALOMAR shown in Figs. 6.8 and 6.9. Another similarity is the large variability of the GWPED values both in summer and in winter. Due to the campaign based type of the University Bonn lidar measurements at the Esrange, *Blum* [2003] does not show GWPED analyses from the equinoxes.

The second data set which can be used for comparisons consists of measurements with meteorological rockets from a number of stations at different latitudes. *Hirota* [1984] used rocket data from the years 1977 – 1980 while *Eckermann et al.* [1995] used an extended data set from the years 1977 – 1987 to investigate gravity wave variances in temperature and winds at different altitudes regions. However, for the Arctic stations Thule (77° N), Chatanika (65° N) and Fort Churchill (59° N), also *Eckermann et al.* [1995] used data from the four years of 1977 – 1980 only. This data set covers all seasons and shows in general much higher temperature variances in winter than in summer at Arctic latitudes. However, the horizontal wind variances in the stratosphere (20 km – 40 km) above Chatanika (65° N) during summer are comparable to the winter values. Unfortunately, the corresponding temperature variances for this station are not shown in this paper. The temperature variances shown by *Eckermann et al.* [1995] for Thule (77° N) and Fort Churchill (59° N) follow the pattern of large variances during winter and much smaller variances during summer. But as shown in the lidar gravity wave analysis by *Blum* [2003], the ratio of summer and winter GWPED varies strongly between different years. So the different behaviour of RMR lidar gravity wave measurements and falling sphere analysis may well be due to the different years investigated in the two studies and the difference in latitude.

A third data set is from falling sphere measurements at the ARR [*Lübken and von Zahn*, 1991]. It shows a similar behaviour as the data set analysed by *Eckermann et al.* [1995] with larger temperature and wind variances in winter than during summer. However, the variance values given in this analyses are calculated for the entire ensemble of temperature profiles and thus comprise the sum of day to day variability and gravity wave induced temperature fluctuations. During winter, the day to day variability is larger than during summer. Hence the larger temperature variances during winter compared to summer published by *Lübken and von Zahn* [1991] do not contradict the smaller differences found in this thesis which compares only the gravity wave induced temperature fluctuations.

Fig. 6.11 explores the differences between the day-to-day temperature variability and the gravity wave induced temperature fluctuations in an extended data set of falling sphere measurements at the ARR [*Müllemann*, 2004]. It is found that the day-to-day variability has a large influence on the calculated temperature variances, especially in winter. First the standard deviation is calculated for 38 original FS temperature profiles from winter (January/February) and 59 original FS temperature profiles from summer (June/July). These

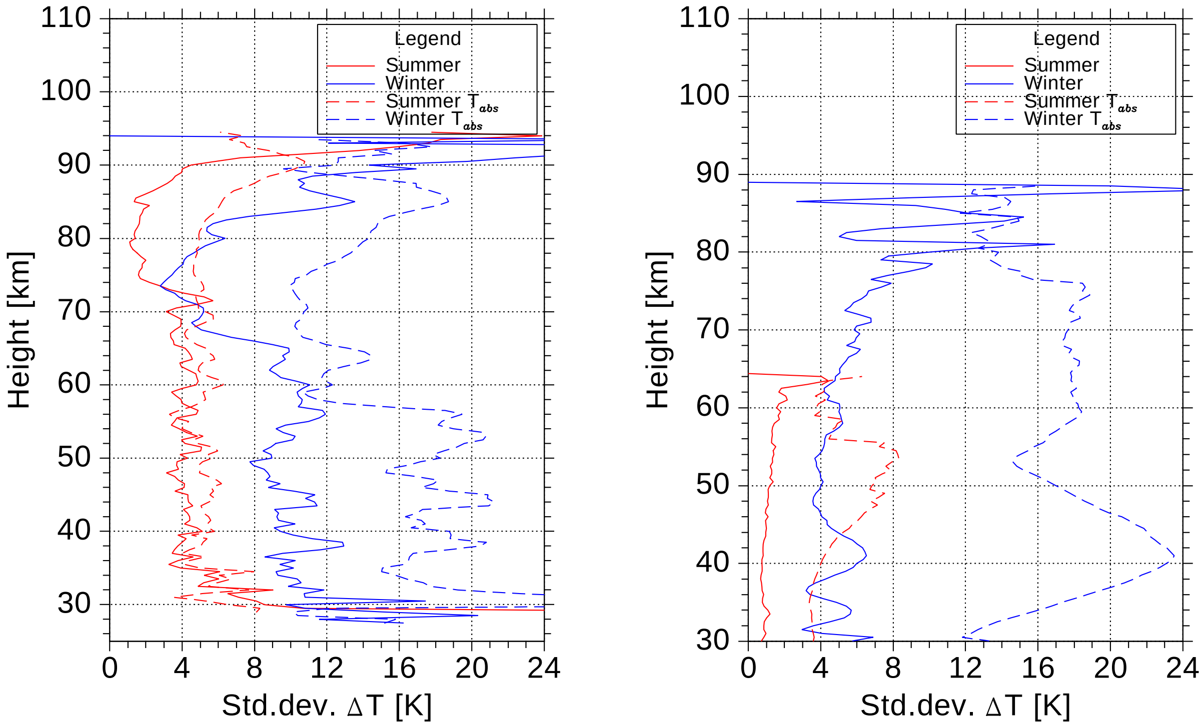

A) Falling spheres B) RMR lidar

Figure 6.11: Temperature variability observed in falling sphere measurements from the ARR (left panel) and in RMR lidar measurements above ALOMAR (right panel). The dashed lines show the standard deviations calculated for the original profiles in winter and summer. The solid lines are the standard deviations for the wave induced temperature fluctuations only (see text for details).

day-to-day variabilities are shown by the blue and red dashed lines in Fig. 6.11A, respectively. Then each temperature profile is fitted by a cubic spline with a fixed knot distance of 15 km using the FITPACK software package [*Dierckx*, 1993]. The fitted background profiles are subtracted from the original temperature profiles to obtain the wave induced temperature fluctuations. The solid blue and red lines in Fig. 6.11A show the standard deviations calculated for the wave induced temperature fluctuations in the FS profiles in winter and summer, respectively. In summer, the temperature variability calculated from the original FS profiles is only slightly larger than the corresponding variability of the temperature fluctuations only (dashed vs. solid red lines in Fig. 6.11A). But in winter, the day-to-day variability leads to a temperature variability for the original FS profiles of 16 K – 20 K in the stratosphere while the wave induced temperature fluctuations in the same altitude region show a variability of 9 K – 11 K only (dashed vs. solid blue line in Fig. 6.11A).

The right panel of Fig. 6.11 shows the same analysis applied to the nightly mean RMR lidar temperature profiles (see Fig. 4.5). The magnitude of the day-to-day variability in the winter stratosphere (dashed blue line) is similar to the FS measurements in the same altitude range. The large values around 40 km are probably due to the SSW profiles that show the largest warming at these altitudes (see Fig. 5.2A). After subtracting the same kind of cubic spline fit as for the FS profiles, only very little variability is left in the nightly mean profiles. This is expected since the long integration time effectively filters out most gravity waves. In summer, the remaining variability is less than 2 K which indicates that the nightly mean is already a very good approximation for the undisturbed background state. In winter, the remaining variability is somewhat larger (solid blue line in Fig. 6.11B). As the average duration of the lidar measurements is shorter in winter than in summer, such a difference is expected and does not conflict with the smaller winter/summer differences shown in Fig. 6.8.

6.5 Gravity wave growth with height

In Sec. 2.5.5 it was shown that the amplitude of an undamped gravity wave propagating upward grows approximately $\propto \exp(z/2H)$ to conserve energy (Eq. 2.27). For the GWPED, this implies a growth approximately $\propto \exp(z/H)$. If the actual observed growth of the GWPED is less than this, the gravity wave field is partially damped, i.e. the gravity wave field looses energy while the waves propagate upwards. This could be either due to gravity wave breaking (Sec. 2.5.6) or due to critical level filtering or reflection (Sec. 2.5.4). In the former case, the gravity wave amplitude is reduced while in the latter case, the number of gravity waves propagating further upwards is reduced. In both cases the energy of the observed gravity wave field decreases with altitude.

It is difficult to investigate the fate of a single gravity wave with a lidar because the lidar instrument always observes the entire gravity wave field. The lidar also observes along its line of sight which in most cases is different from the propagation path of a single gravity wave. Therefore the analysis in this study is restricted to the mean seasonal behaviour of the gravity wave field with height. This is shown in Fig. 6.12 for all gravity wave observations available from the RMR lidar. The different years are distinguished by colour while the mean and median values for all years are shown with black solid and dotted lines, respectively. The coloured diamonds give the means for each altitude and year. The dash-dotted black line gives the GWPED increase expected for an undamped gravity wave field (assuming a constant scale height H of 7 km). The dashed lines show the observed exponential GWPED increase with height. The corresponding GWPED growth lengths are listed in Tab. 6.1.

Fig. 6.12A shows the mean behaviour for all measurements regardless of season. The slightly different GWPED growth lengths calculated from the mean values in the upper stratosphere and mesosphere are probably an artifact of the absence of GWPED measurements in summer above 60 km (see panel C). Interestingly, the median values do not show this difference. The GWPED profiles split by season shown in panels B – E repeat the pattern of lower GWPED during spring and autumn (panels B, D) and larger GWPED in summer

Season	**Mean GWPED** growth lengths	**Mean GWPED** ≈ energy loss / 10 km	**Median GWPED** growth length	**Median GWPED** ≈ energy loss / 10 km
spring	13.5 km	50%	12.7 km	47%
summer	9.6 km	32%	11.8 km	44%
autumn (stratosphere)	10.5 km	38%	11.7 km	44%
autumn (mesosphere)	25.2 km	64%	11.7 km	44%
winter	14.5 km	52%	15.8 km	55%
all seasons (stratosphere)	11.6 km	44%	13.6 km	50%
all seasons (mesosphere)	19.1 km	60%	13.6 km	50%

Table 6.1: GWPED growth lengths for the different seasons calculated from the yearly mean and median values at each altitude. These values were used to draw the dashed lines shown in Fig. 6.12. Additionally the table lists the approximate energy loss relative to an undamped wave which would have a growth length of ≈ 7 km.

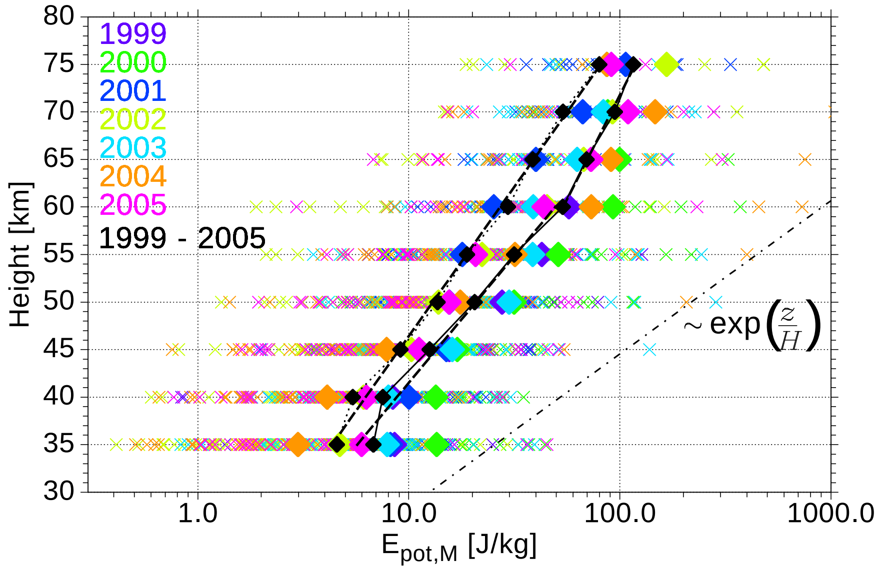

A) mean of all measurements

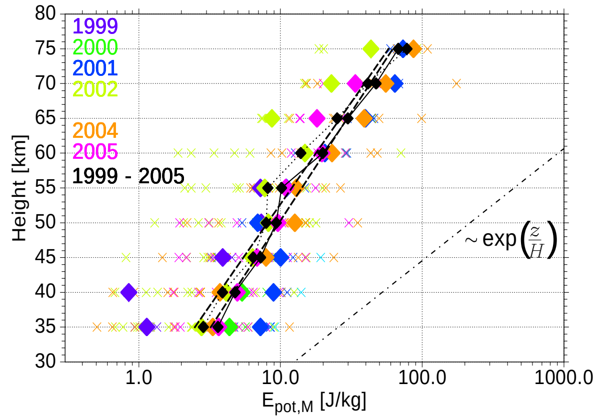

B) spring only

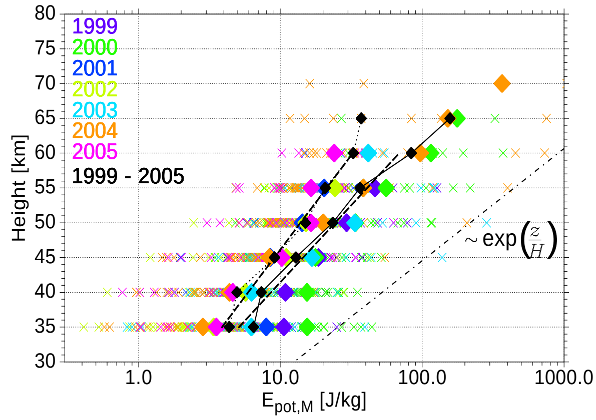

C) summer only

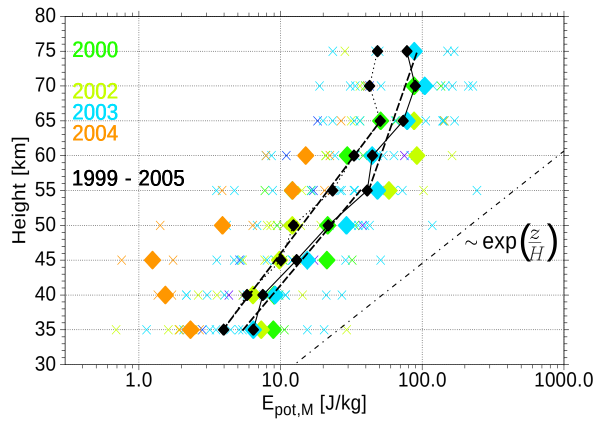

D) autumn only

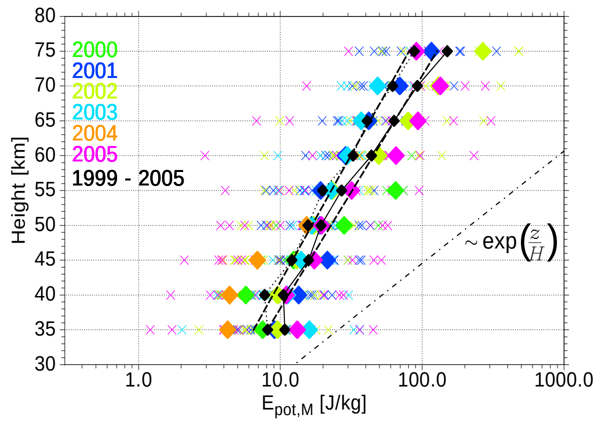

E) winter only

Figure 6.12: Variation of GWPED with height for all seasons (uppermost panel) and divided by seasons (other panels) for the entire data set. The different years are distinguished by colour. The coloured diamonds show the means for each altitude and year. The black solid line gives the mean of all years while the black dotted line gives the median at each altitude range. The dash-dotted black line shows the exponential energy increase with height expected from Eq. 2.27 for an undamped gravity wave of arbitrary amplitude. The observed exponential GWPED increase with height is shown by the dashed lines (see Tab. 6.1).

and winter (panels C, E). Fig. 6.12 also shows that the GWPED growth with height changes in the different seasons. In summer, spring and winter, the observed GWPED does not grow much in the lower two altitude regions. Above 40 km in summer the waves are only weakly damped up to 55 km, while stronger dissipation is observed during the other seasons as indicated by the steeper slope of the dotted lines, i.e. smaller GWPED increase with height, compared to the dashed black line for undamped gravity wave propagation. However, the single years shown by the coloured diamonds exhibit very different energy scale heights. In autumn 2004 (panel D, brown diamonds), strong wave breaking or filtering is observed below 40 km while in 2003, the GWPED values grow steadily with height, albeit still at a slower rate than for undamped gravity wave propagation. Additionally, in autumn the upper mesosphere shows strong gravity wave breaking and filtering indicated by the small increase with height. This could be due to the change of direction of the mesospheric jet from eastward to westward winds during autumn. From falling sphere observations, it is known that the westward zonal wind above ALOMAR peaks at 50 km – 60 km altitude in autumn [*Müllemann and Lübken*, 2005, Fig. 4] whereas the eastward zonal wind in summer increases steadily through the mesosphere. This different wind structure could be a reason for the different observed gravity wave filtering in summer and autumn. The small GWPED increase with height in autumn could also be a special feature of the years 2000 and 2003 as there are no GWPED observations in autumn at these altitudes during the other years.

To quantify the differences in the GWPED increase with height, the dashed lines in Fig. 6.12 were calculated through linear regression of the mean and median GWPED increase with height. The corresponding values for the observed GWPED growth lengths are given in Tab. 6.1. This table also lists the approximate energy loss relative to an undamped gravity wave which would have a growth length of $H \approx 7\,\mathrm{km}$. Dissipation effects are strongest in winter (largest GWPED growth lengths) and in the autumn upper mesosphere, while they are weakest in summer (smallest GWPED growth lengths). But even in summer, the GWPED growth length is larger than expected for an undamped gravity wave field. This indicates significant gravity wave dissipation in all seasons. At the same time, the observed wave dissipation depends on the season and shows very different behaviour in the single years. All panels in Fig. 6.12 also demonstrate the large variability of the single GWPED profiles above ALOMAR. While the values vary by up to one order of magnitude in spring and autumn, the variations are larger in winter and reach nearly up to two orders of magnitude in summer. This stresses the need for case-studies investigating the detailed evolution and strength of the gravity wave field to learn more about the gravity wave propagation for single waves. In this thesis, such a case-study has been presented in Sec. 6.2. A second case-study is discussed below in Sec. 6.9.

6.6 Background wind field and gravity wave energy

The background wind field influences gravity waves through critical level filtering (Sec. 2.5.4) and through its influence on the intrinsic frequency $\hat{\omega}$ (Eq. 2.15). Additionally, the background wind field can act as a gravity wave source through orographic generation of gravity waves or adjustment at the jet stream. The ALOMAR observatory is situated on the Ramnan mountain close to the northern tip of the island of Andøya. It is nearly surrounded by mountains reaching heights of up to 1200 m on the neighbouring islands (e.g. Fig. 1.3). Only in the sector from south-west to north, there is open ocean without any obstacles. Further to the south-east is the Scandinavian mountain ridge rising up to 1900 m above sea level. Therefore, orography could well be an important gravity wave source for the stratosphere above ALOMAR.

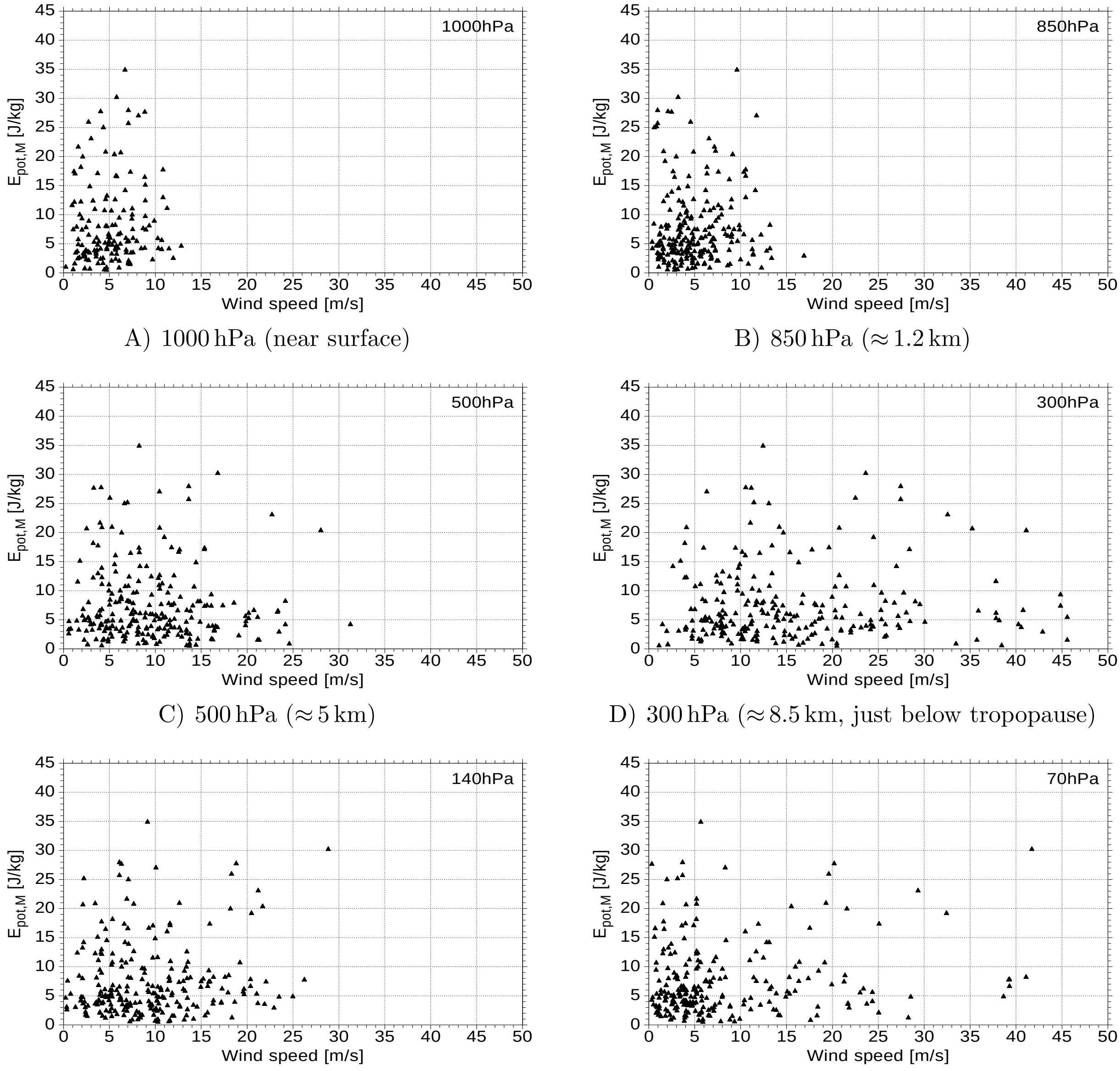

A) 1000 hPa (near surface)

B) 850 hPa (≈ 1.2 km)

C) 500 hPa (≈ 5 km)

D) 300 hPa (≈ 8.5 km, just below tropopause)

E) 140 hPa (≈ 14 km)

F) 70 hPa (≈ 19 km)

Figure 6.13: GWPED in the altitude range 35 km – 45 km shown as a function of the wind speed from ECMWF analyses at different pressure (altitude) levels between the surface (1000 hPa) and the lower stratosphere (70 hPa). No correlation is found in the troposphere. In the lower stratosphere (panels E, F) there is a tendency for lower GWPED with higher wind speeds.

Since most gravity waves observed with the RMR lidar in the upper stratosphere propagate upwards, they should be influenced by the wind field in the troposphere and lower stratosphere before being observed in the upper stratosphere with the RMR lidar. Some investigations into this possible effect will be presented in this section by comparing GWPED values from RMR lidar measurements with the ECMWF wind profile above ALOMAR closest in time to the middle of the measurements. When interpreting the results it has to be kept in mind that the source may be far away when the waves propagate under an oblique angle.

Fig. 6.13 shows the GWPED in the upper stratosphere (35 km – 45 km) as a function of the wind speed at different pressure (altitude) levels between the surface and the lower stratosphere. Panel A shows generally small wind speeds near the surface which increase up to the tropopause region (panel D). For orographically forced gravity waves, higher winds in the lowermost troposphere (panels A and B) should result in larger GWPED values. This is not observed in the RMR lidar measurements in the upper stratosphere. A complicating issue in this analysis is the gravity wave dissipation and filtering between the orographic source in the lower troposphere and the GWPED observation in the upper stratosphere. The effect of the gravity wave transmission is investigated in the next section. The correlation between observed upper stratospheric GWPED and the winds in the lower stratosphere may be slightly negative (Fig. 6.13, panels E, F) but this is not statistically significant. Such a negative correlation would be consistent with gravity wave filtering by the background wind field where higher winds lead to more gravity wave filtering. Since only the wind in the direction of wave propagation matters for the wave filtering, the wind direction may also be important.

The wind direction could also be an important factor for gravity wave generation at ALOMAR as there is only open ocean to the north and west of ALOMAR, but mountains in all other directions. Fig. 6.14 shows that such an effect is not observed in the upper stratospheric GWPED measurements above ALOMAR. The wind direction in the troposphere (panels A – D) has no impact on the observed GWPED values in the upper stratosphere. However, there is a preference for surface winds from easterly directions ($30° - 150°$) during GWPED measurements (panel A). This is expected from the local weather systems at ALOMAR. These winds come from the inland and are typical for stable clear weather conditions which are needed for lidar observations. The gravity wave analysis in this thesis is restricted to measurements longer than six hours which favour stable weather conditions with winds from the east. In contrast, the wind direction in the lower stratosphere is mostly from westerly directions ($240° - 330°$) during GWPED measurements (panel E). There are only few GWPED measurements when the wind in the lowermost stratosphere comes from the east. However, panel F shows that this preference disappears again a few kilometres higher. So the apparent preference for winds from the west seems to be a coincident and not a geophysical feature. Applying this analysis separately to winter and summer measurements does not change the results, namely the absence of correlation between upper-stratospheric GWPED and wind speed or direction in the atmosphere below.

The absence of correlation between the wind direction in the lower troposphere and the GWPED at higher altitudes can have two reasons. On the one hand, it might be that there are other gravity wave sources besides orographic excitation like geostrophic adjustment around the jet-stream or Rossby wave breaking. On the other hand, previous studies have found that the gravity waves observed above ALOMAR may be partly due to orographic excitation at the Scandinavian mountain ridge followed by upwind propagation towards ALOMAR [*Hoffmann et al.*, 1999]. Upwind propagation of orographic gravity waves is well known and depends both on the horizontal scale of the orographic obstacle and the wind speed [see *Holton*, 1992, Sec. 7.4.2]. This could explain why the observed GWPED values are equally large whether the near surface wind comes from the mountainous inland or the flat ocean.

6.7 Gravity wave transmission and observed wave energy

The influence of the wind for the generation of gravity waves has been discussed in the previous section. But as mentioned before, the wind also influences the observed upper stratospheric gravity waves by filtering of the gravity wave field (see Secs. 2.5.4 and 6.2).

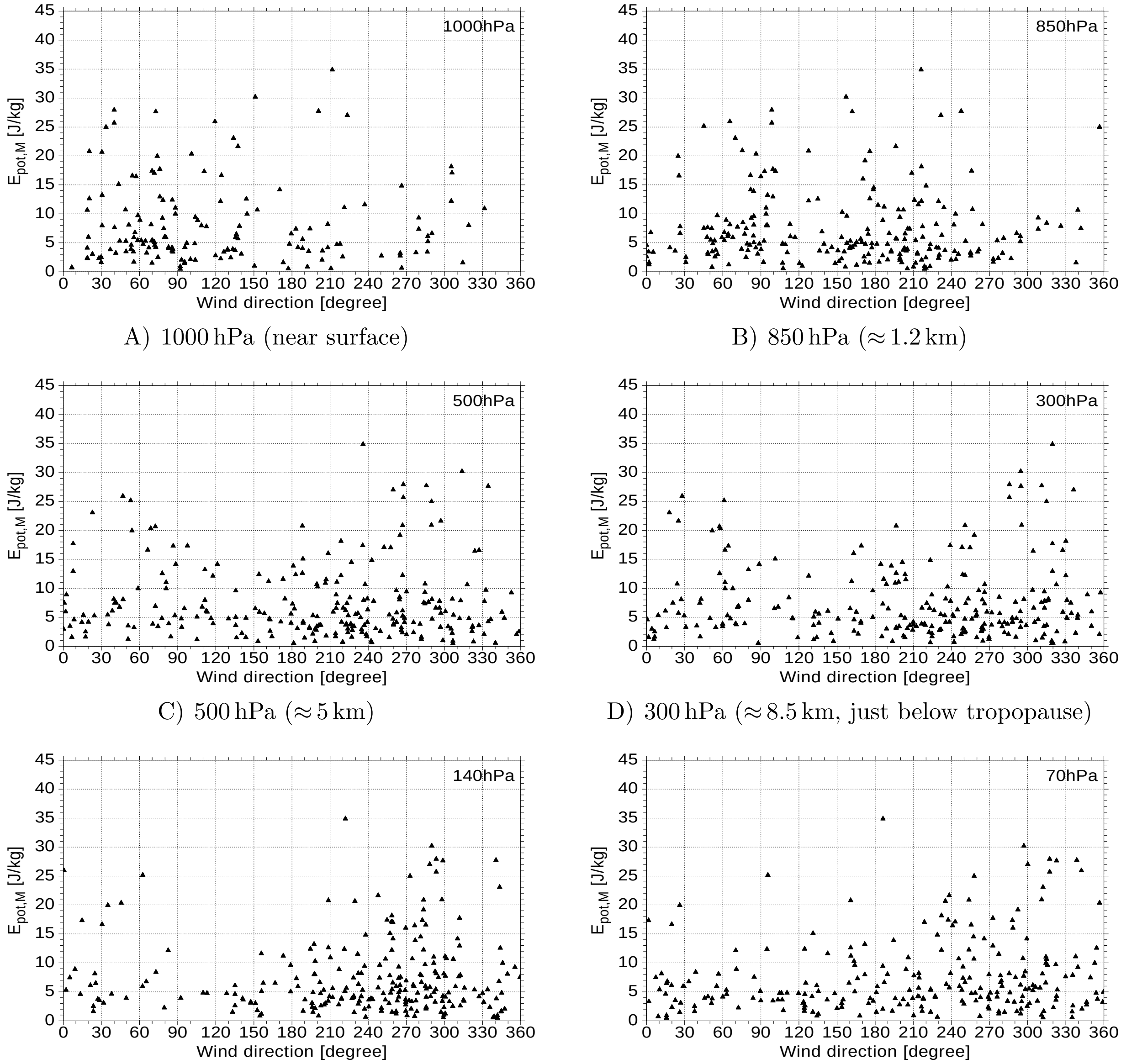

A) 1000 hPa (near surface)

B) 850 hPa (≈ 1.2 km)

C) 500 hPa (≈ 5 km)

D) 300 hPa (≈ 8.5 km, just below tropopause)

E) 140 hPa (≈ 14 km)

F) 70 hPa (≈ 19 km)

Figure 6.14: GWPED in the altitude range 35 km − 45 km shown as a function of the wind direction from ECMWF analyses at different pressure (altitude) levels between the surface (1000 hPa) and the lower stratosphere (70 hPa). The usual meteorological scale is used where wind from the north (east) is listed at 0° (90°). No clear correlation is found to the wind direction in the troposphere. Winds from westerly directions in the lower stratosphere (240° − 330°) seem to favour larger GWPED values in the upper stratosphere.

Such gravity wave filtering by the background wind is investigated in this section for all 250 gravity wave measurements using winds from ECMWF analyses. As discussed in Sec. 6.2 and Eq. 6.2, gravity wave propagation is only possible when $\hat{\omega} = \omega - \vec{k}\vec{u} > 0$. Dividing by the observed frequency ω and solving the vector product gives the condition

$$\frac{u}{c_x} + \frac{v}{c_y} < 1 \quad , \tag{6.4}$$

where c_x and c_y are the zonal and meridional phase speeds of the wave, respectively.

As the gravity wave spectrum in the real atmosphere is not known, this condition can only be tested in a simulation using assumptions about the distribution of the zonal and meridional phase speeds. Lacking detailed information about the gravity wave source at

ALOMAR, a homogeneous and isotropic distribution of the phase speeds is used. The ECMWF wind profiles for each day of RMR lidar gravity wave measurements is interpolated with a cubic spline fit to one kilometre altitude resolution. Then the tentative transmission of the atmosphere for gravity waves originating at the Earth's surface is calculated at each height for different maximum values of the horizontal phase speed $c_h = \sqrt{c_x^2 + c_y^2}$ on a 2 ms^{-1} grid in both c_x and c_y. The transmission is calculated as the ratio of the number of waves in the source to the number of waves at each altitude. An example for a maximum c_h =40 ms^{-1} is shown in Fig. 6.15 for the 03.02.2001 0 UT. For this day, only 37% of all waves reach up to 30 km.

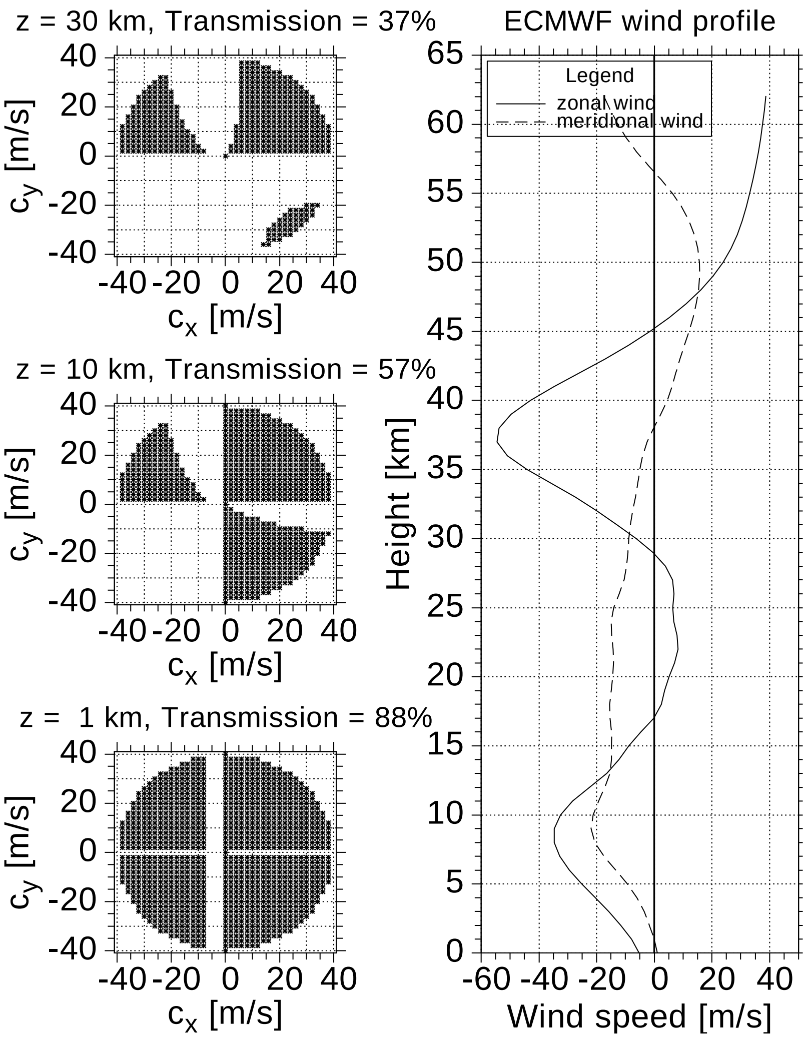

Figure 6.15: Example for the simulated gravity wave transmission on 03.02.2001 at 0 UT. The right plot shows the zonal and meridional winds from ECMWF analyses for this date. The left plots show the simulated gravity wave distribution at 1 km, 10 km and 30 km.

Fig. 6.16 contains the results for all GWPED measurements with the RMR lidar. The mean GWPED values from the altitude range 35 km – 45 km are shown as a function of the gravity wave transmission between the ground and 35 km calculated from the ECMWF winds for different values of the horizontal phase speed c_h. The same ECMWF profiles as in the previous section are used, i.e. closest in time to the middle of the measurements. Summer and winter measurements are marked in red and blue, respectively. Spring and autumn measurements are shown in black. For larger horizontal phase speeds, the mean simulated gravity wave transmission is higher in summer than in winter (panels C and D). This is caused by the generally smaller winds in the troposphere and lower stratosphere in summer compared to winter (see Fig. 2.3A). If transmission alone determines the strength of the observed gravity waves in the upper stratosphere, the GWPED values should get larger with increasing transmission. Such a correlation is not found in the RMR lidar measurements, neither for the full data set nor if every season is analysed separately.

There are a number of geophysical reasons for this lack of correlation. Two of the most obvious are the amplitude distribution in the source and the assumed isotropy of the wave source. The first point has been tested by different weighting of the waves. Mountain waves

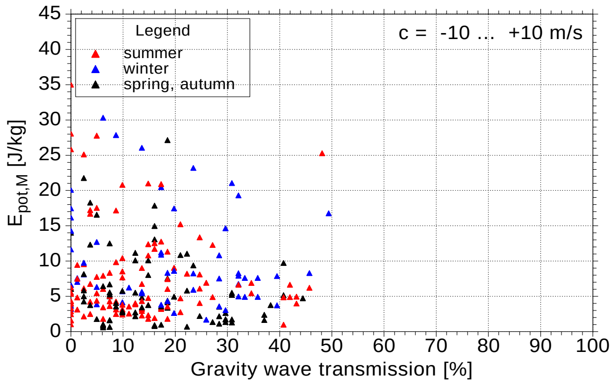

A) $c_h \leq 10\,\mathrm{ms}^{-1}$

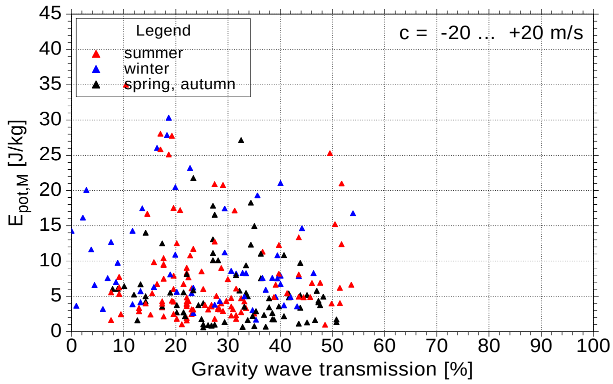

B) $c_h \leq 20\,\mathrm{ms}^{-1}$

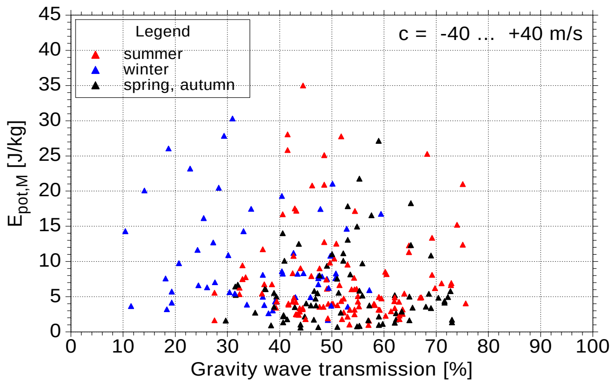

C) $c_h \leq 40\,\mathrm{ms}^{-1}$

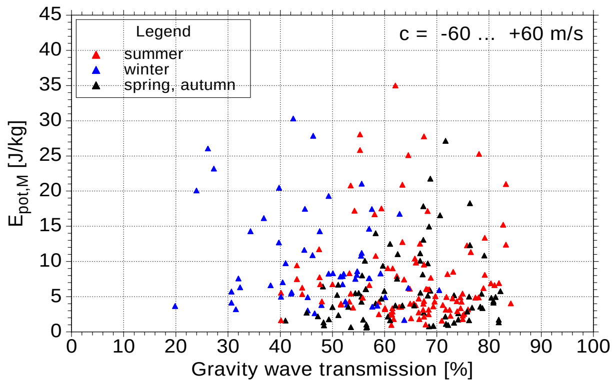

D) $c_h \leq 60\,\mathrm{ms}^{-1}$

Figure 6.16: Mean GWPED in the height range 35 km – 45 km as a function of gravity wave transmission between the ground and 35 km calculated from ECMWF winds. The panels show the result for different values of the horizontal phase speed c_h. Summer, winter and spring/autumn measurements are plotted in red, blue and black, respectively.

with small phase speeds are sometimes assumed to have larger amplitudes than waves with higher phase speeds. This could be simulated by applying a weighting $\propto 1/c_h$ to the wave field. If a strong jet stream would dominate the wave field, waves with $c_x > 0$ should have stronger amplitudes than those with $c_x < 0$. For curiosity, also a weighting $\propto c_h$ was applied to the wave field as well as a partial suppression of waves with $c_x < 0$. Neither of these scalings lead to a correlation in Fig. 6.16. Also maximum horizontal phase speeds up to $100\,\mathrm{ms}^{-1}$ did not qualitatively change the distribution of the points in Fig. 6.16.

Since amplitude scaling does not explain the lack of correlation in Fig. 6.16, an explanation may be an anisotropic gravity wave source. Mountain waves have phase velocities aligned to the near surface wind while gravity waves excited around the jet stream are aligned relative to the background wind [*Pavelin and Whiteway*, 2002; *Plougonven and Snyder*, 2005]. Both mechanisms create an anisotropic wave field which depends in the latter case also on the large-scale meteorological situation. Therefore an anisotropic wave field that changes for each measurement likely could explain that the observed GWPED values in the upper stratosphere are not correlated to the simulated gravity wave transmission in the troposphere and lower stratosphere.

Another complicating effect is that the background wind field is not constant, neither in space nor in time. A gravity wave propagating upward from the troposphere along an oblique path until it reaches the upper stratosphere above ALOMAR meets a wind field which may be quite different than the wind field overhead of ALOMAR, especially in winter. As the waves propagation is not immediately (see Fig. 2.2), even the winds above ALOMAR sometimes change considerably during the wave propagation. This last point has been tested by using ECMWF date from the begin of the measurements or even six hours or twelve hours before the measurements. Also this did not lead to a correlation in Fig. 6.16. So while this probably is an important restriction, it can not be investigated in more detail since this would require ray-tracing of the individual waves during each measurement which is far outside the scope of this thesis.

The analyses presented in this and the previous sections show that gravity wave propagation depends on both the detailed characteristics of the gravity wave source as well as the state of the background atmosphere not only at the site of the gravity wave observation but also in a large region around it. A single measurement at one site is therefore not enough to understand all aspects of the observed gravity waves.

6.8 Gravity waves and noctilucent clouds

Noctilucent clouds (NLCs) are the highest clouds observed in the Earth's atmosphere. They occur only at high latitudes in the cold summer mesopause region around 83 km and have been observed for the first time in 1885 [*Jesse*, 1885]. Their name refers to the spectacular display when it is dark on the ground but the NLCs are still lit by the sun due to its large altitude (see example from Kühlungsborn in Fig. 6.17). NLCs are very faint clouds with optical depths of $10^{-4} - 10^{-5}$. Therefore they are not visible against the sunlit sky during daytime. *Wegener* suggested already in 1912 that they may be composed of water ice particles. The first experimental confirmation for this has been obtained from satellite measurements of NLCs which detected IR spectral lines of water ice [*Hervig et al.*, 2001]. Noctilucent clouds are a very sensitive tracer for the temperature and water vapour concentration in the mesopause region and they have been proposed as an early warning indicator for climate change [e.g. *Thomas et al.*, 1989]. NLCs have been investigated from many aspects and reviews are available in the literature [*Fogle and Haurwitz*, 1966; *Gadsden*, 1982].

Figure 6.17: Noctilucent cloud observed from IAP Kühlungsborn towards the north-east above the Baltic Sea on 24 June 2005 at 22:24 UT. Note the many structures at all scales from 10's to 100's of kilometres (picture by G. Baumgarten).

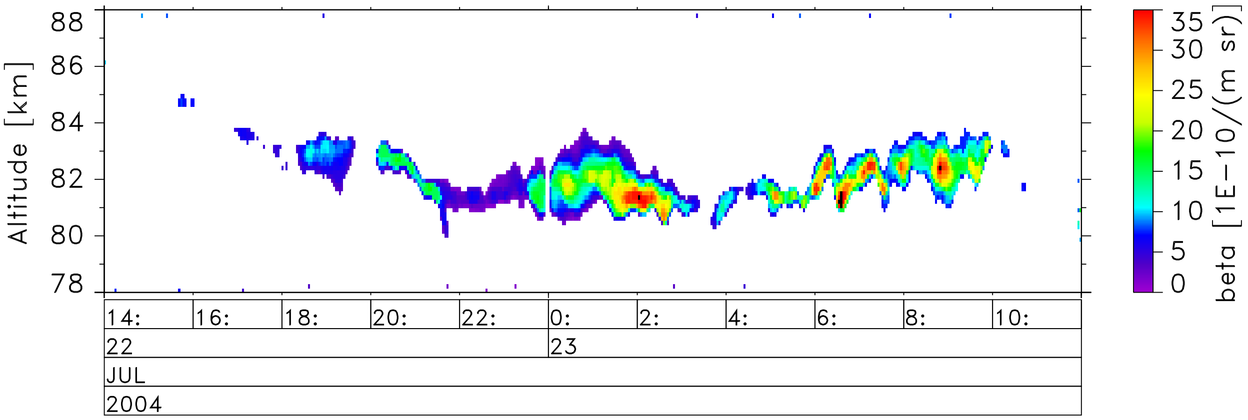

Figure 6.18: Noctilucent cloud above ALOMAR observed with the RMR lidar on 22/23 July 2004. The volume backscatter coefficient (in $10^{-10}\mathrm{m}^{-1}\mathrm{sr}^{-1}$) is shown as a function of altitude and time. Note the large variability of both height, layer thickness and brightness of the NLCs.

The lidar signal from an NLC is very sensitive to the NLC particle size since it depends approximately the sixth power of the NLC particle radius. Only when the particles are larger than ≈ 20 nm they produce a significant lidar signal [*von Cossart et al.*, 1999]. The first NLC observation by lidar was achieved by *Hansen et al.* [1989] with the University Bonn sodium lidar at the ARR. The ALOMAR RMR lidar has acquired the worldwide largest NLC data set from lidar observations now covering more than ten years. An example of an NLC measured in July 2004 by the RMR lidar is shown in Fig. 6.18. It shows the NLC volume backscatter coefficient

$$\beta_{NLC} = \beta - \beta_{air} \tag{6.5}$$

which is derived from the total volume backscatter coefficient (see Eq. 3.1) by estimating the volume backscatter coefficient of air β_{air} using the air density of the Luebken1999 reference atmosphere [*Lübken*, 1999]. Details of this analysis have been described by *Baumgarten* [2001]. NLC occurrence frequency, seasonal variation and diurnal variation at ALOMAR have been investigated by *Fiedler et al.* [2003, 2005]. Also NLC particle size distributions and the first depolarisation measurements of NLC particles have been obtained with the RMR lidar [*von Cossart et al.*, 1999; *Baumgarten*, 2001; *Baumgarten et al.*, 2002a].

NLC observations frequently show periodic structures (see e.g. Fig. 6.17) that have been linked to gravity waves and gravity wave breaking [*Hines*, 1968; *Fritts et al.*, 1993]. And microphysical models predict that NLC particles are influenced by the temperature fluctuations of gravity waves propagating to the mesopause region from below [*Jensen and Thomas*, 1994; *Rapp et al.*, 2002]. *Rapp et al.* [2002] found in their model that short-periodic waves (period less than 6.5 hrs) decrease NLC brightness whereas waves with longer periods favour NLC growth. Evidence for such a relationship has also been found in lidar observations from Alaska and from Søndrestrøm on Greenland (67.0° N, 50.9° W) [*Gerrard et al.*, 1998; *Collins et al.*, 2003]. The latter show a negative correlation between short-periodic (periods of two to three hours) wave fluctuations in the lower stratosphere and NLC brightness [*Gerrard et al.*, 1998, 2004]. This section investigates whether a similar correlation is also present in the RMR lidar measurements above ALOMAR.

The first step in this investigation is to try to reproduce the analysis of *Gerrard et al.* [1998]. They used lidar measurements of two hour length around local midnight in summer. As a measure of gravity wave amplitudes, they calculated the relative density fluctuations $\rho'/\bar{\rho}$ in the altitude range 30 km – 45 km. For the NLCs, they calculated the temporal

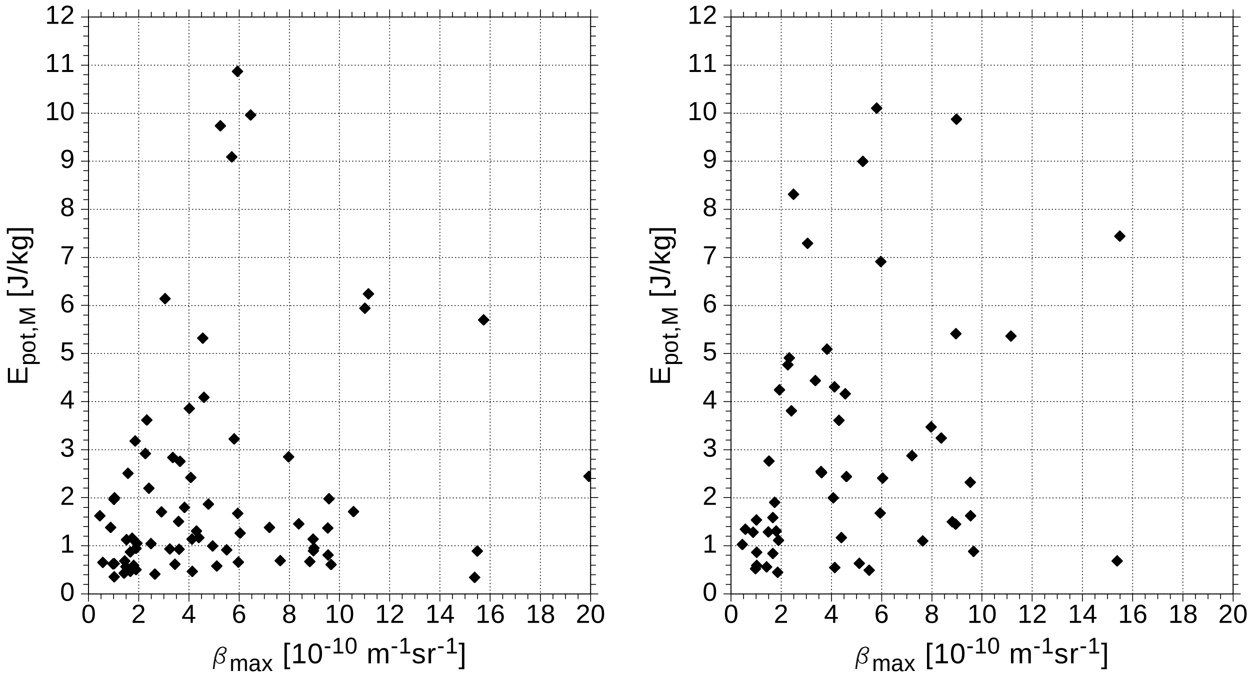

A) 30 km – 45 km B) 40 km – 50 km

Figure 6.19: GWPED in two altitude regions as a function of mean NLC maximum backscatter coefficient β_{max} for RMR lidar GWPED measurements with simultaneous NLCs. This diagram imitates the analysis by *Gerrard et al.* [1998] by limiting the measurements to two hours around local midnight (see text).

mean of the maximum NLC volume backscattering coefficient during the measurement. Since GWPED is used extensively in this chapter, the following analysis will use GWPED as indicator of gravity wave amplitudes and not relative density fluctuation since the latter is proportional to GWPED [see *Gerrard et al.*, 2004]. From all RMR lidar measurements, a total of 84 measurements with durations of two hours close to local midnight are selected for this special analysis. The NLCs above ALOMAR are analysed using 14 min temporal integration of the RMR lidar signal. For each 14 min NLC profile, the maximum volume backscatter coefficient β_{NLC}, the height of this maximum z_{max} and the width of the NLC layer are calculated [see *Fiedler et al.*, 2003].

Fig. 6.19 shows GWPED as a function of the temporal mean of the NLC maximum volume backscatter coefficient β_{max} over the entire time the NLC was present during the measurement. For the left panel, the GWPED is averaged over the same altitude range as in *Gerrard et al.* [1998] (30 km – 45 km). In the right panel, the GWPED is calculated for the altitude range 40 km – 50 km which is a bit closer to the NLC altitudes of around 83 km. The NLC brightness does not show a strong correlation to the GWPED in both altitude ranges. Large GWPED values in the lower altitude range show a tendency of suppressing bright NLCs, i.e. for GWPED values larger than 2 J kg^{-1} there are few NLCs with mean β_{max} larger than $5 \cdot 10^{-10}$ m^{-1}sr^{-1} (Fig. 6.19A). But this tendency disappears when comparing the GWPED in the upper altitude range to the mean NLC brightness (Fig. 6.19B). Both the very weak correlation to the lower altitude range GWPED and the absence of correlation to the upper altitude range GWPED indicate that the geophysical conditions at NLC altitudes are different above ALOMAR compared to Søndrestrøm. The height of the maximum volume backscatter coefficient and the width of the NLC layer have been examined as well (not shown). Neither of these NLC properties shows a significant correlation to the GWPED

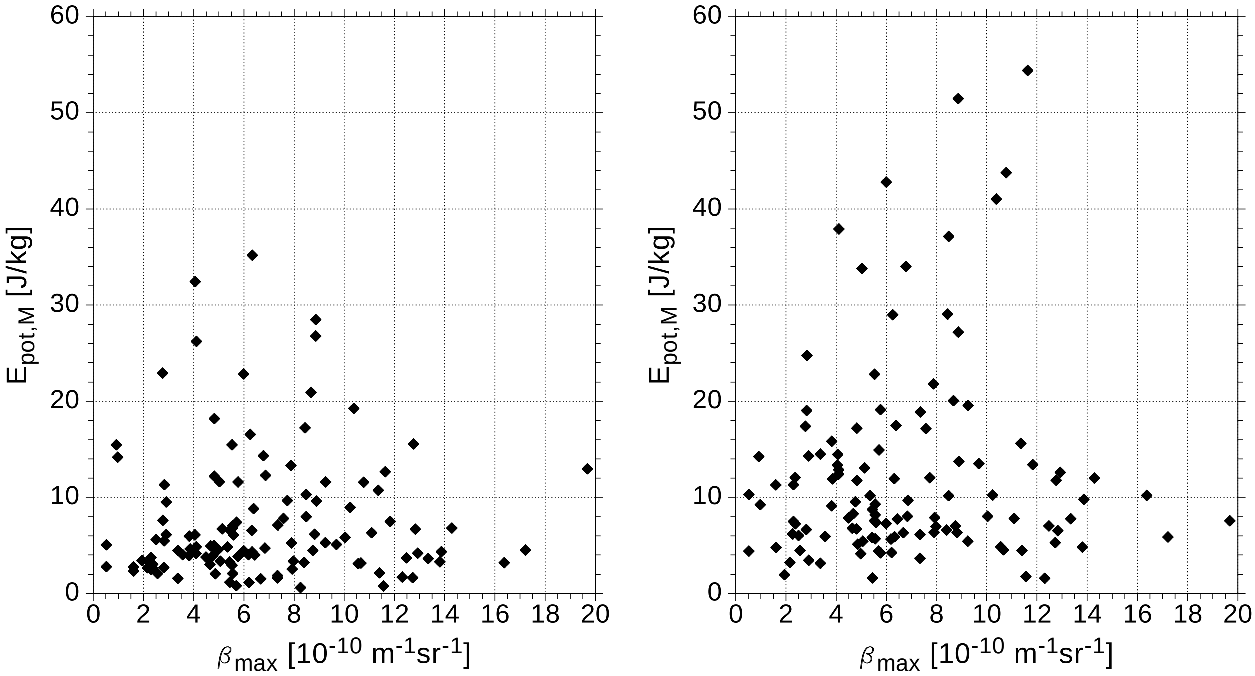

A) 30 km – 45 km B) 40 km – 50 km

Figure 6.20: Same as Fig. 6.19 but using the full length of the measurements.

observed by the RMR lidar in the stratosphere. The missing correlation may be partly explained by the complicating fact that the NLCs observed above ALOMAR are not only influenced by the atmospheric conditions above ALOMAR at the time of the observation but also by advection, the variability of the background atmosphere and the temperature history of the air during NLC particle formation [*Berger and von Zahn*, 2002; *Berger and Lübken*, 2006].

Through the limited length of the measurements, the analysis presented in Fig. 6.19 focused on the short-periodic gravity waves. As discussed at the beginning of this chapter, the GWPED analysis in this thesis was performed on measurements longer than six hours (the only exception is for the results shown in Fig. 6.19). Checking these long RMR lidar measurements gave 126 long measurements with NLC signatures in the lidar signal. Fig. 6.20 shows the same analysis as before but now using the long measurements without any restriction about the time of day of the measurements. As the longer measurements also includes a larger part of the gravity wave spectrum, the GWPED values are larger than in Fig. 6.19. This analysis, comprising both short-periodic and longer-periodic gravity waves, too shows no correlation between GWPED in the stratosphere and mean NLC brightness. Comparing the GWPED from lower and higher altitude ranges (panels A and B) shows no qualitative change in the distribution. The only marked difference is the larger GWPED values due to the increase of the GWPED with height (see Sec. 6.5). Also for this case the mean height of maximum volume backscatter coefficient and NLC layer width have been compared to the stratospheric GWPED (not shown). Again, no significant correlation has been found.

A different way to analyse the relation of GWPED and NLC is presented in Fig. 6.21. The RMR lidar measurements were divided into 14 min time-slices. Each time-slice was checked for the presence of NLC. Fig. 6.21 shows the fraction of time-slices with and without NLC sorted by the GWPED calculated for the respective measurement in the altitude range 40 km – 50 km. If gravity waves suppress NLC, the fraction of time-slices with NLC should decrease with increasing GWPED. Such a decrease is not observed in the RMR lidar measurements, at least for GWPED values below 22 J kg^{-1}. There may be a decrease at larger GWPED values but since there are not that many measurements with such high GWPED values, this is not statistically significant.

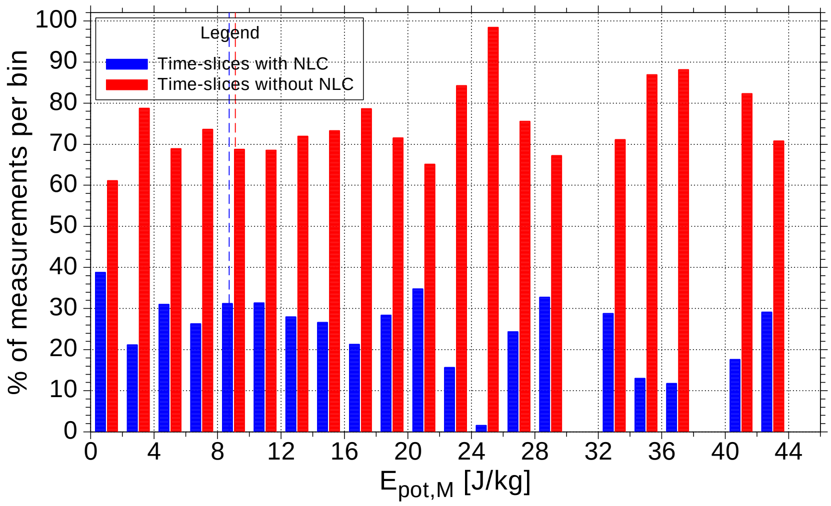

Figure 6.21: Fraction of 14 min time-slices with NLC (blue) and without NLC detection as a function of GWPED in the upper stratosphere (40 km – 50 km). The dashed lines give the median GWPED values for the time-slices with and without NLC.

The conclusion of these investigations is that the clear anti-correlation between GWPED and NLC brightness described by *Gerrard et al.* [2004] for lidar measurements above Søndrestrøm is not found in the RMR lidar measurements above ALOMAR. There may be several possible explanations for this. The NLC observations at ALOMAR show a strong influence of the tidal temperature variation leading to a semi-diurnal variation of NLC brightness and height[*von Zahn et al.*, 1998b; *Fiedler et al.*, 2005]. Such a clear tidal signature is missing from the NLC observations at Søndrestrøm [*Thayer et al.*, 2003]. However, the ARCLITE lidar at Søndrestrøm cannot measure during full daylight which hampers accurate tidal analysis at Søndrestrøm. Still, the fact that at ALOMAR no correlation between GWPED and NLC brightness was found in this thesis supports the explanation given by *Thayer et al.* [2003] for the different NLC behaviour, i.e. that the mesopause region above ALOMAR is dominated by tidal temperature variations while it is dominated by gravity wave induced temperature fluctuations above Søndrestrøm.

As discussed in the previous section, gravity waves propagate under a certain oblique angle. Hence the gravity waves observed in the stratosphere above ALOMAR are not the same waves that influence the mesopause region above ALOMAR. But the lidar only observes in a narrow column directly above the observatory. The gravity waves observed with the RMR lidar in the stratosphere therefore have a different origin as those reaching the mesopause region above ALOMAR. As the orography is very variable around ALOMAR, different geographical origins probably also result in different gravity wave properties in the stratosphere and the mesopause NLC region. This could be different at Søndrestrøm which lies 150 km away from the coast [*Thayer et al.*, 2003].

Interestingly, the GWPED values in the stratosphere are very similar above Søndrestrøm and ALOMAR. *Gerrard et al.* [1998] shows relative density fluctuations $\rho'/\bar{\rho}$ of 0.2% – 0.8%. Using Eq. 2.23 and mean values for the gravitational acceleration in the upper stratosphere of 9.69 ms^{-1} and a Brunt-Väisälä period of 290 s, this can be converted to GWPED values of 0.4 Jkg^{-1} – 6.4 Jkg^{-1}. This range is remarkably close to the values shown in Fig. 6.19A. So the strength of the gravity wave field in the upper stratosphere is similar at both sites. This does not exclude large differences in the spectrum and by this in the impact of the gravity waves on the NLCs.

6.9 The MaCWAVE/MIDAS summer rocket campaign

In July 2002 a comprehensive study of gravity waves and turbulence was conducted at the ARR and ALOMAR. The international Mountain and Convective Waves Ascending Vertically (MaCWAVE) and Middle Atmosphere Dynamics And Structure (MIDAS) summer rocket campaign (for a detailed description of the campaign see *Goldberg et al.* [2003] and *Goldberg and Fritts* [2004]) involved launches of sounding rockets, meteorological rockets (falling spheres) and balloons together with the ground based VHF and MF radars as well as the Rayleigh and sodium resonance lidars at ALOMAR and the Esrange MST radar close to Kiruna in northern Sweden. This section describes the gravity waves observed in the troposphere and stratosphere during salvo 2 of the MaCWAVE/MIDAS summer rocket campaign [*Schöch et al.*, 2004]. Balloon and radar data from the troposphere were combined with RMR lidar, balloon and falling sphere data in the stratosphere to determine propagation directions, vertical wavelengths and observed periods of the gravity waves above ALOMAR on 4/5 July 2002.

While many aspects of gravity waves have been studied in great depth already [e.g. *Fritts and Alexander*, 2003, and references therein], the MaCWAVE/MIDAS summer rocket campaign provided a unique opportunity to investigate gravity waves over the entire altitude range from the ground up to 110 km. During the data analysis for this campaign, it became clear that it took place in a year of extraordinary background conditions in the mesopause region which were accompanied by strong turbulence below the mesopause [*Goldberg et al.*, 2004; *Becker et al.*, 2004; *Palo et al.*, 2005]. In fact turbulence in the mesosphere was seen for the first time below 80 km [*Rapp et al.*, 2004]. Furthermore remarkably large temperature gradients were observed with the ALOMAR Weber sodium lidar directly above the mesopause [*Fritts et al.*, 2004]. The analysis presented here and the paper by *Schöch et al.* [2004] focuses on the observation of gravity wave excitation and propagation in the troposphere and stratosphere. An investigation of the gravity waves in the mesopause region during the MaCWAVE/MIDAS summer rocket campaign has been presented by *Williams et al.* [2004].

The RMR lidar provided continuous data coverage during both salvos of the rocket campaign. The lidar also operated for extended times before and after the salvos which allows comparisons of the salvo nights to the rest of the summer. As for the other gravity waves analyses presented in this chapter, the RMR lidar data was averaged over one hour intervals. The necessary filters to achieve the needed daylight capability of the lidar reduce the signal strength and restrict the usable height range. Applying the same filters as for the other analysis presented in this chapter (see App. B.2), this gives an effective bandwidth of 2 – 14 hours in time and 3 km – 30 km in vertical wavelength where the upper limits are given by the length and the altitude range of the data set. The temporal development of the wave structure for the second salvo is shown in Fig. 6.22. It shows a typical summer measurement with wave amplitudes of a few Kelvin. Fig. 6.23 presents the GWPED profile from the RMR lidar measurement during salvo 2. Comparing it to Fig. 6.12C shows that the local wave activity during salvo 2 was higher than the average wave activity in summer 2002 (light-green diamonds in Fig. 6.12C). However, the average wave activity in summer 2002 was lower than the mean from all years analysed in this thesis (black dashed line in Fig. 6.12C). A Fourier transform has been applied to yield spectra of vertical wavelengths and observed periods. The results of the spectral analysis are discussed below.

Balloons were launched by a NASA team from the town of Andenes, about 4 km northeast of the ARR, roughly every two hours with six launches during salvo 1 between 15:44 UT, July 1, and 02:13 UT, July 2, and another six launches during salvo 2 between 17:50 UT,

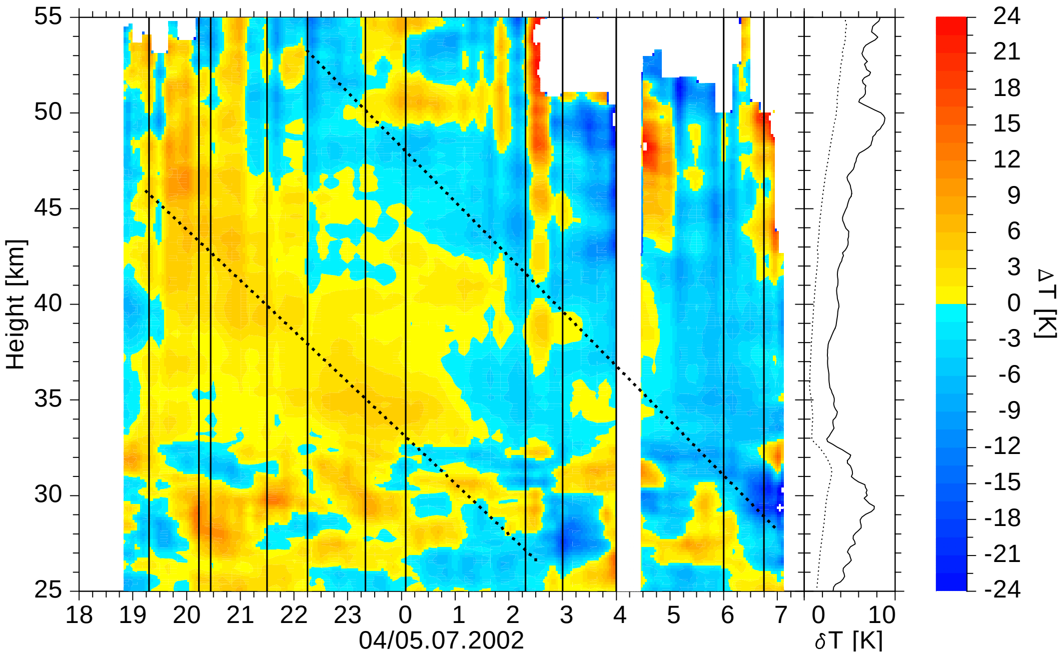

Figure 6.22: Temperature fluctuations in the stratosphere during salvo 2 (4/5 July 2002) of the MaCWAVE summer rocket campaign as observed with the RMR lidar. The gap around 4 am is due to drifting low clouds blocking the FOV of the lidar. Dominating wave phases are marked with dotted lines. The launch times of the falling spheres are indicated by the vertical solid lines. Shown on the right are the height dependent statistical uncertainty (dotted) and the temperature variability (solid line).

July 4, and 04:12 UT, July 5. Most balloons reached an altitude of more than 35 km. Winds were weak during both salvos so the balloons did not drift more than 87 km from the launch site. The falling sphere technique was used to measure temperatures between 36 km and 85 km and winds between 36 km and 80 km [*Schmidlin*, 1991; *Müllemann*, 2004]. The launch schedule has been described in detail by *Goldberg et al.* [2003]. For this case study, wind and temperature profiles from the falling spheres were used to cover the altitude range from 36 km to the stratopause.

A directionality analysis was performed on the radiosonde and falling sphere profiles following closely *Allen and Vincent* [1995] and *Vincent et al.* [1997]. For each individual sounding, an upper stratospheric segment (36 km – 50 km) was defined for gravity wave analysis of the rocket data, while lower stratospheric (15 km – 25 km) and tropospheric (2 km – 8 km) segments were defined for the balloon profiles. The segments were chosen

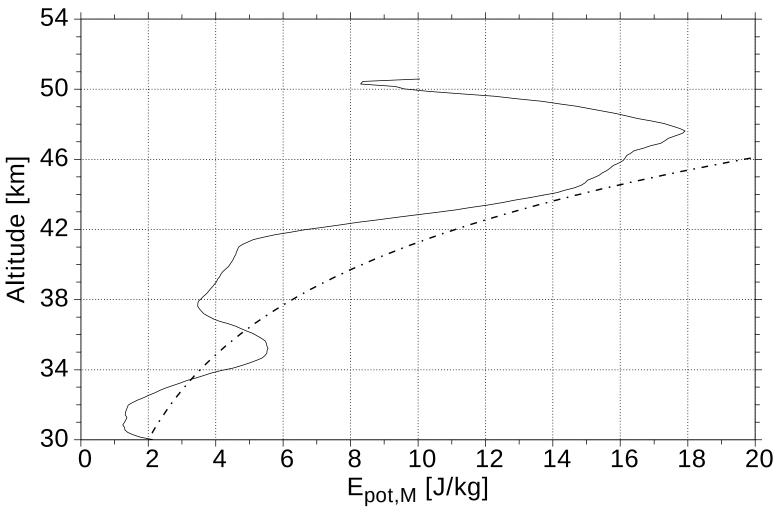

Figure 6.23: GWPED profile for salvo 2 of the MaCWAVE/MIDAS summer campaign smoothed over 3 km in altitude. The dash-dotted line shows the exponential increase of an undamped wave.

to exclude the stratopause and tropopause regions and to achieve approximately constant Brunt-Väisälä frequencies in each segment. The latter condition facilitates the interpretation of the results [*Allen and Vincent*, 1995].

For the balloon soundings, the mean profiles of the zonal and meridional winds and temperature $(\overline{u}, \overline{v}, \overline{T})$ were estimated using second-order polynomial fits within the given altitude ranges. For the rocket data, the arithmetic averages of the soundings for the particular salvo was calculated and then smoothed by a 7 km low-pass filter (suppressing smaller scales) to obtain $(\overline{u}, \overline{v}, \overline{T})$. This procedure both smoothed over high-wavenumber noise due to frequent sampling by the balloon payload at lower altitudes and preserved gravity wave variance at periods longer than the duration of the salvo. As for the RMR lidar temperature profiles, the gravity wave perturbations (u', v', T') were assumed to be the differences between the original sounding profiles and the mean profiles (e.g. $u' = u - \overline{u}$). The perturbation profiles were filtered by a 2 km and a 1 km low-pass filter, respectively, before they were subjected to the directionality analysis. This eliminated contributions to the propagation directions from very short scale perturbations and statistical noise. For each altitude segment, the averaged gravity wave kinetic energy density $E_{kin,M}$ was approximated neglecting the vertical velocity contribution by $E_{kin,M} = \frac{1}{2}(\overline{u'^2} + \overline{v'^2})$ (see Eq. 2.22).

The horizontal wave propagation direction (i.e. its phase velocity) can be determined objectively with the Stokes-parameter technique for gravity waves [*Vincent and Fritts*, 1987]. It determines the horizontal propagation direction from the wind perturbations u' and v'. The remaining ambiguity of 180° is resolved by including the temperature perturbations T' in the analysis. The filtering described above was designed to ensure that the directionality analysis was weighted towards those motions at the largest vertical scales contributing most to the gravity wave kinetic energy. A more detailed description of this kind of hodograph analysis of gravity waves has been assembled by *Eckermann* [1996]. An estimation of the uncertainties of such an analysis has been performed by *Zhang et al.* [2004] and will not be discussed further here.

Additionally, VHF radar wind measurements from two sites west and east of the Scandinavian mountain ridge were used to investigate the gravity wave content in the troposphere and lower stratosphere. The ALOMAR VHF radar (ALWIN, *Latteck et al.* [1999]) and the Esrange MST radar (ESRAD, *Chilson et al.* [1999]) in Kiruna (67.9° N, 21.1° E) are separated by about 250 km, but are otherwise similar in their antenna configurations, frequencies, resolution (300 m and 2 min in height and time, respectively), altitude coverage (2 km – 13 km) and measurement mode. Wind measurements are carried out in the Spaced Antenna mode using the Full Correlation Analysis method [*Briggs*, 1984]. Tropospheric and lower stratospheric wind data are available from the ALWIN radar for the whole of July 2002. ESRAD data are available from 3 July, 2002, 07:00 UT onward.

The radar data were averaged for 30 min intervals to reduce noise and account for data gaps caused by the alternating mode of measurements in the troposphere and mesosphere. Analyses were then applied to estimate the zonal and meridional wind components from both radar sites. A wavelet transform was used to determine the scales of the primary waves. As above, a band-pass filter was employed to exclude waves outside the 2 – 15 hr period and 2 – 4.5 km vertical wavelength bands before further data processing. The rotary spectrum technique was used to determine the vertical propagation directions. Finally, a complex cross-spectral analysis of common wave events was performed using the zonal wind perturbations at both radar sites. After identifying similar horizontal propagation directions and periods by separate Stokes parameter analyses, the horizontal wavelengths and phase velocities were estimated from a cross-correlation in the spectral domain using the phase differences of the coherent waves and the projection of the propagation directions onto the connecting line of the two sites (for details of this method see *Serafimovich et al.* [2005] and *Serafimovich* [2006]).

In the upper mesosphere large fluctuations, strong turbulence and large gradients were observed during both salvos [*Rapp et al.*, 2004; *Fritts et al.*, 2004]. The local wave activity in the stratosphere as observed by the RMR lidar was considerably larger during salvo 2 than during salvo 1. Therefore the following analysis concentrates on salvo 2 (4/5 July).

The temperature perturbations measured with the RMR lidar during salvo 2 are shown in Fig. 6.22 and are dominated by a gravity wave with an observed period of ∼11±0.5 hr, a vertical wavelength of ∼30±1 km and an inferred vertical phase speed of -0.77±0.02 ms^{-1}. This wave is present over the entire altitude range as indicated by the spectral analysis shown in Fig. 6.24 (upper panel). Below 33 km and near 50 km, other waves with observed periods between 2 hrs and 6 hrs are present as well. All these temperature fluctuations are significant since the temperature variance is larger than the statistical uncertainty over the entire altitude range (see right panel of Fig. 6.22). The Stokes analysis of the falling sphere profiles detects waves with periods of ∼2 hrs and ∼4.7 hrs at altitudes of 36 − 50 km in agreement with the lidar data. The suppression of waves with periods smaller than 4 hrs between 33 km and 45 km may be connected to a change in wind direction from 200° below 20 km to 80° above 30 km as indicated by the balloon data (see Fig. 6.25, panel B) changing the filtering for the ascending waves similar to the wave filtering described in the previous section.

The lower panel of Fig. 6.24 shows the mean vertical wavelengths spectrum for salvo 2. The nearly continuous shape of the spectrum suggests a superposition of many waves with a wide range of vertical wavelengths. In the wavelength band 1.5 km − 4 km, the observed mean spectrum follows the m^{-3} dependence expected from gravity wave theory [e.g. *Dewan and Good*, 1986].

The horizontal propagation directions for gravity waves derived from the balloon and falling sphere profiles

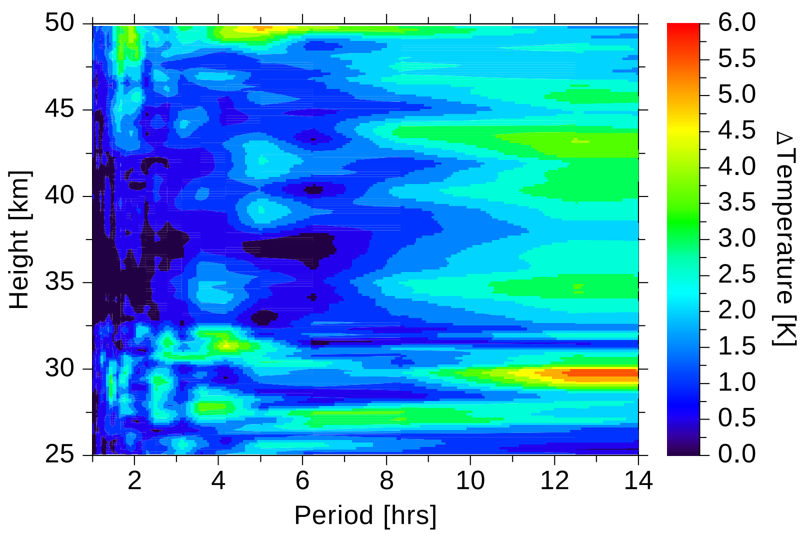

A) Spectra of wave periods

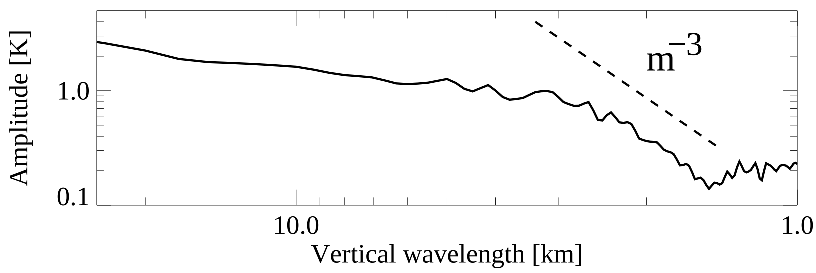

B) Mean vertical wavelength spectrum

Figure 6.24: *Upper panel:* Spectra of observed wave periods for the MaCWAVE summer rocket campaign salvo 2 from the RMR lidar data in Fig. 6.22. *Lower panel:* Mean vertical wavelength spectrum for salvo 2 from RMR lidar data. A theoretically expected m^{-3} dependence (dashed line) is found in the wavelength band 1.5 − 4 km (see text for details).

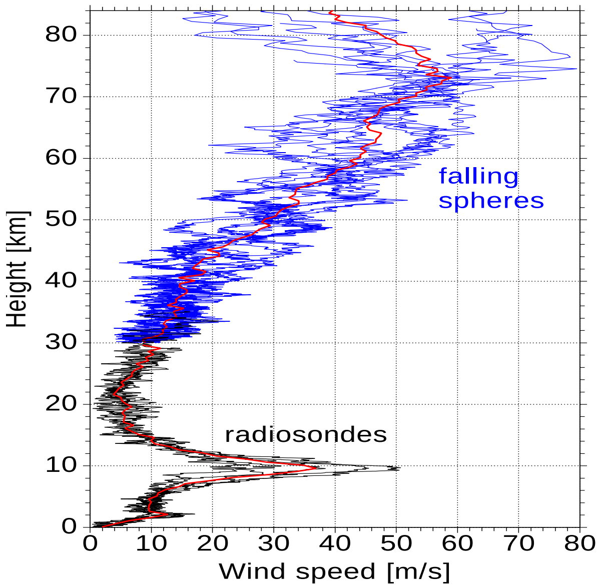

A) Wind speed

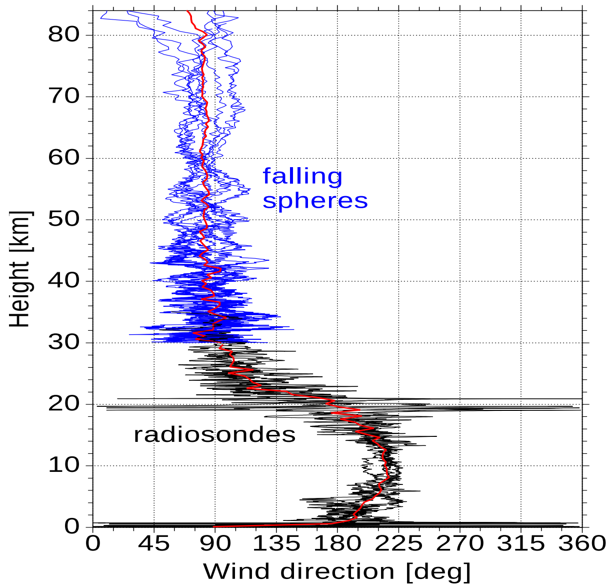

B) Wind direction

Figure 6.25: Mean wind speed (left) and wind direction (right) during the MaCWAVE summer rocket campaign salvo 2. The red line gives the mean of all profiles. The horizontal lines in the right panel close to 0 km and 20 km height are due to measurement uncertainties of the wind direction at very small wind speeds.

are shown in Fig. 6.26. The arrows show the direction of the horizontal phase speed, i.e. the propagation direction of the wave. The length of the arrows is proportional to the kinetic energy density $E_{kin,M}$ of the wave (see scales). In the troposphere and lower stratosphere (panels C and D) gravity wave propagation is nearly isotropic. This may be related to the relatively weak winds in the region (see Fig.6.25A; zonal winds are generally less than 10 ms^{-1} except directly at the tropopause where a jet developed during the night of salvo 2) and the proximity to the gravity wave source levels and is consistent with previous studies at high latitudes [e.g. *Wang*, 2003]. The kinetic energy density increases with altitude, agreeing with theoretical expectations. In the upper stratosphere, waves generally propagate eastward during both salvos. The isotropic gravity wave distribution at lower levels combined with westward wind speeds of -13 ms^{-1} to -25 ms^{-1} (see Fig. 6.25) in the stratosphere, suggest that ascending westward propagating gravity waves have been filtered out by the background winds due to the critical level effect (see Sec. 2.5.4). This change in the observed propagation directions occurs around the same altitude where we detected a change in the gravity wave spectrum (Fig. 6.24A).

The radar detected wave patterns in both zonal and meridional wind components with maximum amplitudes around 2 ms^{-1} during salvo 1 and up to 6 ms^{-1} during salvo 2 in agreement with the larger wave activity in the stratosphere during salvo 2 observed with the RMR lidar. The cross-spectral analysis performed on the radar data from the two sites (Fig. 6.27) shows that the spectrum was similar above Andenes and Kiruna and that the coherence was largest for waves with observed periods of ∼6 hr and ∼11 hr. From the observed phase differences, the estimated horizontal wavelength was ∼400 km and ∼600 km with propagation directions of ∼32° and ∼16° towards NNE. At Andenes, the rotary spectra averaged over the height range 2 km – 4.5 km (not shown here) shows that the 5 hr wave had a vertical wavelength of ∼2.7 km and propagated downward while the 11 hr wave had a vertical wavelength of ∼3.2 km and propagated upward. The radiosonde Stokes analysis yields waves with similar observed periods of 2 – 4 hr in the troposphere and 8 – 11 hr in the lower stratosphere.

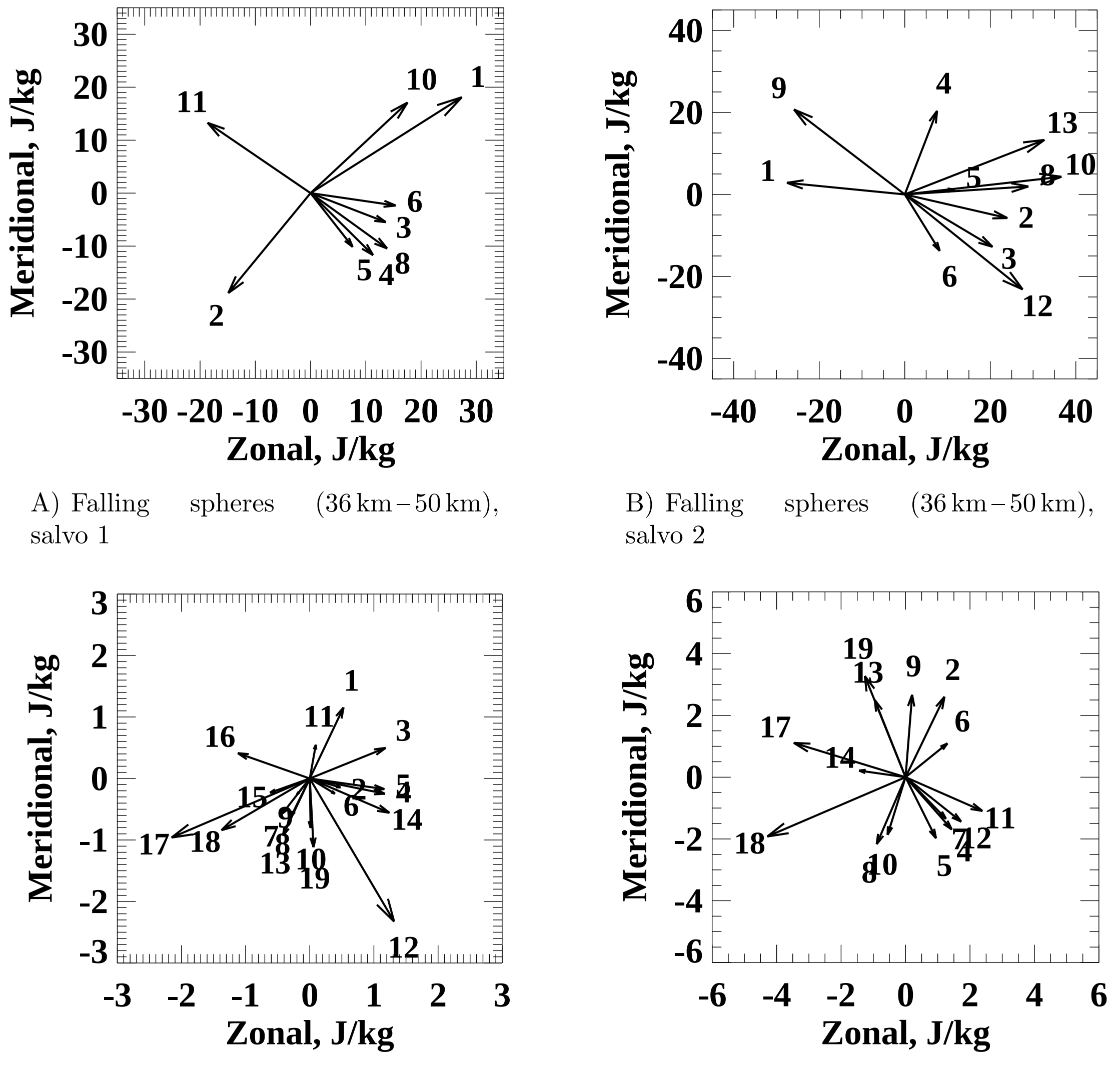

A) Falling spheres (36 km – 50 km), salvo 1

B) Falling spheres (36 km – 50 km), salvo 2

C) Balloon (2 km – 8 km)

D) Balloon (15 km – 25 km)

Figure 6.26: Gravity wave directionality analysis results for the rocket and balloon soundings. The directions of the arrows represent the directions of the horizontal phase propagation of each of the soundings, while the lengths of the arrows correspond to the kinetic energy densities (J kg^{-1}) averaged over the given altitude range (see text for details).

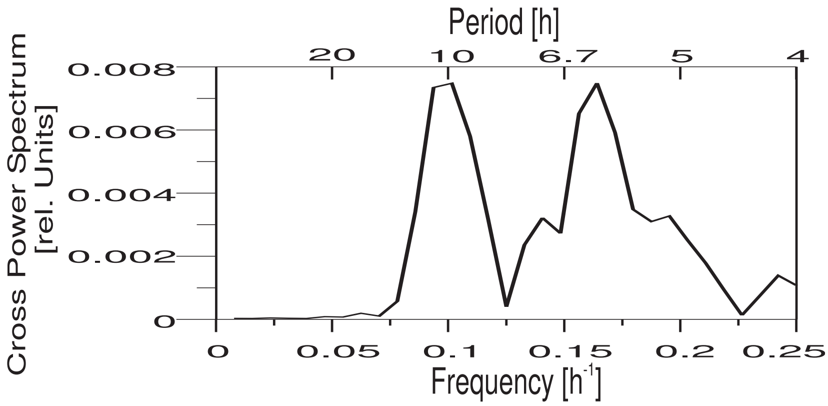

Figure 6.27: Cross-correlation for the radar wind measurements at Andenes and Kiruna. Two waves with an observed period of ~6 hr and ~11 hr were observed above both sites (see text).

Combining this result with the upward propagation of the 11 hr wave in the stratosphere observed with the RMR lidar, it follows that the excitation level for the short-periodic waves must have been in the tropopause or lower stratosphere region while the longer-period wave was excited in the troposphere or orographically. A very detailed and complex analysis of the radiosonde data might reveal the excitation altitude more precisely but is beyond the scope of this work. Comparing RMR lidar and radiosonde or falling sphere data shows that the latter are very sensitive for waves with small scales while the RMR lidar (due to the necessary integration time) only shows waves at larger scales.

Data from the RMR lidar have been combined with balloons, falling spheres and radars to analyse the gravity waves in the troposphere and stratosphere during salvo 2 of the MaCWAVE/ MIDAS campaign. Both radar and RMR lidar data show gravity waves with observed periods of $2-12$ hrs and vertical wavelengths from a few to 10's of kilometre, with the larger scales having larger amplitudes. While the wave propagation directions were rather isotropic in the troposphere and lower stratosphere, there was a dominant eastward propagation direction in the upper stratosphere. These changing propagation directions are consistent with the change in the background wind with altitude. From the radar and lidar data we conclude that the wave source for short-periodic waves must have been in the tropopause or lower stratosphere region while waves with longer periods were excited in the troposphere or at the ground. A cross-spectral analysis for the two radar sites showed strongly correlated waves above Andenes and Kiruna. This confirms that the wave field above both stations is similar at the longer-periodic part of the wave spectrum.

6.10 Summary

The preceeding sections present a survey of gravity wave analysis applied to measurements obtained with the ALOMAR RMR lidar. Through the analysis of the temperature fluctuations during long measurements, an overview of the temperature variability on scales of a few hours has been presented. The gravity wave energy density (GWPED) is largest in summer and winter and smallest around the equinoxes. This seasonal variation is found at all heights in the stratosphere and lower mesosphere. In the upper mesosphere, RMR lidar measurements are not available in summer due to the high solar background when the sky is sunlit all day long at the Arctic latitudes of the ALOMAR observatory. The seasonal variation of GWPED found in the RMR lidar measurements is consistent with lidar measurements performed on the Esrange at the eastern side of the Scandinavian mountain range by [*Blum*, 2003]. Falling sphere measurements of gravity waves show a larger winter/summer difference and no pronounced minima during the equinoxes [*Eckermann et al.*, 1995; *Lübken and von Zahn*, 1991]. This is probably due to the different measurement techniques which leads to the detection of different parts of the gravity wave spectrum.

During all seasons, the observed GWPED grows with increasing altitude as expected for upward propagating gravity waves. However, the increase is less than expected for undamped gravity wave propagation. The observed gravity wave dissipation is largest in winter and smallest in summer and autumn. Gravity wave damping in spring is weaker than in winter but stronger than in summer.

Studying the relation between tropospheric winds and upper stratospheric gravity waves, no correlation was found between either the wind speed or the wind direction at the surface and in the troposphere. From the local topography around ALOMAR, orographic gravity wave generation is expected to be important. But although there are open waters to the west and north of ALOMAR and mountains to the east and south, this does not translate into a correlation of lower tropospheric winds and GWPED in the upper stratosphere. In the lower stratosphere, the preferred wind direction during GWPED measurements is from the west. This is probably due to the requirement of clear skies for RMR lidar operation which favours certain weather patterns over others.

The comparison of GWPED measurements in the summer stratosphere to noctilucent cloud (NLC) measurements does not reproduce the negative correlation of GWPED and NLC brightness found by *Gerrard et al.* [1998] for lidar measurements in Søndrestrøm on Greenland. As their site is 150 km away from the west coast of Greenland, the local geophysical conditions are probably different than above ALOMAR. Also different tidal characteristics are observed above ALOMAR and Søndrestrøm. The influence of the tides on NLCs may mask the changes caused by gravity waves in the NLC layer above ALOMAR.

Two case-studies of gravity waves above ALOMAR were presented in this chapter. The first showed the influence of the background wind on the gravity wave field during a winter night in February 2001. Wavelet analyses clearly showed how the background wind leads to filtering of the gravity wave field depending on its wind speed and direction. The second case presented was from the international MaCWAVE/MIDAS summer rocket campaign conducted at the ARR in July 2002. Using measurements of the RMR lidar together with measurements from radiosondes and a VHF radar in the troposphere and falling spheres in the upper stratosphere showed that only the joint use of these instruments revealed the excitation height and mechanism for gravity waves propagating through the troposphere and middle atmosphere. During this case-study, the horizontal propagation directions of the gravity waves were isotropic in the troposphere and lower stratosphere while they were predominantly eastward in the upper stratosphere. A source for short-periodic waves was identified in the lower stratosphere/tropopause region while longer-periodic waves had been excited in the troposphere or at the ground. This combination of different instruments, especially including radar wind measurements, has a great potential for further and more detailed analysis of the gravity waves above ALOMAR.

Chapter 7

Conclusions and Outlook

The three previous chapters have given an overview of the temperature measurements in the middle atmosphere above ALOMAR with the RMR lidar in the years 1997 to 2005. Chap. 4 introduced the data set and discussed the seasonal variation of the night-mean temperatures and compared them to other data sets. Mesospheric cooling associated with stratospheric warming events and mesospheric inversion layers were discussed in Chap. 5. Gravity waves were analysed from the temperature fluctuations during a single measurement in Chap. 6. This chapter now gives a short summary of the results described in detail in the previous three chapters. It also includes an outlook with some ideas and suggestions for the further analysis of the RMR lidar measurements and for the future development of the RMR lidar instrument.

7.1 Conclusions

The middle atmosphere temperature data set obtained with the ALOMAR RMR lidar is unique because it covers the entire stratosphere and lower mesosphere over nine years from 1997 to 2005 and because it is not restricted to night-time measurements, i.e. it includes the entire polar summer. During these nine years, 7180 hrs of lidar measurements have been performed, including 4230 hrs obtained within this thesis. This makes it the most extensive lidar temperature data set in the middle atmosphere at polar latitudes. The large number of temperature profiles and good coverage of all seasons also is an advantage over other temperature climatologies from campaign based lidar or falling sphere measurements [*von Zahn and Neuber*, 1987; *von Zahn and Meyer*, 1989; *Lübken*, 1999]. The high temporal and vertical resolution of the RMR lidar is also better suited for the investigation of high-frequency waves with short vertical scales than satellite measurements. The following list summarises the main results achieved in this thesis:

– **Seasonal temperature variation**
The temperature climatology discussed in Sec. 4.4 and listed in App. A.3 is one of the main results of this thesis. For this high latitude, a lidar climatology spanning the whole year including the polar summer has not been available before. On the lower border at 30 km, the RMR lidar temperature climatology fits well to the ECMWF analyses averaged over the same period as the RMR lidar data. The single temperature profiles and monthly means show a relatively small variability of the temperatures in the summer month compared to a larger variability during winter (Fig. 4.5) when many temperature profiles are influenced by SSW events with stratopause temperatures of

up to 300 K. However, the monthly mean profiles still are a good representation of the average state of the atmosphere due to the large number of profiles being averaged (Fig. 4.5).

- **Comparison of temperatures to other data sets**
  Comparing the RMR lidar temperature measurements with other data sets it is found that in summer, the RMR lidar temperatures are up to 5 K colder than the Luebken1999 reference atmosphere in the stratosphere and up to 10 K colder in the mesosphere. Part of this difference is probably due to the different years used in the compilation by *Lübken* [1999]. The differences to other reference atmospheres like NRLMSISE00 and CIRA86 are significantly larger (see Fig. 4.12), reaching 15 K in summer and up to 25 K in winter. The detailed comparison of simultaneous RMR lidar and ECMWF temperature profiles in Sec. 4.5 shows the best agreement in summer and the largest mean difference and variability of the differences in winter. Winter temperatures in the polar middle atmosphere are often disturbed by dynamic events like stratospheric warmings that create large temperature deviations from the mean state and are often restricted to certain regions. This may explain why the operational ECMWF analyses do not fully resolve these temperature variations leading to the large observed temperature differences between RMR lidar measurements and ECMWF analyses. All these comparisons stress the need for continuous lidar measurements to determine the correct middle atmosphere temperatures. As the temperature structure influences the atmospheric chemistry and also the atmospheric dynamics by changing the wave propagation conditions, it is important to determine the correct temperature structure in order to understand many different processes in the middle atmosphere.

- **Stratopause temperature and height**
  The stratopause above ALOMAR shows a large variability in height and temperature in winter and a good agreement with the reference atmospheres in summer (Sec. 4.6). The only significant correlation between stratopause temperatures and heights and the solar cycle found is an anti-correlation of stratopause temperature and solar Lyman-α flux in winter. This is different to what is observed at mid-latitudes [*Keckhut et al.*, 2005]. However, in model calculations performed by *Shibata and Kodera* [2005], a similar anti-correlation is found at high northern latitudes, in agreement with the RMR lidar measurements which hence support their model. *Shibata and Kodera* [2005] explain their finding by the predominance of dynamics over radiation at high latitudes contrary to mid-latitudes where radiative effects dominate.

- **Stratospheric warmings**
  In 332 RMR lidar winter night-mean temperature profiles, only 44 profiles are found to show the clear signature of an SSW event with a stratopause temperature increase of more than 25 K compared to the undisturbed winter state. They are evenly distributed throughout the winters between 1997 and 2005, excluding only the winter 2001/2002. The relatively large number of SSW events is a special feature of the last decade which had not been observed before since such observations became available in the 1950s and may be related to climate change [*Manney et al.*, 2005]. 25 of these profiles reach above 70 km and show a simultaneous cooling in the mesosphere. This effect had been predicted by SSW theory [*Matsuno*, 1971] and had been recently observed during three case-studies with the SABER satellite instrument [*Siskind et al.*, 2005]. It was confirmed in the RMR lidar measurements for a much larger data set. The mean

mesospheric cooling observed with the RMR lidar is on average somewhat less than the cooling observed with SABER. This may be due to the larger number of profiles included or the accidental selection of the three case-studies in the SABER analysis. The magnitude of the mesospheric cooling indicates that the decrease or even reversal of the mesospheric jet during the SSW events blocks the westward propagating gravity waves responsible for the relatively warm undisturbed winter mesosphere but that no eastward propagating waves reach the mesosphere. Interestingly, there are five RMR lidar temperature profiles during SSW which do not show such a mesospheric cooling. Further studies are required to find the reason for the different temperature response with altitude during these five SSW events.

– **Mesospheric inversion layers**
  Mesospheric inversion layers (MILs) are common in the mid-latitude and tropical mesosphere but rare at polar latitudes. They are distinguished from gravity waves by their large amplitude and hence persistence in the night-mean temperature profiles. The RMR lidar observed 45 MILs in the years 1997 – 2005, all of them during winter, and none in summer. With two exceptions, this is also true for the falling sphere measurements. Therefore the reduced altitude coverage of the RMR lidar during summer is not the reason for the lack of MIL observations in the summer mesosphere but it must have a geophysical reason like the different wave spectrum in summer and winter. The MIL analysis presented in this thesis shows an occurrence rate of 4.6%, in agreement with other MIL analyses at high latitudes [*Cutler et al.*, 2001; *Duck and Greene*, 2004]. Applying the same MIL detection algorithm to falling sphere (FS) temperature profiles gives an occurrence rate of 21%. A possible explanation for this difference may be the different measurement techniques which result in different temporal resolutions. A MIL with downward phase speed would be detected in the FS measurements but averaged-out in the night-mean RMR lidar temperature profile. Similarly, a large amplitude gravity wave could be erroneously identified as a MIL in the FS profile while the wave would be averaged-out in the RMR lidar profile. Another reason for the different occurrence rates may be that the measurements of both instruments are from different time periods.

– **Gravity wave seasonal variation**
  Chap. 6 investigates temperature fluctuations during single measurements of more than six hours duration which are due to atmospheric gravity waves propagating through the middle atmosphere. Most gravity waves observed with the RMR lidar are found to propagate upwards, i.e. they are excited in the troposphere or lower stratosphere. Gravity wave energies show a large day-to-day variability. The monthly mean gravity wave potential energy density (GWPED) in the upper stratosphere and lower mesosphere has maxima in winter and summer and minima around the equinoxes (see Fig. 6.8). For the temperature variances, the difference between summer and winter in the lowermost altitude range is somewhat larger than for the GWPED. This is in qualitative agreement with falling sphere studies of the temperature variability [*Lübken*, 1999]. The differences between the temperature variabilities observed with the RMR lidar and with the falling spheres can be explained with the different measurement techniques which resolve different parts of the gravity wave spectrum. It is also important to separate temperature fluctuations caused by gravity waves from the day-to-day variability during such comparisons (see Fig. 6.11).

– **Gravity wave damping**
The GWPED of an undamped gravity wave grows exponentially with a growth length equal to the scale height H_ρ. Sec. 6.5 shows that the observed gravity wave field above ALOMAR is always partially damped. Wave damping is largest in winter and smallest in summer (Tab. 6.1). The corresponding Fig. 6.12 also shows that the GWPED values vary over orders of magnitudes between the single measurements.

– **Gravity waves and the background wind**
For orographically excited gravity waves, a correlation of wave amplitude and near surface wind would be expected. However, in the RMR lidar measurements, no significant correlation was found between GWPED in the stratosphere and wind speed or direction at any level below. Another mechanism influencing the gravity wave field is filtering by the background wind. ECMWF winds were used to calculate the expected transmission for an isotropic gravity wave field. It is found that this simulated transmission is not significantly correlated to the observed GWPED in the stratosphere. There are a number of possible reasons for this lack of correlation. Probably the gravity waves observed above ALOMAR are not only excited orographically but also by other processes in the lower atmosphere like geostrophic adjustment at the jet streams. The transmission calculations also assumes an isotropic wave field which definitely is an over simplification. Probably this assumption also marks the difference to the case-studies presented in this thesis where wave filtering by the background wind is indeed found to be important. Another possibly big uncertainty is the path of the upward travelling gravity waves. These waves are not propagating vertically but under a slant angle and may therefore have experienced different conditions in the lower atmosphere than seen directly above ALOMAR.

– **Gravity wave case-studies**
The gravity wave analyses in Chap. 6 also include two case-studies from winter 2001 and summer 2002. For the winter case, the wavelet transformation technique is used to demonstrate the strong influence of the background wind on the gravity wave field. It is clearly shown that high winds and large wind shears lead to strong gravity wave filtering with reduced gravity wave amplitudes and GWPED values in the altitude region directly above. The second case-study is from salvo 2 of the international MaCWAVE/MIDAS summer rocket campaign. Here, RMR lidar temperature measurements are combined with temperature and wind measurements by radiosondes and falling spheres and wind measurements with the ALWIN VHF radar to identify the source regions of the dominating gravity waves in the troposphere and stratosphere. The study found a short-periodic wave excited in the tropopause or lower stratosphere region and a longer-period wave excited at or close to the surface. This result could only be obtained through the combination of all instruments and would not have been available from any single instrument alone.

– **Noctilucent clouds and gravity waves**
Due to its high latitude site north of the polar circle, the RMR lidar observes noctilucent clouds (NLC) extensively in summer. In microphysical model calculations and observations at other sites, an anti-correlation between gravity waves and NLC brightness has been observed [*Jensen and Thomas*, 1994; *Gerrard et al.*, 1998]. Using the CARMA microphysical model, *Rapp et al.* [2002] found that waves with periods longer than 6.5 hrs amplify NLC while waves with shorter periods tend to destroy NLC. In the NLC observations with the RMR lidar however, no significant correlation was found

between GWPED and NLC brightness, height of maximum or width of the NLC layer. Interestingly, the GWPED values observed in the upper stratosphere above ALOMAR are similar to those found above Søndrestrøm in Greenland where the above mentioned anti-correlation of gravity waves and NLC brightness has been observed. A possible explanation are the differences in the tidal influence on NLC which are strong above ALOMAR but seem to be absent above Søndrestrøm [*Fiedler et al.*, 2005; *Thayer et al.*, 2003]. Another reason may be differences in the gravity wave spectrum due to the different topography around the coastal site of ALOMAR and the inland site of Søndrestrøm.

7.2 Outlook

The ALOMAR RMR lidar is constantly improved and developed further. In September 2005, the large aluminium mirrors of the telescopes have been replaced with dielectrically coated glass mirrors. Together with the exchange of several optical elements in the detector bench and the replacement of photomultipliers in the 532 nm detection branch with avalanche photodiodes, this has led to more than a tripling of the count rate in the 532 nm channels and significant improvements in the 355 nm and 1064 nm channels as well. In addition, the exchange of several mirrors in the emitter systems has increased the laser power emitted into the atmosphere. All these signal improvements enable the calculation of Rayleigh temperatures to higher altitudes or with shorter integration times. Together with the continued routine operation of the RMR lidar, this gives a range of possibilities for new or additional analyses, some of which are listed below:

– A more regular operation of the ALOMAR Weber sodium lidar would allow to combine the temperature profiles from the RMR lidar and the Weber sodium lidar during night-time measurements to yield continuous temperature profiles from 30 km to 105 km. The increased altitude coverage allows more extended studies of wave propagation and breaking in the mesopause region. The Weber lidar temperature measurements would be also very interesting for detailed studies of the formation and temporal development of the NLC measured simultaneously with the RMR lidar.

– Independently from the increased altitude range, the gravity wave analyses presented for case-studies should be extended to yield climatological means of vertical wavelengths, vertical phase speeds and observed periods. The wavelet transformation analysis could be used to extract spectrally resolved vertical phase speeds.

– The increased signal should be used to use shorter integration times and hence to resolve shorter-periodic gravity waves, if possible down to the lower frequency limit for gravity waves given by the Brunt-Väisälä period T_{BV} of ≈ 5 min. These high frequency gravity waves are important for atmospheric dynamics as they transfer momentum from the lower to the upper atmosphere.

– Gravity waves are influenced in many ways by the background wind. And some gravity wave parameters like the horizontal propagation direction can only be inferred from a vertical measurement above a single station if the wave induced fluctuations are observed in both temperature and wind. Therefore the combination of RMR lidar temperature measurements with radar wind measurements should be extended at those altitudes where RMR lidar temperatures and radar winds are available (lower stratosphere, upper mesosphere).

– A new Doppler Rayleigh Iodine System (DoRIS) is developed for use with the RMR lidar. It measures the Doppler shift of the Rayleigh scattering at 532 nm due to the wind along the line-of-sight of the RMR lidar. Temperature stabilised iodine cells are used to spectrally stabilise the power lasers and as a high-resolution spectrometer to deduce the Doppler shift of the received signal. The new DoRIS system allows wind measurements with a similar resolution as the temperature measurements up to the lower mesosphere, thus including the upper stratosphere/lower mesosphere region not accessible through radar wind measurements. This new capability of the RMR lidar improves its ability to detect and analyse gravity waves considerably, including the derivation of kinetic energy density and hence total energy density and of the horizontal propagation direction over the entire RMR lidar altitude range.
– Extended gravity wave analyses could also include the detection of static instability regions ($N \lesssim 0$) from the temperature field and its possible correlation to gravity wave breaking. With the new DoRIS wind measurements, regions of dynamical instability ($Ri \lesssim 0.25$) can be detected and compared to gravity wave breaking as well.
– The capability of the RMR lidar to perform temperature measurements both during night-time and daylight conditions yields a good data set for the analysis of temperature tides in the polar middle atmosphere. Sorting the one hour temperature profiles from the gravity wave analysis by time-of-day and temporally averaging all measurements over a week up to a month should give a good picture of the tidal amplitudes and phases in the middle atmosphere above ALOMAR.
– A so-called super-controller has been developed within this thesis to automate various tests with the RMR lidar that had been performed manually before (see App. C.2). The super-controller program should be extended to analyse the lidar data recorded during the tests and use this information to automatically modify the tests. Such an extended capability could be e.g. applied to perform automated laser beam searches at many different telescope pointing angles. The correct focusing of the telescopes (see App. C.1) could also be tested automatically at the start of each measurement by analysing the recorded lidar data while changing the focusing of the telescopes.

Finally, for the support of other measurement campaigns at ALOMAR and ARR, the algorithm for temperature calculation presented in App. B should be incorporated into the RMR lidar online data display (http://iap0.rocketrange.no/rmr/). This could aide rocket or balloon campaigns looking for special launch conditions (large waves, inversion layers) in the thermal structure of the middle atmosphere.

Appendix A

A.1 Monthly distribution of measurements

This section lists the measurements used in the analysis of the mean temperatures and for the gravity wave analysis.

Year	**Jan**	**Feb**	**Mar**	**Apr**	**May**	**Jun**	**Jul**	**Aug**	**Sep**	**Oct**	**Nov**	**Dec**	**Sum**
1997	5	9	2	3	2	8	11	3	1	3	6	5	58
1998	6	5	8	2	1	11	17	15	3	3	3	3	77
1999	11	5	5	3	13	7	9	6	4	1	2	3	69
2000	3	6	3	4	7	6	19	10	0	6	12	5	81
2001	8	13	11	0	0	13	10	10	0	0	2	2	69
2002	15	8	7	7	11	26	27	13	7	14	10	7	152
2003	9	9	2	9	7	18	21	16	10	10	11	0	122
2004	7	4	15	20	4	9	24	16	4	9	1	4	117
2005	14	11	9	8	13	9	13	12	-	-	-	-	89
Sum	78	70	62	56	58	107	151	101	29	46	47	29	834

Table A.1: Number of measurements per month used for calculating mean temperature profiles.

Year	**Jan**	**Feb**	**Mar**	**Apr**	**May**	**Jun**	**Jul**	**Aug**	**Sep**	**Oct**	**Nov**	**Dec**	**Sum**
1999	1	0	0	0	2	5	1	3	0	0	1	0	13
2000	1	2	0	1	1	2	15	7	0	0	2	0	31
2001	1	9	3	0	0	3	2	2	0	0	1	1	22
2002	4	3	4	3	6	13	15	5	0	3	3	4	63
2003	5	2	0	0	1	4	17	4	3	2	7	0	45
2004	1	1	4	3	1	7	13	8	0	2	0	0	40
2005	0	9	1	2	6	5	7	6	-	-	-	-	36
Sum	13	26	12	9	17	39	70	35	3	7	14	5	250

Table A.2: Number of measurements per month used for gravity wave analysis.

A.2 Tabulated monthly mean temperatures

The monthly mean temperature profiles from Fig. 4.5 are listed as a function of altitude in Tab. A.3 below:

Height [km]	Jan	Feb	Mar	Apr	May	Jun	Jul	Aug	Sep	Oct	Nov	Dec
30.0	208.0	216.2	215.5	219.4	226.6	229.7	230.2	227.2	217.8	208.4	195.8	202.0
32.0	214.4	222.0	219.0	224.7	231.0	235.1	235.1	231.8	221.4	211.3	198.4	208.3
34.0	220.5	229.2	223.2	231.0	236.0	241.0	241.0	237.0	226.3	215.6	200.9	217.0
36.0	226.7	236.9	227.3	237.3	241.5	246.6	246.3	242.0	230.9	220.1	202.7	226.4
38.0	233.3	244.1	232.2	244.4	247.6	252.6	252.1	247.3	236.5	225.1	209.5	234.1
40.0	238.9	250.0	237.8	251.1	253.9	258.9	258.2	253.0	241.6	230.3	219.8	241.2
42.0	243.7	254.0	243.9	257.9	260.0	265.1	264.1	258.6	247.0	236.4	227.4	247.3
44.0	247.9	258.3	249.2	263.5	265.7	270.2	269.7	263.5	252.3	242.5	235.3	252.7
46.0	250.8	262.2	253.4	267.7	270.6	274.5	274.3	267.6	256.8	247.9	243.4	257.7
48.0	253.4	263.5	256.5	269.6	273.6	276.9	277.1	270.1	259.6	252.0	250.8	260.0
50.0	255.4	264.0	259.0	271.1	275.3	278.0	278.4	271.2	260.7	254.5	255.7	263.1
52.0	258.2	263.3	259.1	270.6	275.4	278.4	278.3	271.2	258.8	255.4	259.3	263.8
54.0	259.4	261.4	258.2	268.3	274.2	276.1	276.4	270.0	256.5	254.3	261.2	262.7
56.0	257.6	259.6	258.1	264.5	271.6	271.8	271.6	267.4	253.7	253.9	261.0	260.3
58.0	254.6	257.0	255.7	259.6	267.2	268.0	267.4	264.0	250.0	252.6	260.3	256.2
60.0	251.5	253.1	252.4	254.8	260.8	260.5	261.0	256.9	244.8	251.7	258.9	252.6
62.0	247.2	249.2	249.3	249.6	254.5		255.7	251.3	240.3	248.9	256.8	247.2
64.0	242.0	244.9	245.5	243.1	247.4			243.7	235.2	247.1	253.4	243.1
66.0	238.2	240.5	241.6	236.4				234.2	228.5	244.2	251.0	235.1
68.0	236.0	237.0	238.7	229.2				225.3	221.9	240.9	248.1	229.2
70.0	233.3	233.3	236.0	224.1					214.7	234.4	244.2	223.1
72.0	229.3	232.0	231.5	218.8					210.0	229.2	242.4	218.7
74.0	225.8	227.7	227.0	213.6					203.8	222.2	238.3	215.2
76.0	220.2	223.6	221.3	207.6					200.8	216.4	235.5	215.2
78.0	215.7	214.9	216.6	207.0					196.8	214.0	230.8	215.0
80.0	210.8	212.9	211.3	201.8					195.8	212.5	226.9	216.7
82.0	205.6	213.3	211.2						189.5	210.8	220.5	216.3
84.0	204.9	212.3	210.8							213.2		212.9
86.0												

Table A.3: Monthly mean temperatures for the middle atmosphere above ALOMAR from RMR lidar measurements.

A.3 Tabulated temperatures climatology

The seasonal temperatures variations above ALOMAR from RMR lidar, falling spheres and ECMWF (Fig. 4.7) are listed as a function of altitude in Tabs. A.4 and A.5 below.

Height [km]	01.01.	11.01.	21.01.	01.02.	11.02.	21.02.	01.03.	11.03.	21.03.	01.04.	11.04.	21.04.	01.05.	11.05.	21.05.	01.06.	11.06.	21.06.
0.0	273.4	272.8	273.3	272.1	273.5	273.9	273.0	273.3	273.1	274.4	274.6	275.9	276.9	278.1	278.2	279.4	280.9	282.6
2.0	261.6	261.7	260.1	259.2	261.1	261.1	259.9	260.0	260.6	261.7	261.9	264.5	265.7	266.6	267.3	268.6	271.5	273.0
4.0	249.0	249.6	247.7	246.3	248.3	248.3	246.8	247.8	248.4	249.7	250.0	253.5	254.5	255.7	256.3	257.8	260.5	262.0
6.0	234.9	235.3	233.6	232.6	234.0	233.8	232.2	233.7	234.8	235.9	236.7	239.5	240.4	241.9	242.0	243.5	246.8	248.3
8.0	220.8	221.1	220.4	219.7	220.7	220.7	219.4	220.6	222.3	223.0	224.0	224.9	226.4	228.1	228.1	229.1	231.6	232.7
10.0	212.8	212.9	213.8	213.6	213.8	214.2	214.4	214.9	217.5	218.2	219.7	219.5	221.4	222.9	224.6	224.9	224.8	225.4
12.0	211.0	211.4	212.4	212.4	212.5	213.1	213.7	214.6	218.1	219.0	220.7	221.2	223.6	224.8	227.1	227.6	226.9	227.8
14.0	209.3	209.5	210.3	210.0	210.7	211.8	212.1	213.7	217.2	218.5	220.1	221.2	223.0	224.6	226.0	226.6	227.0	227.7
16.0	205.5	205.7	206.7	206.4	207.3	209.3	209.5	211.5	215.3	216.7	218.3	220.0	221.4	223.4	225.0	225.5	225.9	226.4
18.0	201.8	202.3	203.5	203.2	204.5	206.8	207.3	209.8	213.6	215.4	217.0	219.4	220.6	222.8	224.9	225.6	226.0	226.2
20.0	198.9	199.4	200.9	200.9	202.3	205.2	206.2	209.0	212.6	214.9	216.1	219.0	220.2	222.5	224.7	225.6	226.0	226.4
22.0	197.2	197.6	198.9	199.6	200.9	204.4	205.9	208.8	212.1	214.6	215.8	218.8	220.4	222.9	224.9	225.8	226.4	226.9
24.0	197.1	197.4	198.3	199.8	200.3	204.4	206.7	209.3	212.2	214.8	215.9	219.1	221.1	223.7	225.7	226.7	227.5	228.0
26.0	194.8	197.8	197.1	198.8	197.3	201.8	206.2	209.3	211.9	214.6	215.7	219.0	222.2	225.0	226.0	228.1	229.1	229.8
28.0	204.5	202.5	203.0	206.0	205.1	209.0	212.2	213.4	214.5	216.4	218.1	221.3	224.3	226.4	228.7	230.3	231.1	231.7
30.0	214.1	207.3	208.9	213.3	213.0	216.2	218.1	217.5	217.0	218.2	220.5	223.6	226.3	227.8	231.4	232.6	233.1	233.7
32.0	223.7	212.0	214.9	220.5	220.8	223.4	224.1	221.7	219.6	220.0	222.9	225.9	228.4	229.2	234.1	234.8	235.0	235.7
34.0	234.3	217.3	221.6	227.8	228.5	231.6	230.5	225.8	223.0	225.5	228.8	232.1	232.6	232.7	238.7	239.9	240.3	241.0
36.0	245.9	222.5	227.3	234.6	235.1	239.1	235.9	228.8	226.3	232.3	235.6	238.8	238.4	238.7	243.0	245.2	246.3	246.5
38.0	251.3	228.8	233.9	241.3	241.6	246.6	241.0	232.3	231.2	239.3	242.9	246.2	244.4	245.4	249.3	250.9	252.3	252.6
40.0	255.6	233.9	238.9	245.8	247.1	251.6	245.7	236.6	236.4	247.1	249.2	253.1	250.6	252.0	255.4	257.3	258.6	259.0
42.0	261.1	239.3	243.3	249.5	251.3	255.5	249.8	242.5	243.3	253.9	255.1	260.3	257.2	258.1	261.7	263.4	265.0	265.3
44.0	266.1	245.2	247.4	252.4	255.8	259.4	252.8	247.8	249.4	259.2	259.9	266.3	262.8	263.7	267.3	268.5	270.1	270.3
46.0	266.4	249.1	250.3	255.3	261.3	262.8	255.3	251.9	254.0	263.7	264.3	270.2	268.1	269.1	271.7	271.6	274.6	274.6
48.0	266.4	253.1	251.8	256.6	263.7	265.0	256.9	254.3	257.2	264.8	266.8	272.0	270.4	272.3	275.2	276.3	277.3	276.5
50.0	265.8	256.2	253.5	257.3	266.0	266.7	258.3	257.6	260.0	266.7	268.3	273.6	272.5	275.5	276.4	276.9	277.3	277.3
52.0	266.1	258.7	256.0	257.7	265.1	265.1	257.8	257.9	260.9	267.3	267.3	272.4	272.4	274.8	276.3	276.9	277.5	278.9
54.0	264.7	261.1	256.5	257.0	264.2	262.2	256.0	257.5	261.4	263.6	265.1	269.8	268.8	272.6	274.6	274.7	275.7	276.9
56.0	261.1	258.2	253.9	254.3	262.7	260.3	255.3	258.5	261.9	263.0	262.9	266.1	266.2	268.8	272.5	272.4	272.6	272.9
58.0	252.9	253.4	251.2	250.9	263.0	258.2	253.0	256.2	258.5	260.9	260.2	260.0	262.7	265.4	270.5	270.5	270.8	270.6
60.0	248.1	250.5	248.6	247.8	260.2	252.5	249.4	254.8	254.9	257.5	255.9	255.5	258.0	260.8	268.5	268.6	269.1	268.3
62.0	238.5	246.2	244.9	244.1	256.8	248.1	245.9	252.9	251.9	252.4	250.4	250.4	253.3	256.1	262.6	266.6	267.4	266.0
64.0	234.6	239.5	241.1	241.9	254.7	244.9	243.7	249.6	246.8	245.4	243.9	242.5	248.7	251.5	254.8	256.6	257.0	256.8
66.0	228.6	235.3	238.7	238.6	250.9	240.4	240.8	246.3	241.6	237.0	234.3	236.6	244.0	246.9	245.8	247.1	247.5	247.0
68.0	223.4	236.4	237.3	235.5	246.3	234.0	241.2	245.8	237.6	231.0	227.8	228.7	231.6	234.4	235.7	236.5	236.5	236.0
70.0	228.7	234.5	234.8	231.6	241.5	230.6	239.7	242.9	234.9	225.0	223.8	223.8	222.3	224.2	225.0	225.0	224.7	224.0
72.0	220.2	234.9	230.2	228.2	240.7	229.5	237.2	240.3	231.5	219.5	219.7	219.3	213.5	213.7	213.5	212.8	212.2	211.3
74.0	217.6	236.9	224.5	223.3	236.3	220.0	231.9	235.6	226.2	214.7	214.4	211.5	205.0	203.5	202.2	200.7	199.3	198.3
76.0	215.7	236.9	219.0	216.7	227.4	217.0	225.7	230.7	219.2	211.5	208.4	203.7	197.0	193.5	190.8	188.4	186.6	185.3
78.0		232.8	212.7	213.0		215.5	227.5	227.0	215.0			195.9	189.5	183.6	179.9	176.4	174.2	172.8
80.0			206.1	206.6		216.9	216.9	219.2	206.2			192.0	182.3	174.6	169.5	165.1	162.5	160.8
82.0			197.0	199.4					204.6			187.5	176.0	166.4	160.0	154.9	151.8	150.0
84.0			197.0	199.0					202.3			183.0	170.2	159.2	151.9	146.0	142.6	140.8
86.0												178.3	165.2	153.3	145.1	139.0	135.3	133.0
88.0												173.0	160.6	149.4	141.4	135.3	131.5	129.5
90.0												167.3	157.0	148.2	141.8	137.0	134.2	133.0
92.0												160.8	154.1	150.0	148.0	146.7	146.8	146.8

Table A.4: Middle atmosphere temperatures above ALOMAR from combined RMR lidar, falling sphere and ECMWF profiles (January – June). Temperatures below 30 km are from ECMWF at (70° N, 15° E) while falling sphere data from the ARR is used in the summer upper mesosphere (see Sec. 4.4 for details).

Height [km]	01.07.	11.07.	21.07.	01.08.	11.08.	21.08.	01.09.	11.09.	21.09.	01.10.	11.10.	21.10.	01.11.	11.11.	21.11.	01.12.	11.12.	21.12.
0.0	282.4	284.3	284.6	284.9	284.5	284.5	284.4	283.7	281.5	280.2	279.0	277.5	276.4	276.6	276.4	275.4	276.2	274.6
2.0	274.9	275.6	276.4	274.9	274.7	273.9	273.3	271.8	269.9	269.1	268.2	265.6	265.5	264.5	264.4	263.8	263.0	261.2
4.0	263.9	264.8	265.7	264.4	264.0	263.4	262.8	261.2	259.0	258.7	257.7	254.4	253.9	252.6	252.2	251.7	250.8	248.3
6.0	250.1	251.2	252.2	250.8	250.3	249.7	249.4	247.8	245.6	245.2	244.2	240.7	239.8	238.4	238.0	237.5	236.6	234.1
8.0	234.0	235.2	235.8	234.6	233.9	233.6	233.9	232.3	231.1	230.4	229.3	226.8	225.4	224.4	223.7	223.3	222.8	220.4
10.0	225.7	226.1	226.1	225.4	224.7	224.0	223.8	223.1	222.9	221.7	220.4	219.8	218.7	217.3	216.0	215.6	215.6	214.2
12.0	227.3	226.9	226.4	226.3	225.3	224.2	222.3	222.6	221.8	220.3	219.1	218.9	218.5	216.3	214.5	214.2	213.6	212.9
14.0	227.1	227.2	227.3	227.1	226.2	225.5	223.6	222.8	221.9	220.5	219.5	218.3	217.4	214.9	213.1	212.9	212.2	211.2
16.0	226.1	226.2	226.4	226.5	225.8	225.2	223.2	222.0	220.8	219.3	217.7	216.2	214.9	212.2	209.7	209.1	208.7	207.9
18.0	226.3	226.6	226.4	226.6	226.0	225.2	223.1	221.6	219.9	218.0	216.1	213.7	212.3	209.0	205.9	204.9	204.6	204.1
20.0	226.7	227.0	226.6	226.5	225.8	224.5	222.5	220.6	218.1	216.0	213.7	210.9	209.2	205.6	202.1	200.9	200.8	200.9
22.0	227.2	227.4	226.9	226.6	225.6	224.0	221.8	219.7	216.9	214.5	211.7	208.3	206.2	202.4	198.5	197.0	197.0	198.3
24.0	228.2	228.4	227.8	227.1	225.9	224.3	221.6	219.4	216.5	213.7	210.3	206.4	203.8	199.7	195.4	193.6	193.7	196.8
26.0	230.2	230.5	229.7	229.1	227.7	225.5	222.0	219.6	215.5	212.1	207.2	203.0	199.8	195.8	191.6	188.6	188.3	189.0
28.0	232.2	232.4	231.6	230.7	229.2	227.4	223.9	220.7	217.7	213.5	209.4	204.8	201.6	197.6	193.2	191.0	193.5	205.2
30.0	234.1	234.4	233.5	232.3	230.8	229.3	225.7	221.8	219.9	214.9	211.6	206.5	203.5	199.4	194.8	193.4	198.7	221.4
32.0	236.1	236.4	235.5	234.0	232.3	231.2	227.5	222.9	222.1	216.3	213.8	208.3	205.3	201.3	196.4	195.7	203.8	237.6
34.0	241.5	241.6	240.7	238.7	236.7	235.3	232.1	227.7	226.8	220.4	218.4	212.7	209.1	204.5	198.5	200.3	213.4	250.3
36.0	247.0	247.0	245.7	244.0	241.7	240.1	236.5	231.6	230.7	225.6	222.7	217.4	213.6	209.4	198.1	204.7	223.6	255.8
38.0	252.8	252.8	251.8	249.5	246.9	245.2	241.9	237.0	236.4	231.2	227.7	222.8	217.6	214.3	205.4	212.0	232.7	257.6
40.0	259.3	259.0	257.8	255.4	252.5	250.7	247.3	242.2	241.6	236.4	233.4	228.5	221.8	219.5	217.3	221.8	239.7	259.4
42.0	265.5	265.1	263.5	261.3	258.1	256.0	252.5	247.8	247.3	242.0	239.4	234.5	228.2	226.6	225.2	229.8	245.3	263.4
44.0	271.2	270.8	268.9	266.3	262.8	261.0	257.6	252.9	252.7	247.4	245.1	241.3	235.1	238.3	232.1	236.9	249.5	267.0
46.0	275.8	275.4	273.4	270.7	267.0	265.4	261.7	256.9	256.2	251.9	249.9	246.7	241.8	245.8	240.6	245.2	254.1	269.3
48.0	278.1	278.4	276.6	273.8	269.5	267.8	264.7	260.0	259.7	254.6	253.8	250.5	246.9	253.1	248.0	251.9	257.1	266.7
50.0	278.2	278.8	278.8	275.9	270.7	268.7	265.7	260.7	260.4	255.8	256.6	253.6	249.9	258.8	252.3	257.6	262.1	263.3
52.0	278.6	278.8	278.5	276.8	270.4	268.6	265.1	259.6	259.9	254.9	256.9	254.4	255.2	264.6	255.8	261.4	263.2	258.5
54.0	276.3	276.6	276.4	275.2	269.5	267.7	263.0	258.4	258.9	252.8	255.8	254.6	258.8	265.9	258.1	262.8	265.0	254.2
56.0	272.8	271.3	271.0	271.4	267.5	266.0	260.1	255.8	257.9	250.0	254.1	252.6	259.2	265.0	258.1	263.0	264.1	249.1
58.0	270.9	268.2	267.7	266.4	264.0	262.3	255.8	253.2	257.0	246.9	251.1	249.1	256.0	267.6	258.1	262.8	261.9	241.0
60.0	268.9	263.6	261.6	261.5	258.6	257.0	251.4	248.8	250.8	241.9	248.6	250.6	255.6	266.2	257.8	261.3	257.8	235.7
62.0	267.0	259.0	255.6	255.5	252.4	250.4	245.6	244.5	244.5	237.6	245.9	249.1	250.5	257.3	256.5	257.2	258.9	228.7
64.0	256.1	254.4	248.6	249.4	246.1	243.8	237.9	240.2	237.0	234.5	242.9	247.0		250.7	253.0	254.3	255.4	223.8
66.0	246.3	244.5	241.5	243.3	239.9	237.1	233.2	229.9	227.8	230.6	235.2	243.6		247.3	251.2	249.6	246.6	218.3
68.0	235.1	233.5	234.5	229.9	227.9	225.7	223.6	219.9	218.3	225.9	232.0				248.4	244.9	238.5	216.1
70.0	223.0	221.7	220.2	218.4	216.8	215.7	214.0	211.3	209.8	219.8	227.6				244.5	239.6	223.2	
72.0	210.3	209.2	207.9	206.7	205.6	205.1	204.4	203.6	203.3	217.8	225.0				243.8	240.4	218.1	
74.0	197.3	196.3	195.6	194.7	194.5	194.8	195.2	196.9	199.0	212.9	221.2				238.3	237.2	214.3	
76.0	184.4	183.7	183.3	183.0	183.4	184.7	186.7	191.3	197.0	209.2	217.0				234.5	235.6		
78.0	171.8	171.3	171.4	171.6	172.7	175.2	179.2	186.6	196.3	205.9	219.3				228.5	232.8		
80.0	160.2	159.8	160.0	160.8	163.0	166.4	172.6	182.7	196.8	208.6	210.1				224.3	225.6		
82.0	149.5	149.3	149.4	150.9	153.9	158.4	167.2	179.5	198.0						218.8			
84.0	140.0	140.0	140.4	142.5	146.0	151.8	162.6	177.3	199.5									
86.0	132.5	132.7	133.8	136.5	140.6	146.6	159.7	175.6	201.0									
88.0	129.5	129.9	131.6	134.5	138.4	144.4	157.8	174.9	202.0									
90.0	133.1	134.1	135.6	137.4	140.5	145.8	157.7	174.7	202.0									
92.0	147.1	147.5	147.4	147.3	148.2	151.9	158.9	175.2	200.8									

Table A.5: Middle atmosphere temperatures above ALOMAR from combined RMR lidar, falling sphere and ECMWF profiles (July – December). Temperatures below 30 km are from ECMWF at (70° N, 15° E) while falling sphere data from the ARR is used in the summer upper mesosphere (see Sec. 4.4 for details).

A.4 List of sudden stratospheric warmings

Tab. A.6 lists all nightly-mean RMR lidar profiles that were identified as SSW based on the detection algorithm described in Sec. 5.1.

Measurement duration [UT]	**Stratopause height [km]**	**Stratopause temperature [K]**	**major SSW**
28.02.2005 15:24:53 – 28.02.2005 19:54:48	45.25	286.6	no
25.02.2005 02:35:28 – 25.02.2005 04:49:42	40.45	301.4	no
22.02.2005 06:01:53 – 22.02.2005 11:45:13	48.85	296.8	no
21.02.2005 16:57:39 – 22.02.2005 05:35:43	46.49	288.5	no
18.01.2005 20:54:43 – 19.01.2005 00:11:23	39.25	276.3	no
18.01.2005 20:50:16 – 19.01.2005 00:11:23	39.10	277.9	no
15.01.2005 17:35:11 – 15.01.2005 21:56:18	45.55	295.8	no
06.01.2005 20:59:08 – 06.01.2005 23:12:28	48.10	294.5	no
21.03.2004 18:36:02 – 21.03.2004 22:17:42	56.05	288.5	no
28.02.2004 08:41:48 – 28.02.2004 13:11:16	43.30	281.7	no
04.01.2004 11:49:38 – 04.01.2004 15:28:35	46.45	289.7	yes
03.01.2003 13:25:56 – 03.01.2003 15:33:42	42.55	311.0	no
02.01.2003 14:41:35 – 02.01.2003 17:31:04	37.45	291.2	no
28.12.2002 12:02:08 – 28.12.2002 16:34:29	36.10	307.8	no
31.01.2001 17:08:14 – 01.02.2001 05:01:56	43.15	303.0	no
30.01.2001 17:08:14 – 30.01.2001 19:24:20	39.10	296.6	no
26.01.2001 18:15:17 – 26.01.2001 21:32:30	44.05	287.1	no
23.01.2001 18:14:18 – 23.01.2001 22:24:18	60.25	287.4	no
13.12.2000 17:04:44 – 13.12.2000 21:51:43	44.80	281.0	no
12.12.2000 18:15:30 – 12.12.2000 20:38:11	41.50	281.8	no
11.12.2000 21:19:57 – 12.12.2000 00:51:10	40.90	286.3	no
10.12.2000 18:04:14 – 10.12.2000 22:14:14	37.45	295.2	no
22.01.2000 20:08:08 – 22.01.2000 22:42:24	46.30	281.8	no
21.01.2000 22:26:59 – 22.01.2000 01:33:25	40.90	289.0	no
25.02.1999 18:59:40 – 25.02.1999 22:00:55	35.05	282.1	yes
24.02.1999 18:44:53 – 24.02.1999 22:52:11	39.25	297.3	yes
21.02.1999 19:00:52 – 21.02.1999 22:40:23	55.30	288.8	no
20.01.1999 04:53:34 – 20.01.1999 07:21:03	59.65	291.7	no
19.01.1999 17:10:32 – 19.01.1999 21:24:09	56.05	285.5	no
12.01.1999 18:07:58 – 12.01.1999 21:59:52	55.00	300.7	no
11.01.1999 19:01:14 – 11.01.1999 21:16:05	57.25	295.0	no
24.02.1998 02:23:22 – 24.02.1998 05:36:09	53.50	288.3	no
03.02.1998 20:11:05 – 03.02.1998 23:16:34	41.35	320.6	no
03.02.1998 14:34:14 – 03.02.1998 16:50:58	41.20	323.5	no
01.02.1998 23:56:00 – 02.02.1998 02:27:37	45.40	276.9	no
19.01.1998 19:39:19 – 19.01.1998 23:29:02	56.20	286.1	no
31.12.1997 14:32:42 – 31.12.1997 17:42:46	44.95	271.1	no
28.12.1997 14:02:16 – 28.12.1997 19:25:03	44.20	289.3	no
28.11.1997 15:55:23 – 28.11.1997 17:59:59	54.85	287.2	no
17.02.1997 16:09:07 – 18.02.1997 05:55:32	51.10	304.1	no
14.02.1997 16:08:53 – 15.02.1997 06:21:52	56.35	299.4	no
19.01.1997 14:18:32 – 19.01.1997 22:12:40	46.00	293.0	no
19.01.1997 01:34:05 – 19.01.1997 07:03:04	45.85	298.7	no
16.01.1997 16:59:23 – 17.01.1997 02:27:24	54.70	308.7	no

Table A.6: List of SSW events identified in the nightly-mean temperature profiles of the RMR lidar above ALOMAR. See Sec. 5.1 for details. ECMWF (ERA40 or operational model) data were used to identify major SSWs.

A.5 Lists of mesospheric inversion layers

Tab. A.7 lists all MILs found in the nightly-mean RMR lidar profiles based on the detection algorithm described in Sec. 5.2.1. All MILs found in the FS profiles are listed in Tab. A.8.

Measurement duration [UT]	MIL altitude range [km]	MIL amplitude [K]
24.01.2005 16:34:14 – 24.01.2005 18:30:53	66.51 – 72.15	24.18
24.01.2005 17:57:49 – 24.01.2005 18:27:33	49.88 – 52.27	10.65
24.01.2005 17:57:49 – 24.01.2005 18:27:33	64.54 – 68.48	20.30
24.01.2005 17:57:49 – 24.01.2005 18:27:33	71.73 – 74.54	11.45
18.01.2005 20:54:43 – 19.01.2005 00:11:23	46.15 – 50.95	15.53
18.01.2005 20:54:43 – 19.01.2005 00:11:23	71.35 – 76.30	16.00
18.01.2005 20:50:16 – 19.01.2005 00:11:23	45.70 – 50.80	16.29
18.01.2005 20:50:16 – 19.01.2005 00:11:23	71.20 – 75.70	15.50
15.01.2005 17:35:11 – 15.01.2005 21:56:18	66.25 – 70.15	19.32
10.01.2005 03:13:47 – 10.01.2005 07:51:49	77.50 – 81.40	10.50
08.12.2004 18:21:44 – 08.12.2004 21:44:26	73.42 – 80.46	29.93
02.12.2004 16:17:57 – 02.12.2004 18:37:53	75.55 – 79.15	10.76
16.10.2004 21:08:34 – 16.10.2004 23:01:53	60.55 – 65.05	12.61
04.01.2004 11:49:38 – 04.01.2004 15:28:35	65.80 – 69.25	14.22
26.11.2003 16:30:29 – 26.11.2003 19:42:09	68.35 – 72.55	10.16
21.11.2003 20:41:08 – 22.11.2003 09:03:38	69.25 – 74.05	14.30
20.02.2003 23:22:34 – 21.02.2003 00:28:32	63.85 – 66.40	11.27
27.01.2003 18:15:35 – 27.01.2003 20:59:28	49.45 – 54.67	19.11
27.01.2003 18:15:35 – 27.01.2003 20:59:28	57.35 – 59.74	14.81
27.01.2003 15:04:56 – 27.01.2003 21:02:15	49.03 – 54.81	21.48
07.12.2002 13:18:27 – 07.12.2002 20:48:35	58.30 – 61.75	10.34
15.11.2002 15:56:20 – 15.11.2002 19:41:38	61.90 – 66.40	14.99
11.11.2002 16:18:51 – 11.11.2002 21:27:17	70.45 – 78.10	28.52
12.03.2002 17:03:54 – 12.03.2002 20:56:51	78.40 – 80.65	10.40
10.02.2002 16:33:24 – 10.02.2002 19:58:58	70.00 – 73.60	18.22
05.02.2002 01:23:58 – 05.02.2002 06:19:51	78.25 – 80.95	11.36
25.01.2002 14:40:57 – 25.01.2002 18:20:44	62.35 – 65.65	15.01
17.01.2002 22:14:08 – 18.01.2002 03:15:23	66.65 – 71.98	10.48
14.01.2002 20:51:22 – 14.01.2002 23:18:35	70.30 – 74.35	22.37
25.02.2001 18:49:18 – 26.02.2001 04:14:13	78.55 – 83.80	16.42
02.02.2001 17:18:38 – 03.02.2001 04:58:41	76.45 – 85.15	13.58
31.01.2001 17:08:14 – 01.02.2001 05:01:56	80.35 – 85.15	10.61
09.01.2001 19:40:20 – 09.01.2001 22:20:29	65.05 – 68.20	12.05
20.12.2000 16:05:30 – 20.12.2000 20:24:10	62.95 – 73.60	18.19
20.12.2000 16:05:30 – 20.12.2000 20:24:10	78.10 – 80.95	12.00
13.12.2000 17:04:44 – 13.12.2000 21:51:43	78.70 – 81.85	15.05
12.12.2000 18:15:30 – 12.12.2000 20:38:11	74.20 – 78.10	18.77
10.12.2000 18:04:14 – 10.12.2000 22:14:14	71.05 – 77.65	12.26
10.12.2000 18:04:14 – 10.12.2000 22:14:14	78.25 – 83.05	16.60
20.11.2000 19:30:04 – 20.11.2000 23:06:14	68.05 – 72.55	12.89
19.11.2000 19:16:00 – 19.11.2000 22:05:50	72.70 – 76.00	10.58
29.10.2000 20:16:26 – 29.10.2000 23:20:10	78.25 – 80.50	10.12
28.12.1997 14:02:16 – 28.12.1997 19:25:03	67.60 – 71.50	13.78
20.11.1997 15:32:41 – 20.11.1997 20:48:21	59.05 – 65.50	11.59
15.10.1997 17:08:27 – 15.10.1997 19:55:56	66.10 – 68.95	16.94

Table A.7: List of MILs identified in the nightly-mean temperature profiles of the RMR lidar above ALOMAR. See Sec. 5.2.1 for details.

Launch time [UT]	MIL altitude range [km]	MIL amplitude [K]
25.01.2005 07:30:00	41.00 – 44.00	10.97
25.01.2005 07:30:00	53.00 – 56.40	24.16
25.01.2005 05:30:00	56.60 – 60.20	16.36
25.01.2005 05:30:00	67.80 – 77.40	16.41
25.01.2005 03:30:00	73.00 – 79.00	10.09
25.01.2005 01:30:00	65.80 – 69.60	13.89
20.01.2005 12:19:00	66.60 – 70.80	14.81
20.01.2005 12:19:00	74.60 – 84.40	27.38
20.01.2005 11:30:00	66.80 – 72.00	21.42
20.01.2005 08:46:00	72.60 – 79.80	21.38
18.01.2005 18:35:00	48.40 – 54.60	13.13
18.01.2005 15:31:00	46.20 – 55.80	18.96
18.01.2005 15:31:00	70.60 – 77.00	10.40
18.01.2005 14:42:00	51.40 – 55.80	14.62
18.01.2005 14:42:00	71.40 – 77.80	12.61
18.01.2005 13:15:00	51.00 – 55.80	17.48
18.01.2005 13:15:00	71.60 – 79.80	32.39
18.01.2005 12:36:00	52.60 – 56.00	20.81
18.01.2005 12:36:00	71.60 – 80.00	17.57
30.09.2002 23:05:00	77.00 – 88.00	18.53
26.05.1992 14:30:00	52.20 – 58.00	10.87
20.09.1991 23:23:00	54.00 – 57.40	10.20
18.09.1991 01:06:00	79.00 – 90.40	27.82
11.03.1990 21:32:00	71.80 – 78.80	10.79
11.03.1990 20:24:00	52.20 – 54.60	14.61
11.03.1990 19:21:00	68.00 – 70.60	10.69
09.03.1990 20:19:00	68.60 – 73.60	14.25
09.03.1990 00:45:00	58.40 – 61.40	19.01
08.03.1990 22:37:00	61.80 – 68.40	17.73
07.03.1990 19:32:00	51.20 – 57.60	11.33
07.03.1990 19:32:00	67.40 – 70.20	11.40
06.03.1990 03:31:00	53.40 – 55.60	19.55
02.03.1990 19:31:00	60.60 – 63.00	19.68
28.02.1990 21:09:00	52.60 – 56.60	17.94
28.02.1990 21:09:00	68.40 – 72.20	12.19
28.02.1990 21:09:00	78.80 – 82.60	14.79
25.02.1990 20:04:00	65.80 – 72.20	18.29
25.02.1990 19:04:00	56.00 – 58.20	12.04
25.02.1990 19:04:00	70.80 – 75.60	15.04
24.02.1990 20:48:00	66.60 – 70.60	11.52
21.02.1990 20:05:00	56.00 – 59.40	11.73
14.02.1990 20:00:00	44.60 – 50.60	21.73
31.01.1990 20:00:00	70.00 – 77.00	21.82
28.01.1990 20:00:00	53.60 – 56.80	23.92
24.01.1990 20:01:00	67.60 – 70.20	13.90
24.01.1990 20:01:00	76.80 – 84.80	51.03
22.01.1990 11:45:00	54.20 – 57.40	22.96
22.01.1990 11:45:00	79.60 – 85.40	34.31
22.01.1990 09:55:00	78.60 – 83.60	10.91
19.01.1990 20:00:00	69.20 – 74.20	16.68
19.01.1990 20:00:00	79.80 – 85.00	62.06
15.01.1990 20:05:00	48.80 – 51.80	10.81
15.01.1990 20:05:00	58.20 – 60.40	12.97
13.01.1990 21:34:00	74.00 – 82.40	22.63
12.01.1990 21:00:00	79.20 – 82.80	12.56
17.06.1987 11:03:00	57.30 – 60.40	14.10

Table A.8: List of MILs identified in the FS temperature profiles at 69° N. See Sec. 5.2.1 for details.

A.6 Details of the seasonal variation of GWPED

The following three figures complement Figs. 6.8, 6.9 and 6.10 shown in Sec. 6.3 where the seasonal variations of GWPED and temperature deviations were discussed. As an extension to the figures shown in Sec. 6.3, the diagrams shown here include all single data points in addition to the monthly means shown previously.

Fig. A.1 shows the seasonal GWPED variation for different altitude regions between 30 km and 75 km. The diamonds show the values for all 250 measurements where the single years are distinguished by different colours. The number of measurements per month and year is indicated by the coloured bars in the upper part of the diagrams. They show again that the majority of the long measurements which are used in the gravity wave analysis has been obtained during the summer months. The GWPED values of the single measurements range from a few $\mathrm{J\,kg^{-1}}$ up to a few hundred $\mathrm{J\,kg^{-1}}$ with a tendency of increasing GWPED with height which will be investigated in more detail in the next section. The black solid line shows the monthly mean values calculated from all measurements while the black dashed line gives the median for each month. The error bars show the statistical uncertainty of the monthly mean values. The data gap during summer in panels F – H is caused by missing temperature data above 55 km in summer due to the increased solar background during the summer daylight measurements.

Fig. A.2 shows the same analysis as in Fig. A.1 but now restricted to measurements longer than 12 hours. Note the much lower number of measurements, especially in the winter months.

The seasonal variation of the mean absolute temperature deviation (Eq. 6.3) is shown in Fig. A.3. The different years are again distinguished by their colour and the monthly mean and median values are shown by the solid and dotted black lines, respectively. The general form of the seasonal variation of the temperature deviations resembles the seasonal variation of the GWPED.

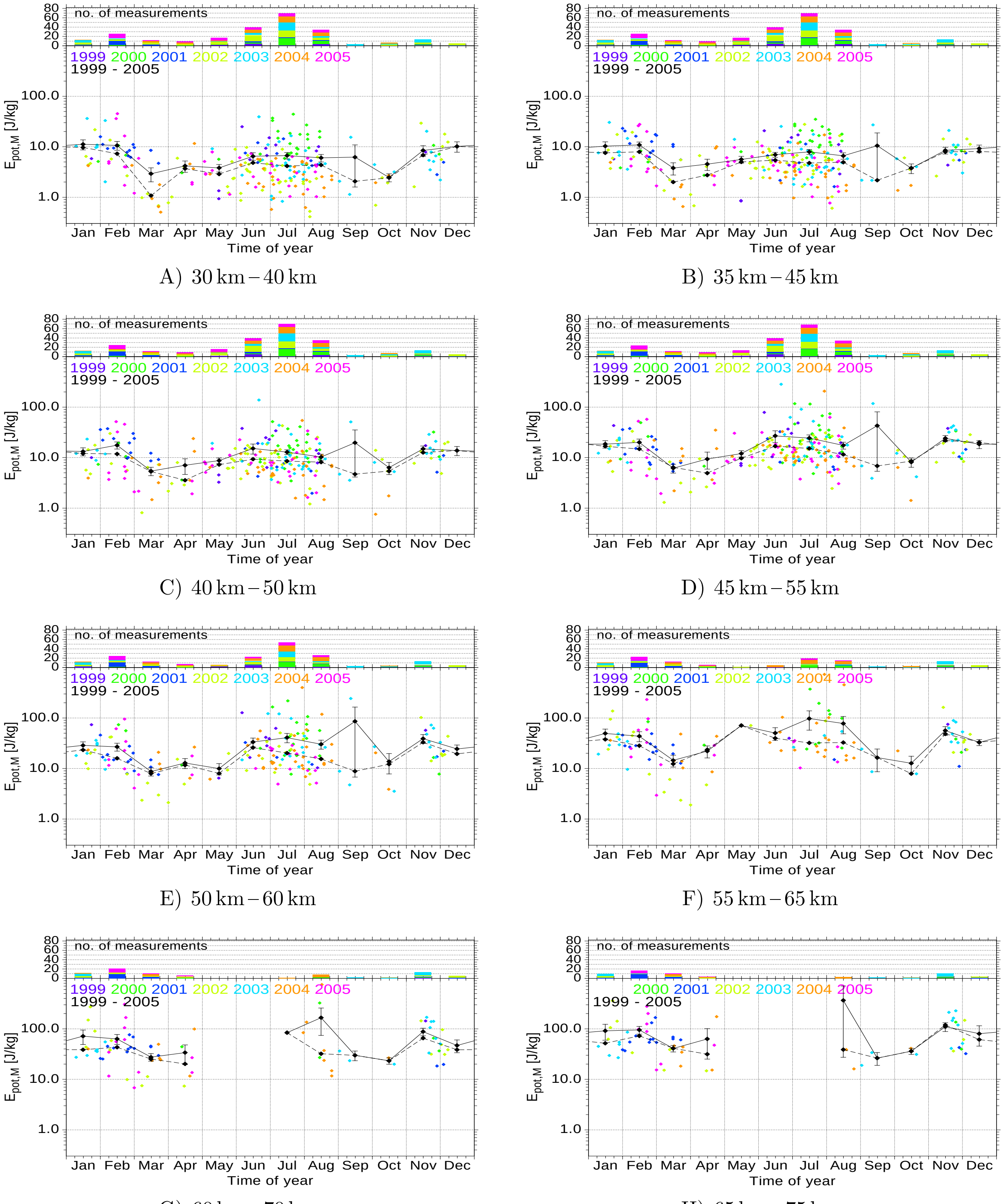

A) 30 km – 40 km
B) 35 km – 45 km
C) 40 km – 50 km
D) 45 km – 55 km
E) 50 km – 60 km
F) 55 km – 65 km
G) 60 km – 70 km
H) 65 km – 75 km

Figure A.1: Seasonal variation of GWPED for different altitude regions. The different years are distinguished by colours. The black solid line gives the monthly mean of all years, the black dashed line the corresponding median. The error bars show the errors of the monthly mean GWPED values. The coloured bars in the upper part of the diagrams give the number of measurements in each month. Above 55 km there is only limited temperature data available during summer due to the high solar background. This causes the data gap in panels F – H.

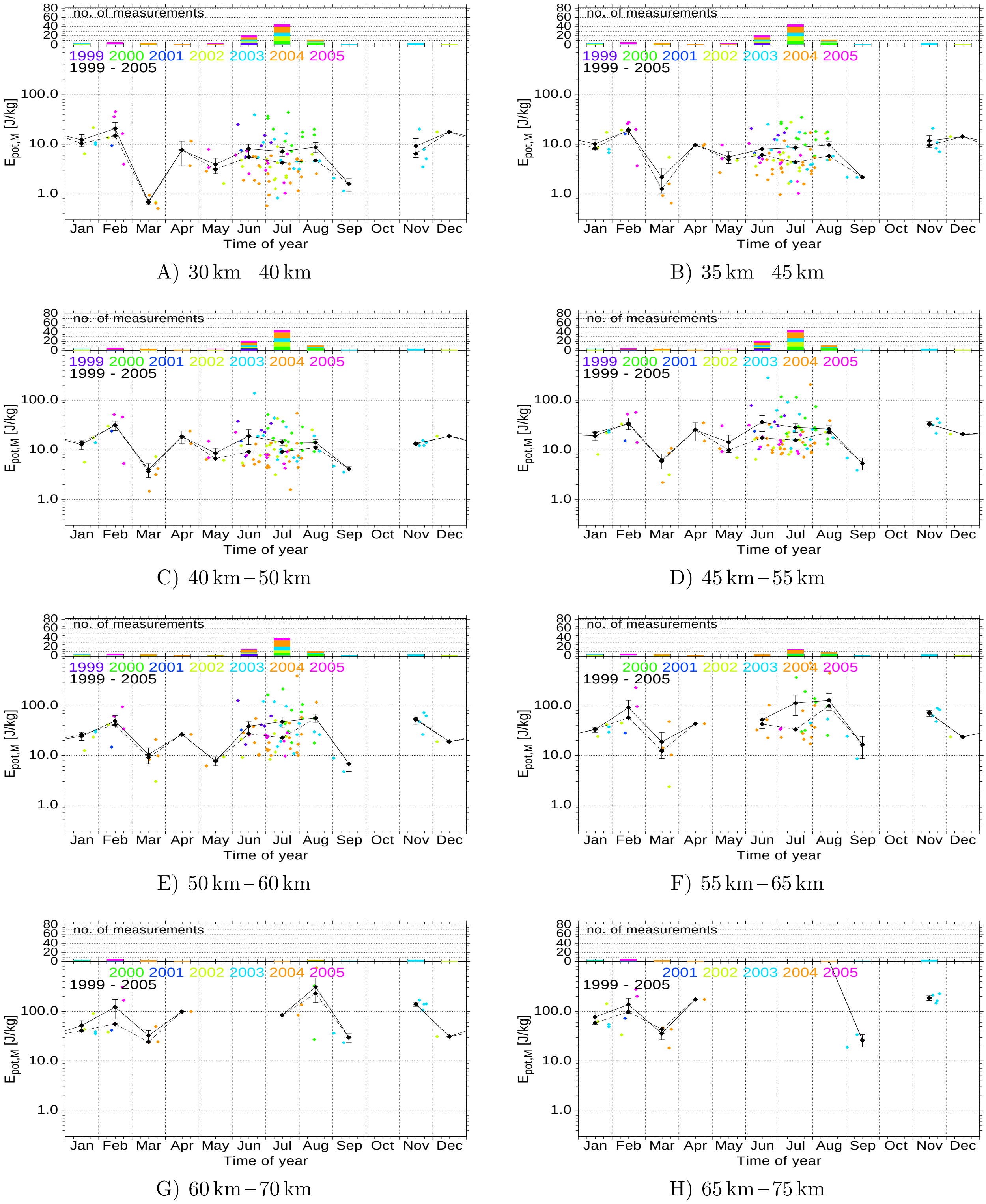

Figure A.2: Same as Fig. 6.8 but using only measurements longer than 12 hours. This leads to much fewer measurements, especially outside the summer months. Nevertheless, the general behaviour of the seasonal variation of GWPED does not change much.

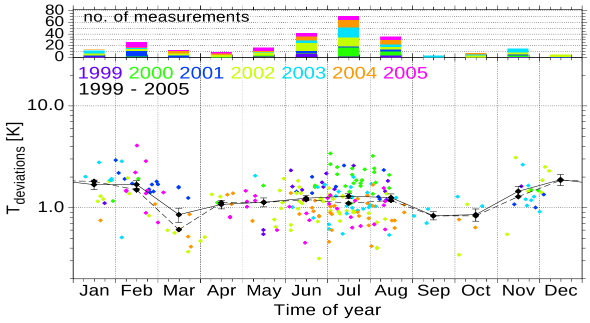

A) 30 km – 40 km

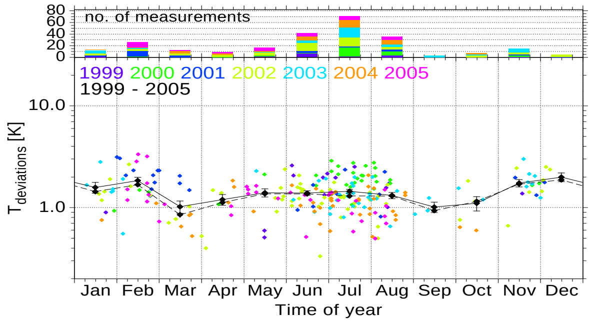

B) 35 km – 45 km

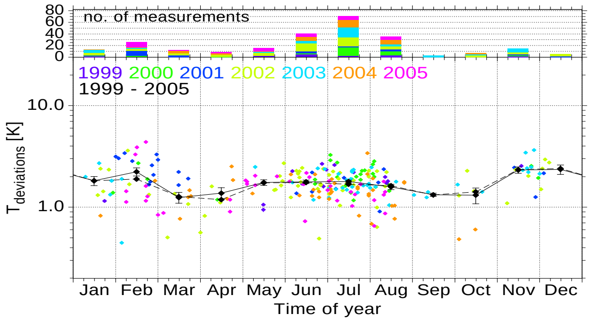

C) 40 km – 50 km

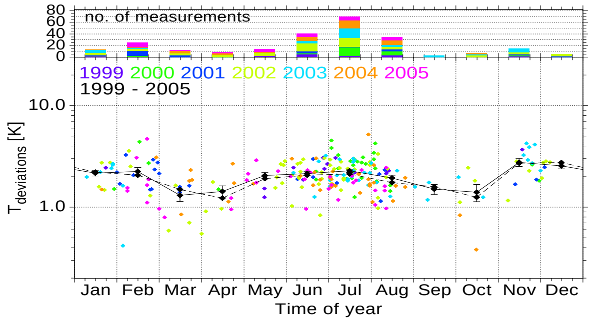

D) 45 km – 55 km

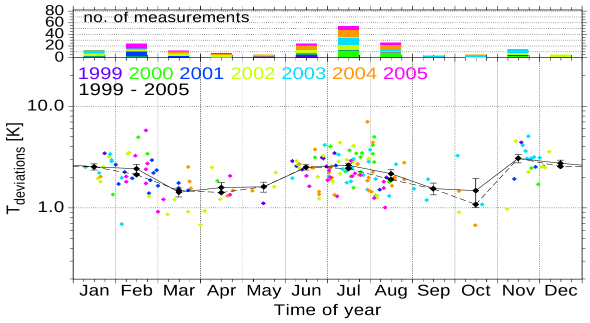

E) 50 km – 60 km

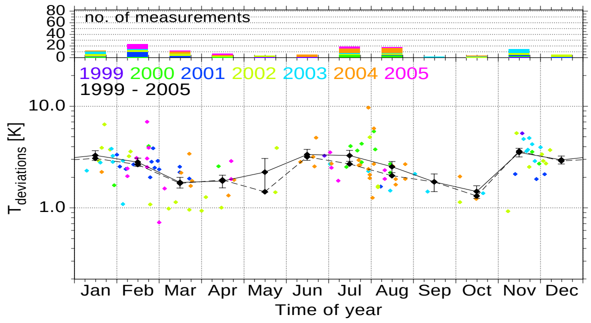

F) 55 km – 65 km

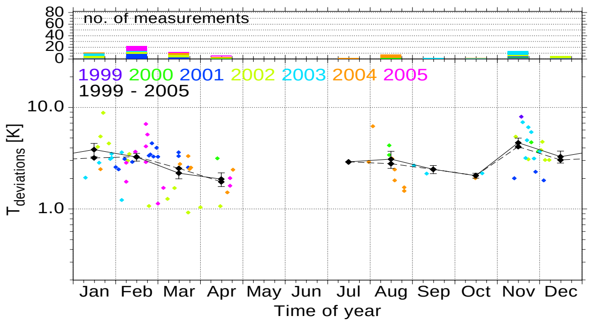

G) 60 km – 70 km

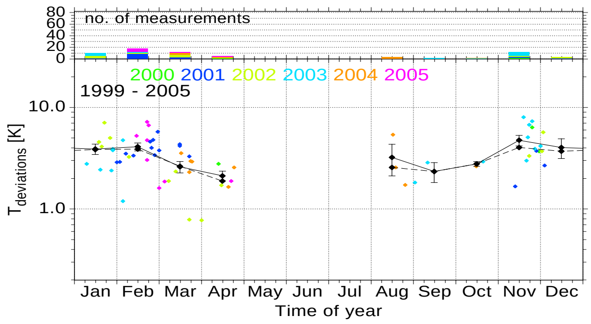

H) 65 km – 75 km

Figure A.3: Same as Fig. 6.8 but for the observed temperature fluctuations (Eq. 6.3).

Appendix B

B.1 Record selection algorithm

The ALOMAR RMR lidar is operated whenever permitted by the weather conditions. This includes times when tropospheric clouds or fog intermittently attenuate or even completely block the lidar signal. While the lidar electronics still record these profiles, they have to be excluded from the temperature calculations. The general strategy in selecting the periods for the summation is to maximise the S/N ratio [*Keckhut et al.*, 2002; *Keckhut*, 1998]. The selection algorithms applied in this thesis are described in the following paragraphs.

The electronic counters connected to the detectors of the RMR lidar sum the received signal over 2000 – 5000 laser pulses (67 s – 167 s) before a raw count rate altitude profile is stored on disk. Such a single profile will be called "record" in the following discussion. Fig. B.1 shows the Rayleigh backscatter signal of four records from the RMR lidar measurement on 5 February 2002 17:54 UT – 04:42 UT. The Rayleigh signal decreases exponentially with altitude due to the exponential decrease of the atmospheric density. The lower end of the records is defined by electronic gating of the detectors, i.e. they are switched off below this height.

The first step is to remove records which obviously have disturbances caused by electronic interference. Although great care has been taken to shield all components of the detection system, occasionally a record shows spikes in single altitude bins or signal bursts over a broader height range which are caused by electronic disturbances. To identify disturbed records, the background altitude range, i.e. the altitude range at the upper end of the profiles where no signal is left, is divided into five subranges and mean and variance are calculated separately for each subrange. When the mean of the subranges differs by more than twice the variance, a disturbed record is detected which then is excluded from all further analysis. As a second step, records which are empty because a low cloud had blocked the laser light are excluded. In the remaining records, the solar background in the 532 nm channels may still vary by as much as five orders of magnitude due to solar elevation changes while the signal may be strongly attenuated when the atmospheric transmission

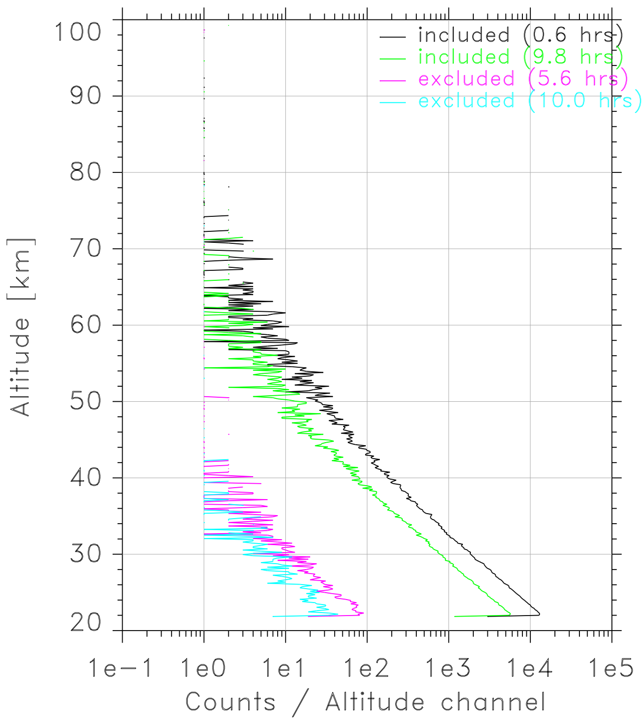

Figure B.1: Raw signal of four records (5000 laser pulses each) from the same channel for the measurement on 05.02.2002 17:54 UT – 04:42 UT. Note the logarithmic x-axis. The times in the legend are relative to the start of the measurement. The black and green records entered the summation whereas the violet and cyan records were excluded (see also Fig. B.2 and text for details).

in the troposphere is low. Therefore the following algorithm is used to select those records which, when summed together, result in the largest S/N ratio:

– The height where the Rayleigh lidar signal disappears into the background noise is determined for each record. This so-called "top altitude" is useful for the record selection since it is large for profiles with strong signal and low background and low when either the background is large or the signal weak.

  The top altitude is determined for each record by comparing the count rate in each altitude bin to the statistical error in this bin. Starting in the region with signal and stepping upwards, the top altitude is defined as the lowermost altitude where the signal is less than twice the error in five consecutive altitude bins.

– Sort all records according to their individual top altitude.

– Select all records with top altitudes that are within 20% of the maximum top altitude. If the minimum top altitude is larger than 95% of the top altitude, select all records. The latter case marks a measurement under stable conditions where no special selection is necessary.

– A second parameter, called "maximum available photons", is calculated by summing the product of the normed count rate at 30 km with the number of shots in the record over all records. The record selection starts at the record with the highest top altitude and continues to lower top altitudes. Each time a record is added, the "available photons" value is calculated again. This is repeated until at least 50% of the "maximum available photons" value is achieved. When this limit is reached, the summation only continues if the top altitude of the records added is still larger than the limit determined in the previous step.

– As a last step, a list of all records that have not passed these criteria is written. This list is used to exclude those records from the summation of the records later during the data processing.

The result of this record selection is shown in Fig. B.2 for the RMR lidar measurement on 5 February 2002 17:54 UT – 04:42 UT. The normalised count rate at 30 km altitude of each record is shown as red diamonds while the top altitude of the records is given by the blue dots. Empty symbols mark records which are excluded from the summation. Obviously, records with either small signal or low top altitude are left out. The objective determination of this selection is achieved through the procedure described above.

B.2 Data processing steps

Once the record selection has been done as described in the previous section, all remaining records inside the integration period are summed together. This section gives a summary of the processing steps applied to this summed lidar raw data profile to convert it into a temperature profile taking into account the different effects described in the lidar equation (Eq. 3.1) and a few other technical effects.

An example of summed RMR lidar count rate profiles at the visible wavelength 532 nm is given in Fig. B.3A for 13/14 February 2005 17:00 UT – 5:00 UT. The integration time corresponds to 1,292,000 laser pulses. The three channels are intensity-cascaded by means of partially reflecting optical beam-splitters dividing the incoming photons onto three detectors. This is necessary because the dynamical range of the lidar signal is too large for a single

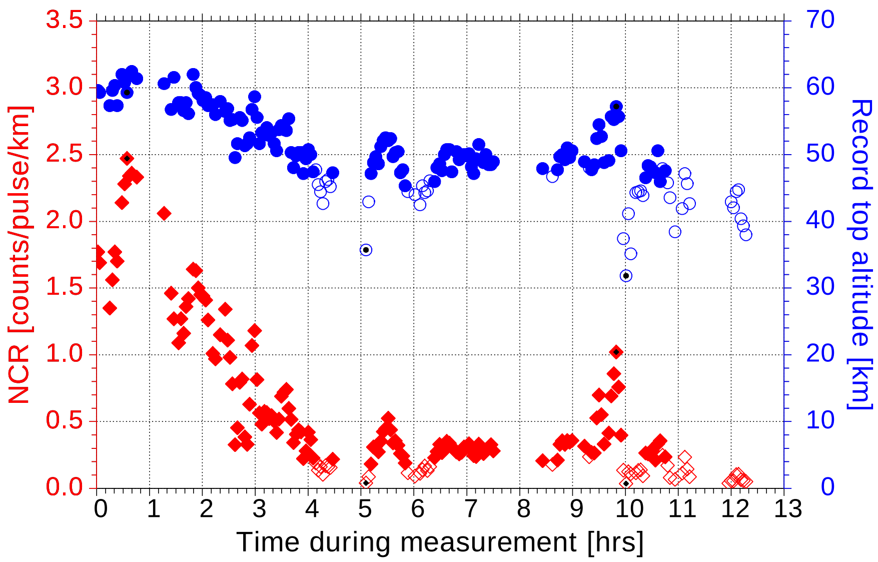

Figure B.2: Example of the record selection based on normed count rate at 30 km (red, left scale) and top altitude (blue, right scale) for the measurement from 05.02.2002 17:54 UT – 04:42 UT. Empty symbols mark records which are excluded from the signal summation (see text for details). The records from Fig. B.1 are marked with black dots.

detector. The channels are marked as "high" (in red), "middle" (in violet) and "low" (in blue) according to the covered altitude range which is determined by the reflectivity of the beam-splitters and the electronic gating of the detectors. For the "middle" channel, electronic noise in the detection system contributes to the count rate profile below 20 km. The constant background at the upper end of the profiles is caused by the atmospheric background due to scattered solar photons, moonlight and air glow as well as electronic noise of the detection system.

To obtain a relative density profile from the lidar count rate profiles, several effects must be taken into account. The magnitudes of the different effects are shown in Fig. B.3B as percent adjustment to the lidar count rate profiles. From Eq. 3.4 it can be seen that this corresponds to a similar change of the derived temperature. Since temperatures during this measurement were between 200 K and 275 K (see Fig. B.4B), an adjustment of e.g. 2% to the lidar count rate profiles corresponds to a change of the derived temperature of 4 K – 5.5 K. Applying the adjustments for the different effects to the lidar raw signal it is important to follow the same order in which they are described here.

Detector dead-time:

The RMR lidar uses photomultipliers and avalanche photo diodes to detect the photons received by the telescopes. Both work in the photon counting mode. These detectors have a limit for the shortest interval between two successive photons that can be detected separately. If the photons arrive at shorter intervals, the second photon is lost and will not be counted. As photon counting is a statistical Poisson process, this happens occasionally even if the signal is much lower than the maximum count rate of the detectors. The counts in each altitude bin are converted to a count frequency $N_{counted}$. The effect of the detector dead-time is then calculated from the dead-time τ of the detector or the corresponding maximum count rate $N_{max} = 1/\tau$ as

$$\frac{1}{1 - \frac{N_{counted}}{N_{max}}} = \frac{1}{1 - \tau N_{counted}} \quad . \tag{B.1}$$

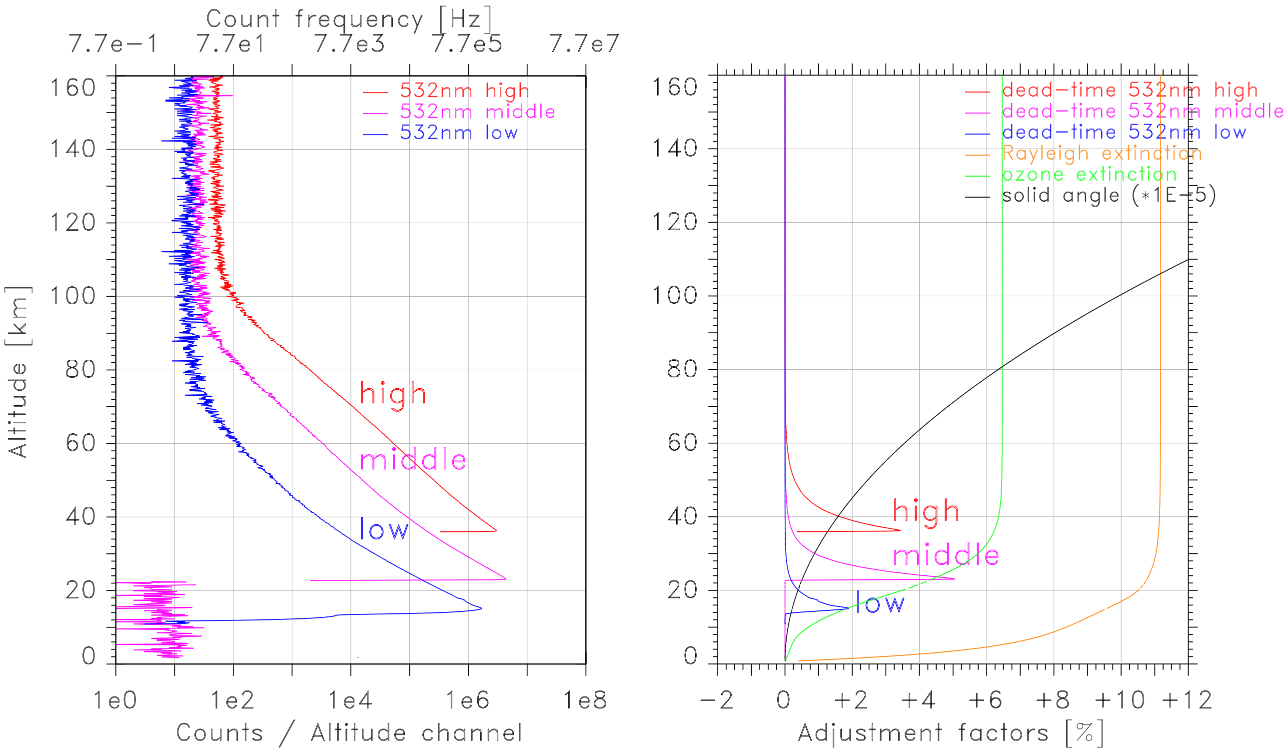

A) Lidar count rate profiles

B) Adjustment factors for different effects vs. height

Figure B.3: *Left panel:* Raw data profiles from the three intensity-cascaded channels at 532 nm after summation for the RMR lidar measurement on 13.02.2005 17 UT − 5 UT (1,292,000 laser pulses). The lower end of the profiles is given by the electronic gating of the detectors. The upper scale gives the equivalent count rate for the detectors. Note the exponential scale on the x-axis. *Right panel:* Adjustment factors for detector dead-time, extinction by air and ozone and the viewing geometry of the lidar (see text for details).

More details about the dead-time compensation can be found in *Hübner* [1998] and *Keckhut et al.* [1993]. For the photomultipliers used in the 532 nm channels, a dead-time of 7 ns is used. As the effect depends on the count rate, it is strongly height dependent and most important at the lower boundary of the channels where their signal is largest (see red, violet and blue lines in Fig. B.3B).

Tilted telescopes:

One of the advantages of the ALOMAR RMR lidar over many other lidar systems is its ability to tilt the telescopes by up to 30° from zenith. Since the altitude bins of the data acquisitioning are defined as constant 1μs bins, the altitude resolution changes from 150 m for vertical measurements to 129.9 m when the telescopes are tilted 30° from zenith. Also the altitude of the lowermost bin is determined by a constant time-lag after the firing of the laser and thus changes when the telescopes are tilted. During data analysis the correct altitude bins are computed from the known tilting angle of the telescopes. Since the optical way also gets longer when the laser light traverses the atmosphere under a slant angle, the signal has to be scaled as well to get the correct normalised count rate that can be compared to vertical measurements.

Rayleigh extinction:

As the laser light propagates upward through the atmosphere, it is continuously attenuated by atmospheric extinction, i.e. photons are scattered out of the laser beam by air molecules. The downward propagating back-scattered light experiences the same fate.

The magnitude of this effect changes with the wavelength of the laser light because the Rayleigh scattering cross-section depends on the wavelength (see Sec. 3.2). It is compensated using a pressure and density profile from the CIRA86 reference atmosphere and the known Rayleigh scattering cross-sections (see *Bakan et al.* [1988, Sec. 7.4]). Above 40 km atmospheric extinction becomes negligible (see orange line in Fig. B.3B).

Ozone extinction:

The ozone layer in the stratosphere also attenuates the lidar signal. For a perfect compensation, a simultaneously measured ozone profile would be necessary. As this is not available for most of the measurements of the RMR lidar, an ozone climatology by *Fortuin and Langematz* [1995] is used to calculate the ozone extinction and compensate for it. The ozone scattering cross-section is taken from *Burrows et al.* [1999]. Above 50 km there is very little ozone so that its extinction of the lidar signal can be neglected (see green line in Fig. B.3B).

Determination of upper end of Rayleigh signal:

Fig. B.3A shows that the exponentially decreasing Rayleigh signal disappears into the background around 105 km, 95 km and 85 km for the “high”, “middle” and “low” channel, respectively. Since only the Rayleigh signal is of interest for the further analysis, this top altitude has to be determined for each channel. In this work, the quality of a polynomial fit to the background is used for this purpose. First the background is smoothed with a median filter over 9 altitude bins and then it is fitted with a square polynomial between 150 km and 250 km altitude. The lower altitude limit is lowered in steps of 5 km until the difference between fitted background and raw signal in this altitude range is getting larger than twice the mean statistical uncertainty in the altitude range 150 km – 250 km. This altitude is taken as the first guess for the upper height limit of the Rayleigh signal. The background is then fitted by a square polynomial between 50 km above the upper height limit of the Rayleigh signal and 250 km altitude and subsequently subtracted from the raw lidar profile.

Now the lowest height is determined where the signal after background subtraction is negative. This height is taken as the new upper height limit of the Rayleigh signal and the background is fitted again with a square polynomial. This procedure is iterated until the calculated upper height limit of the Rayleigh signal converges (up to five times). The upper altitude limit of the Rayleigh signal for the further analyses is then taken to be 10 km below the limit determined from this iteration.

Background subtraction:

The background due to scattered solar photons, air glow, stars and electronic noise of the detection system can be determined at the uppermost heights of the count rate profiles above the maximum altitude of the Rayleigh signal determined in the previous step. In this thesis, the background is determined in the altitude range from 25 km above the Rayleigh signal to 250 km. For ideal detectors, the background should be constant over the entire altitude range. However, under certain circumstances the detectors of the RMR lidar produce a background which is decreasing with altitude. In this case the background has to be approximated by a linear or parabolic fit in the background altitude range. This fit is then used to extrapolate the background over the entire altitude range. To avoid erroneous fits due to statistical outliers, the background is smoothed with a median filter over 25 altitude bins before the fit is applied. Once the background is determined, it is subtracted from the lidar signal. The procedure applied in this thesis to determine the shape of the background for each summed relative density profile is described in the next section.

Solid angle:

This is a pure geometric effect. The solid angle covered by the receiving telescope at the height of the scattering process decreases like the square of the distance between the scatterer and the telescope. Therefore the signal has to be multiplied by the square of the distance between telescope and scatterer to compensate for this geometric effect (see $1/z^2$ term in Eq. 3.1 and black line in Fig. B.3B).

Concatenation of lidar profiles:

After all the above effects have been compensated for, the lidar profiles from the three 532 nm channels are attached to each other to form a continuous profile throughout the middle atmosphere. This is done by calculating a mean scaling factor over 2 km altitude in the overlap region of two channels. Then the two channels are combined using the calculated scaling factor. The RMR lidar has been run in many different configurations in the years 1997 – 2005. Usually there were three intensity-cascaded green channels (as shown in Fig. B.3). However, sometimes only two green channels are available for the temperature calculation. In both cases the result is a relative atmospheric density profile as shown in Fig. B.4A. It is smoothed with a running-average filter over 15 altitude bins ($\widehat{=}$ 2250 m when the telescope points to zenith) to improve the S/N ratio. Due to the exponential decrease of the atmospheric density with height, a simple smoothing with a running-average filter would be dominated by the lower altitude (higher density) bins. Therefore the smoothing is performed after taking the logarithm of the relative density profile. Afterwards the profile is exponentiated again.

Temperature integration:

The smoothed relative density profile is now integrated as described in Sec. 3.3 to yield a temperature profile in the aerosol-free part of the atmosphere above 30 km altitude. The corresponding temperature profile is shown in Fig. B.4B (red line) together with the NRLMSISE00 reference atmosphere from which the start temperature for the integration is taken at 94.8 km. Fig. B.4B includes two additional violet lines which were obtained by varying the start temperature by ± 20 K. This is also the uncertainty assumed for the start temperature in the error propagation (see below). These lines show that the uncertainty introduced by the start temperature decreases rapidly below the start height and has virtually disappeared two scale heights below the start height. Starting the temperature integration five kilometres higher (blue line in Fig. B.4B) gives a slightly different temperature profile because of the different start temperature and the noise of the relative density profile. However, the profiles agree well within the error bars. The determination of the optimal start height depends on the individual relative density profile and is described in detail in the next section. The gray error bars are shown below the height where the statistical error of the red temperature profile drops below 5 K. All temperature profiles in this thesis have been restricted to the altitude range where the statistical error is below 5 K.

Temperature correction in 1998:

A comparison of temperature profiles calculated in 1998 from simultaneous measurements with both telescopes pointing vertically showed that there was a difference between the two telescopes due to different focusing of the telescopes with seemingly

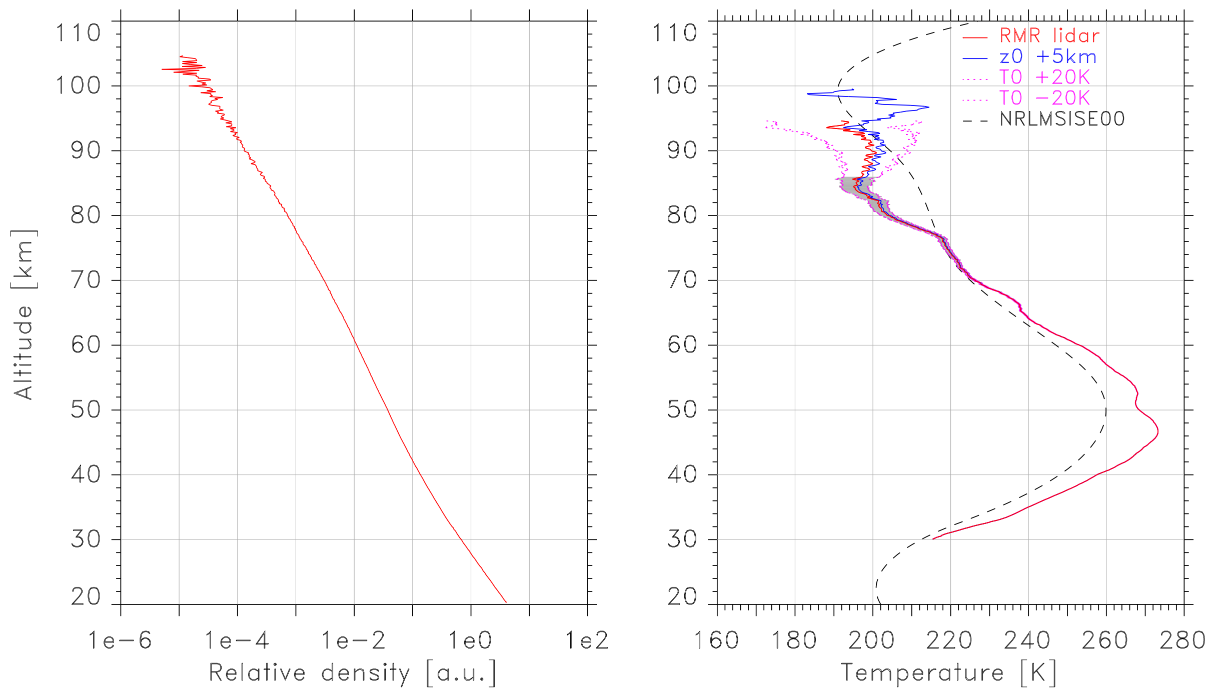

A) Concatenated density profile B) Calculated temperature profile

Figure B.4: Example for the downward temperature integration as described in Sec. 3.3 for the measurement on 13.02.2005 17 UT − 5 UT. *Left panel:* Concatenated relative density profiles (note the exponential scale on the x-axis). *Right panel:* Corresponding temperature profile in red with the start temperature taken from NRLMSISE00 (black dashed line). The violet lines show the resulting temperature profiles when the start temperature is varied by ± 20 K. For the blue line the temperature integration was started 5 km higher. The gray error bars are shown where the statistical error of the red profile drops below 5 K.

lower calculated temperatures in the North-West telescope compared to the South-East telescope. Comparisons with radiosondes showed that the South-East telescope temperatures were correct. Therefore all temperatures measured with the North-West telescope in 1998 are corrected for this offset. The temperature difference changes with height and decreases from 5 K at 30 km to 1 K at 90 km altitude as

$$T_{NWT,\,corr.}(z) = T_{NWT}(z) + (7.0679 - 0.067358z) \quad , \tag{B.2}$$

[*Fiedler*, *priv. comm.*, 2005]. For the measurements after 1998, the focusing was checked regularly to avoid this error in the later years.

Statistical uncertainty:
All error bars given in this thesis show the 1-σ statistical uncertainty. The photon counting in the data acquisitioning of a lidar system is a Poisson process. For a raw data bin with N counts, the statistical uncertainty is $\sqrt{N}$. All subsequent quantities are derived from this raw data signal and the corresponding error bars are calculated from Gaussian error propagation. For a quantity $y(x_1, x_2, \ldots, x_n)$, the statistical uncertainty Δy is calculated from

$$\Delta y^2 = \left(\frac{\partial f}{\partial x_1}\Delta x_1\right)^2 + \left(\frac{\partial f}{\partial x_2}\Delta x_2\right)^2 + \ldots + \left(\frac{\partial f}{\partial x_n}\Delta x_n\right)^2 \quad . \tag{B.3}$$

This formula is applied in all steps of the data analysis described in the previous section to include the statistical uncertainty introduced at every step into the calculated error bars.

Gaussian error propagation is strictly speaking only valid for statistically independent data points. After smoothing or integration, the single data points are no longer fully statistically independent. A strict error calculation would increase the error bars shown in this thesis. This should be kept in mind when comparing measurements and error bars. Systematic errors, as far as they have not been described in this section, are not represented by the error bars shown in this thesis. If present, they would also increase the error bars. A more detailed discussion of statistical errors in lidar measurements has been published by *Liu et al.* [2006].

These are the steps necessary to convert the summed raw count rate profiles from the RMR lidar measurements to temperatures. The next section will discuss in more detail the determination of the background shape and of the start height for the temperature integration.

B.3 Selection of optimal start height

For an ideal lidar instrument, the background is constant with altitude and can be determined at high altitudes where no atmospheric signal is present. However, for real lidar instruments, the background is sometimes distorted and has to be approximated by a linear or parabolic fit over an altitude range without atmospheric signal rather than by a constant. For the RMR lidar data processing in this thesis, the determination of the background shape is combined with the identification of the optimal start height for the temperature integration as described below.

Selecting the optimal start height is important because it involves a trade-off between larger altitude coverage and smaller error. An outlier value of the relative density profile forces the temperature calculation far off the true temperature. Due to the algorithm design, the calculated temperature profile will eventually return to the true temperature but this may take up to two scale heights (see Fig. B.4B). Therefore it is sometimes better to start a few kilometres lower than the upper end of the available relative density profile. As the atmospheric density increases exponentially downwards in the atmosphere, the statistical spread of the relative density profile decreases rapidly when starting a few kilometres lower which diminishes the chance of outliers considerably.

All temperature profiles presented in this thesis are calculated according to the following algorithm which tries to identify the most credible temperature profile from a set of profiles obtained by varying the background shape and the start height of the temperature integration. The background shape is determined either as constant, linear or parabolic fit in the altitude range from 25 km above the upper end of the Rayleigh signal to 250 km. The start height is lowered in steps of 2 km from 1 km above the upper end of the Rayleigh lidar signal determined earlier to 21 km below. A set of such temperature profiles is shown in Fig. B.5 for the RMR lidar measurement on 13 February 2005 17:00 UT – 5:00 UT. Temperature profiles calculated after subtraction of a constant background are shown in blue. Using a linear or parabolic fit as approximation for the background results in the green and orange temperature profiles, respectively.

For each start height temperature profiles are calculated assuming a constant, a linear and a parabolic background and are then restricted to altitudes where the statistical uncertainty is smaller than 5 K. If any of the three temperature integrations failed, the algorithm proceeds to the next start height. Otherwise the standard deviation of the three temperature profiles is calculated for each altitude bin in a common height range of 10 km at the upper end of the temperature profiles. Then the mean standard deviation is determined from the 10 km altitude range. This mean standard deviation is used as a measure for the quality of the calculated temperature profiles. If the different background shapes yield strongly deviating temperature profiles, the mean standard deviation is large and the start height is not suitable for an unambiguous determination of the true temperature profile.

As the influence of the background shape on the relative density signal after background subtraction decreases with decreasing height, the mean standard deviation of the temperature profiles calculated for the different background shapes decreases as the start height is lowered. After calculating the mean standard deviation for all start heights, they are therefore used to find the most credible temperature profile. First the median of the mean standard deviations is calculated. Then the uppermost start height is determined for which the mean standard deviation is smaller than two times the median of the mean standard deviations. For this start height the influence of the different background shapes is small, i.e. all three background shapes yield a similar temperature profile. The temperature profile calculated using a constant background and the selected start height is therefore identified as the most credible temperature profile (see red line in Fig. B.5).

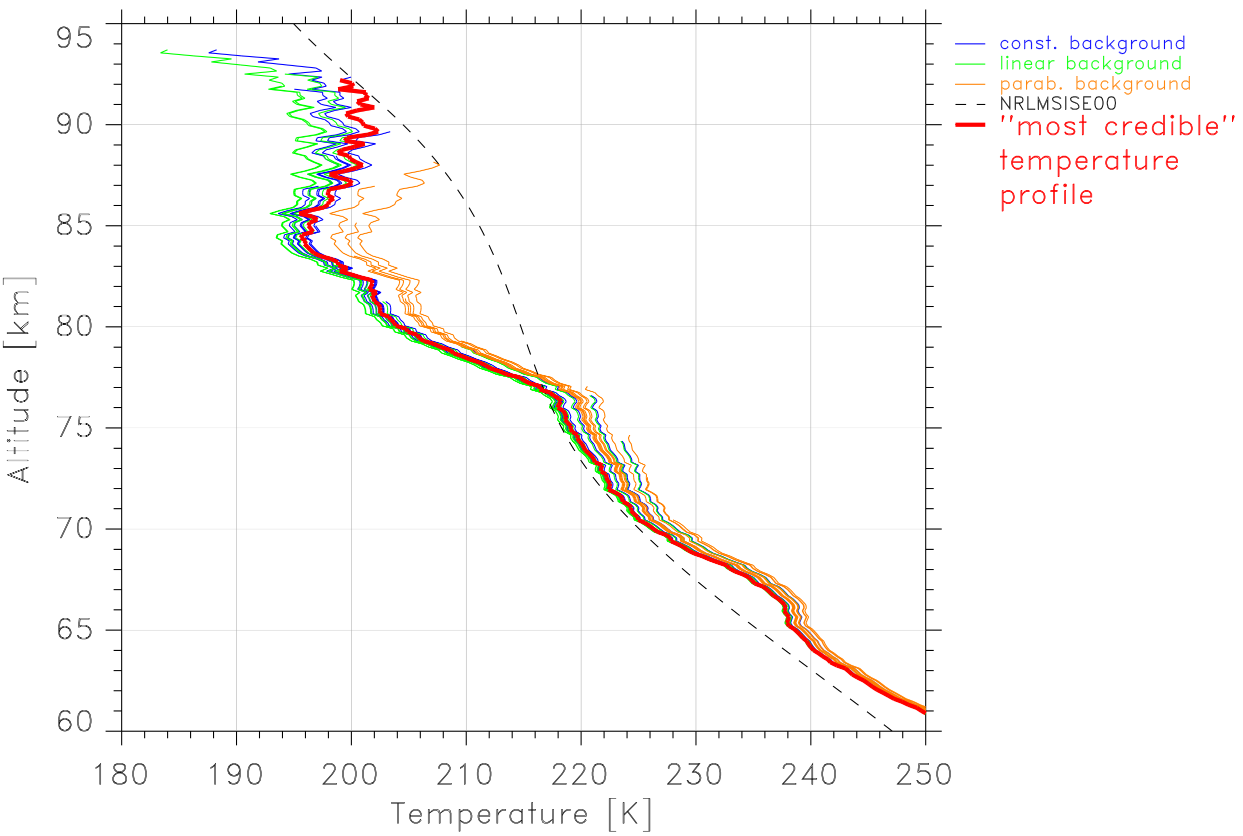

Figure B.5: Set of temperature profiles for the measurement on 13.02.2005 17 UT – 5 UT for three background shapes (blue, green and orange) and twelve different start heights. The red profile is the selected most credible temperature profile (see text for details)

B.4 Spectral ranges for different gravity wave observational techniques

Tab. B.1 below lists the spectral regions of gravity waves observed by different instruments and techniques. It lists the altitude range of each instrument or technique and the vertical wavelengths, horizontal wavelengths and observed periods of the measured gravity waves. These numbers have been used to create Fig. 6.1 and are discussed in Sec. 6.1. The italic numbers have been estimated from the dispersion relation for mid-frequency gravity waves as explained in the caption of Tab. B.1. This is necessary because for most instruments, only two of the three parameters listed below is directly determined by the applied measurement technique.

Instrument	**Altitude range** [km]	**Vertical wavelength** [km]	**Horizontal wavelength** [km]	**Wave period** [min]	**References**
ALOMAR RMR lidar	30 – 80	1 – 25	*10 – 7.500*	60 – 1200	*this work*
IAP RMR lidar	1 – 105	1 – 50	*10 – 7.500*	60 – 750	*Rauthe et al.* [2006]
lidar	30 – 80 and 80 – 110	1 – 20	10 – 6.000	60 – 1500	*Gardner and Taylor* [1998]
meteorological rockets	40 – 80	2 – 20	>200	*>60*	*Hirota and Niki* [1985]; *Alexander* [1998]
radiosondes	0 – 30	0,1 – 8	>200	*>120*	*Vincent and Alexander* [2000]
radar	0 – 20 or 60 – 90	1 – 20	10 – 6.000	60 – 1500	*Gardner and Taylor* [1998]
SABER	20 – 100	5 – 30	>100	*>15*	*Krebsbach and Preusse* [2007]
airglow imager	≈ 83 – 95	10 – 100	1 – 600	5 – 300	*Gardner and Taylor* [1998]

Table B.1: Comparison of the ranges of horizontal wavelength, vertical wavelength and periods of gravity waves measured with different instruments. The italic values were estimated from Eq. 2.19 assuming no wind as $\omega = \frac{\lambda_z}{\lambda_x} N$ with a Brunt-Väisälä period of 5 min. The data listed here is shown in Fig. 6.1 in Sec. 6.1.

Appendix C

This appendix contains an overview of the technical improvements of the ALOMAR RMR lidar that were implemented during the time of this thesis and where the author had been involved in.

C.1 Improvement of the automatic beam stabilisation system

The total overlap of laser beam and telescope FOV at all times is essential for the derivation of temperatures from the Rayleigh lidar signal through integration as described in Sec. 3.3. The automatic beam stabilisation system first described by *Hübner* [1994] and later improved by *Wagner* [2000] has been upgraded during this thesis and the software has been rewritten to allow for faster corrections to the laser beam position. The new beam stabilisation system allows for very stable measurements even in marginal weather conditions when clouds drift through the FOV. The system reaches a precision better than 10 μrad as will be shown here. This makes it possible to decrease the FOV, thus decreasing the solar background and thereby increasing the instrument sensitivity under sunlit conditions. The system is described in this section and some results are shown from simulations of the effect of incomplete focusing in the near-field of the telescopes which limits the reduction of the FOV that is feasible without limiting the usable height range of the instrument.

The FOV of the RMR lidar telescopes is 180 μrad (which corresponds to 18 m at 100 km height). The power lasers have a divergence of less than 100 μrad (i.e. 10 m at 100 km height) [*Fiedler and von Cossart*, 1999] after expanding the beam to a diameter of 20 cm. Each laser beam is guided by three beam guiding mirrors (BGMs) from the laser room to the top of the telescopes to transmit the beam coaxially to the viewing direction for all tilting angles of the telescopes as illustrated in Fig. C.1.

Changing temperature conditions during the measurements in the telescope hall e.g. due to a change of the weather conditions or varying solar position lead to changes in the beam pointing relative to the required stability given by the difference of FOV and beam divergence of only

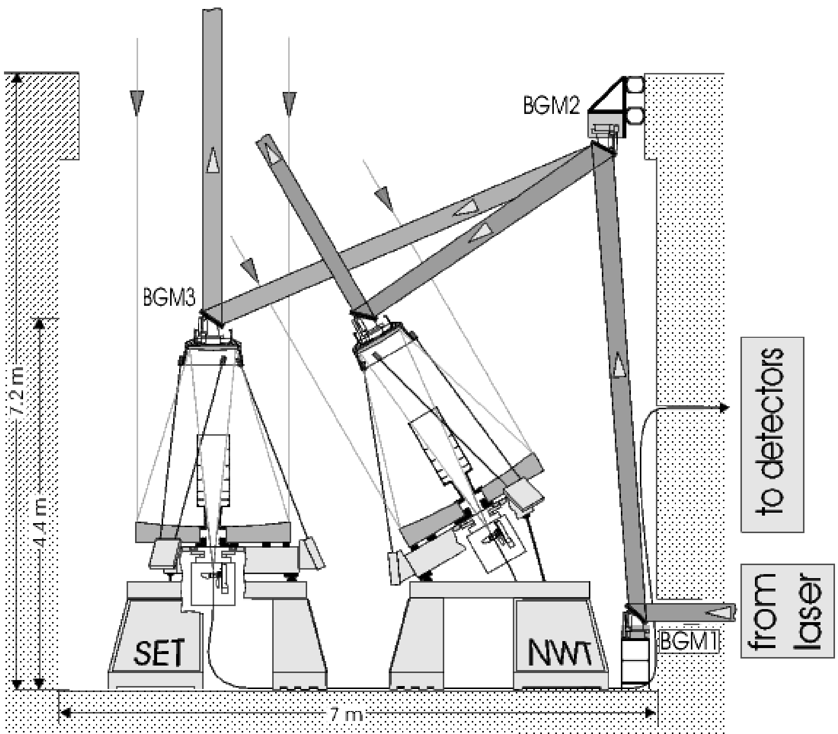

Figure C.1: The laser beams are guided each by three beam guiding mirrors (BGMs) from the laser room to the telescopes to transmit the laser beams coaxially to the viewing direction of the telescope (Fig. from [*Baumgarten*, 2001]).

about 80 μrad (8 m at 100 km height). Figure C.2 shows the change of the beam pointing during two days in 1998 in the upper part and the temperature change in the lower part. During these two days, a thermal deformation of the transceivers was corrected by the beam stabilisation system. Roughly 100 μrad per centigrade temperature change had to be corrected.

A large telescope with a focal length of 8345 mm as used for the RMR lidar is subject to certain restrictions in the focusing because the lower part of the measurement height range of 15 km to 100 km still lies in the near-field of the telescopes. This implies that the echo of the laser beam at the image plane defined by the position of the collecting fibre is blurred due to defocusing. The range of full overlap is optimised by varying the position of the fibre leading to the detectors with respect to the focal point of the telescope. The effect grows larger as the FOV of the receiving system decreases (see *Baumgarten* [2001] for details). As the overlap gets incomplete due to defocusing, also the derived temperatures deviate from the true temperatures. The resulting overlap functions for two different laser divergences are shown in Fig. C.3 together with the impact on the derived temperatures. Tests with both laser systems have shown the laser divergence to be less than 100 μrad.

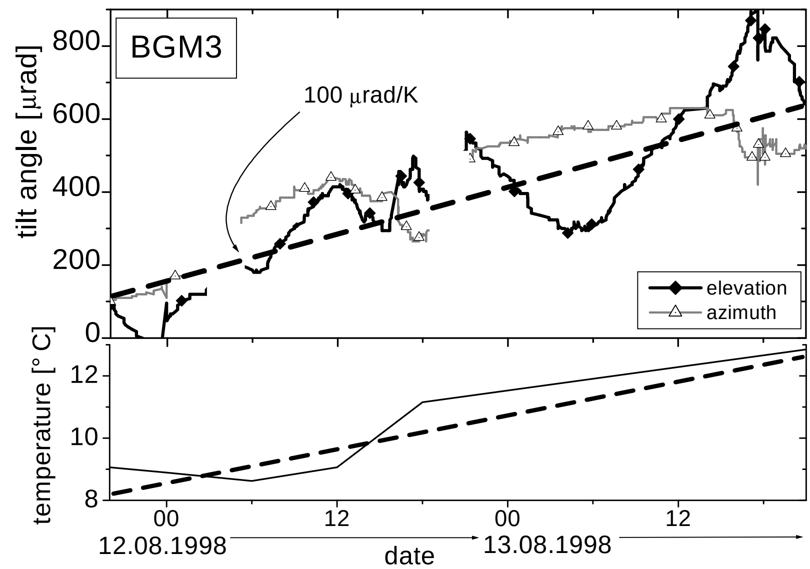

Figure C.2: Change of the optimal position of the BGM3 mirror as a function of the temperature in the telescope hall [*Baumgarten*, 2001].

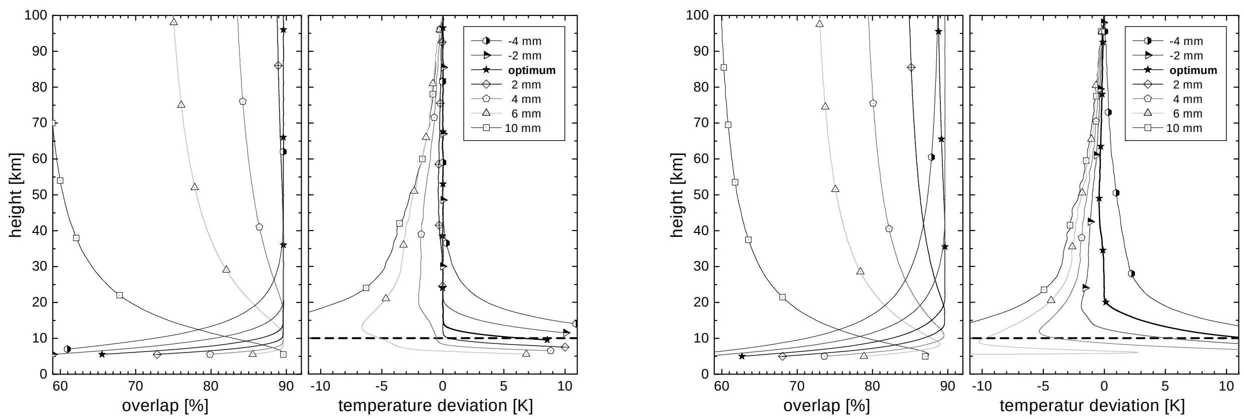

A) 100 μrad divergence B) 150 μrad divergence

Figure C.3: Effect of the defocusing of the telescopes for different values of the laser divergence and different fibre positions in the focal point relative to the optimum position (Δf>0: focused to the near-field, Δf<0: focused to the far-field). *Left:* Overlap (10 % of the primary mirror area is covered by the secondary mirror). *Right:* Temperature deviation induced by altitude dependent vignetting of the molecular Rayleigh backscatter (adapted from *Baumgarten* [2001]).

Laser beams (after beam widening)	
beam diameter	200mm
beam divergence	$< 100\,\mu$rad
pulse rate	30 Hz
Telescopes (Cassegrain design)	
diameter primary mirror	1.8 m
focal length	8345 mm
field-of-view (FOV)	$180\,\mu$rad
off-zenith tilt angle	$\leq 30°$
azimuth range	$2\times\ 90°$
BSS camera	
resolution	768 x 576 monochrome
exposure time	$2\,\mu$sec
exposure delay	$6\,\mu$sec
acquisition rate	30 Hz
BGM3 mirror mount	
two motorised axis (azimuth, elevation)	
resolution	$\approx 10\,\mu$rad

Table C.1: Specifications of the transceiver and the beam stabilisation system.

The FOV and thus the background noise level from scattered sunlight is determined by the diameter of the fibre used to guide the light from the focal point of the telescopes to the detectors. By choosing a smaller fibre, the FOV – and hence the background noise – is decreased. A lower background level enhances the sensitivity of the lidar system which is especially helpful in summer to improve the measurements of noctilucent clouds in the mesopause region. But when the FOV of the receiving system is decreased, a more stable pointing of the laser beam is needed to still ensure full overlap at all heights. This improvement of the pointing stability is achieved with the automated BSS.

The technical parameters important for the BSS are described in Tab. C.1. The technical realisation is sketched in Fig. C.4. A pick-off mirror in the focal box guides defocused light from the first few kilometres onto a camera. The image taken by this camera is digitised by a frame-grabber and an image processing programme is analysing

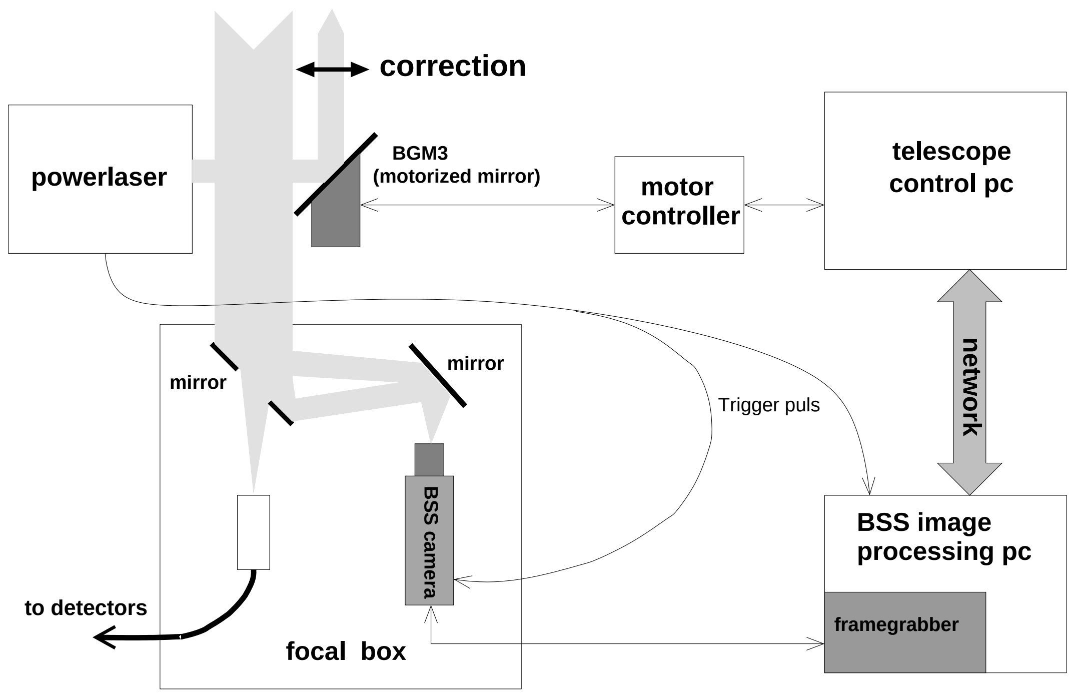

Figure C.4: Schematic drawing of the beam stabilisation system. The control loop consists of the passive analyser part (BSS camera, BSS image processing pc) and the active control of the beam direction with the motorised mirror BGM3 [*Schöch and Baumgarten*, 2003].

the images to find the position of the laser beam on the CCD chip. This information is transmitted to the telescope control computer using the local network. The telescope control computer analyses the messages to identify useful beam spot positions that are not compromised by Mie scatter from clouds. This step is very important to avoid that multiple scattering by inhomogeneous low altitude clouds leads to wrong corrections. Once a position is classified as good, a number of them are averaged and the averaged position is compared to a target position determined during the alignment of the telescope structure. This averaging procedure smoothes over short-periodic jitter of the laser beam direction due to atmospheric seeing. The computed difference is then translated into steps for the mirror motors and the uppermost BGM3 is moved (thereby closing the control loop).

The existing BSS [*Wagner*, 2000] was upgraded with new hardware and software to speed up the control loop allowing to compensate for beam fluctuations on shorter time scales. The new system installed in January 2003 now is capable of capturing and analysing the images at the full 30 Hz repetition rate of the lasers. Together with minor changes of the algorithm for the image processing, this improved the performance of the BSS considerably.

While testing the improved system, it turned out that the parameters of the control loop (like number of averaged positions, limits for detecting bad positions and a proportionality factor for the size of the correction applied to the BGM3 motor axis) have to be carefully adjusted to avoid resonances of the control loop. This is especially important during measurements with marginal weather conditions, i.d. broken clouds, cirrus bands or when fog patches drift through the beam.

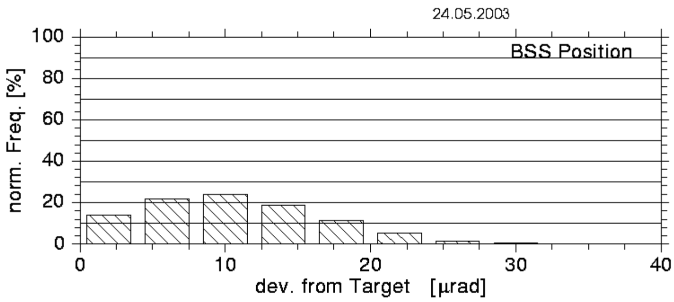

Figure C.5: Histogram of the deviations from the optimum target position. The BSS reaches a mean deviation of 10 μrad which makes it possible to decrease the FOV during summer from 180 μrad to 120 μrad to gain instrument sensitivity for noctilucent cloud measurements.

The performance of the BSS is analysed automatically after each measurement run and archived on a web-server to allow for easy inspection and control of the performance of the BSS. The parameter that best describes the quality of the BSS is the mean deviation from the target position. A histogram of the deviations from the target is shown in Fig. C.5. It shows a mean deviation of less than 10 μrad corresponding to a mean deviation of the beam at 100 km height of less than 1 m. Considering the mechanical resolution of the BGM3 mirror drive of around 10 μrad, a perfect control loop with immediate response would achieve a mean deviation of not less than 5 μrad. So the performance of the upgraded BSS is very close to its theoretical limits.

Simulations have shown that this stability of the beam direction makes it possible to decrease the FOV from the current 180 μrad to 120 μrad by changing from a 1.5 mm fibre to a 1 mm fibre without loosing much signal due to defocusing in the near-field of the telescope. Such a reduction of the FOV results in a lower background caused by scatter sunlight under sunlit conditions and thus increases the sensitivity of the system considerably under daylight conditions. While helping to extend the usable range for temperature measurements, this increased sensitivity is especially useful for detecting weak noctilucent clouds and to improve the ability of the RMR lidar for multi-wavelength measurements of these clouds.

C.2 New software development

When the RMR lidar was installed in 1994, the electronic counters were connected to a Hewlett-Packard workstation running HP-UX. A graphical user interface based on the Unix X-server system was programmed to allow the lidar operators to configure the settings of the detector system and to start and end the data acquisitioning. With a few smaller updates in the first years of operation, this software remained basically unchanged until 2003. After some hardware failure due to ageing, it was decided to replace the workstation with a Windows-based PC. At the same time it became necessary to replace the software and improve the user interface and the flexibility for the measurement configurations. The discussions about the design and the requirements of the new software started in July 2002. The development of the new software was done by our colleagues at SA/CNRS Jean-Pierre Marcovici and André Jean Vieau since SA/CNRS originally built the counting electronics and has experience with the hardware. A first outline of the new software was demonstrated at the annual RMR lidar team meeting in Norderstedt/Germany, in March 2003. In November 2003 the new software was installed and tested at ALOMAR. It performed well and has made the operations of the RMR lidar both easier and more flexible. The author has been heavily involved in the discussion around the specifications of the new software and in the installation and testing at ALOMAR.

The new software is written in MS Visual C++. A major improvement has been the introduction of a client-server concept for the software where the server is managing the hardware and the data storage while the clients are used to interact with the operator for the configuration and control of the measurements and the display of the raw lidar profiles. Only one client can control the measurement, but many clients can connect and display the raw data. The communication of server and client is network-based and can be accessed from every PC connected to the internet. This facilitates testing and trouble-shooting of the RMR lidar system. The new software's client-server concept also is a prerequisite for the development of the "super-controller" which is described below.

The new software also has a network-based access to the raw data read from the counting electronics. This has been used by the author of this thesis to implement a small additional program which displays time-series of signal strength with the highest possible temporal resolution. Such a tools is very useful for adjustment purposes of the optical bench and the detectors.

The RMR lidar instrument consists of three sub-systems: the emitting power lasers and the seeder laser (LAS), the receiving telescopes (TEL) and the detectors and counters for the data acquisitioning (DAS). This structure is schematically shown in Fig. C.6. The communication between the sub-systems in this setup (denoted by the blue arrows) is restricted to the exchange of status information. While starting and running the measurements, the operator has to control all three sub-systems separately. During routine measurements, this can be easily handled by one operator.

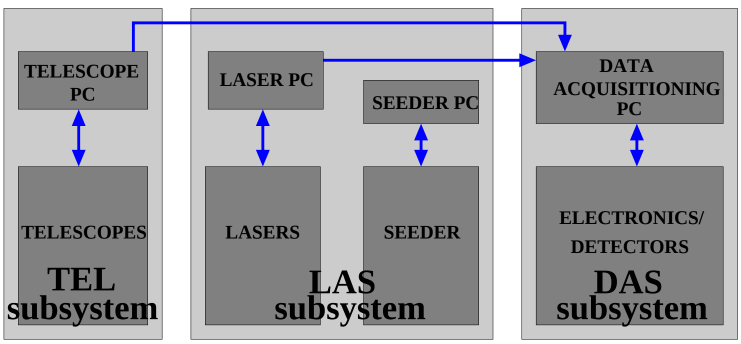

Figure C.6: Configuration of the system before the introduction of the super-controller. The light gray boxes show the three sub-systems of the RMR lidar. The arrows indicate the communication channels between the sub-systems.

However, for various tests and instrument checks which need to be performed occasionally, repeated interaction with all three sub-systems is required. Even for a quick scan of the polarising cube in the focal box or of the FOV of the telescopes, this becomes a tedious and time-consuming procedure. Therefore the need for a super-controller was recognised which is able to interact and control all sub-systems as shown in Fig. C.7. It gets status information from the sub-systems and sends commands to control them. A simple script language is used to define the tasks for the super-controller. These scripts can include commands to set parameters for the data acquisitioning, to control all motors and functions of the telescopes, to start or stop the emission by the lasers and to start or stop the data recording.

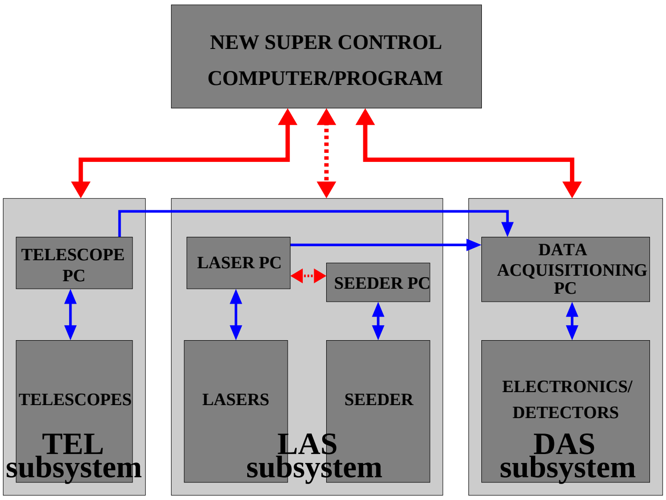

Figure C.7: Configuration of the system after the introduction of the super-controller. The red arrows indicate the new communication channels between the sub-systems and the super-controller

```
DAS SYSTEM 1 2
DAS CHANNELS DH DM DL
DAS PRESUMS 8

# Turn polarising cube from position 45000
# to position 55000 in steps of 500
FOR d1 = 45000,55000,500

  # Turn polarising cube & wait for completion
  FOR d2 = 1, 5, 1
    TEL SET POL ABS <d1>
    WAIT (<SET_POL_ANG> == <d1>)
    IF (<d1> == <SET_POL_ANG>)
      BREAK
    ENDIF
  ENDFOR
  SLEEP 5

  # Note position in data files and
  # start data recording
  DAS COMMENT 2 "polariser test, SET pol=<d1>"
  DAS START
  WAIT (<RECORDS> == 2)
  DAS STOP
ENDFOR
```

Figure C.8: Super-controller script example to measure the linear polarisation of the backscattered light at different angles relative to the emitted plane of polarisation by turning the polarising cube in the focal box of the South-East-Telescope.

Such a super-controller was implemented in Spring 2005 as a Linux command-line program that reads and processes a script file with a given name. It was written in C++ and includes a script interpreter which can handle “FOR” loops, “IF” constructs and “WAIT” commands to wait for specified states of the instrument. The communication with the subsystems is network-based. A complete description of the super-controller including a list of all implemented commands can be found in a separate technical report [*Schöch*, 2007]. Fig. C.8 shows a very simple example of the capabilities of the super-controller. First a few parameters for the data acquisition are set. Then the polarising cube of the South-East-Telescope is stepped in one degree increments (500 steps of the stepper motor). At each position of the polarising cube, a profile is recorded. The position of the polarising cube is noted in the raw data files enabling an automatic analysis of the polarising cube test by another program. This is only a short example for the kind of tasks that the super-controller can process. Others include moving the laser beam through the FOV of the telescopes to check the FOV and the laser beam divergence, searching for the optimum position of the laser beam inside the FOV which maximises the atmospheric signal, or stepping the laser frequency to test the daylight filters in the detection system.

Appendix D

D.1 Mathematical treatment of inertio-gravity waves

This section will present the mathematical formalism used to describe inertio-gravity waves. Starting from Eqs. 2.9 – 2.13, a perturbation analysis is performed assuming a small perturbation of a constant background state:

$$\begin{aligned} u(\vec{x},t) &= \bar{u} + u'(\vec{x},t) \\ v(\vec{x},t) &= \bar{v} + v'(\vec{x},t) \\ w(\vec{x},t) &= \bar{w} + w'(\vec{x},t) \ , \\ \rho(\vec{x},t) &= \bar{\rho} + \rho'(\vec{x},t) \\ p(\vec{x},t) &= \bar{p} + p'(\vec{x},t) \end{aligned} \tag{D.1}$$

where the perturbed quantities are assumed to be much smaller than the background (e.g. $u' \ll \bar{u}$). The mean vertical wind $\bar{w}$ in the atmosphere is very small and can be neglected here. The background state $(\bar{u}, \bar{v}, \bar{\rho}, \bar{p})$ is assumed to fulfil Eqs. 2.9 – 2.13. Terms of higher order in the perturbations are neglected as well as shear terms (e.g. $w'\frac{\partial \bar{u}}{\partial z}$). Hydrostatic equilibrium is assumed for the background state (i.e. $\frac{\partial \bar{p}}{\partial z} = -g\bar{\rho}$). The Boussinesque approximation is also used which assumes that the mean pressure $\bar{p}$ and density $\bar{\rho}$ only changes as a function of height (this is equal to the assumption that it is only retained in terms where it is combined with the Earth's acceleration g). This assumption is valid as long as the vertical scale of the waves is smaller than the scale height [e.g. *Miesen et al.*, 1988].

If this linearisation scheme is applied to the set of Eqs. 2.9 – 2.13, a set of somewhat simpler equations results where now the total derivation resulting from the Eulerian view is stated explicitely:

$$\frac{\partial u'}{\partial t} + \bar{u}\frac{\partial u'}{\partial x} + \bar{v}\frac{\partial u'}{\partial y} - fv' + \frac{1}{\bar{\rho}}\frac{\partial p'}{\partial x} = 0 \tag{D.2}$$

$$\frac{\partial v'}{\partial t} + \bar{u}\frac{\partial v'}{\partial x} + \bar{v}\frac{\partial v'}{\partial y} + fu' + \frac{1}{\bar{\rho}}\frac{\partial p'}{\partial y} = 0 \tag{D.3}$$

$$\frac{\partial w'}{\partial t} + \bar{u}\frac{\partial w'}{\partial x} + \bar{v}\frac{\partial w'}{\partial y} + \frac{1}{\bar{\rho}}\frac{\partial p'}{\partial z} + \frac{g}{\bar{\rho}}\rho' = 0 \tag{D.4}$$

$$\frac{\partial \rho'}{\partial t} + \bar{u}\frac{\partial \rho'}{\partial x} + \bar{v}\frac{\partial \rho'}{\partial y} + w'\frac{\partial \bar{\rho}}{\partial z} + \bar{\rho}\left(\frac{\partial u'}{\partial x} + \frac{\partial v'}{\partial y} + \frac{\partial w'}{\partial z}\right) = 0 \tag{D.5}$$

$$\gamma R\bar{T}\left[\frac{\partial \rho'}{\partial t} + \bar{u}\frac{\partial \rho'}{\partial x} + \bar{v}\frac{\partial \rho'}{\partial y} + w'\frac{\partial \bar{\rho}}{\partial z}\right] - \left[\frac{\partial p'}{\partial t} + \bar{u}\frac{\partial p'}{\partial x} + \bar{v}\frac{\partial p'}{\partial y} + w'\frac{\partial \bar{p}}{\partial z}\right] = 0 \ . \tag{D.6}$$

Since we are looking for harmonic oscillations as solutions of this set of equations, we will proceed by substituting wave-form solutions of the form

$$\begin{pmatrix} u' \\ v' \\ w' \\ \rho' \\ p' \end{pmatrix} = \begin{pmatrix} \bar{\rho}^{-1/2}\ \tilde{u} \\ \bar{\rho}^{-1/2}\ \tilde{v} \\ \bar{\rho}^{-1/2}\ \tilde{w} \\ \bar{\rho}^{+1/2}\ \tilde{p} \\ \bar{\rho}^{+1/2}\ \tilde{\rho} \end{pmatrix} \cdot \exp i(kx + ly + mz - \omega t) \ , \tag{D.7}$$

where the factor $\bar{\rho}^{\pm 1/2}$ is introduced to conserve energy in upward propagation and k, l, and m are the zonal, meridional and vertical wavenumbers, respectively. The wave amplitudes in wind, pressure and density are denoted by ($\tilde{u}$, $\tilde{v}$, $\tilde{w}$, $\tilde{p}$, $\tilde{\rho}$).

To simplify the equations, the intrinsic frequency $\hat{\omega}$ in introduced as

$$\hat{\omega} = \omega - \vec{k}\vec{u} \ . \tag{D.8}$$

It is defined as the frequency of the wave in a reference system moving with the mean background wind. The above set of equations can then be written as

$$\begin{aligned}
-i\hat{\omega}u' - fv' + \frac{ik}{\bar{\rho}}p' &= 0 && \text{(D.9)}\\
-i\hat{\omega}v' + fu' + \frac{il}{\bar{\rho}}p' &= 0 && \text{(D.10)}\\
-i\hat{\omega}w' + \frac{1}{\rho^{1/2}}\left(im + \frac{1}{2\,H_\rho}\right)p' + \frac{g}{\bar{\rho}}\rho' &= 0 \ . && \text{(D.11)}\\
-i\hat{\omega}\rho' + \bar{\rho}\left[iku' + ilv' + \left(im + \frac{1}{2\,H_\rho}\right)w'\right] &= 0 && \text{(D.12)}\\
-i\hat{\omega}\rho' + \frac{\partial\bar{\rho}}{\partial z}w' + \frac{1}{c_s^2}\left[i\hat{\omega}p' + \bar{\rho}gw'\right] &= 0 && \text{(D.13)}
\end{aligned}$$

Cancelling common exponential terms and density factors finally results in this linear set of equations:

$$\begin{pmatrix}
-i\hat{\omega} & -f & 0 & +ik & 0\\
+f & -i\hat{\omega} & 0 & +il & 0\\
0 & 0 & -i\hat{\omega} & +i\left(m - \frac{i}{2H_\rho}\right) & g\\
+ik & +il & +i\left(m - \frac{i}{2H_\rho}\right) & 0 & -i\hat{\omega}\\
0 & 0 & \frac{N^2}{g} & -\frac{i}{c_s^2}\hat{\omega} & +i\hat{\omega}
\end{pmatrix} \cdot \begin{pmatrix} \tilde{u}\\ \tilde{v}\\ \tilde{w}\\ \tilde{p}\\ \tilde{\rho}\end{pmatrix} = 0 \ . \tag{D.14}$$

This linear set of equations is used in Sec. 2.5.2 in the main text to derive the dispersion relation for inertio-gravity waves.

D.2 Mathematical treatment of the residual meridional circulation

The mathematical description of the residual meridional circulation is most instructive in the Eulerian mean zonal approximation [*Holton*, 1992]. After zonal averaging, the zonal mean zonal momentum and zonal mean temperature derived from Eq. 2.9 and 2.13 are

$$\begin{aligned}
\frac{\partial\overline{u}}{\partial t} - f_0\overline{v} &= -\frac{\partial(\overline{u'v'})}{\partial y} + \overline{X} && \text{(D.15)}\\
\frac{\partial\overline{T}}{\partial t} + \frac{N^2H}{R}\overline{w} &= \frac{\overline{J}}{c_p} - \frac{\partial(\overline{v'T'})}{\partial y} \ , && \text{(D.16)}
\end{aligned}$$

where overlines denote zonal mean quantities, f_0 is a mean Coriolis parameter for the latitude range under consideration and H is again the pressure scale height. Here additional forcing terms due to small-scale eddy zonal drag $\overline{X}$, diabatic heating $\overline{J}/c_p$ and eddy heat flux convergence $-\frac{\partial \overline{v'T'}}{\partial y}$ are introduced. In Eq. D.16, the eddy heat flux convergence and the adiabatic cooling $\frac{N^2 H}{R} w$ nearly cancel each other with the diabatic heating as a small effect to this balance.

Therefore the transformed Eulerian mean [*Andrews et al.*, 1987; *Holton*, 1992] equations are introduced which describe the effective meridional mass transport due to diabatic processes. A residual meridional circulation is defined by

$$\overline{v}^* = \overline{v} - \frac{R}{\bar{\rho} H} \frac{\partial (\frac{\overline{\bar{\rho} v'T'}}{N^2})}{\partial z} \tag{D.17}$$

$$\overline{w}^* = \overline{w} + \frac{R}{H} \frac{\partial (\frac{\overline{v'T'}}{N^2})}{\partial y} , \tag{D.18}$$

where $\overline{v}^*$ and $\overline{w}^*$ are the zonal mean meridional and vertical wind components in the transformed Eulerian mean, respectively. Rewriting Eq. D.15 and D.16 for $\overline{v}^*$ and $\overline{w}^*$ then yields

$$\frac{\partial \overline{u}}{\partial t} - f_0 \overline{v}^* = \frac{1}{\bar{\rho}} \vec{\nabla} \cdot \vec{F} + \overline{X} \tag{D.19}$$

$$\frac{\partial \overline{T}}{\partial t} + \frac{N^2 H}{R} \overline{w}^* = \frac{\overline{J}}{c_p} \tag{D.20}$$

$$\frac{\partial \overline{v}^*}{\partial y} + \frac{1}{\bar{\rho}} \frac{\partial (\bar{\rho} \overline{w}^*)}{\partial z} = 0 , \tag{D.21}$$

where the last equation is the continuity equation and $\vec{F}$ is the Eliassen-Palm flux with the components $\vec{F} = (0, -\bar{\rho}\overline{u'v'}, \frac{\bar{\rho} f_0 R}{N^2 H} \overline{v'T'})$ resulting from large-scale eddies [*Andrews et al.*, 1987].

Under steady-state conditions, $\frac{\partial \overline{u}}{\partial t}$ and $\frac{\partial \overline{T}}{\partial t}$ are very small or zero. An eddy flux convergence from the Eliassen-Palm flux or from gravity waves will lead to a negative right side of Eq. D.19 and hence will result in a positive $\overline{v}^*$. As the forcing is zero at the poles, this gives a meridional gradient $\frac{\partial \overline{v}^*}{\partial y} \neq 0$ which implies a vertical wind through the continuity equation (Eq. D.21). Balancing Eq. D.20 then requires atmospheric cooling. Through this process breaking gravity waves induce a residual meridional circulation which induces considerable adiabatic cooling in the mesopause region. This gravity wave driven circulation thus explains the observed cold summer mesopause which is far from radiative equilibrium.

Bibliography

Achatz, U. (2005), On the role of optimal perturbations in the instability of monochromatic gravity waves, *Phys. Fluids*, *17*(9), 094107, doi:10.1063/1.2046709.

Achatz, U. (2007), The primary nonlinear dynamics of modal and nonmodal perturbations of monochromatic inertia-gravity waves, *J. Atmos. Sci.*, *64*(1), 74–95, doi:10.1175/JAS3827.1.

Alexander, M. J. (1998), Interpretations of observed climatological patterns in stratospheric gravity wave variance, *J. Geophys. Res.*, *103*(D8), 8627–8640, doi:10.1029/97JD03325.

Alexander, M. J., and T. J. Dunkerton (1999), A spectral parameterization of mean-flow forcing due to breaking gravity waves, *J. Atmos. Sci.*, *56*(24), 4167–4182, doi:10.1175/1520 − 0469(1999)056 < 4167 : ASPOMF > 2.0.CO; 2.

Alexander, M. J., and J. R. Holton (2004), On the spectrum of vertically propagating gravity waves generated by a transient heat source, *Atmos. Chem. Phys.*, *4*(4), 923–932, SRef-ID:1680-7324/acp/2004-4-923.

Allen, S. J., and R. A. Vincent (1995), Gravity wave activity in the lower atmosphere: Seasonal and latitudinal variations, *J. Geophys. Res.*, *100*(D1), 1327–1350, doi:10.1029/94JD02688.

Alpers, M., R. Eixmann, C. Fricke-Begemann, M. Gerding and J. Höffner (2004), Temperature lidar measurements from 1 to 105 km altitude using resonance, Rayleigh, and rotational Raman scattering, *Atmos. Chem. Phys.*, *4*(3), 793–800, SRef-ID:1680-7324/acp/2004-4-793.

Andrews, D. G., and M. E. McIntyre (1978), On wave-action and its relatives, *J. Fluid Mech.*, *89*(4), 647–664.

Andrews, D. G., J. R. Holton and C. B. Leovy (1987), *Middle atmosphere dynamics*, *International Geophysics Series*, vol. 40, 489 pp., Academic Press Inc., Orlando, USA, ISBN:0-120-58576-6.

Ansmann, A., M. Riebesell and C. Weitkamp (1990), Measurement of atmospheric aerosol extinction profiles with a Raman lidar, *Opt. Lett.*, *15*(13), 746–748.

Bakan, S., H. Hinzpeter, H. Höller, H. Jeske, M. Laube, H. Volland, P. Warneck and C. Wurzinger (1988), *Meteorology – Physical and chemical properties of the air*, *Landolt-Börnstein – Numerical data and functional relationships in science and technology*, vol. V/4b, Springer Verlag, Berlin, ISBN:3-540-17603-9.

Baldwin, M. P., L. J. Gray, T. J. Dunkerton, K. Hamilton, P. H. Haynes, W. J. Randel, J. R. Holton, M. J. Alexander, I. Hirota, T. Horinouchi, D. B. A. Jones, J. S. Kinnersley, C. Marquardt, K. Sato and M. Takahashi (2001), The quasi-biennial oscillation, *Rev. Geophys.*, *39*(2), 179–229, doi:10.1029/1999RG000073.

Baldwin, M. P., D. W. J. Thompson, E. F. Shuckburgh, W. A. Norton and N. P. Gillett (2003), Weather from the stratosphere ?, *Science*, *301*(5631), 317–319, doi:10.1126/science.1085688.

Baumgarten, G. (2001), Leuchtende Nachtwolken an der polaren Sommermesopause: Untersuchungen mit dem ALOMAR Rayleigh/Mie/Raman Lidar, Ph.D. thesis, Universität Bonn, Bonn, Germany.

Baumgarten, G., K. H. Fricke and G. von Cossart (2002a), Investigation of the shape of noctilucent cloud particles by polarization lidar technique, *Geophys. Res. Lett.*, *29*(13), 8/1–4, doi:10.1029/2001GL013877.

Baumgarten, G., F.-J. Lübken and K. H. Fricke (2002b), First observation of one noctilucent cloud by a twin lidar in two different directions, *Ann. Geophys.*, *20*(11), 1863–1868, SRef-ID:1432-0576/ag/2002-20-1863.

Becker, E. (2004), Direct heating rates associated with gravity wave saturation, *J. Atmos. Solar-Terr. Phys.*, *66*(6-9), 683–696, doi:10.1016/j.jastp.2004.01.019.

Becker, E., and D. C. Fritts (2006), Enhanced gravity-wave activity and interhemispheric coupling during the MaCWAVE/MIDAS northern summer program 2002, *Ann. Geophys.*, *24*(4), 1175–1188, SRef-ID:1432-0576/ag/2006-24-1175.

Becker, E., A. Müllemann, F.-J. Lübken, H. Körnich, P. Hoffmann and M. Rapp (2004), High Rossby-wave activity in austral winter 2002: Modulation of the general circulation of the MLT during the MaCWAVE/MIDAS northern summer program, *Geophys. Res. Lett.*, *31*(24), L24S03, doi:10.1029/2004GL019615.

Berger, U. (1994), Numerische Simulation klimatologischer Prozesse und thermischer Gezeiten in der mittleren Atmosphäre, Ph.D. thesis, Universität Köln, Köln, Germany.

Berger, U. (2007), Modeling of middle atmosphere dynamics with LIMA, *J. Atmos. Solar-Terr. Phys.*, *submitted*.

Berger, U., and F.-J. Lübken (2006), Weather in mesospheric ice layers, *J. Geophys. Res.*, *33*(4), L04806, doi:10.1029/2005GL024841.

Berger, U., and U. von Zahn (2002), Icy particles in the summer mesopause region: Three-dimensional modeling of their environment and two-dimensional modeling of their transport, *J. Geophys. Res.*, *107*(A11), 1366, doi:10.1029/2001JA000316.

Birkeli, G. (2003), Gravity wave activity observed with lidar in the altitude region 30 – 55 km above ALOMAR, Northern Norway during July 2002, Master's thesis, University of Oslo, Oslo, Norway.

Blum, U. (2003), Lidarbeobachtungen der polaren Atmosphäre: Wolken und Wellen – Phänomene und Mechanismen, Ph.D. thesis, Universität Bonn, Bonn, Germany.

Blum, U., and K. H. Fricke (2005), The Bonn University lidar at the Esrange: Technical description and capabilities for atmospheric research, *Ann. Geophys.*, *23*(5), 1645–1658, SRef-ID:1432-0576/ag/2005-23-1645.

Blum, U., K. H. Fricke, G. Baumgarten and A. Schöch (2003), Lidar observations of atmospheric dynamics on both sides of the Scandinavian mountains, in *Proceedings of the 16th ESA Symposium on European Rocket and Balloon Programmes and Related Research*, vol. ESA SP–530, edited by B. Warmbein, pp. 389–394, St. Gallen, Switzerland.

Blum, U., K. H. Fricke, G. Baumgarten and A. Schöch (2004), Simultaneous lidar observations of temperatures and waves in the polar middle atmosphere on both sides of the Scandinavian mountains: A case study on January 19/20, 2003, *Atmos. Chem. Phys.*, *4*(3), 809–816, SRef-ID:1680-7324/acp/2004-4-809.

Blum, U., F. Khosrawi, G. Baumgarten, K. Stebel, R. Müller and K. H. Fricke (2006), Simultaneous lidar observations of a polar stratospheric cloud on the east and west sides of the scandinavian mountains and microphysical box model simulations, *Ann. Geophys.*, *24*(12), 3267–3277, SRef-ID:1432-0576/angeo/2006-24-3267.

Booker, J. R., and F. P. Bretherton (1967), The critical level for internal gravity waves in a shear flow, *J. Fluid Mech.*, *27*, 513–539.

Brasseur, G., and S. Solomon (1986), *Aeronomy of the middle atmosphere*, 2 ed., 452 pp., D. Reidel Publishing Company, Dordrecht, The Netherlands, ISBN:90-277-2343-5.

Briggs, B. H. (1984), The analysis of spaced sensor records by correlation techniques, in *Handbook for MAP*, vol. 13, edited by R. A. Vincent, pp. 166–186, SCOSTEP Secr., Univ. of Ill., Urbana.

Burden, R. L., and J. D. Faires (1993), *Numerical analysis*, 768 pp., PWS Publishing company, Boston, MA, USA, ISBN:0-534-93219-3.

Burrows, J. P., A. Richter, A. Dehn, B. Deters, S. Himmelmann, S. Voigt and J. Orphal (1999), Atmospheric remote-sensing reference data from GOME2. Temperature-dependent absorption cross sections of O_3 in the 231–794 nm range, *J. Quant. Spectros. Rad. Trans.*, *61*(4), 509–517, doi:10.1016/S0022 − 4073(98)00037 − 5.

Chanin, M. L., and A. Hauchecorne (1981), Lidar observations of gravity and tidal waves in the stratosphere and mesosphere, *J. Geophys. Res.*, *86*(C10), 9715–9721.

Charbonnel, C., and S. Talon (2005), Influence of gravity waves on the internal rotation and Li abundance of solar-type stars, *Science*, *309*(5744), 2189–2191, doi:10.1126/science.1116849.

Chilson, P., S. Kirkwood and A. Nilsson (1999), The Esrange MST radar: A brief introduction and procedure for range validation using balloons, *Radio Sci.*, *34*(2), 427–436, doi:10.1029/1998RS900023.

Chimonas, G., and C. O. Hines (1986), Doppler ducting of atmospheric gravity waves, *J. Geophys. Res.*, *91*(D1), 1219–1230.

Cho, Y.-M., G. G. Shepherd, Y.-I. Won, S. Sargoytchev, S. Brown and B. Solheim (2004), MLT cooling during stratospheric warming events, *Geophys. Res. Lett.*, *31*(10), L10104, doi:10.1029/2004GL019552.

Christiansen, B. (2005), Downward propagation and statistical forecast of the near-surface weather, *J. Geophys. Res.*, *110*(D14), D14104, doi:10.1029/2004JD005431.

Clancy, R. T., D. W. Rusch and M. T. Callan (1994), Temperature minima in the average thermal structure of the middle mesosphere (70-80 km) from analysis of 40- to 92-km SME global temperature profiles, *J. Geophys. Res.*, *99*(D9), 19,001–19,020, doi:10.1029/94JD01681.

Collins, R. L., M. C. Kelley, M. J. Nicolls, C. Ramos, T. Hou, T. E. Stern, K. Mizutani and T. Itabe (2003), Simultaneous lidar observations of a noctilucent cloud and an internal wave in the polar mesosphere, *J. Geophys. Res.*, *108*(D8), 8435, doi:10.1029/2002JD002427.

Coy, L., D. E. Siskind, S. D. Eckermann, J. P. McCormack, D. R. Allen and T. F. Hogan (2005), Modeling the August 2002 minor warming event, *Geophys. Res. Lett.*, *32*(7), L07808, doi:10.1029/2005GL022400.

Cutler, L. J., R. L. Collins, K. Mizutani and T. Itabe (2001), Rayleigh lidar observations of mesospheric inversion layers at Poker Flat, Alaska (65° N, 147° W), *Geophys. Res. Lett.*, *28*(8), 1467–1470, doi:10.1029/2000GL012535.

de la Torre, A., P. Alexander and A. Giraldez (1999), The kinetic to potential energy ratio and spectral separability from high-resolution balloon soundings near the Andes mountains, *Geophys. Res. Lett.*, *26*(10), 1413–1416, doi:10.1029/1999GL900265.

Dewan, E. M., and R. E. Good (1986), Saturation and the "universal" spectrum for vertical profiles of horizontal scalar winds in the atmosphere, *J. Geophys. Res.*, *91*(D2), 2742–2748.

Dierckx, P. (1993), *Curve and surface fitting with splines*, Monographs on numerical analysis, 285 pp., Oxford University Press, Oxford, USA, ISBN:0-198-53440-X.

Dubin, M., A. R. Hull and K. S. W. Champion (Eds.) (1976), *U.S. Standard Atmosphere 1976*, 227 pp., NOAA, NASA, USAF, Washington, USA.

Duck, T. J., and M. D. Greene (2004), High Arctic observations of mesospheric inversion layers, *Geophys. Res. Lett.*, *31*(2), L02105, doi:10.1029/2003GL018481.

Duck, T. J., J. A. Whiteway and A. I. Carswell (2000), A detailed record of High Arctic middle atmospheric temperatures, *J. Geophys. Res.*, *105*(D18), 22,909–22,918, doi:10.1029/2000JD900367.

Dunkerton, T. J., and N. Butchart (1984), Propagation and selective transmission of internal gravity waves in a sudden warming, *J. Atmos. Sci.*, *41*(8), 1443–1460, doi:$10.1175/1520-0469(1984)041 < 1443 : \mathrm{PASTOI} > 2.0.\mathrm{CO};2$.

Eckart, L. (2004), Dimensionierung, Aufbau und Integration eines optischen Nachweiskanals für das ALOMAR RMR-Lidar, Master's thesis, Westsächsische Hochschule Zwickau, Zwickau, Germany.

Eckermann, S. D. (1992), Ray-tracing simulation of the global propagation of inertia gravity waves through the zonally averaged middle atmosphere, *J. Geophys. Res.*, *97*(D14), 15,849–15,866.

Eckermann, S. D. (1996), Hodographic analysis of gravity waves: Relationships among Stokes parameters, rotary spectra and cross-spectral methods, *J. Geophys. Res.*, *101*(D14), 19,169–19,174, doi:10.1029/96JD01578.

Eckermann, S. D., and P. Preusse (1999), Global measurements of stratospheric mountain waves from space, *Science*, *286*(5444), 1534–1537, doi:10.1126/science.286.5444.1534.

Eckermann, S. D., I. Hirota and W. K. Hocking (1995), Gravity wave and equatorial wave morphology of the stratosphere derived from long-term rocket soundings, *Quart. J. Roy. Meteorol. Soc.*, *121*(521), 149–186, doi:10.1256/smsqj.52107.

Enke, M. (1994), Berechnung, Aufbau und Erprobung einer aktiven Laserstrahlführung, Master's thesis, Universität Rostock, Rostock, Germany.

Fiedler, J., and G. von Cossart (1999), Automated lidar transmitter for multiparameter investigations within the Arctic atmosphere, *IEEE Trans. Geosci. Remote Sensing*, *37*(2), 748–755, doi:10.1109/36.752191.

Fiedler, J., G. von Cossart, F. Hübner, H. Mehrtens, U. von Zahn, K. H. Fricke, G. Nelke, A. Hauchecorne, F. Fierli and D. Rees (1997), Status of the ALOMAR Rayleigh/Mie/Raman lidar, in *Proceedings of the* 13^{th} *ESA Symposium on European Rocket and Balloon Programmes and Related Research*, vol. ESA SP–397, edited by B. Kaldeich-Schürmann, pp. 105–110, Öland, Sweden.

Fiedler, J., G. von Cossart and U. von Zahn (1999), Stratospheric/Mesospheric temperature profiles obtained by the ALOMAR RMR–lidar over Andøya, in *Proceedings of the* 14^{th} *ESA Symposium on European Rocket and Balloon Programmes and Related Research*, vol. ESA SP–437, edited by B. Kaldeich-Schürmann, pp. 263–268, Potsdam, Germany.

Fiedler, J., G. von Cossart and G. Baumgarten (2003), Noctilucent clouds above ALOMAR between 1997 and 2001: Occurrence and properties, *J. Geophys. Res.*, *108*(D8), 8453, doi:10.1029/2002JD002419.

Fiedler, J., G. Baumgarten and G. von Cossart (2005), Mean diurnal variations of noctilucent clouds during 7 years of lidar observations at ALOMAR, *Ann. Geophys.*, *23*(4), 1175–1181, SRef-ID:1432-0576/ag/2005-23-1175.

Fiocco, G., and L. D. Smullin (1963), Detection of scattering layers in the upper atmosphere ($60-140$ km) by optical radar, *Nature*, *199*(4900), 1275–1276, doi:10.1038/1991275a0.

Fleming, E. L., S. Chandra, J. J. Barnett and M. Corney (1990), Zonal mean temperature, pressure, zonal wind, and geopotential height as functions of latitude, COSPAR international reference atmosphere: 1986, Part II: Middle atmosphere models, *Adv. Space Res.*, *10*(12), 11–59, doi:$10.1016/0273-1177(90)90386-\mathrm{E}$.

Fogle, B., and B. Haurwitz (1966), Noctilucent clouds, *Space Sci. Rev.*, *6*(3), 279–340, doi:10.1007/BF00173768.

Forbes, J. M., and G. V. Groves (1990), Atmospheric tides below 80 km, *Adv. Space Res.*, *10*(12), 119–125, doi:$10.1016/0273-1177(90)90391-\mathrm{C}$.

Fortuin, J. P. F., and U. Langematz (1995), An update on the global ozone climatology and on concurrent ozone and temperature trends, in *Proceedings of the SPIE symposium "Atmospheric sensing and modelling"*, vol. 2311, edited by R. P. Santer, pp. 207–216, SPIE, Bellingham, WA, Rome, Italy, doi:10.1117/12.198578.

Franke, P. M., and R. L. Collins (2003), Evidence of gravity wave breaking in lidar data from the mesopause region, *Geophys. Res. Lett.*, *30*(4), 1155, doi:10.1029/2001GL014477.

Fricke, K. H., and U. von Zahn (1985), Mesopause temperatures derived from probing the hyperfine structure of the D_2 resonance line of sodium by lidar, *J. Atmos. Terr. Phys.*, *47*(5), 499–512, doi:10.1016/0021 − 9169(85)90116 − 3.

Fritts, D. C. (1984), Gravity wave saturation in the middle atmosphere: A review of theory and observations, *Rev. Geophys. Space Phys.*, *22*(3), 275–308.

Fritts, D. C., and M. J. Alexander (2003), Gravity wave dynamics and effects in the middle atmosphere, *Rev. Geophys.*, *41*(1), 1003, doi:10.1029/2001RG000106.

Fritts, D. C., and G. D. Nastrom (1992), Sources of mesoscale variability of gravity waves. Part II: Frontal, convective, and jet stream excitation, *J. Atmos. Sci.*, *49*(2), 111–127, doi:10.1175/1520 − 0469(1992)049 < 0111 : SOMVOG > 2.0.CO; 2.

Fritts, D. C., and P. K. Rastogi (1985), Convective and dynamical instabilities due to gravity wave motions in the lower and middle atmosphere – Theory and observations, *Radio Sci.*, *20*(6), 1247–1277.

Fritts, D. C., J. R. Isler, G. E. Thomas and Ø. Andreassen (1993), Wave breaking signatures in noctilucent clouds, *Geophys. Res. Lett.*, *20*(19), 2039–2042.

Fritts, D. C., B. P. Williams, C.-Y. She, J. D. Vance, M. Rapp, F.-J. Lübken, A. Müllemann, F. J. Schmidlin and R. A. Goldberg (2004), Observations of extreme temperature and wind gradients near the summer mesopause during the MaCWAVE/MIDAS rocket campaign, *Geophys. Res. Lett.*, *31*(24), L24S06, doi:10.1029/2003GL019389.

Fritts, D. C., S. L. Vadas, K. Wan and J. A. Werne (2006), Mean and variable forcing of the middle atmosphere by gravity waves, *J. Atmos. Solar-Terr. Phys.*, *68*(3-5), 247–265, doi:10.1016/j.jastp.2005.04.010.

Fritz, S., and S. Soules (1970), Large-scale temperature changes in the stratosphere observed from Nimbus III, *J. Atmos. Sci.*, *27*(7), 1091–1097, doi:10.1175/1520 − 0469(1970)027 < 1091 : LSTCIT > 2.0.CO; 2.

Gadsden, M. (1982), Noctilucent clouds, *Space Sci. Rev.*, *33*(3), 279–334, doi:10.1007/BF00196999.

Garcia, R. R., and S. Solomon (1985), The effect of breaking gravity waves on the dynamics and chemical composition of the mesosphere and lower thermosphere, *J. Geophys. Res.*, *90*(D2), 3850–3868.

Gardner, C. S., and M. J. Taylor (1998), Observational limits for lidar, radar, and airglow imager measurements of gravity wave parameters, *J. Geophys. Res.*, *103*(D6), 6427–6437, doi:10.1029/97JD03378.

Geller, M. A. (1983), Dynamics of the middle atmosphere, *Space Sci. Rev.*, *34*(4), 359–375, doi:10.1007/BF00168828.

Gerrard, A. J., T. J. Kane and J. P. Thayer (1998), Noctilucent clouds and wave dynamics: Observations at Søndrestrøm, Greenland, *Geophys. Res. Lett.*, *25*(15), 2817–2820, doi:10.1029/98GL02107.

Gerrard, A. J., T. J. Kane, J. P. Thayer and S. D. Eckermann (2004), Concerning the upper stratospheric gravity wave and mesospheric cloud relationship over Søndrestrøm, Greenland, *J. Atmos. Solar-Terr. Phys.*, *66*(3-4), 229–240, doi:10.1016/j.jastp.2003.12.005.

Goldberg, R. A., and D. C. Fritts (2004), Introduction to special section: The MaCWAVE-MIDAS program to study the polar summer mesosphere, *Geophys. Res. Lett.*, *31*(24), L24S01, doi:10.1029/2004GL021789.

Goldberg, R. A., D. C. Fritts, B. P. Williams, F. J. Schmidlin, C. L. Croskey, J. D. Mitchell, F.-J. Lübken, M. Rapp, W. Singer, R. Latteck, T. A. Blix, M. Friedrich, S. Kirkwood, N. Mitchell and K. H. Fricke (2003), The MaCWAVE program to study gravity wave forcing of the polar mesosphere during summer and winter, in *Proceedings of the 16^{th} ESA Symposium on European Rocket and Balloon Programmes and Related Research*, vol. ESA SP–530, edited by B. Warmbein, pp. 345–350.

Goldberg, R. A., D. C. Fritts, B. P. Williams, C.-Y. She, F.-J. Lübken, M. Rapp, W. Singer, R. Latteck, P. Hoffmann, A. Müllemann, G. Baumgarten, F. J. Schmidlin, C.-Y. She and D. A. Krueger (2004), The MaCWAVE/MIDAS rocket and ground-based measurements of polar summer dynamics: Overview and mean state structure, *Geophys. Res. Lett.*, *31*(24), L24S02, doi:10.1029/2004GL019411.

Hansen, G., M. Servazi and U. von Zahn (1989), First detection of a noctilucent clouds by lidar, *Geophys. Res. Lett.*, *16*(12), 1445–1448.

Hauchecorne, A., and M. L. Chanin (1980), Density and temperature profiles obtained by lidar between 35 and 70 km, *Geophys. Res. Lett.*, *7*(8), 565–568.

Hauchecorne, A., and A. Maillard (1990), A 2-d dynamical model of mesospheric temperature inversions in winter, *Geophys. Res. Lett.*, *17*(12), 2197–2200.

Hauchecorne, A., M. L. Chanin and R. Wilson (1987), Mesospheric temperature inversion and gravity wave breaking, *Geophys. Res. Lett.*, *14*(9), 933–936.

Hertzog, A., F. Vial, C. R. Mechoso, C. Basdevant, P. Cocquerez, V. Dubourg and F. Nouel (2002), Planetary and gravity wave activity in the equatorial lower stratosphere as seen by ultra-long duration balloons, *Adv. Space Res.*, *30*(5), 1381–1386, doi:10.1016/S0273 − 1177(02)00555 − 0.

Hervig, M., R. E. Thompson, M. McHugh, L. L. Gordley, J. Russell, III and M. E. Summers (2001), First confirmation that water ice is the primary component of polar mesospheric clouds, *Geophys. Res. Lett.*, *28*(6), 971–974, doi:10.1029/2000GL012104.

Hines, C. O. (1960), Internal atmospheric gravity waves at ionospheric heights, *Can. J. Phys.*, *38*, 1441–1481.

Hines, C. O. (1968), A possible source of waves in noctilucent clouds, *J. Atmos. Sci.*, *25*(5), 937–942, doi:10.1175/1520 − 0469(1968)025 < 0937 : APSOWI > 2.0.CO; 2.

Hines, C. O. (1989), Tropopausal mountain waves over Arecibo: A case study, *J. Atmos. Sci.*, *46*(4), 476–488, doi:10.1175/1520 − 0469(1989)046 < 0476 : TMWOAA > 2.0.CO; 2.

Hirota, I. (1984), Climatology of gravity waves in the middle atmosphere, *J. Atmos. Terr. Phys.*, *46*(9), 767–773, doi:10.1016/0021 − 9169(84)90057 − 6.

Hirota, I., and T. Niki (1985), A statistical study of inertia-gravity waves in the middle atmosphere, *J. Meteorol. Soc. Japan*, *63*(6), 1055–1065.

Hodges, R. R., Jr. (1967), Generation of turbulence in the upper atmosphere by internal gravity waves, *J. Geophys. Res.*, *72*(13), 3455–3458.

Hoffmann, P., W. Singer, D. Keuer and K. Schulz-Schöllhammer (1999), Observations of 3D winds and waves in the tropopause region above Northern Norway with the ALOMAR SOUSY radar during winter 1996/97, in *Proceedings of the European workshop on Mesoscale processes in the stratosphere*, vol. 69, edited by K. S. Carslaw and G. T. Amanatidis, pp. 121–126, Air Pollution Research Report, Bad Tölz, Germany.

Holton, J. R. (1983), The influence of gravity wave breaking on the general circulation of the middle atmosphere, *J. Atmos. Sci.*, *40*(10), 2497–2507, doi:10.1175/1520 − 0469(1983)040 < 2497 : TIOGWB > 2.0.CO; 2.

Holton, J. R. (1992), *An introduction to dynamic meteorology*, *International Geophysics Series*, vol. 48, 3 ed., 511 pp., Academic Press, San Diego, USA, ISBN:0-123-54355-X.

Hübner, F. (1994), Die Fokalinstrumentierung der ALOMAR Teleskope: Konzeption und Aufbau, Master's thesis, Universität Bonn, Bonn, Germany, BONN-IB-95-22.

Hübner, F. (1998), Temperaturen der mittleren polaren Atmosphäre (15 − 80 km): Beobachtungen mit dem ALOMAR Rayleigh/Mie/Raman–Lidar 1995 und 1996 und Vergleiche, Ph.D. thesis, Universität Rostock, Rostock, Germany, available from http://www.iap-kborn.de/optik/Publications_e.htm.

Isler, J. R., M. J. Taylor and D. C. Fritts (1997), Observational evidence of wave ducting and evanescence in the mesosphere, *J. Geophys. Res.*, *102*(D22), 26,301–26,313, doi:10.1029/97JD01783.

Jarvis, M. J., R. E. Hibbins, M. J. Taylor and T. J. Rosenberg (2003), Utilizing riometry to observe gravity waves in the sunlit mesosphere, *Geophys. Res. Lett.*, *30*(19), 1979, doi:10.1029/2003GL017885.

Jasperson, W. H., G. D. Nastrom and D. C. Fritts (1990), Further study of terrain effects on the mesoscale spectrum of atmospheric motions, *J. Atmos. Sci.*, *47*(8), 979–987, doi:10.1175/1520 − 0469(1990)047 < 0979 : FSOTEO > 2.0.CO; 2.

Jensen, E. J., and G. E. Thomas (1994), Numerical simulations of the effects of gravity waves on noctilucent clouds, *J. Geophys. Res.*, *99*(D2), 3421–3430, doi:10.1029/93JD01736.

Jesse, O. (1885), Auffallende Abenderscheinungen am Himmel, *Meteor. Z.*, *2*, 311–312.

Junge, C. E., C. W. Chagnon and J. E. Manson (1961), Stratospheric aerosols, *J. Meteor.*, *18*(1), 81–108, doi:10.1175/1520 − 0469(1961)018 < 0081 : SA > 2.0.CO; 2.

Keckhut, P. (1998), Tri des fichiers en vu d'une sommation par un test relatif, *unpublished; private communication.*

Keckhut, P., A. Hauchecorne and M. L. Chanin (1993), A critical review of the database acquired for the long-term surveillance of the middle atmosphere by the French Rayleigh lidars, *J. Atmos. Ocean. Technol.*, *10*(6), 850–867, doi:10.1175/1520 − 0426(1993)010 < 0850 : ACROTD > 2.0.CO; 2.

Keckhut, P., A. Hauchecorne, E. Collado, A. Garnier, E. Riedinger and U. Singh (2002), Averaging methodology of raw lidar signal used for direct detection, *NAI 19*, Institut Pierre Simon Laplace, SA/CNRS.

Keckhut, P., C. Cagnazzo, M. L. Chanin, C. Claud and A. Hauchecorne (2005), The 11-year solar-cycle effects on the temperature in the upper-stratosphere and mesosphere: Part I – Assessment of observations, *J. Atmos. Solar-Terr. Phys.*, *67*(11), 940–947, doi:10.1016/j.jastp.2005.01.008.

Kent, G. S., and R. W. H. Wright (1970), A review of laser radar measurements of atmospheric properties, *J. Atmos. Terr. Phys.*, *32*(5), 917–943, doi:10.1016/0021 − 9169(70)90036 − X.

Kerr, R. A. (2005a), The story of O_2, *Science*, *308*(5729), 1730–1732, doi:10.1126/science.308.5729.1730.

Kerr, R. A. (2005b), A better atmosphere for life, *Science*, *308*(5729), 1732, doi:10.1126/science.308.5729.1732.

Kim, Y.-J., S. D. Eckermann and H.-Y. Chun (2003), An overview of the past, present and future of gravity-wave drag parameterization for numerical climate and weather prediction models, *Atmosphere-Ocean*, *41*(1), 65–98.

Kodera, K., and Y. Kuroda (2002), Dynamical response to the solar cycle, *J. Geophys. Res.*, *107*(D24), 4749, doi:10.1029/2002JD002224.

Krebsbach, M., and P. Preusse (2007), Spectral analysis of gravity wave activity in SABER temperature data, *Geophys. Res. Lett.*, *34*(3), L03814, doi:10.1029/2006GL028040.

Krüger, K., B. Naujokat and K. Labitzke (2005), The unusual midwinter warming in the southern hemisphere stratosphere 2002: A comparison to northern hemisphere phenomena, *J. Atmos. Sci.*, *62*(3), 603–613, doi:10.1175/JAS − 3316.1.

Kurzawa, H., and U. von Zahn (1990), Sodium density and atmospheric temperature in the mesopause region in polar summer, *J. Atmos. Terr. Phys.*, *52*(10-11), 981–993, doi:10.1016/0021 − 9169(90)90029 − M.

Labitzke, K. (1972a), Temperature changes in the mesosphere and stratosphere connected with circulation changes in winter, *J. Atmos. Sci.*, *29*(4), 756–766, doi:10.1175/1520 − 0469(1972)029 < 0756 : TCITMA > 2.0.CO; 2.

Labitzke, K. (1972b), The interaction between stratosphere and mesosphere in winter, *J. Atmos. Sci.*, *29*(7), 1395–1399, doi:10.1175/1520 − 0469(1972)029 < 1395 : TIBSAM > 2.0.CO; 2.

Labitzke, K. (1987), Sunspots, the QBO and the stratospheric temperature in the north polar region, *Geophys. Res. Lett.*, *14*(5), 535–537.

Labitzke, K. (2001), The global signal of the 11-year sunspot cycle in the stratosphere: Differences between solar maxima and minima, *Meteor. Z.*, *10*(2), 83–90, doi:10.1127/0941 − 2948/2001/0010 − 0083.

Labitzke, K., and collaborators (2002), The Berlin Stratospheric Data Series, *Tech. rep.*, Meteorological Institute, Free University Berlin, Berlin, Germany.

Labitzke, K., and B. Naujokat (2000), The lower Arctic stratosphere in winter since 1952, *SPARC Newsletter*, *15*, 11–14.

Latteck, R., W. Singer and H. Bardey (1999), The ALWIN MST radar - Technical design and performances, in *Proceedings of the 14th ESA Symposium on European Rocket and Balloon Programmes and Related Research*, vol. ESA SP–437, edited by B. Kaldeich-Schürmann, pp. 179–184, Potsdam, Germany.

Leblanc, T., and A. Hauchecorne (1997), Recent observations of mesospheric temperature inversions, *J. Geophys. Res.*, *102*(D16), 19,471–19,482, doi:10.1029/97JD01445.

Leblanc, T., A. Hauchecorne, M. L. Chanin, C. Rodgers, F. Taylor and N. Livesey (1995), Mesospheric temperature inversions as seen by ISAMS in December 1991, *Geophys. Res. Lett.*, *22*(12), 1485–1488, doi:10.1029/94GL03274.

Lindzen, R. S. (1981), Turbulence and stress owing to gravity wave and tidal breakdown, *J. Geophys. Res.*, *86*(C10), 9707–9714.

Lindzen, R. S. (1984), Gravity waves in the mesosphere, in *Dynamics of the middle atmosphere*, edited by J. R. Holton and T. Matsuno, pp. 3–18, Terra Scientific Publishing Co., Tokyo, Japan.

Liu, H.-L., and J. W. Meriwether (2004), Analysis of a temperature inversion event in the lower mesosphere, *J. Geophys. Res.*, *109*(D2), D02S07, doi:10.1029/2002JD003026.

Liu, H.-L., M. E. Hagan and R. G. Roble (2000), Local mean state changes due to gravity wave breaking modulated by the diurnal tide, *J. Geophys. Res.*, *105*(D10), 12,381–12,396, doi:10.1029/1999JD901163.

Liu, Z., W. Hunt, M. Vaughan, C. Hostetler, M. McGill, K. Powell, D. Winker and Y. Hu (2006), Estimating random errors due to shot noise in backscatter lidar observations, *Appl. Opt.*, *45*(18), 4437–4447.

Loßow, S. (2003), Bestimmung von Schwerewellen-Parametern aus Temperaturprofilen gemessen mit einem Lidar in Nord-Norwegen im Sommer 2002, Master's thesis, Freie Universität Berlin.

Lübken, F.-J. (1999), Thermal structure of the Arctic summer mesosphere, *J. Geophys. Res.*, *104*(D8), 9135–9149, doi:10.1029/1999JD900076.

Lübken, F.-J., and U. von Zahn (1991), Thermal structure of the mesopause region at polar latitudes, *J. Geophys. Res.*, *96*(D11), 20,841–20,857.

Manney, G. L., K. Krüger, J. L. Sabutis, S. Amina Sena and S. Pawson (2005), The remarkable 2003 − 2004 winter and other recent warm winters in the Arctic stratosphere since the late 1990s, *J. Geophys. Res.*, *110*(D4), D04107, doi:10.1029/2004JD005367.

Martin, W. E., and R. J. Winfield (1988), Nonlinear effects on pulsed laser propagation in the atmosphere, *Appl. Opt.*, *27*(3), 567–577.

Matsuno, T. (1971), A dynamical model of the stratospheric sudden warming, *J. Atmos. Sci.*, *28*(8), 1479–1494, doi:10.1175/1520 − 0469(1971)028 < 1479 : ADMOTS > 2.0.CO; 2.

McCormack, J. P., and L. L. Hood (1996), Apparent solar cycle variations of upper stratospheric ozone and temperature: Latitude and seasonal dependences, *J. Geophys. Res.*, *101*(D15), 20,933–20,944, doi:10.1029/96JD01817.

Meriwether, J. W., and A. J. Gerrard (2004), Mesosphere inversion layers and stratosphere temperature enhancements, *Rev. Geophys.*, *42*(3), RG3003, doi:10.1029/2003RG000133.

Meriwether, J. W., and M. G. Mlynczak (1995), Is chemical heating a major cause of the mesosphere inversion layer ?, *J. Geophys. Res.*, *100*(D1), 1379–1387, doi:10.1029/94JD01736.

Mie, G. (1908), Beiträge zur Optik trüber Medien, speziell kolloidaler Metallösungen, *Ann. Phys. (Leipzig)*, *25*(3), 377–445, doi:10.1002/andp.19083300302.

Miesen, R. H. M., L. P. J. Kamp and F. W. Sluijter (1988), On the application of the Boussinesq approximation for nonlinear gravity waves in the atmosphere, *Phys. Scripta*, *38*(6), 857–859.

Mishchenko, M. I., J. W. Hovenier and L. D. Travis (1999), *Light scattering by nonspherical particles: Theory, measurements, and applications*, 690 pp., Academic Press, San Diego, USA, ISBN:0-124-98660-9.

Mitchell, N. J., L. Thomas and A. K. P. Marsh (1990), Lidar studies of stratospheric gravity waves: A comparison of analysis techniques, *Ann. Geophys.*, *8*(10), 705–712, SRef-ID:1432-0576/ag/1990-8-705.

Miyoshi, Y. (2003), Effects of the stratospheric sudden warming on the temperature in the MLT region, *Advances in Polar Upper Atmosphere Research, National Institute of Polar Research, Tokyo, Japan*, *17*, 1–12.

Müllemann, A. (2004), Temperaturen, Winde und Turbulenz in der polaren Sommermesosphäre, Ph.D. thesis, Universität Rostock, Rostock, Germany.

Müllemann, A., and F.-J. Lübken (2005), Horizontal winds in the mesosphere at high latitudes, *Adv. Space Res.*, *35*(11), 1890–1894, doi:10.1016/j.asr.2004.11.014.

Murgatroyd, R. J., and R. M. Goody (1958), Sources and sinks of radiative energy from 30 to 90 km, *Quart. J. Roy. Meteorol. Soc.*, *84*(361), 225–234.

Nash, J. D., and J. N. Moum (2005), River plumes as a source of large-amplitude internal waves in the coastal ocean, *Nature*, *437*(7057), 400–403, doi:10.1038/nature03936.

Nastrom, G. D., and D. C. Fritts (1992), Sources of mesoscale variability of gravity waves. Part I: Topographic excitation, *J. Atmos. Sci.*, *49*(2), 101–110, doi:$10.1175/1520-0469(1992)049 < 0101:\mathrm{SOMVOG} > 2.0.\mathrm{CO};2$.

Nastrom, G. D., B. B. Balsley and D. A. Carter (1982), Mean meridional winds in the mid- and high-latitude summer mesosphere, *Geophys. Res. Lett.*, *9*(2), 139–142.

Nastrom, G. D., T. E. VanZandt and J. M. Warnock (1997), Vertical wavenumber spectra of wind and temperature from high-resolution balloon soundings over Illinois, *J. Geophys. Res.*, *102*(D6), 6685–6702, doi:10.1029/96JD03784.

Nedeljkovic, D., A. Hauchecorne and M. L. Chanin (1993), Rotational Raman lidar to measure the atmospheric temperature from the ground to 30 km, *IEEE Trans. Geosci. Remote Sensing*, *31*(1), 90–101, doi:10.1109/36.210448.

Nelke, G., and M. Hayk (2000), Systemdokumentation der Fokalboxen der ALOMAR-Teleskope, *Tech. rep.*, Optisense GmbH, Bochum, Germany.

Neuber, R., P. von der Gathen and U. von Zahn (1988), Altitude and temperature of the mesopause at 69° N latitude in winter, *J. Geophys. Res.*, *93*(D2), 11,093–11,101.

Palo, S. E., J. M. Forbes, X. Zhang, J. M. Russell, III, C. J. Mertens, M. G. Mlynczak, G. B. Burns, P. J. Espy and T. D. Kawahara (2005), Planetary wave coupling from the stratosphere to the thermosphere during the 2002 southern hemisphere pre-stratwarm period, *Geophys. Res. Lett.*, *32*(23), L23809, doi:10.1029/2005GL024298.

Pan, W., and C. S. Gardner (2003), Seasonal variations of the atmospheric temperature structure at South Pole, *J. Geophys. Res.*, *108*(D18), 4564, doi:10.1029/2002JD003217.

Pavelin, E., and J. A. Whiteway (2002), Gravity wave interactions around the jet stream, *Geophys. Res. Lett.*, *29*(21), 2024, doi:10.1029/2002GL015783.

Pawson, S., and B. Naujokat (1999), The cold winters of the middle 1990s in the northern lower stratosphere, *J. Geophys. Res.*, *104*(D12), 14,209–14,222, doi:10.1029/1999JD900211.

Petzoldt, K., R. Lenschow, A. Hauchecorne, G. A. Kokin, W. Meyer, A. O'Neill, C. R. Philbrick, F. J. Schmidlin and R. Thomas (1987), Large scale structure of the stratosphere and the lower mesosphere (20 – 60 km) over the northern hemisphere during the MAP/WINE campaign, *J. Atmos. Terr. Phys.*, *49*(7-8), 621–637, doi:$10.1016/0021-9169(87)90008-0$.

Picone, J. M., A. E. Hedin, D. P. Drob and A. C. Aikin (2002), NRLMSISE-00 empirical model of the atmosphere: Statistical comparison and scientific issues, *J. Geophys. Res.*, *107*(A12), 1468, doi:10.1029/2002JA009430.

Pielke, R. A. (1984), *Mesoscale meteorological modeling*, 612 pp., Academic Press, Inc., San Diego, CA, USA, ISBN:0-12-554820-6.

Plougonven, R., and C. Snyder (2005), Gravity waves excited by jets: Propagation versus generation, *Geophys. Res. Lett.*, *32*(18), L18802, doi:10.1029/2005GL023730.

Plumb, R. A. (1983), Baroclinic instability of the summer mesosphere: A mechanism for the quasi-two-day wave?, *J. Atmos. Sci.*, *40*(1), 262–270, doi:$10.1175/1520-0469(1983)040<0262:\mathrm{BIOTSM}>2.0.\mathrm{CO};2$.

Polvani, L. M., and R. Saravanan (2000), The three-dimensional structure of breaking Rossby waves in the polar wintertime stratosphere, *J. Atmos. Sci.*, *57*(21), 3663–3685, doi:$10.1175/1520-0469(2000)057<3663:\mathrm{TTDSOB}>2.0.\mathrm{CO};2$.

Prata, A. J. (1989), Observations of the 5-day wave in the stratosphere and mesosphere, *J. Atmos. Sci.*, *46*(15), 2473–2477, doi:$10.1175/1520-0469(1989)046<2473:\mathrm{OOTWIT}>2.0.\mathrm{CO};2$.

Preusse, P., M. Ern, S. D. Eckermann, C. D. Warner, R. H. Picard, P. Knieling, M. Krebsbach, J. M. Russell, III, M. G. Mlynczak, C. J. Mertens and M. Riese (2006), Tropopause to mesopause gravity waves in August: Measurement and modeling, *J. Atmos. Solar-Terr. Phys.*, *68*(15), 1730–1751, doi:10.1016/j.jastp.2005.10.019.

Quiroz, R. S. (1969), The warming of the upper stratosphere in February 1966 and the associated structure of the mesosphere, *Mon. Weather Rev.*, *97*(8), 541–552, doi:$10.1175/1520-0493(1969)097<0541:\mathrm{TWOTUS}>2.3.\mathrm{CO};2$.

Rapp, M., F.-J. Lübken, A. Müllemann, G. E. Thomas and E. J. Jensen (2002), Small-scale temperature variations in the vicinity of NLC: Experimental and model results, *J. Geophys. Res.*, *107*(D19), 4392, doi:10.1029/2001JD001241.

Rapp, M., B. Strelnikov, A. Müllemann, F.-J. Lübken and D. C. Fritts (2004), Turbulence measurements and implications for gravity wave dissipation during the MaCWAVE/MIDAS rocket program, *Geophys. Res. Lett.*, *31*(24), L24S07, doi:10.1029/2003GL019325.

Rauthe, M., M. Gerding, J. Höffner and F.-J. Lübken (2006), Lidar temperature measurements of gravity waves over Kühlungsborn (54° N) from $1-105$ km: A winter-summer comparison, *J. Geophys. Res.*, *111*(D24), D24108, doi:10.1029/2006JD007354.

Rees, D., U. von Zahn, G. von Cossart, K. H. Fricke, W. Eriksen and J. A. McKay (2000), Daytime lidar measurements of the stratosphere and mesosphere at the ALOMAR observatory, *Adv. Space Res.*, *26*(6), 893–902, doi:$10.1016/S0273-1177(00)00027-2$.

Rodgers, C. D. (1976), Evidence for the five-day wave in the upper stratosphere, *J. Atmos. Sci.*, *33*(4), 710–711, doi:$10.1175/1520-0469(1976)033<0710:\mathrm{EFTFDW}>2.0.\mathrm{CO};2$.

Rowlett, J. R., C. S. Gardner, E. S. Richter and C. F. Sechrist, Jr. (1978), Lidar observations of wave-like structure in the atmospheric sodium layer, *Geophys. Res. Lett.*, *5*(8), 683–686.

Rüster, R., P. Czechowsky, P. Hoffmann and W. Singer (1996), Gravity wave signatures at mesopause heights, in *Proceedings of the 7^{th} Workshop on Technical and Scientific aspects of MST radars*, edited by B. Edwards, pp. 58–61, Hilton Head Island, South Carolina, USA.

Salby, M., F. Sassi, P. Callaghan, D. Wu, P. Keckhut and A. Hauchecorne (2002), Mesospheric inversions and their relationship to planetary wave structure, *J. Geophys. Res.*, *107*(D4), ACL 4/1–13, doi:10.1029/2001JD000756.

Salby, M. L. (1981), The 2-day wave in the middle atmosphere: Observation and theory, *J. Geophys. Res.*, *86*(C10), 9654–9660.

Salby, M. L. (1996), *Fundamentals of atmospheric physics*, 627 pp., Academic Press, San Diego, USA, ISBN:0-126-15160-1.

Sassi, F., R. R. Garcia, B. A. Boville and H. Liu (2002), On temperature inversions and the mesospheric surf zone, *J. Geophys. Res.*, *107*(D19), 4380, doi:10.1029/2001JD001525.

Sato, K., and M. Yamada (1994), Vertical structure of atmospheric gravity waves revealed by the wavelet analysis, *J. Geophys. Res.*, *99*(D10), 20,623–20,631, doi:10.1029/94JD01818.

Scheffler, A. O., and C. H. Liu (1986), The effects of Doppler shift on gravity wave spectra observed by MST radar, *J. Atmos. Terr. Phys.*, *48*(11-12), 1225–1231, doi:$10.1016/0021-9169(86)90041-3$.

Scherhag, R. (1952), Die explosionsartige Stratosphärenerwärmung des Spätwinters 1951/52, *Ber. Deut. Wetterdienstes i.d. US-Zone*, *6*(38), 51–63.

Schlüter, T. (1996), Modifikation und Weiterentwicklung der Fokalinstrumentierung für die ALOMAR – 1,8 m – Empfangsteleskope, Master's thesis, Universität Bonn, Bonn, Germany, BONN-IB-96-15.

Schmidlin, F. J. (1976), Temperature inversions near 75km, *Geophys. Res. Lett.*, *3*(3), 173–176.

Schmidlin, F. J. (1991), The inflatable sphere: A technique for the accurate measurement of middle atmosphere temperatures, *J. Geophys. Res.*, *96*(D12), 22,673–22,682.

Schöch, A. (2001), Untersuchung der Schwerewellen-Aktivität in der polaren Atmosphäre mit einem Rayleigh-Lidar auf Andøya in Nord-Norwegen, Master's thesis, Universität Rostock, Rostock, Germany.

Schöch, A. (2007), Technical improvements to the ALOMAR RMR lidar, *Tech. rep.*, Leibniz-Institute of Atmospheric Physics, Kühlungsborn, Germany, *in preparation*.

Schöch, A., and G. Baumgarten (2003), A new system for automatic beam stabilisation of the ALOMAR

RMR-lidar at Andøya in Northern Norway, in *Proceedings of the* 16^{th} *ESA Symposium on European Rocket and Balloon Programmes and Related Research*, vol. ESA SP–530, edited by B. Warmbein, pp. 303–307, St. Gallen, Switzerland.

Schöch, A., G. Baumgarten, D. C. Fritts, P. Hoffmann, A. Serafimovich, L. Wang, P. Dalin, A. Müllemann and F. J. Schmidlin (2004), Gravity waves in the troposphere and stratosphere during the MaCWAVE/MIDAS summer rocket program, *Geophys. Res. Lett.*, *31*(24), L24S04, doi:10.1029/2004GL019837.

Scorer, R. S. (1949), Theory of waves in lee of mountains, *Quart. J. Roy. Meteorol. Soc.*, *75*, 41–56.

Serafimovich, A. (2006), Investigation of gravity waves with vhf radar measurements, Ph.D. thesis, Universität Rostock, Rostock, Germany.

Serafimovich, A., P. Hoffmann, D. Peters and V. Lehmann (2005), Investigation of intertia-gravity waves in the upper troposphere/lower stratosphere over Northern Germany observed with collocated VHF/UHF radars, *Atmos. Chem. Phys.*, *5*(2), 295–310, SRef-ID:1680-7324/acp/2005-5-295.

She, C.-Y. (2001), ALOMAR Weber Sodium Lidar: A new lidar for measuring temperature, winds, and dynamics in the Arctic mesopause region, in *OWD1 - OSA/Optical Remote Sensing of Atmosphere*, invited paper.

She, C.-Y., J. D. Vance, B. P. Williams, D. A. Krueger, H. Moosuller, D. Gibson-Wilde and D. C. Fritts (2002), Lidar studies of atmospheric dynamics near polar mesopause, *Trans. Am. Geophys. Union (EOS)*, *83*(27), 289–293, doi:10.1029/2002EO000206.

Shibata, K., and K. Kodera (2005), Simulation of radiative and dynamical responses of the middle atmosphere to the 11-year solar cycle, *J. Atmos. Solar-Terr. Phys.*, *67*(1-2), 125–143, doi:10.1016/j.jastp.2004.07.022.

Shine, K. P. (1987), The middle atmosphere in the absence of dynamical heat fluxes, *Quart. J. Roy. Meteorol. Soc.*, *113*(476), 603–633, doi:10.1256/smsqj.47609.

Sica, R. J., and M. D. Thorsley (1996), Measurements of superadiabatic lapse rates in the middle atmosphere, *Geophys. Res. Lett.*, *23*(20), 2797–2800, doi:10.1029/96GL02642.

Sica, R. J., T. Thayaparan, P. S. Argall, A. T. Russell and W. K. Hocking (2002), Modulation of upper mesospheric temperature inversions due to tidal-gravity wave interactions, *J. Atmos. Solar-Terr. Phys.*, *64*(8-11), 915–922, doi:10.1016/S1364 − 6826(02)00046 − 9.

Siebert, J. S. (1996), Die ALOMAR Lidar–Teleskope: Justierverfahren und Laserstrahlführung, Master's thesis, Universität Bonn, Bonn, Germany.

Sigernes, F., N. Shumilov, C. S. Deehr, K. P. Nielsen, T. Svenøe and O. Havnes (2003), Hydroxyl rotational temperature record from the auroral station in Adventdalen, Svalbard (78° N, 15° E), *J. Geophys. Res.*, *108*(A9), 1342, doi:10.1029/2001JA009023.

Siskind, D. E., L. Coy and P. Espy (2005), Observations of stratospheric warmings and mesospheric coolings by the TIMED SABER instrument, *Geophys. Res. Lett.*, *32*(9), L09804, doi:10.1029/2005GL022399.

Skatteboe, R. (1996), ALOMAR: Atmospheric science using lidars, radars and ground based instruments, *J. Atmos. Terr. Phys.*, *58*(16), 1823–1826, doi:10.1016/0021 − 9169(95)00173 − 5.

States, R. J., and C. S. Gardner (1998), Influence of the diurnal tide and thermospheric heat sources on the formation of mesospheric temperature inversion layers, *Geophys. Res. Lett.*, *25*(9), 1483–1486, doi:10.1029/98GL00850.

Stein, B., M. D. Guasta, J. Kolenda, M. Morandi, P. Rairoux, L. Stefanutti, J. P. Wolf and L. Wöste (1994), Stratospheric aerosol size distributions from multispectral lidar measurements at Sodankylä during EASOE, *Geophys. Res. Lett.*, *21*(13), 1311–1314, doi:10.1029/93GL02891.

Stockwell, R. G., and R. P. Lowe (2001a), Airglow imaging of gravity waves – 1. Results from a small network of OH nightglow scanning imagers, *J. Geophys. Res.*, *106*(D15), 17,185–17,203, doi:10.1029/2001JD900035.

Stockwell, R. G., and R. P. Lowe (2001b), Airglow imaging of gravity waves – 2. Critical level filtering, *J. Geophys. Res.*, *106*(D15), 17,205–17,220, doi:10.1029/2001JD900036.

Suzuki, S., K. Shiokawa, Y. Otsuka, T. Ogawa and P. Wilkinson (2004), Statistical characteristics of gravity waves observed by an all-sky imager at Darwin, Australia, *J. Geophys. Res.*, *109*(D20), D20S07, doi:10.1029/2003JD004336.

Thayer, J. P., N. B. Nielsen, R. E. Warren, C. J. Heinselmann and J. Sohn (1997), Rayleigh lidar system for middle atmosphere research in the Arctic, *Optical Engineering*, *36*(7), 2045–2061.

Thayer, J. P., M. Rapp, A. G. Gerrard, E. Gudmundsson and T. J. Kane (2003), Gravity-wave influences on Arctic mesospheric clouds as determined by a Rayleigh lidar at søndrestrøm, greenland, *J. Geophys. Res.*, *108*(D8), 8449, doi:10.1029/2002JD002363.

Theon, J. S., W. Nordberg, L. B. Katchen and J. J. Horvath (1967), Some observations on the thermal behaviour of the mesosphere, *J. Atmos. Sci.*, *24*(4), 428–438, doi:10.1175/1520 − 0469(1967)024 < 0428 : SOOTTB > 2.0.CO; 2.

Thomas, G. E., J. J. Olivero, E. J. Jensen, W. Schröder and O. B. Toon (1989), Relation between increasing methane and the presence of ice clouds at the mesopause, *Nature*, *338*(6215), 490–492, doi:10.1038/338490a0.

Thomas, L., A. K. P. Marsh, D. P. Wareing, I. Austin and H. Chandra (1996), VHF echoes from the midlatitude mesosphere and the thermal structure observed by lidar, *J. Geophys. Res.*, *101*(D8), 12,867–12,877, doi:10.1029/96JD00218.

Torrence, C., and G. P. Compo (1998), A practical guide to wavelet analysis, *Bull. Amer. Meteorol. Soc.*, *79*(1), 61–78, doi:10.1175/1520 − 0477(1998)079 < 0061 : APGTWA > 2.0.CO; 2.

van Loon, H., and K. Labitzke (1990), Association between the 11-year solar cycle and the atmosphere. Part IV: The stratosphere, not grouped by the phase of the QBO, *J. Climate*, *3*(8), doi:10.1175/1520 − 0442(1990)003 < 0827 : ABTLYS > 2.0.CO; 2.

VanZandt, T. E. (1985), A model for gravity wave spectra observed by Doppler sounding system, *Radio Sci.*, *20*(6), 1323–1330.

Vincent, R. A., and M. J. Alexander (2000), Gravity wave in the tropical lower stratosphere: An observational study of seasonal and interannual variability, *J. Geophys. Res.*, *105*(D14), 17,971–17,982, doi:10.1029/2000JD900196.

Vincent, R. A., and D. C. Fritts (1987), A climatology of gravity wave motions in the mesopause region at Adelaide, Australia, *J. Atmos. Sci.*, *44*(4), 748–760, doi:10.1175/1520 − 0469(1987)044 < 0748 : ACOGWM > 2.0.CO; 2.

Vincent, R. A., S. J. Allen and S. D. Eckermann (1997), Gravity-wave parameters in the lower stratosphere, in *Gravity wave processes: Their parameterization in global climate models*, edited by K. Hamilton, pp. 7–25, Springer-Verlag.

von Cossart, G., J. Fiedler, U. von Zahn, K. H. Fricke, V. Nußbaumer, G. Nelke, F. Hübner, A. Hauchecorne, J. P. Marcovici, F. Fassina, D. Nedeljkovic, D. Rees and N. P. Meredith (1995), Modern technologies employed in the ALOMAR Rayleigh/Mie/Raman lidar, in *Proceedings of the* 12^{th} *ESA Symposium on European Rocket and Balloon Programmes and Related Research*, vol. ESA SP–370, edited by T. A. Blix, pp. 387–394, Lillehammer, Norway.

von Cossart, G., J. Fiedler and U. von Zahn (1999), Size distributions of NLC particles as determined from 3-color observations of NLC by ground-based lidar, *Geophys. Res. Lett.*, *26*(11), 1513–1516, doi:10.1029/1999GL900226.

von Zahn, U., and W. Meyer (1989), Mesopause temperatures in summer, *J. Geophys. Res.*, *94*(D12), 14,647–14,651.

von Zahn, U., and R. Neuber (1987), Thermal structure of the high latitude mesopause region in winter, *Contributions to Atmospheric Physics*, *60*(3), 294–304.

von Zahn, U., E. V. Thrane and R. Skatteboe (1995), The ALOMAR facility: Status and outlook, in *Proceedings of the* 12^{th} *ESA Symposium on European Rocket and Balloon Programmes and Related Research*, vol. ESA SP–370, edited by T. A. Blix, pp. 379–385, Lillehammer, Norway.

von Zahn, U., J. Fiedler, B. Naujokat, U. Langematz and K. Krüger (1998a), A note on record-high temperatures at the northern polar stratopause in winter 1997/98, *Geophys. Res. Lett.*, *25*(22), 4169–4172, doi:10.1029/1998GL900091.

von Zahn, U., G. von Cossart, J. Fiedler and D. Rees (1998b), Tidal variations of noctilucent clouds measured at 69° N latitude by groundbased lidar, *Geophys. Res. Lett.*, *25*(9), 1289–1292, doi:10.1029/98GL00546.

von Zahn, U., G. von Cossart, J. Fiedler, K. H. Fricke, G. Nelke, G. Baumgarten, D. Rees, A. Hauchecorne and K. Adolfsen (2000), The ALOMAR Rayleigh/Mie/Raman lidar: Objectives, configuration, and performance, *Ann. Geophys.*, *18*(7), 815–833, SRef-ID:1432-0576/ag/2000-18-815.

Wagner, D. (2000), Eine automatisierte Laserstrahl-Stabilisierung für das ALOMAR RMR-Lidar, Master's thesis, Universität Bonn, Bonn, Germany.

Wallace, J. M., and P. V. Hobbs (1977), *Atmospheric science – An introductory survey*, 467 pp., Academic Press, San Diego, USA, ISBN:0-127-32950-1.

Walterscheid, R. L., G. G. Sivjee and R. G. Roble (2000), Mesospheric and lower thermospheric manifestations of a stratospheric warming event over Eureka, Canada (80° N), *Geophys. Res. Lett.*, *27*(18), 2897–2900, doi:10.1029/2000GL003768.

Wang, L. (2003), Gravity wave analysis of four years of high vertical resolution U.S. radiosonde data, Ph.D. thesis, Stony Brook University, Stony Brook, NY, USA.

Wegener, A. (1912), Die Erforschung der obersten Atmosphärenschichten, *Zeitschrift für anorganische Chemie*, *75*(1), 107–131, doi:10.1002/zaac.19120750112.

Whiteway, J. A., and A. I. Carswell (1994), Rayleigh lidar observations of thermal structure and gravity wave activity in the high Arctic during a stratospheric warming, *J. Atmos. Sci.*, *51*(21), 3122–3136, doi:10.1175/1520 − 0469(1994)051 < 3122 : RLOOTS > 2.0.CO; 2.

Wiegand, R. C., and E. C. Carmack (1986), The climatology of internal waves in a deep temperate lake, *J. Geophys. Res.*, *91*(C3), 3951–3958.

Williams, B. P., D. C. Fritts, L. Wang, C.-Y. She, J. D. Vance, F. J. Schmidlin, R. A. Goldberg, A. Müllemann and F.-J. Lübken (2004), Gravity waves in the Arctic mesosphere during the MaCWAVE/MIDAS summer rocket program, *Geophys. Res. Lett.*, *31*(24), L24S05, doi:10.1029/2004GL020049.

Wu, D. L. (2006), Small-scale fluctuations and scintillations in high-resolution GPS/CHAMP SNR and phase data, *J. Atmos. Solar-Terr. Phys.*, *68*(9), 999–1017, doi:10.1016/j.jastp.2006.01.006.

Wu, D. L., and J. W. Waters (1996), Gravity-wave-scale temperature fluctuations seen by UARS MLS, *Geophys. Res. Lett.*, *23*(23), 3289–3292, doi:10.1029/96GL02924.

Young, A. T. (1981), Rayleigh scattering, *Appl. Opt.*, *20*(4), 533–535.

Zhang, F., S. Wang and R. Plougonven (2004), Uncertainties in using the hodograph method to retrieve gravity wave characteristics from individual soundings, *Geophys. Res. Lett.*, *31*(11), L11110, doi:10.1029/2004GL019841.

Zink, F., and R. A. Vincent (2004), Some inferences on turbulence generation by gravity waves, *J. Geophys. Res.*, *109*(D11), D11109, doi:10.1029/2003JD003992.

Zülicke, C., and D. Peters (2006), Simulation of inertia-gravity waves in a poleward breaking Rossby wave, *J. Atmos. Sci.*, *63*(12), 3253–3276, doi:10.1175/JAS3805.1.

List of Figures

List of Tables

List of abbreviations

ACVE	Atmospheric Chemistry Validation of ENVISAT
ALOMAR	Arctic Lidar Observatory for Middle Atmosphere Research
ALWIN	ALOMAR wind profiler
App.	appendix
ARCLITE	Arctic lidar technology
ARR	Andøya Rocket Range
CARMA	Community Aerosol and Radiation Model for Atmospheres
CHAMP	CHAllenging Minisatellite Payload
Chap.	chapter
CIRA86	COSPAR international reference atmosphere 1986
CNRS	Centre national de la recherche scientifique
CO_2	carbon dioxide
COSPAR	Committee on Space Research
DAS	Data Acquisitioning Subsystem
doi	digital object identifier
DoRIS	Doppler Rayleigh Iodine System
EASOE	European Arctic Stratospheric Ozone Experiment
ECMWF	European Centre for Medium-Range Weather Forecasts
Eq.	equation
ERA40	ECMWF re-analysis project ERA-40
ESA	European Space Agency
FFI	Norwegian Defence Research Establishment
Fig.	figure
FOV	field of view
GOME	Global Ozone Monitoring Experiment
GPS	Global Positioning System
GW	gravity waves
GWPED	gravity wave potential energy density
H_2O	water
IAP	Leibniz-Institute of Atmospheric Physics
IEEE	Institute of Electrical and Electronics Engineers Inc.
IPSL	Institut Pierre Simon Laplace
IR	infrared
ISAMS	Improved Stratospheric And Mesospheric Sounder
LAS	Emitting power lasers and seeder laser subsystem
laser	light amplification by stimulated emission of radiation
LASP	Laboratory for Atmospheric and Space Physics (University of Colorado)
lidar	light detection and ranging
LIMA	Leibniz-Institute Middle Atmosphere model
Luebken1999	Reference atmosphere published by *Lübken* [1999]
MaCWAVE	Mountain and Convective Waves Ascending Vertically
MAP	Middle Atmosphere Program
MAP/WINE	Middle Atmosphere Program / Winter In Northern Europe
MIDAS	MIddle atmosphere Dynamics And Structure

MIL	mesospheric inversion layer
MLS	Microwave Limb Sounder
MLT	Mesosphere/Lower-Thermosphere
MST	Mesosphere, Stratosphere, Troposphere
N_2	nitrogen
NAI	Notes des activités instrumentales de l'IPSL
NASA	National Aeronautics and Space Administration
Nd:YAG	Neodym:Yttrium Aluminium Garnet
NILU	Norwegian Institute for Air Research
NLC	noctilucent clouds
NO	nitric oxide
NOAA	National Oceanic & Atmospheric Administration
NRL	US Naval Research Laboratory
NRLMSISE00	NRL Mass Spectrometer Incoherent Scatter Radar Extended Model 2000
O	atomic oxygen
O_2	molecular oxygen
O_3	ozone
OH	hydroxyl radical
OSA	Optical Society of America
PC	personal computer
QBO	Quasi-biennial oscillation
radar	radio detection and ranging
RMR	Rayleigh/Mie/Raman
SA	Service d'aéronomie du CNRS
SABER	Sounding of the Atmosphere using Broadband Emission Radiometry
SCOSTEP	Scientific Committee On Solar-TErrestrial Physics
Sec.	section
SME	Solar Mesophere Explorer
S/N	signal-to-noise ratio
SOLSTICE	Studies Of Layered STructures and ICE
SOUSY	SOUnding SYstem for atmospheric structure and dynamics
SPIE	The International Society for Optical Engineering
SRef-ID	scientific reference identification key
SSW	sudden stratospheric warming
Tab.	table
TEL	Receiving telescope subsystem
TIMED	Thermosphere Ionosphere Mesosphere Energetics and Dynamics
UARS	Upper Atmosphere Research Satellite
USAF	United States Air Force
UT	universal time
UV	ultraviolet
VHF	very high frequency
VIS	visible
WKB	Wentzel-Kramers-Brillouin
WMO	World Meteorological Organisation

List of symbols

$\vec{\ }$	denotes vectors $\in \mathbb{R}^3$
$\hat{\ }$	denotes intrinsic parameters of gravity waves
$\frac{D}{dt}$	denotes Eulerian derivation including advection $\frac{D}{dt} = \frac{\partial}{\partial t} + \vec{u}(\vec{x}, t) \cdot \vec{\nabla}$
A	wave action density
$\tilde{A}$	gravity wave amplitude
A_0	gravity wave amplitude at source
β	total volume backscatter coefficient
β_{air}	volume backscatter coefficient of air
β_{NLC}	volume backscatter coefficient of NLC
$\vec{c_g}$	group velocity
c_h	horizontal phase speed
c_p	specific heat at constant pressure (1004.64 $\mathrm{Jkg^{-1}K^{-1}}$ for air at atmospheric conditions)
$\vec{c_{ph}}$	phase velocity
c_s	speed of sound $c_s = \sqrt{\gamma RT}$
c_v	specific heat at constant volume
c_x	zonal phase speed
c_y	meridional phase speed
$E_{kin,M}$	gravity wave kinetic energy per mass
$E_{pot,M}$	available gravity wave potential energy per mass
$E_{pot,V}$	gravity wave potential energy per volume
$E_{tot,M}$	total gravity wave energy per mass
$\vec{F}$	Eliassen-Palm flux
$\vec{F_r}$	friction force near the Earth's surface
f	Coriolis parameter $f = 2\,\Omega \sin(\phi)$ ($\widehat{=}$ 12.8 hrs at 69.3° N)
f_0	mean Coriolis parameter in Eulerian mean
γ	adiabatic index (1.4 for air at atmospheric conditions)
g	gravitational acceleration
H	pressure scale height $H = \frac{k_B T}{g M}$
H_ρ	density scale height $\frac{1}{H_\rho} = \frac{1}{\bar{\rho}} \frac{\partial \bar{\rho}}{\partial z}$
I	intensity
$Im\{x\}$	Imaginary part of x
$\overline{J}$	zonal mean diabatic heating
$\vec{k}$	wave number vector $\vec{k} = (k, l, m)$
k	zonal wave number
k_B	Boltzmann constant $1.38 \cdot 10^{-23}$ $\mathrm{J\,K^{-1}}$
l	meridional wave number
λ	wavelength
λ_z	vertical wavelength
M	mean molecular weight of air (28.97 g $\mathrm{mol^{-1}}$ = $4.81 \cdot 10^{-26}$ kg $\mathrm{atom^{-1}}$)

m	vertical wave number
N	Brunt-Väisälä or buoyancy frequency
$N_{counted}$	measured count frequency
N_{max}	maximum detector count frequency
n	molecular number density
n	number of single temperature profiles
Ω	Earth's angular rotation rate ($7.27{\cdot}10^{-5}$ rad s^{-1})
$\hat{\omega}$	intrinsic frequency $\hat{\omega} = \omega - \vec{k}\vec{u}$
ω	observed wave frequency
ω_c	critical frequency
p	pressure
$\tilde{p}$	pressure wave amplitude
ϕ	latitude
R	universal gas constant ($8.134\,\mathrm{J\,K^{-1}mol^{-1}}$)
Ri	Richardson number
ρ	density
$\tilde{\rho}$	density wave amplitude
S	entropy
σ	scattering cross-section
T	temperature
T'	temperature fluctuations around mean
$\mathcal{T}$	atmospheric transmission
T_0	start temperature for temperature integration
τ	detector dead-time
Θ	potential temperature
T_i	single temperature profile
$\overline{T}$	mean temperature
t	time
$\vec{u}$	wind field vector $\vec{u} = (u, v, w)$
u	zonal wind
$\tilde{u}$	zonal wind wave amplitude
v	meridional wind
$\tilde{v}$	meridional wind wave amplitude
v^*	meridional wind in transformed Eulerian mean
w	vertical wind
w^*	vertical wind in transformed Eulerian mean
$\tilde{w}$	vertical wind wave amplitude
$\vec{X}$	gravity waves drag
$\overline{X}$	zonal mean small-scale eddy zonal drag
$\vec{x}$	position vector
z	altitude (geometric)
z_0	reference height
Δz	spacing of the lidar altitude bins
z_{min}	minimum altitude for integration

Acknowledgements

The data presented in this thesis has been acquired over many years at the ALOMAR observatory. I would like to thank all current and previous colleagues at ALOMAR for their effort to run the RMR lidar, to support us in all possible ways when we are at ALOMAR and to help us with the maintenance of the RMR lidar system. This big thank you includes but is not restricted to Reidar Lyngra, Kolbjørn Bekkelund, Sandra Blindheim, Asbjørn Eliassen, Dr. Michael Gausa, Martin Langteigen, Anette Pedersen, Werner Eriksen, Sven Larsen, Ivar Nyheim, Dimitri Antonov, Per-Egil Nilsen, Sven Sæther, Leon Olsen and all the ARR personnel which offers support when needed at ALOMAR.

A number of people from IAP have also been at ALOMAR during the summer measurement campaigns to run the lidar. I would like to extend my thanks to everybody who helped collect the huge data set which we now have from the ALOMAR RMR lidar.

Many ideas, suggestions and help I received from Dr. Gerd Baumgarten. He introduced me to the telescopes when I started my diploma thesis at IAP and has ever since helped me in countless discussions and provided guidance during my Ph.D. thesis work. A similar big thank you is also due to the other colleagues of the IAP ALOMAR group, namely Dr. Jens Fiedler, Prof. Götz von Cossart and Prof. Ulf von Zahn. They all contributed in many ways to the team achievement of running the RMR lidar at its Arctic location and gave many helpful comments in the 7 years I spent at IAP. Different parts of the gravity wave analysis were developed with the support of the diploma students Stefan Loßow and Gaute Birkeli.

Prof. Lübken offered the chance to take my diploma at IAP and later continue for a Ph.D. thesis at IAP. He also offered many suggestions which influenced the work as presented in this thesis. I would like to thank him for the opportunity to perform this work at IAP.

All other colleagues at IAP deserve thanks as well for always being helpful and open to all my questions even though they may have been silly or little thought through at times.

Many useful hints and information was also provided by Dr. K. H. Fricke at Bonn University and Dr. Ulrich Blum (currently at FFI in Kjeller/Norway).

I would also like to extend a big thank you to my girlfriend for all the support I got from her when the amount of work still to be done seemed unsurmountable and when the analysis and the writing of this thesis took more time than I had hoped.

The author is also grateful to NILU for providing ECMWF data. Part of the data presented here was acquired during stays at ALOMAR supported by the European Commission through the ALOMAR (enhanced) Access to Research Infrastructure programs.

Most plots in this thesis have been produced with the DISLIN scientific plotting library under Linux (see http://www.dislin.de/). The wavelet transformations have been calculated using code from *Torrence and Compo* [1998] (http://atoc.colorado.edu/research/wavelets/). The FITPACK library from *Dierckx* [1993] (http://www.netlib.org/dierckx/) has been used to estimate the background state during falling sphere profile processing.

Curriculum Vitae

Armin Rudolf Schöch

(born 5 September 1975 in Ulm/Germany)

Dec 2001	–	present	Ph.D. position at the Leibniz-Institute of Atmospheric Physics in Kühlungsborn. Lidar data analysis to investigate middle atmosphere temperatures and gravity waves. Study of mesospheric cooling during sudden stratospheric warmings and of mesospheric inversion layers. Involvement in the international MaCWAVE/MIDAS rocket campaign. Programming of control software for the instrument.
Aug 2003	–	Sep 2003	6 weeks IAESTE traineeship at the University of Tel Aviv/Israel in the group of Prof. Avi Gover.
Jul 2000	–	Sep 2001	Diploma thesis work at the Leibniz-Institute of Atmospheric Physics in Kühlungsborn/Germany. Thesis work on "Untersuchung der Schwerewellen-Aktivität in der polaren Atmosphäre mit einem Rayleigh-Lidar auf Andøya in Nord-Norwegen". Participation in the international MIDAS/SOLSTICE rocket campaign.
Apr 1999	–	Sep 2001	Physics study at the University of Rostock/Germany. Graduation in September 2001 with the "Diploma in Physics".
Jan 1999	–	Mar 1999	Traineeship at the Max-Planck-Institute of Meteorology in Hamburg under the supervision of Dr. S. Bakan and L. Fiedler. Programming of control software for an IR-interferometer instrument and for several other meteorological instruments. Participation in instrument validation and measurement campaigns.
Aug 1998	–	Dec 1998	Taking courses at the University Centre on Svalbard (UNIS) in "Polar Meteorology", "The Middle Polar Atmosphere", "Space Activity and Remote Sensing" and "Arctic Technology" as part of the studies at the University in Tromsø.
Aug 1997	–	Dec 1998	Physics study at the University of Tromsø/Norway. Graduated with "Candidatus Magisterii" (Bachelor of Science) degree.
Oct 1995	–	Jul 1997	Physics study at the University of Ulm/Germany. Finished with the "Vordiplom" degree.
Dec 1994	–	Oct 1995	Au-pair in a Norwegian/German family in Hasvik/Norway where I learnt Norwegian.
Aug 1981	–	Jul 1994	Primary and secondary education at the "Freie Waldorfschule Römerstraße" in Ulm/Germany. Graduation with the "Abitur".

Erklärung

Hiermit versichere ich an Eides statt, die vorgelegte Arbeit selbstständig und ohne fremde Hilfe verfasst, keine außer den von mir angegebenen Hilfsmitteln und Quellen dazu verwendet und die den benutzten Werken inhaltlich oder wörtlich entnommenen Stellen als solche kenntlich gemacht zu haben.

Die Arbeit wurde bisher weder im Inland noch im Ausland in gleicher oder ähnlicher Form einer anderen Prüfungsbehörde vorgelegt. Weiterhin erkläre ich, dass ich ein Verfahren zur Erlangung des Doktorgrades an keiner anderen wissenschaftlichen Einrichtung beantragt habe.

Kühlungsborn, den 7. März 2007

(Armin Schöch)